Modeling Pluto's Atmosphere and Volatile Inventory Throughout Time

by

Perianne E. Johnson

B.S., New Mexico Institute of Mining and Technology, 2016

M.S., New Mexico Institute of Mining and Technology, 2017

M.S., University of Colorado Boulder, 2019

A thesis submitted to the

Faculty of the Graduate School of the

University of Colorado in partial fulfillment

of the requirements for the degree of

Doctor of Philosophy

Department of Astrophysical and Planetary Sciences

2023

Committee Members:

Larry Esposito, Chair

Leslie Young, Co-Chair

Zachory Berta-Thompson

Carolyn Crow

Dave Brain

Johnson, Perianne E. (Ph.D., Astrophysical and Planetary Sciences)

Modeling Pluto's Atmosphere and Volatile Inventory Throughout Time

Thesis directed by Drs. Leslie Young and Larry Esposito

In this thesis, I explore feedbacks between Pluto's surface and atmosphere over three distinct timescales. Through volatile transport, Pluto's atmosphere affects and is affected by a myriad of other systems and processes active on the dwarf planet throughout the age of the solar system.

In Chapter 2, I model Pluto's atmosphere in the modern day. Constrained by historical ground-based occultations and the *New Horizons* mission, I predict the annual surface temperature and atmospheric pressure variation for four assumptions about the distribution of nitrogen ice on Pluto's surface. Pluto's atmosphere is not likely to collapse at aphelion or winter solstice, and the minimum pressure will remain at or above the 0.1 microbar level for all but extreme ice assumptions. Additionally, I model the atmospheric temperature and pressure over the past 10 million years to encompass several of Pluto's obliquity cycles and periods of extreme seasons. Even on this longer timescale, haze production is not likely to be interrupted by a reduction in atmospheric pressure, so another mechanism must be responsible for the observed surface heterogeneity.

In Chapter 3, I model the infill of Pluto's Sputnik Planitia basin via condensation from the atmosphere and the subsequent reorientation of the basin. The timing of the infill is uncertain, but likely occurred around 4 billion years ago. Sputnik Planitia, Pluto's "heart," is a 1000-km wide purported impact basin that is filled with a several kilometer thick ice sheet of nitrogen and methane ice and is located very close to the anti-Charon point. This location near the tidal axis is a hallmark of true polar wander, and in fact it has been previously shown that true polar wander is a plausible mechanism for reorienting Sputnik Planitia. My work strengthened this argument by coupling a true polar wander model and a climate model in order to realistically model the growth of the ice sheet subject to insolation patterns. I constrained the total amount of ice in Sputnik Planitia to 1 - 2 km, and the initial location to most likely the 35° - 55°N latitude band.

In Chapter 4, I step back even further in time to model the loss of nitrogen from Pluto's atmosphere during the time period of giant planet migration, 4.5 billion years ago. Pluto and its neighboring Plutinos formed closer to the Sun and were driven outwards in a chaotic process when the orbits of the giant planets of the solar system were unstable, a time period I term the "Wild Years." In order to know the amount of nitrogen that Pluto started out with, this time period of much hotter and much cooler environmental conditions needs to be modeled. I estimate the loss of nitrogen via three mechanisms: photochemical destruction, atmospheric escape, and impact erosion. While these losses will be significantly underestimated if the present-day rates are used, even accounting for higher rates of loss during the Wild Years results in a small overall loss relative to the amount of nitrogen observed on Pluto today. Thus, I conclude that Pluto's primordial nitrogen inventory was not significantly different to its present-day inventory.

Dedication

Dedicated to explorers, past and future

Acknowledgements

The life of a theorist can be a solitary affair, but I am very lucky to have had such a strong support system.

Firstly, I have an amazing advisor, advocate, mentor, and role model in Leslie. There are so many things I could say, but Leslie has a habit of saying "here are two reasons why...," so here are two reasons (by her count) why Leslie has been a great advisor. Leslie always had time for me, to answer questions or talk over next steps or read paper drafts. She is very proactive about introducing me to other scientists and promoting my work, and challenging me to self-promote as well, for which I am immensely grateful. Leslie is great about sharing her excitement for my results, even at times when I myself didn't know they were exciting, which was more motivating than I think she knows. Thank you for everything, Leslie.

I would not have achieved all I did with Leslie if it had not been for my first research group, Raúl Morales-Juberías and Rick Cosentino at New Mexico Tech. Raúl was an immense help throughout my five years at NMT, starting by encouraging me to take a coding class in my first semester of college and continuing through my time as a masters student in his Jovian atmosphere research group. Rick was, and still is, my go-to fount of professional wisdom, from helping me survive my first conference to giving advice on applying to graduate school (he's the one who suggested CU!) and now to figuring out post-grad plans.

My first foray down the astro path was watching *Stargate* and *Stargate: Atlantis* every week with my self-described nerdy family (Mom excluded). From my dad's "there is no crying in ~~baseball~~ math" rule growing up to being forced to watch *Mythbusters* and *How It's Made* by my brother

Zach, we are a STEM family, through and through. I am super grateful to my family for supporting and understanding me in my 23 years of school.

A final thank you to a variety of groups: to my best friends, Aylecia and Raven, for encouraging me, distracting me, and telling me to stop being such a baby, at the appropriate times throughout my time at CU. And to the rest of my friends in Boulder, at CU, SwRI, and beyond. To the *New Horizons* mission science team, for welcoming me in and supporting my research endeavors, in addition to the small task of running the first mission to Pluto. Thank you.

Contents

Chapter

Tables

Table

Figures

Figure

Chapter 1

An Introduction to Pluto

1.1 History of Pluto Observations

Dim, distant, and diminutive Pluto was not known to the ancient astronomers, unlike many of the other solar system worlds. Its namesake, the Greek and Roman god of the underworld, evokes an ancient origin, but in fact Pluto was discovered by Clyde Tombaugh at Arizona's Lowell Observatory not even a century ago, in 1930. Pluto was discovered by painstakingly comparing photographic plates taken with a 13-inch telescope several nights apart and looking for objects that moved between the two observations (Binzel and Schindler, 2021).

After Pluto's discovery, the logical follow-on question was "are there more objects beyond Pluto?" Tombaugh searched for more objects like Pluto for 13 years, but didn't discover any. Mid-century astronomers Edgeworth and Kuiper both proposed a ring of icy bodies beyond the orbit of Neptune (Edgeworth, 1943, 1949; Kuiper, 1951), which would become known as the Kuiper Belt. Pluto was thus retroactively the first known Kuiper Belt Object (KBO). It wasn't until 60 years after the discovery of Pluto that improvements to telescope technology, namely CCDs, allowed for the discovery of the next KBO, 1992 QB_1, by the team of Jewitt and Luu (Jewitt and Luu, 1993). This discovery was followed by many more, and at time of writing the number of known KBOs is in the thousands, while the predicted total number of KBOs greater than 100 km in size is in the hundreds of thousands (Morbidelli et al., 2021).

Pluto's large moon, Charon, was discovered in 1978 (Christy and Harrington, 1978) by noticing that images of Pluto were consistently elongated, rather than circular. Repeated observations

and analysis of the elongation implied a period of 6.3867 days and a combined system mass of 0.0017 Earth masses. This mass, along with an estimate of 1500 km for Pluto's radius, suggested a bulk density of 700 kg/m^3, implying a composition dominated by ices. Indeed, spectroscopic observations by Cruikshank et al. (1976) had recently detected the presence of methane frost on Pluto's surface.

Serendipitously, shortly after the discovery of Charon it was noted that the orbital geometry of Pluto and Charon would create an epoch of "mutual events" (in which Pluto and Charon pass in front of and behind each other as seen from the Earth) (Andersson, 1978), beginning in 1985. These mutual events occurred every 3 days (twice per Charon orbital period about Pluto) for 6 years, and they won't be observable from Earth again until the year 2130 or so (half of a Pluto year from 1985) (Binzel et al., 1985). Repeated observations of mutual events allowed for the construction of an albedo map of the Charon-facing (also called the "sub-Charon") hemisphere of Pluto (as well as the Pluto-facing hemisphere of Charon, not discussed here) (Young and Binzel, 1993; Buie et al., 1992; Young et al., 1999). Pluto and Charon are tidally locked to one another, so the same hemisphere of each body is always facing the other body, and thus the mutual events only reveal information about one hemisphere of each body. Figure 1.1 shows the normal reflectance map of the sub-Charon hemisphere of Pluto created by (Young et al., 1999), combining data from many mutual event observations at both the University of Texas McDonald Observatory and the University of Hawaii's 88-inch telescope. The mutual event map showed large contrasts in normal reflectance, with bright polar caps and a dark equatorial feature (reminiscent of Cthulhu Macula, seen in Figure 1.2), suggestive of a dynamic world where volatile transport could be responsible for "refreshing" and brightening ice deposits as the seasons changed on Pluto.

An occultation, observed on the ground in Australia (Hubbard et al., 1988) and by the Kuiper Airborne Observatory (Elliot et al., 1989) confirmed for the first time that Pluto had an atmosphere. An occultation, similar to an exoplanet transit, is the process in which a nearby object (in this case Pluto) passes in front of a background star relative to the observer, temporarily dimming the light from the star. An atmosphere, if present, will dim the starlight slightly based on the

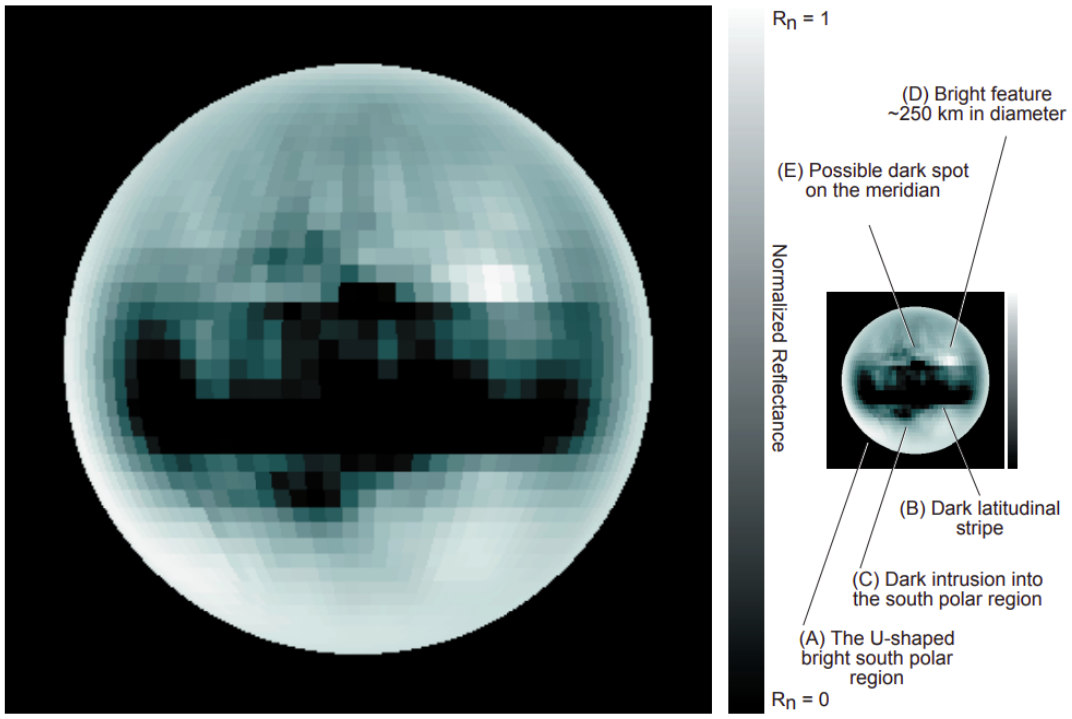

Figure 1.1: Figure and caption reproduced from Young et al. (1999), their Figure 7: B-Filter map of normal reflectances of Pluto's sub-Charon hemisphere. Units are normal reflectances.

thickness of the atmosphere, while the solid body of the object will entirely block the starlight from being observed. Modeling of the 1988 occultation lightcurve suggested an atmospheric pressure at the half-light level (1214 ± 20 km from Pluto's center) of 0.78 μbar, assuming a pure-methane atmosphere.

Several years after the first detection of Pluto's atmosphere, nitrogen and carbon monoxide ices were spectroscopically observed at Pluto (Owen et al., 1993). The nitrogen observation implied that it was 50 times more abundant than the other trace species and nitrogen is more volatile than the others, indicating that the atmosphere must be predominately nitrogen, rather than methane. The surface temperature was not known at this point, so Owen et al. (1993) reported surface pressures at two possible temperatures: 1.2 μbar at 34 K and 590 μbar at 45 K. Over the next decade or so, continued observations and spectral modeling of Pluto refined knowledge of the composition of the surface ices, working towards untangling the patchwork of pure methane ices, methane-rich ices with a small amount of nitrogen dissolved, nitrogen-rich ices with a small amount of methane dissolved, and pure nitrogen ices (e.g., Grundy and Fink, 1996; Douté et al., 1999; Grundy and Buie, 2001). Carbon monoxide was observed to be in the various ice components as well. The importance of a Titan-like tholin material was also discovered to be necessary for models to match spectral observations (Olkin et al., 2007). Adding to the complicated composition story is the fact that observed changes to the spatial distribution of the various ices could be due to either volatile transport or observing/orbital geometry, or both. Pluto was observed with the Hubble Space Telescope in 2002 and 2003, and these spatially-resolved visible observations revealed even more of Pluto's heterogeneous surface (Buie et al., 2010).

At the same time as these ground-based spectroscopic observations, a myriad of Pluto occultations were being observed. Similar to the serendipity of the mutual event timing, in the lead-up to the *New Horizons* flyby Pluto's orbit took it "through" the galactic plane along the line of sight from Earth, so Pluto passed in front of many bright background stars and many occultations were observed (see Meza et al. (2019) for a comprehensive review of all of the occultations). The general trend taken from these occultations was a steady increase in atmospheric pressure, from 4.28 ± 0.44

μbar in 1988 (Hubbard et al., 1988; Elliot et al., 1989) to 12.0 $\pm$ 0.09 μbar in 2013 (Dias-Oliveira et al., 2015). This increase continued even after Pluto passed through perihelion in 1990, because the surface pressure depends more on the subsolar latitude than on the heliocentric distance (see Chapter 2 for more details).

In these few pages, I have attempted to summarize nearly 100 years of Pluto study. I will next discuss the *New Horizons* mission to Pluto, which revolutionized our knowledge of the world and was the dawn of a new era of Pluto exploration.

1.1.1 The *New Horizons* Mission

NASA's *New Horizons* mission was the eventual winner of a long and complicated process to get a spacecraft mission to Pluto approved and launched. *New Horizons* was the first mission to an unexplored world, placing it in a class with the Pioneer and Voyager missions in terms of the breadth of reconnaissance that needed to be done, but with a much smaller budget, and due to the improved technology, the ability to return far more data than the early exploratory missions to other planets. The mission launched in 2006, performed a gravity assist (and collected scientific data) at Jupiter in 2007, before continuing its long cruise to the outer solar system. The intense final approach and the encounter flyby of Pluto occurred on July 14, 2015. The closest approach distance was 12,500 km from Pluto's surface, and occurred when Pluto was 32.9 AU from the Sun. Due to the speed of the flyby, high-spatial-resolution data was limited to essentially one hemisphere. After the flyby of the Pluto system, *New Horizons* went on to have a successful close encounter of Cold-Classical KBO Arrokoth in an extended mission, and as of the time of this writing, was still fully operational and on the hunt for a potential third KBO close encounter.

The highest priority science objectives for *New Horizons* were to (1) characterize the global geology and morphology of Pluto and Charon, (2) map the surface composition of Pluto and Charon, and (3) characterize the neutral atmosphere of Pluto and its escape rate (Weaver, 2021). This thesis builds upon observations undertaken from each of these three objectives: Chapter 2 utilizes surface composition data from objective (2), Chapter 3 is dependent on geologic and topographic data

relevant to objective (1), and Chapter 4 uses the escape rate and atmospheric structure models derived to satisfy objective (3). *New Horizons* was an enormous success, satisfying all of these objectives, along with lower-priority objectives as well, enabling the creation of this thesis (and I'm sure many others!).

New Horizons carried seven science instruments with it to Pluto (see Weaver (2021) for a more detailed description of instrument capabilities):

(1) Ralph (consisting of two components, the Multispectral Visible Imaging Camera (MVIC) and the Linear Etalon Imaging Spectral Array (LEISA))

(2) Alice (an ultraviolet imaging spectrograph)

(3) Radio EXperiment (REX)

(4) LOng-Range Reconnaissance Imager (LORRI)

(5) Solar Wind At Pluto (SWAP, a low-energy plasma in- strument)

(6) Pluto Energetic Particle Spectrometer Science Investigation (PEPSSI, a high-energy plasma instrument)

(7) Venetia Burney Student Dust Counter (VB-SDC)

The research in this thesis uses surface composition data from LEISA, albedo and topographic maps derived from LORRI and MVIC images, surface pressures from a REX radio occultation, and atmospheric structure and escape rates derived from Alice and REX data.

Listing all of the scientific discoveries and advancements from *New Horizons* here would be infeasible. Instead, I will focus on those directly relevant to this thesis. Figure 1.2 shows the highest-resolution global mosaic map of Pluto from *New Horizons*. Most of the southern hemisphere was in polar night and thus unobservable by *New Horizons*; this region is shown as black in the map. The higher resolution area of the map is the encounter hemisphere, or "nearside," the hemisphere facing the spacecraft as it made its closest approach. The lower-resolution area, or "farside" was

imaged by the spacecraft from slightly further away. The large, bright, tear-drop shaped region called Sputnik Planitia is an expansive ice sheet partially filling a large topographic depression, hypothesized to be an ancient impact basin. Sputnik Planitia is the focus of Chapter 3.

Figure 1.3 is adapted from Protopapa et al. (2017), and shows the spatial distribution of methane-rich ice (CH_4:N_2), nitrogen-rich ice (N_2:CH_4), water ice (H_2O-ice) and tholin material across the surface of Pluto, resulting from spectral modeling of LEISA data from *New Horizons*. The colorscale, which is the same for all four maps, indicates fractional abundance of a given material, meaning the percentage of each pixel that needs to be covered by the given material in order for the modelled spectrum to match the observed spectrum. Tholins are the dominant surface material only in Cthulhu Macula, the dark region to the west of Sputnik Planitia. Water ice, which forms Pluto's bedrock, is a minor surface material across the observed surface, because most of the surface is covered with a layer of volatile ice or tholin material. Nitrogen-rich ice is the most abundant material in a midlatitude band between roughly 30° and 60°N, while methane-rich ice dominates at the north pole and in Eastern Tombaugh Regio (the area directly to the east of Sputnik Planitia). Sputnik Planita itself seems to consist of nearly equal abundances of methane- and nitrogen-rich ices, at least at the surficial levels probed by these observations. The spatial distribution of nitrogen-rich ice in particular, both from Protopapa et al. (2017) for the encounter hemisphere and from Gabasova et al. (2021) for the farside, feature extensively in Chapter 2.

1.1.2 Post-Flyby Observations of Pluto

Pluto occultations have continued to be observed in the time since the flyby. Occultations observed in the summers of 2016 (Meza et al., 2019), 2018 (Young et al., 2021), and 2020 (Sicardy et al., 2021) all yielded surface pressures in the range of 11 - 12.5 μbar, similar to the *New Horizons* value of 11.5 μbar, indicating that Pluto's atmosphere remains in a pressure plateau. One of the teams observing the 2020 occultation (Poro et al., 2021), and a separate team observing an occultation in 2019 (Arimatsu et al., 2020) have reported much larger decreases in surface pressure (6.72 μbar and 9.56 μbar, respectively, for the 2020 and 2019 pressures). Such a rapid decrease is

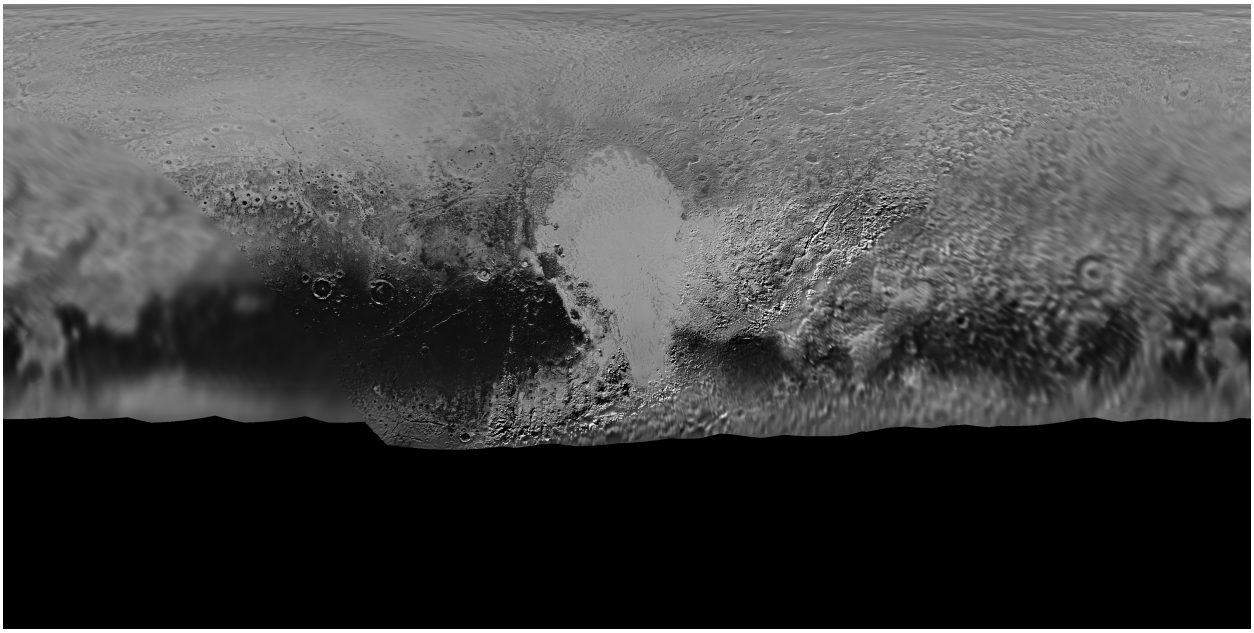

Figure 1.2: Global mosaic map of Pluto from *New Horizons* (NASA/Johns Hopkins University Applied Physics Laboratory/Southwest Research Institute)

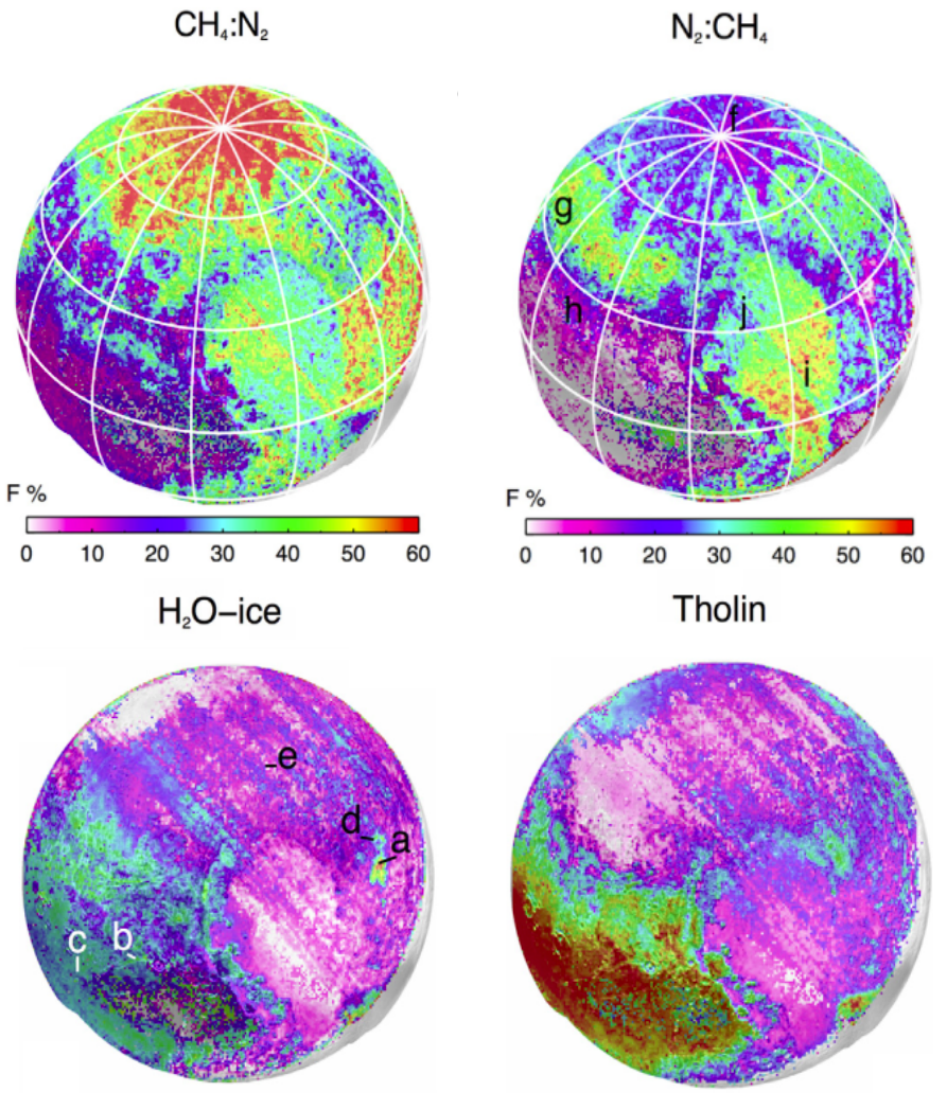

Figure 1.3: Composition maps of Pluto's surface, adapted from Protopapa et al. (2017). The colorscale represents the fraction of each pixel that is covered by the indicated material: methane-rich ice (CH_4:N_2, top left), nitrogen-rich ice (N_2:CH_4, top right), water ice (H_2O-ice, bottom left) and tholin material (bottom right).

not supported by models (see for example Chapter 2), and is unexplained at this point. Continued monitoring of Pluto's surface pressure over the next decade or so will be crucial for distinguishing between models and could even serve as a constraint for the distribution of nitrogen ice in Pluto's unobservable southern hemisphere.

Buie et al. (2021) gives a comprehensive explanation of possible future exploration pathways for Pluto. Existing and near-future observatories, such as JWST, should prove useful for characterizing Pluto's composition and atmosphere from the Earth or near-Earth orbit. If the path set by NASA's exploration of other planets in the solar system is to be followed, the next step for spacecraft exploration of Pluto would be an "orbital tour"-style mission, providing global coverage at high spatial and temporal resolution which was missing from the *New Horizons* flyby-style mission. One such orbiter mission concept is *Persephone* (Howett et al., 2021). While follow-on missions would be almost invaluable for their ability to detect changes on the dynamic world of Pluto and to be more technologically-equipped than *New Horizons*, any follow-on mission would be severely challenged by the long cruise to reach Pluto as it recedes from the Sun, power limitations, and data downlink difficulties from a mission past 30 AU (Buie et al., 2021).

1.2 An Overview of the Pluto System

Pluto is the largest known KBO, with a radius of 1188.3 ± 1.6 km (Nimmo et al., 2017), and the second most massive KBO at 1.303 ± 0.0003 x 10^{22} kg (Brozović et al., 2015) (dwarf planet Eris in the scattered disk is the most massive (Brown and Schaller, 2007)). Its density is 1854 ± 11 kg/m^3, falling between that of water ice (1000 kg/m^3) and most rocks ($\sim$ 3000 kg/m^3) indicating a mixed ice/rock bulk composition, with 70% rock by mass (Nimmo and McKinnon, 2021). *New Horizons* images placed an upper limit of <0.6% on Pluto's oblateness, meaning the equatorial radius is at most 7 km larger than the polar radius (Nimmo et al., 2017). This minimal flattening implies that Pluto's interior must have remained warm and deformable during the early orbital evolution of Charon; otherwise, a remnant "fossil bulge" would be preserved and the equatorial radius would be even larger than the polar radius.

Pluto is highly likely to be fully differentiated, although this cannot be definitively proven with the available data (Nimmo and McKinnon, 2021). Figure 1.4 shows three possible internal structures, reproduced from Figure 1 of Nimmo and McKinnon (2021). In general, Pluto's rock and hydrated rock core most likely has a radius of 850 km, overlain by a liquid water (potentially mixed with ammonia) ocean of around 100 km thickness, which is covered by a solid water ice crust. While there is no direct evidence for a subsurface ocean on Pluto, there is ample circumstantial evidence, as detailed by Nimmo and McKinnon (2021):

- Radioactive decay inside of Pluto's core produces enough heat over the age of the solar system to fully melt Pluto's entire ice inventory.
- Pluto's surface records primarily extensional faults, consistent with the refreezing of an ocean, implying Pluto had a subsurface ocean for at least part of its history.
- If Pluto never had an ocean, it would record a larger "fossil bulge" from its earlier rotational state before Charon's orbit expanded to its current configuration.
- Purported cryovolcanic features south of Sputnik Planitia, if they are indeed cryovolcanic in origin, could be explained with ocean pressurization occurring during the refreezing process (Martin and Binzel, 2021).
- The location of Sputnik Planitia near the anti-Charon point can be explained with a true polar wander reorientation if it is a positive mass anomaly, which could occur if Pluto has a subsurface ocean (Nimmo et al., 2017; Keane et al., 2016). See Chapter 3 for more details.

None of these lines of evidence require a subsurface ocean, but taken together, it is probable that Pluto had in the past or has to this day a subsurface liquid ocean, adding it to the emerging class of "Ocean Worlds" within the solar system.

Pluto is in an unusual orbit, far different from the major planets in the solar system. Pluto's orbital eccentricity is 0.25 and its semi-major axis is 39.5 AU, meaning its orbital distance varies between a perihelion of 29.5 AU (just inside the orbital of Neptune) and an aphelion of 49.5 AU.

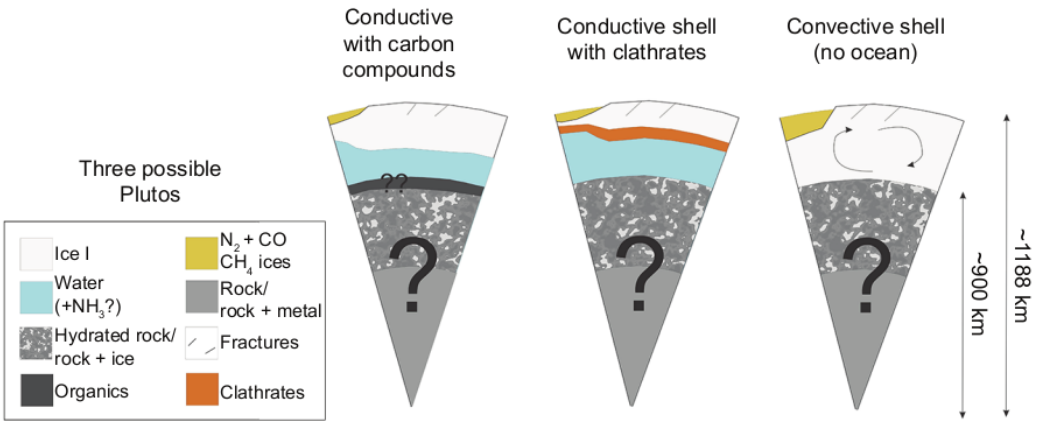

Figure 1.4: Figure and caption reproduced from Nimmo and McKinnon (2021), their Figure 1: Schematic view of three possible Pluto interiors. Interfaces are to scale, except the depth of the surface Sputnik Planitia basin is exaggerated for clarity. Question marks denote inferences (e.g., the presence of carbon compounds) that are uncertain. In the absence of an ocean, the Sputnik Planitia basin would have to be deeper to explain its location.

Pluto's inclination is 17°, taking the dwarf planet 8 AU above and 13 AU below the ecliptic plane that the major planets all orbit in (Malhotra and Williams, 1997). Pluto's orbital period is 248 years, with the most recent perihelion occurring in 1989 and the next aphelion occurring in 2113. Pluto has yet to be observed for a full orbit. It was discovered officially in 1930, but has been seen in precovery images going back to 1915 (Lampland, 1933; Schindler and Grundy, 2018), meaning that Pluto has been observed for 108 years or just over 40% of a Pluto year.

Another special aspect to Pluto's orbit is the resonance with Neptune. Pluto completes 2 orbits for every 3 orbits that Neptune completes, placing it in the 3:2 mean motion orbital resonance with Neptune (Malhotra and Williams, 1997). Pluto is not alone in this orbit; there are many other resonant KBOs in or near the 3:2 resonance, called "Plutinos." Pluto is never closer than 18 AU to Neptune however, due to orbital geometry causing Pluto's perihelion to occur when Neptune is 90° away. Pluto's presence in the 3:2 resonance can be explained by a resonance capture process as Neptune's orbit expanded very early in solar system history (e.g., Malhotra, 1993). Early solar system dynamics as they relate to Pluto's orbit are discussed more in Chapter 4.

Pluto has one large moon, Charon, and four small moons, Styx, Nix, Kerberos, and Hydra (in order of increasing orbital distance), as shown in Figure 1.5. Charon's radius of 606 ± 1 km is just over 50% of Pluto's radius, (Nimmo et al., 2017) and its mass, 1.587 ± 0.015 x 10^{21}kg is about 10% of Pluto's mass (Brozović et al., 2015). Pluto and Charon are mutually tidally locked, with a rotation period of 6.3872 days. The Pluto-Charon barycenter is outside of the body of Pluto, so the four outer small moons have circumbinary orbits about both Pluto and Charon. The four small moons are not spherical, range in size from around 12 km (Styx) to 52 km (Hydra) along their longest axes, and are thought to be leftover debris from the collision that resulted in the Pluto-Charon binary (Porter et al., 2021). Their orbits range in semi-major axis from 42,413 km (35 R_{pluto}) to 64,721 (55 R_{pluto}) km, much larger than Charon's semi-major axis of 19,602 km (16.5 R_{pluto}) (Canup et al., 2021).

The Pluto-Charon binary is currently best-explained by a giant impact origin, as detailed in Canup et al. (2021), and briefly summarized here. In order for a giant impact to produce a moon

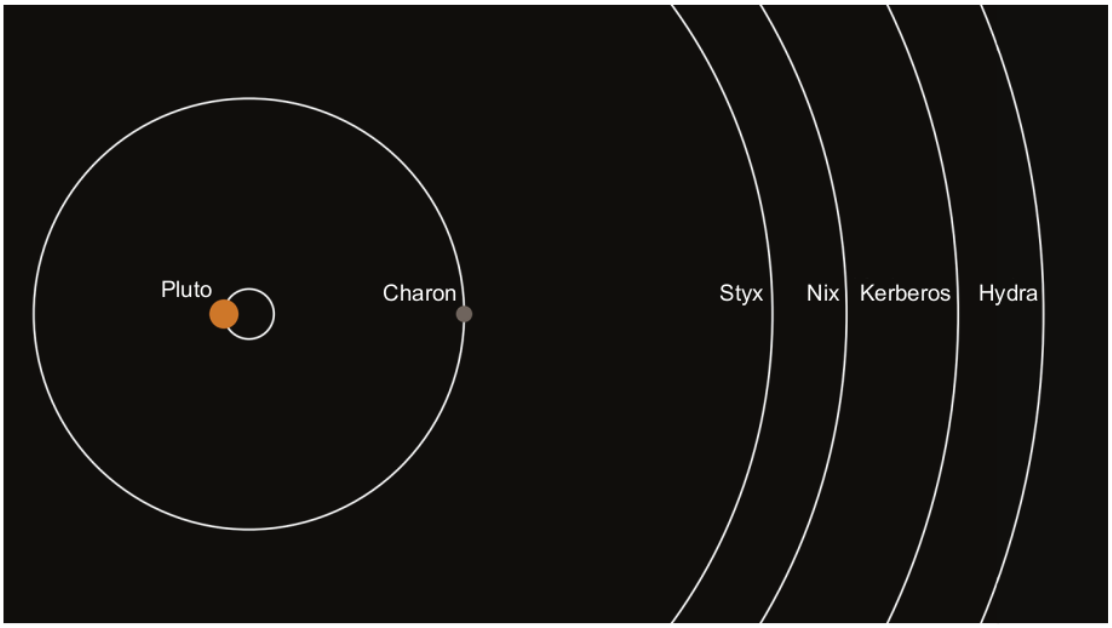

Figure 1.5: Figure and caption reproduced from Porter et al. (2021), their Figure 1: The orbital configuration of the Pluto system. The sizes of Pluto and Charon are shown to scale. The orbits of the small satellites are roughly circular and coplanar with the mutual orbits of Pluto and Charon around the system barycenter.

as large as Charon (relative to the size of Pluto), the impact needs to be oblique and low-velocity. These conditions are best met very early in solar system history, potentially before the dispersal of the protoplanetary gas disk and certainly before the onset of Neptune's migration, which would have increased impact velocities far above the $\simeq 1.2\ v_{esc}$ needed to match the Pluto system (Canup, 2011). Additionally, the proto-Pluto and proto-Charon involved in the impact were most likely at least partially differentiated. Impact simulations with undifferentiated impactors fail to reproduce the observed densities and compositions of Charon and the small moons (Canup, 2011; Arakawa et al., 2019). These constraints on the timing and differentiation state of Pluto at the time of Charon's formation are used to justify the assumptions in Chapter 4.

Pluto's orbital obliquity is 122°, where an obliquity over 90° indicates that Pluto exhibits retrograde rotation relative to its heliocentric orbit. This obliquity varies over a ~ 3 My timescale (see Section 1.4). Such a high obliquity has significant implications for the amount of sunlight that a given latitude receives, as shown in Figure 1.6. Counter-intuitively (for Earthlings, at least), Pluto's poles receive more annually-averaged insolation than its equator. This has implications for the infilling and subsequent reorientation of Sputnik Planitia, as discussed in Chapter 3.

1.3 Pluto's Atmosphere

The radio occultation by the REX instrument onboard *New Horizons* measured a surface atmospheric pressure of 11.5 ± 0.7 μbar and surface temperature of nitrogen ice of 38.9 K (Hinson et al., 2017), close to the vapor pressure equilibrium temperature for nitrogen ice (Fray and Schmitt, 2009). Pluto's atmospheric gases are in vapor pressure equilibrium with their surface ice deposits, meaning that the surface atmospheric pressure is set by the temperature of the ices. This is very different than Earth's nitrogen-dominated atmosphere for example, because on Pluto the dominant atmospheric gas (also nitrogen) can condense into solid form on the surface. On Pluto, the pressure is highly dependent on the ice temperature; above a block of nitrogen ice at 35 K, the vapor pressure is 3.1 μbar, while at 40 K the pressure increases an order of magnitude to 65 μbar (Fray and Schmitt, 2009). This effect causes large pressure variations between Pluto's seasons, as modeled in Chapter

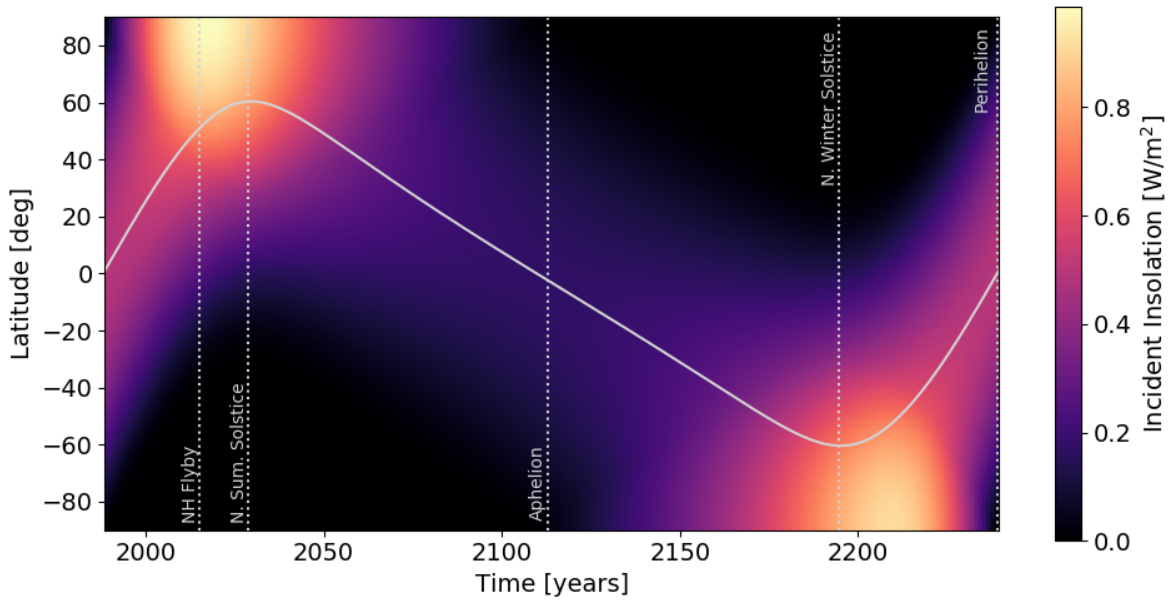

Figure 1.6: Instantaneous incident insolation onto Pluto as a function of latitude. Several important times are shown for references as the vertical dotted lines. The subsolar latitude is shown as the solid line.

2.

The observed temperature, nitrogen, and methane profiles are shown in Figure 1.7. At the surface, nitrogen is the dominant component of the atmosphere and methane is the most abundant trace species at 0.3%, as measured by the Alice UV spectrograph on *New Horizons* (Young et al., 2018). The atmospheric temperature increases rapidly from the surface value of 38.9 K to a peak of about 110 K at 20 km, and then decreases to around 65-68 K at an altitude of 400 km. Above this level, the atmosphere is isothermal. Pluto's isothermal upper atmosphere temperature was lower than pre-flyby predictions. This cold upper atmosphere can be explained by the balance between haze heating and cooling rates, rather than gas heating and cooling (Zhang et al., 2017). A simplified version of this temperature profile is used in the escape model presented in Chapter 4.

Images of Pluto's limb taken by *New Horizons* showed an extensive haze layer in the atmosphere, made up of solid particles suspended in the atmospheric gas (Gladstone et al., 2016). The haze is present up to altitudes of 200 km and is organized into distinct layers that are separated by $\sim$ 10 km and cohesive across 1000 km or more. The presence of haze had been suggested for Pluto's atmosphere prior to the flyby, based on an inflection point in occultation lightcurves (Elliot et al., 1989) and from theoretical similarities to the atmospheres of Saturn's moon Titan and Neptune's moon Triton, which both were known to have haze (Summers et al., 1997). However, the spatial extent of the haze, as well as its significant role in controlling the atmospheric temperature and structure were surprises from the *New Horizons* mission.

Modeling suggests that the haze particles are fractal aggregates on the order of 100 nm in size, composed of smaller spherical monomer particles on the order of 10 nm in size (Gao et al., 2017). Observations from MVIC on *New Horizons* revealed a blue color for the haze particles, indicating very small particles, but the scattering pattern indicated larger particles; fractal aggregates are able to satisfy both of these constraints (Cheng et al., 2017). Haze production begins high in the atmosphere as solar EUV (Extreme UV) and UV radiation, interplanetary Lyman-α emission, and galactic cosmic rays hit nitrogen, methane, and other hydrocarbon molecules, causing them to photodissociate and photoionize (Mandt et al., 2021). Then there is a complex chain of reactions

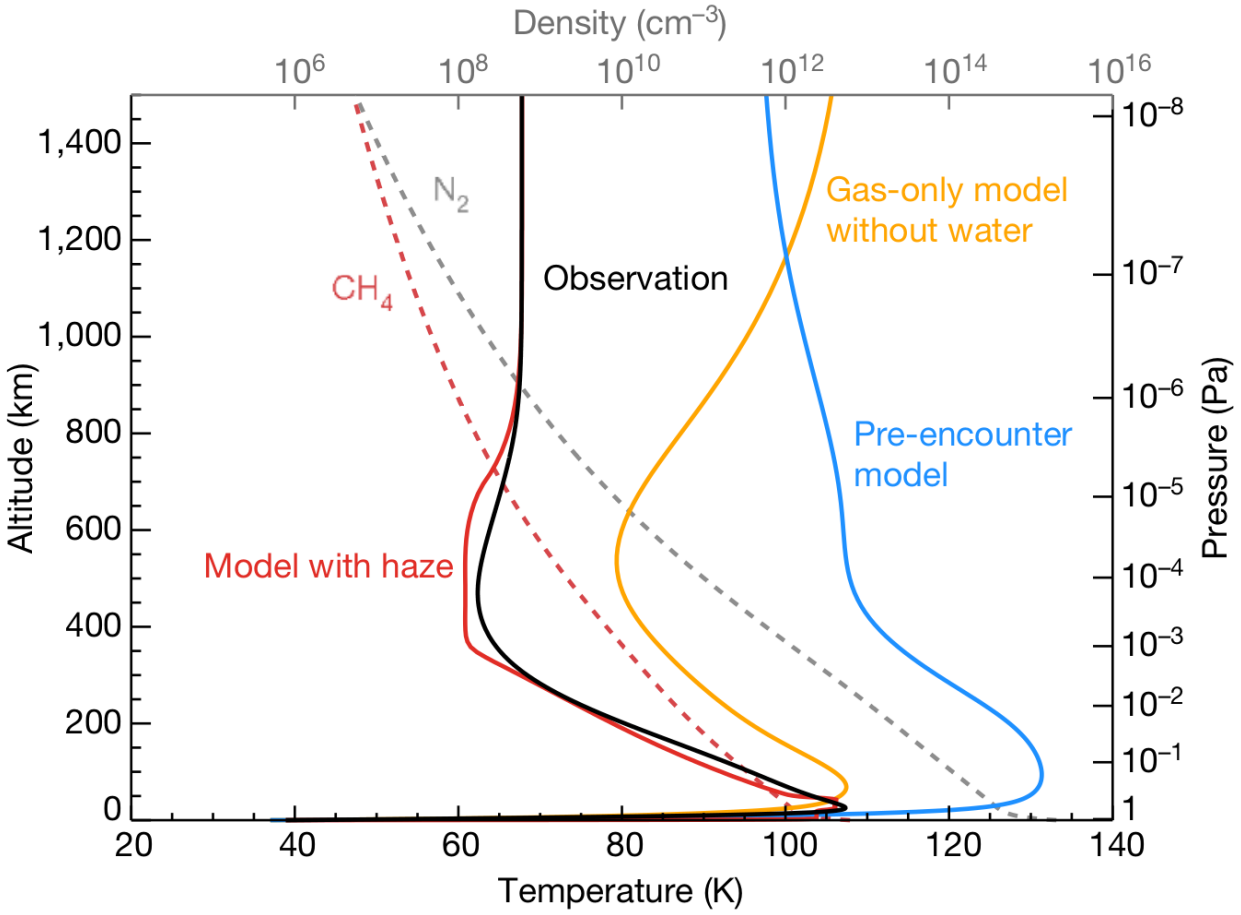

Figure 1.7: Figure and caption reproduced from Zhang et al. (2017): Atmospheric temperature and gas-density profiles of Pluto. Dashed lines represent the densities of nitrogen (N_2) and methane(CH_4) (in number of molecules per cm^3) (Gladstone et al., 2016). Carbon monoxide (CO; not shown) is well mixed in the atmosphere, with a volume mixing ratio of 5 x 10^{-4}. Solid lines show the actual temperature profile derived by the *New Horizons* spacecraft (black line) (Gladstone et al., 2016), as well as profiles calculated using the New Horizons pre-encounter model (pale blue line) (Zhu et al., 2014) and the latest gas-only model (yellow line) (Strobel and Zhu, 2017); the latter includes hydrogen cyanide (HCN) and acetylene (C_2H_2) but not water. The red curve shows the temperature modelled herein, which includes haze-mediated heating and cooling.

that leads to the production of even more hydrocarbons and nitriles. See Krasnopolsky (2020) for an example of a photochemical model of Pluto's atmosphere. In the presence of nucleation points, these hydrocarbons and nitrile gases will condense and form the monomers (Cheng et al., 2017). The monomers then begin to fall through the atmosphere, with the sedimentation rate dependent on properties of the atmosphere and the monomers themselves. While falling, monomers stick together and aggregate into larger fractal shapes (similar to a bunch of grapes). Gladstone et al. (2016) estimates the deposition rate by using the methane photolysis rate of 10^{-14} g/cm^2/s, equivalent to a global layer 1 μm thick each Pluto orbit, or a layer more than 10 m thick over the age of the solar system. Chapter 2 was motivated by a desire to reconcile this haze deposition rate, which should blanket the surface in a uniform layer of haze particles, with the observed heterogeneity of the surface.

1.4 Pluto's Superseasons

The Sun exerts a torque on the Pluto-Charon binary, causing the obliquity to vary with a 3 My period (Dobrovolskis and Harris, 1983), and the longitude of perihelion varies with a 3.7 My period as well (Earle and Binzel, 2015). Combined, these create epochs of "extreme seasons" in which Pluto's sub-solar latitude at perihelion reaches a maximum northern value (Extreme Northern Summer) or a maximum southern value (Extreme Southern Summer). Figure 1.8, reproduced from Earle and Binzel (2015), shows these variations as function of time for the past 3 My. If the northern summer solstice occurs at perihelion, the northern hemisphere is receiving the most direct insolation at the same time as it is receiving the most intense insolation, due to being closer to the Sun, creating extremely hot northern summers (and vice versa for the southern hemisphere). At present, Pluto's subsolar latitude at perihelion is close to 0°, so the two hemispheres experience nearly equal illumination conditions over their seasons. The effect of these superseasonal cycles on the surface pressure is explored further in Chapter 2, and the effect of the variable obliquity on the infilling of Sputnik Planitia is described in Chapter 3.

Pluto is dynamic, across many different timescales and across seemingly all aspects of the

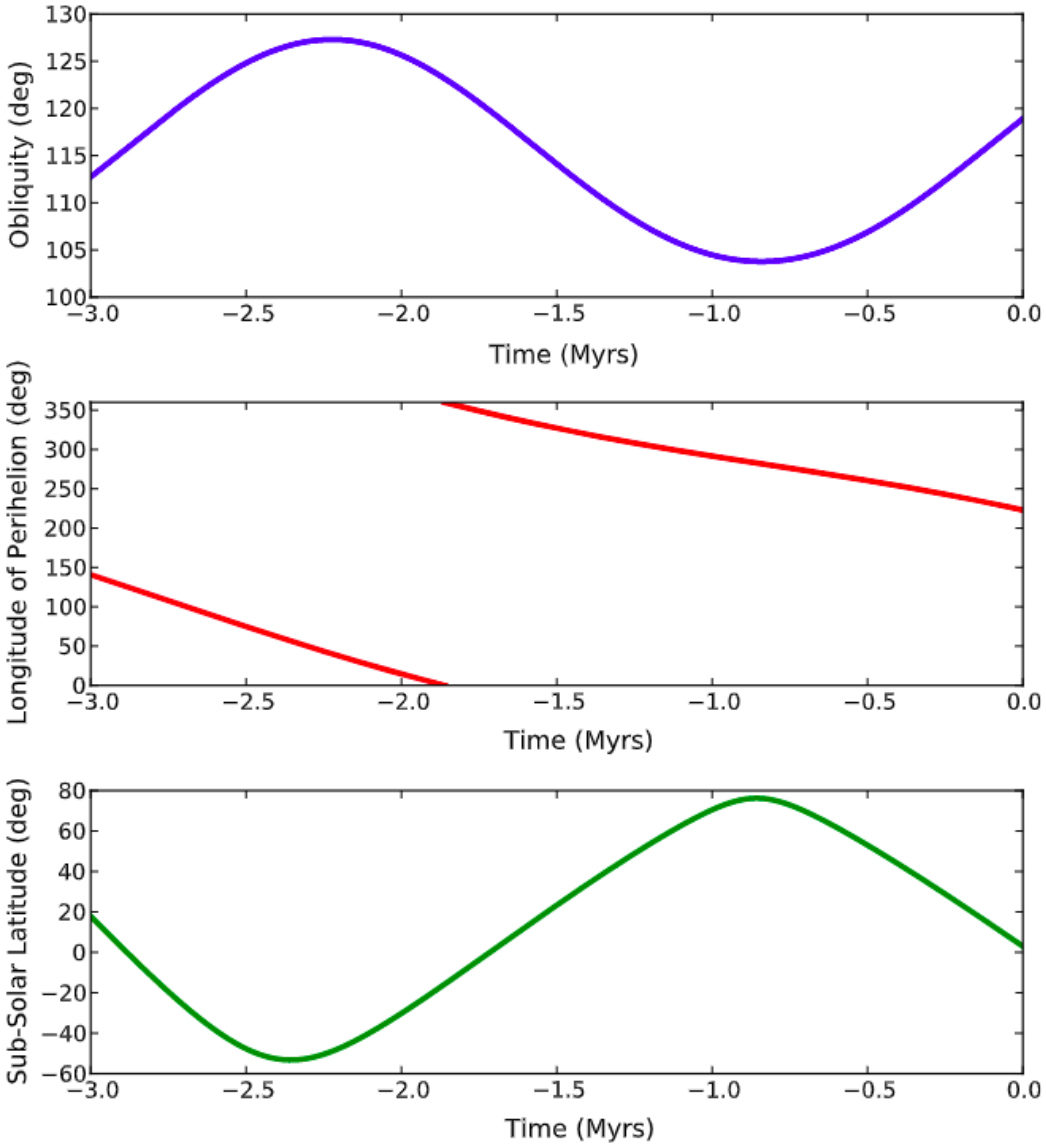

Figure 1.8: Figure and caption reproduced from Earle and Binzel (2015), their Figure 1: (Top) Pluto's changing obliquity as a function of time over the past 3 Myrs. (Middle) Regression of Pluto's longitude of perihelion over the same interval. (Bottom) Pluto's resulting sub-solar latitude at perihelion as a function of time. As noted in the text, possible long-term chaotic orbital variations occur over substantially longer timescales than considered here. Calculations are based on the analysis of Dobrovolskis et al. (1997).

world. In Chapter 2, I explore Pluto's climate variability, over annual and superseasonal timescales, motivated by the curiosity of Pluto maintaining a heterogeneous surface despite potentially uniform haze deposition. Chapter 3 deals with dynamics of Pluto's interior, and how the transport of volatile ices on the surface can change the orientation of the entire body. Finally, in Chapter 4, Pluto's orbital dynamics early in solar system history and the resulting effect on the volatile inventory throughout time are the focus.

Chapter 2

Modeling Pluto's Minimum Pressure: Implications for Haze Production

This chapter, along with Appendix A, was originally published in the Icarus "Pluto System, Kuiper Belt, and Kuiper Belt Objects" Special Issue (Johnson et al., 2021b).

Abstract: Pluto has a heterogeneous surface, despite a global haze deposition rate of $\sim$1 μm per orbit (Cheng et al., 2017; Grundy et al., 2018). While there could be spatial variation in the deposition rate, this has not yet been rigorously quantified, and naively the haze should coat the surface more uniformly than was observed. One way (among many) to explain this contradiction is for atmospheric pressure at the surface to drop low enough to interrupt haze production and stop the deposition of particles onto part of the surface, driving heterogeneity. If the surface pressure drops to less than 10^{-3} - 10^{-4} μbar and the CH_4 mixing ratio remains nearly constant at the observed 2015 value, the atmosphere becomes transparent to ultraviolet radiation (Young et al., 2018), which would shut off haze production at its source. If the surface pressure falls below 0.06 μbar, the atmosphere ceases to be global, and instead is localized over only the warmest part of the surface, restricting the location of deposition (Spencer et al., 1997). In Pluto's current atmosphere, haze monomers collect together into aggregate particles at beginning at 0.5 μbar; if the surface pressure falls below this limit, the appearance of particles deposited at different times of year and in different locations could be different. We use VT3D, an energy balance model (Young, 2017), to model the surface pressure on Pluto in current and past orbital configurations for four possible static N_2 ice distributions: the observed northern hemisphere distribution with (1) a bare southern hemisphere, (2) a south polar cap, (3) a southern zonal band, and finally (4) a distribution that

is bare everywhere except inside the boundary of Sputnik Planitia. We also present a sensitivity study showing the effect of mobile N_2 ice. By comparing the minima of the modeled pressures to the three haze-disruption pressures, we can determine if or when haze production is disrupted. We find that Pluto's minimum surface pressure in its current orbit is predicted to be between 0.01 - 3 μbar, and that over the past 10 million years the surface pressure has not fallen below 0.004 μbar. According to our model, southern N_2 ice is required for haze aggregation to be interrupted, and southern N_2 with very low thermal inertia is required for the possibility of a local atmosphere.

2.1 Introduction

The New Horizons mission to Pluto revealed a surprisingly active surface, with dramatic albedo, color, and composition contrasts (Stern et al., 2015). The flyby also detected haze in the atmosphere, and haze particles should settle through the atmosphere and be deposited onto the surface. These two observations presented a major question: how is the heterogeneity maintained despite a global blanket of deposited haze particles on the surface? This work investigates one possible answer to this question, which is that the atmospheric pressure could drop low enough for long enough over Pluto's orbit to disrupt haze production at its source, preventing the haze particles from being deposited onto the surface.

Pluto's normal reflectance varies across its surface by over a factor of ten, with some regions reaching a normal reflectance value of unity and the darkest regions dropping to a minimum of 0.08 (Buratti et al., 2017). The equatorial region is dark and red, interrupted by bright, more neutral Sputnik Planitia (the expansive volatile-ice sheet that makes up the western half of Tombaugh Regio, Pluto's "heart"; hereafter called SP); midlatitudes, especially where covered by volatile ices, are similar to SP's neutral color, while the north polar region (north of 60°N) has a yellow hue (Stern et al., 2015; Olkin et al., 2017; Protopapa et al., 2020). Composition also varies across the encounter hemisphere, with SP showing very strong N_2 and CH_4 spectral signatures, while the dark equatorial region appears to be free of both species and instead has a spectrum that is consistent with tholins, an unknown mix of hydrocarbons and carbonaceous material produced by energetic

radiation (including cosmic rays and UV) interactions with N_2 and CH_4 (Protopapa et al., 2017, 2020; Schmitt et al., 2017).

New Horizons observed haze extending up to 300 km, which was globally present but not spatially uniform (Stern et al., 2015; Cheng et al., 2017). The haze was brighter towards northern latitudes rather than in the direction of the Sun. Cheng et al. (2017) compared I/F values for 44°N and -0.5°S, and found that the northern latitude haze was systematically brighter by factors of 2 to 3 compared with the equatorial haze. Pluto's haze is created by radiolysis and photolysis of the atmospheric species, primarily CH_4, N_2, and CO, using a variety of energy sources (Mandt et al., 2021). Solar UV radiation, including Lyman-α, is important to haze photochemistry and its flux is greatest at the sub-solar point on Pluto, which could potentially increase the haze production rate there. Lyman-α is also scattered by the interplanetary medium and impinges on Pluto's nightside. Cosmic rays, another important energy source, will hit Pluto's atmosphere isotropically. Solar wind particle fluxes were time-variable, as measured by New Horizons, and their interaction with Pluto's atmosphere is uncertain (Bagenal et al., 2016). Accounting for the space- and time-variability of these energy sources for haze production makes it difficult to predict the expected variability in haze deposition and its distribution on the surface.

Deposition rates from Cheng et al. (2017), Grundy et al. (2018), and Krasnopolsky (2020) all predict that a layer of haze particles roughly one micron thick would accumulate over one Pluto orbit, amounting to more than 10 m over the age of the solar system. While the haze was not observed to be spatially uniform and the production mechanism might vary spatially or temporally as well, these authors do not address such variations and instead present deposition rates as approximate global averages. Grundy et al. (2018) conclude that in order to produce the observed heterogeneity, the haze particles must either be differentially processed once on the surface, or the production and deposition must be spatially variable, although they do not suggest a mechanism to cause this spatial variability. Cheng et al. (2017) suggest that haze deposition may be interrupted by atmospheric collapse (here, we define collapse to mean when the atmosphere is localized and "patchy" rather than global). Grundy et al. (2018) discuss this possibility as well, and

also raise other mechanisms such as a spatially or temporally variable gaseous CH_4 column, or the movement of haze particles by wind once they have settled on the surface (explored further in Forget et al. (2017) and Bertrand et al. (2020)). Neither Cheng et al. (2017) nor Grundy et al. (2018) quantifies the possibility of interrupting or diminishing haze production within the atmosphere. Bertrand and Forget (2017) explored the production and atmospheric transport of haze particles, and found that the column mass of haze aerosols in the atmosphere varies spatially by a factor of 10 if there is no condensation of volatiles at the southern pole in winter, or only a factor of 2 if south pole condensation is allowed. Forget et al. (2017) used a Pluto Global Climate Model to investigate the atmospheric circulation, and found that zonal flows were on the order of a few m s^{-1} (varying with latitude and with the assumed N_2 distribution), while meridional flows were much smaller, on the order of a few tens of cm s^{-1}. Both of these flows could redistribute the haze particles, either through atmospheric transport pre-deposition, or near-surface winds could blow haze particles around and collect them into localized regions post-deposition.

If the atmospheric pressure at the surface gets low enough, haze production may be altered, suppressed or stopped completely. Gao et al. (2017) use a microphysical model to show that haze particles begin to grow at around 150 to 300 km altitude (depending on the size of the initial monomers) and this growth continues as the particles fall to the surface. This altitude range encompasses pressures from 0.1 μbar to 0.6 μbar; we select 0.5 μbar to be representative of the pressure level where aggregation begins. Below the 150-300 km level, sedimentation timescales are longer than coagulation timescales, due to the increased atmospheric density, allowing haze particles more time to collide and coagulate into larger aggregates (Cheng et al., 2017; Gao et al., 2017). If the surface pressure drops below this level, monomer haze particles (which are created around 1000 km altitude in the 2015 atmosphere) may sediment out onto the surface instead of aggregates, potentially changing the appearance on the surface. We refer to this as a "non-aggregating" atmosphere. This pressure limit is based on the atmosphere as observed by New Horizons in 2015; we assume that the pressure level where haze aggregation occurs stays constant throughout Pluto's orbit. However, the sedimentation and coagulation timescales depend on quantities such as the at-

mospheric density, temperature, and dynamic viscosity and the sizes of the monomer and aggregate particles, and the temporal behavior of these quantities has not yet been well studied for Pluto. For surface pressures less than ∼0.06 μbar Pluto cannot support a global atmosphere (Spencer et al., 1997), and instead the atmosphere becomes local, or patchy, which would restrict the region in which haze particles are deposited. Additionally, if the surface pressure drops to less than 10^{-3} - 10^{-4} μbar, the atmosphere would be transparent to ultraviolet radiation (Young et al., 2018). This would shut off the photolysis of atmospheric N_2 and CH_4, suppressing haze production at its source (Gao et al., 2017), while simultaneously boosting the photolysis of surface ices and existing tholins, which can lead to a different composition and appearance of tholins than those produced in the atmosphere (Bertrand et al., 2019).

Pluto's obliquity varies with a 2.8-million year period, and this obliquity cycle creates "extreme seasons" during which perihelion occurs simultaneously with northern summer solstice (most recently occurred 0.9 Mya) or aphelion occurs simultaneously with northern summer solstice (most recently occurred 2.4 My ago) (Earle et al., 2017; Bertrand et al., 2018). During these two extreme orbital configurations the minimum surface pressure will be different from that in the current configuration, providing an opportunity for historic haze disruption that might not be seen in today's Pluto. This could affect the present-day surface heterogeneity.

Trafton and Stern (1983) considered a CH_4 atmosphere (CH_4 was then the only species detected at Pluto) and predicted a globally-uniform surface pressure for CH_4 column abundances greater than 6.7 cm-Am (using the now-known surface gravity of 0.62 ms^{-2}, this corresponds to a pressure of 0.3 μbar). At the time, the best estimate for the column abundance was 27 ± 7 m-Am (12 ± 3 μbar), which implied that energy could be efficiently transported from high-insolation areas to low-insolation areas, and that vapor pressure equilibrium could maintain a uniform surface temperature of 58 ± 0.9 K. After the discovery of Pluto's atmosphere via occultations in 1988 (Elliot et al., 1989; Hubbard et al., 1988), and the detection of abundant N_2 by Owen et al. (1993), Hansen and Paige (1996) adapted their existing Triton energy balance model to Pluto. They found that volatile transport would be a significant process coupling the surface and atmosphere, allowing

surface ices to move around on seasonal timescales. They also found that perennial zonal bands of ice could form in their model, as opposed to perennial polar ice caps, due to Pluto's high obliquity. For some cases, "polar bald spots" were created by sublimation that began at the center of a polar cap rather than at the equatorward edge. N_2 ice temperatures between 30 and 40 K were predicted, based on the balance between insolation, infrared thermal emission, conduction to and from the subsurface, and the latent heat of subliming and condensing N_2.

Bertrand and Forget (2016) used a simplified Pluto GCM to simulate Pluto's climate and volatile transport for thousands of orbits in a reasonable computation time. They found that, for an initial globally uniform distribution of N_2 ice and thermal inertias above 700 tiu (Thermal Inertia Units, J m^{-2} K^{-1} $s^{-1/2}$), all of the N_2 ice migrated into their modeled 3-km deep SP basin within 10,000 Earth years. This motivated the "strawman" example we present in Section 3.2 using a SP-only N_2 distribution. For lower thermal inertias, their model had seasonal deposits of N_2 ice outside of SP. When the thermal inertia of the N_2 ice was >700 tiu, their model predicted pressures that were consistent with pre-existing occultation measurements (implying a roughly two- to three-fold increase in pressure between 1988 and 2015), as well as a peak value of about 11.5 μbar near 2015. Bertrand et al. (2018) explored the N_2 cycles using their parameterized Pluto GCM on million year timescales, capturing the response to the obliquity cycles described above. They found that a net value of 1 km of N_2 ice has sublimed from the northern edge of SP and recondensed onto the southern edge over the past 2 million years, driven by the change in subsolar latitude at perihelion, which shifted from the southern hemisphere to the north (and is now moving back towards the south, currently near 0°, see Figure 1 in Earle et al. (2017)). They also found that over millions of years the surface pressure on Pluto never drops below tens of nanobars, nor exceeds tens of microbars.

We aim to test the hypothesis of haze disruption via thermal modelling of the surface. Our model, VT3D, is described in Section 2, along with our choices for thermal parameters and the distribution of surface volatiles. Sections 3 presents the resulting pressure evolution curves for the current Pluto orbit and past orbits with different obliquities and subsolar latitudes at perihelion,

assuming four different N_2 distributions, as well as a sensitivity study for the effect of mobile N_2 ice. Finally, we discuss the implications of these modelled pressure curves in relation to haze production in Section 4.

2.2 Methods

2.2.1 VT3D Model Overview

This section provides an overview of the Volatile Transport Three Dimensional (VT3D) model as used in this study; for a complete description of the model and its full capabilities, see Young (2017). VT3D is an energy balance model, including thermal conduction into and within a substrate, internal heat (not used here), latent heat of sublimation, insolation, and thermal emission. Locally, the energy balance equation is:

$$\frac{S_{1AU}(1-A)\mu}{r^2} - \epsilon\sigma T^4 - k\frac{dT}{dz} + L\dot{m} = 0 \tag{2.1}$$

where S_{1AU} is the solar constant (1361 W m^{-2}), A is the Bond albedo of the surface, μ is the solar incidence angle at the given location, r is the heliocentric distance in AU, ϵ is the emissivity of the surface, σ is the Stefan-Boltzmann constant, T is the volatile temperature, k is the thermal conductivity, z is the depth beneath the surface (zero at the surface and decreasing downward), L is the latent heat of sublimation, and $\dot{m}$ is the condensation rate, in mass per area per time. The partition between sublimation and conduction is determined by global mass balance (Young, 2012, 2013), since the rate of change of the total atmospheric bulk (areal integral of $\dot{m}$) is related to the change in N_2 ice temperature through the change in the surface pressure and atmospheric column density. As implemented here, VT3D depends on three free parameters (the Bond albedo, A, the emissivity, ϵ, and the seasonal thermal inertia, Γ, of the surface N_2 ice) as well as on the spatial distribution of N_2 ice. N_2 is the dominant atmospheric constituent and it is more volatile than the minor constituents of CH_4 and CO, so we consider only the N_2 temperature when we model the atmospheric pressure.

We run VT3D using the explicit form of the equations (rather than its semi-implicit Crank-Nicholson scheme). The explicit scheme is only stable for small timesteps; we calculate the temperature at 500 points per Pluto orbit, corresponding to a timestep of about 0.5 Earth year. The volatiles are discretized vertically into $J = 40$ layers for a total depth of roughly 10 thermal skin depths. The temperature at the next timestep of a given layer depends on the temperature at the current timestep in the layer above, in the layer itself, and in the layer below. To evaluate the insolation term, we average the insolation at the start and end of the current timestep: $(S_n + S_{n+1})/2$, where subscript n represents the current timestep, and $n+1$ is the next timestep. We use the diurnally- and spatially-averaged insolation, as discussed more in the following section. To evaluate the average thermal emission term for the timestep from t_n to t_{n+1}, VT3D uses the first-order Taylor expansion of T^4: $\epsilon\sigma T_{0,n}^4 + 2\epsilon\sigma T_{0,n}^3(T_{0,n+1} - T_{0,n})$, where the first subscript indicates the layer (0 corresponds to the top layer) and the second indicates the timestep. The conduction term is discretized using a first-order finite difference scheme; for example the term describing conducted heat from the layer below into the top layer is: $\sqrt{\omega}\Gamma(T_{0,n} - T_{1,n})/\delta$, where ω is the orbital frequency of Pluto, in seconds, and δ is the dimensionless distance between layers. The sublimation rate is related to the rate of change of temperature since we assume vapor pressure equilibrium; in response to an increase in the ice temperature, the vapor pressure above it must also increase, which means particles sublime from the ice surface, removing latent heat. Thus, the sublimation term is written: $\Phi^A(T_{0,n+1} - T_{0,n})$, where Φ^A is given by: $\Phi^A = L^2 m_{N_2} p\omega/(f_v g k_B T_{0,n}^2 \tau)$ (L is the latent heat of sublimation for N_2, m_{N_2} is the molecular mass of N_2, p is the vapor pressure at temperature $T_{0,n}$, f_v is the fraction of the surface covered by N_2, g is the surface gravity, k_B is the Boltzmann constant, and τ is a dimensionless time step). After inserting these terms into Equation 1, temperatures at the next timestep are a function of temperatures at the current timestep and various parameters of the N_2 ice. VT3D finds the temperatures by stepping forward in time for one Pluto orbit.

VT3D begins with an analytic approximation to the solution, which is used as the initial guess in the more accurate numerical solution to decrease convergence time. A description on how

Table 2.1: Coefficients needed to calculate the equilibrium vapor pressure as a function of temperature.

	A_0	A_1	A_2	A_3	A_4	A_5
α-phase	12.404174	-807.35728	-3925.5143	62965.429	-463269.99	1.324999.3
β-phase	8.51384232	-458.386541	-19871.6407	480001.675	-4523786.13	0

to implement the analytic solution for quick calculation is included in the Appendix.

To convert temperatures into pressures, we use the equation for solid N_2 vapor pressure as a function of temperature presented in Fray and Schmitt (2009):

$$ln\left(P_{sub}\right) = A_0 + \sum_{i=1}^{n} \frac{A_i}{T^i} \tag{2.2}$$

Fray and Schmitt (2009) compile previously-published empirical relations and experimental data to find the best-fit coefficients A_i for solid N_2 ice, with separate sets of coefficients for the α- and β-crystalline phases, shown in Table 2.1.

2.2.2 Volatile Distribution

Observations of the surface volatile distribution were performed by the LEISA infrared spectrometer on the New Horizons spacecraft. N_2 ice is detectable by a weak 2.15 μm spectral feature, but only for sufficiently large grain sizes. Its presence can also be inferred from a wavelength shift in CH_4 spectral bands that occur when CH_4 is dissolved in N_2, and from the overall infrared brightness (Protopapa et al., 2017; Schmitt et al., 2017). Protopapa et al. (2017) use a combination of these features along with Hapke radiative transfer modeling to produce a map of N_2 on the encounter hemisphere. Other analyses relying on spectral parameters like band depth or equivalent width are not able to distinguish between relative abundance changes and grain size changes across the surface. Protopapa et al. (2017) produce separate fractional abundance and grain size maps. The modeled grain sizes (where grain size refers to distance between scattering centers, see Hapke (1993)) range from a few centimeters to larger than 1 meter. The fractional abundance map highlights the large, flat ice sheet of SP, along with a latitudinal band stretching from 35°N to 55°N, as the main N_2 reservoirs on the surface, containing up to about 60% N_2 (assuming an

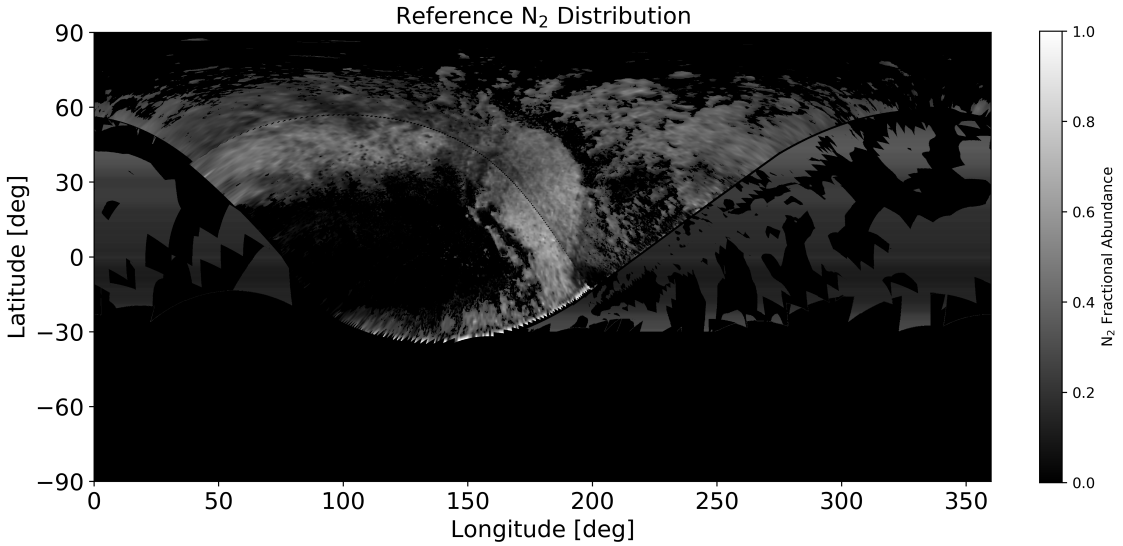

Figure 2.1: The spatial distribution of N_2 ice in our reference map. The grayscale represents the fractional abundance of N_2 ice coverage in that pixel. This distribution incorporates data from Protopapa et al. (2017), Schmitt et al. (2017), and Gabasova et al. (2021).

areal mixture with the other species that are present in that region). The fractional abundance of N_2 is the fraction of a given area that needs to be covered by N_2 to produce a spectra consistent with the observed spectra; the remaining area is covered by other species, namely CH_4, water ice, and tholins in Protopapa et al. (2017). Schmitt et al. (2017) present a spatial distribution map of the N_2 ice band depth, as well as a map of the presence of the N_2-rich phase (called the 'CH4 band position index' map) and their correlation, which make use of principal component analysis to reduce the noise and remove some instrument artifacts in the spectro-images of the high resolution LEISA data. Lewis et al. (2019) created a N_2 presence map which combines the band depth map from Schmitt et al. (2017) and the fractional abundance map from Protopapa et al. (2017). This map assumes a band depth above 0.005 or a fractional abundance of greater than 0% indicates the presence of N_2.

The high resolution LEISA images are limited to the encounter hemisphere, which was visible to the spacecraft during the flyby. The encounter hemisphere is centered near SP at longitudes around 150°, where the high resolution coverage reaches from north pole to 30°S. The region tapers off to the east and west until it reach the permanently lit north polar region extending out to 60°N. Much of the southern hemisphere (south of 40°S) is currently in polar night.

Gabasova et al. (2021) have used lower-resolution approach data in combination with the higher resolution flyby data to create a global N_2 distribution map that includes both the non-encounter and encounter hemispheres. This map shows the spatial distribution of the 2.15 μm N_2 band depth alone, and does not consider the shifting of the CH_4 bands nor the overall brightness of the pixel. A band depth value of 0.005 or greater indicates the presence of N_2 ice; however since band depth does not directly relate to the fractional abundance of N_2, this cannot be directly converted into a fractional abundance map. Attempts to correlate band depth and fractional abundance using the overlapping encounter hemisphere data did not yield a clear relationship, due in part to the grain size dependence of band depth. Instead, we turn the band depth map from Gabasova et al. (2021) into a N_2 presence map by applying a band depth threshold of 0.005, analogous to the procedure used by Lewis et al. (2019). We then find the zonal-average fractional abundance in

	Percentage covered by N_2	Equivalent Area [m^2]
Reference	10.18%	1.81 x 10^6
SP-only	1.72%	1.05 x 10^5
Southern Polar Cap	11.52%	2.05 x 10^6
Southern Zonal Band	12.64%	2.25 x 10^6

Table 2.2: Amount of Pluto's surface that is covered by N_2 in each of the four distributions.

each latitude band, defined by a row of pixels, from the Protopapa et al. (2017) N_2 map (excluding pixels that fall within SP), and assign every pixel on the non-encounter hemisphere in that row this mean value. The final map combines these as follows: on the encounter hemisphere, we assume the product of the Lewis et al. (2019) N_2 presence map and the Protopapa et al. (2017) fractional abundance map, while on the non-encounter hemisphere we assume the product of the Gabasova et al. (2021) N_2 presence map and the Protopapa et al. (2017) fractional abundance map. Hereafter referred to as the reference map, our assumed N_2 spatial distribution map for latitude north of 35°S is shown in Figure 2.1. The fractional abundance of N_2 in each location affects our calculation of the insolation, as described below, and also of the thermal emission, since only the fraction of the area covered by N_2 is assumed to radiate. In Figure 2.1, the grayscale indicates the fractional abundance of N_2 ice, with black indicating N_2-free areas and white indicating 100% coverage of N_2 ice. In reality, the N_2-covered areas have varying thicknesses of ice, with SP having perhaps 5 km of ice (McKinnon et al., 2016) while the midlatitude deposits may be much thinner.

We make several different assumptions for the unobserved southern hemisphere (south of 35°S). We use (i) a bare southern hemisphere, (ii) a south polar cap extending from the pole to 60°S with a fractional abundance of 20%, and (iii) a southern zonal band of N_2 ice between 35°S and 55 °S with a fractional abundance of 20%. We also present results from a simplified case assuming SP contains the only surface deposit of N_2, to emphasize the significant effect of this feature on the global pressure.

For each choice of N_2 distribution, we calculate the diurnally- and spatially-averaged insolation onto the surface ices as a function of time, which is an input to VT3D, as shown in Figure 2.2.

Table 2.2 shows the amount of the surface that is covered by N_2 in each distribution. Equation A.3 in the Appendix shows how we calculate the diurnally-averaged insolation as a function of latitude and time. From this, we find the spatial-average insolation using equation A.4, taking into account both N_2 presence and the fractional abundance of N_2 in each location. In doing so, we assume that the distributions are static in time, and that the surface ices are in vapor pressure equilibrium with the atmosphere, and can thus be described by a single temperature dependent on the average insolation. We investigate the effect seasonal, mobile N_2 would have on the model results in Section 3.5, finding that it is difficult to match observations with the inclusion of mobile N_2. Assuming a static distribution is a simplification, which allows us to investigate multiple distributions at a lower computational cost, but it is also motivated by the fact that many of Pluto's N_2 ice deposits appear to be perennial (persisting for longer than one orbit). SP is a perennial feature: the surface of the ice sheet is estimated to be less than 10 My old (White et al., 2017) based on the lack of impact craters, but the ice sheet is undergoing convection with an overturning timescale of 0.5 My which cyclically refreshes the surface, allowing the ice sheet to be much older than the crater-derived age. The underlying basin is ancient and likely greater than 4 Gy old (Moore et al., 2016). Numerical simulations from Bertrand and Forget (2016) found that all of the N_2 ice was sequestered into a 3-km deep SP-like basin within 10,000 Earth years, where it stayed for the remainder of the 50,000-year simulation, strengthening the argument for a perennial SP. It is not as obvious if the other N_2 deposits in the reference map are perennial and last for many Pluto years, or only seasonal and disappear (and reappear) due to sublimation (and condensation) on timescales of tens of Earth years. N_2 is observed at lower altitudes in the northern mid-latitudes (e.g., Howard et al. (2017)) in depression floors that appear flat and smooth. This suggests a deeper, perennial N_2 deposit, coating and smoothing underlying rough terrain, rather than an seasonal deposit of a few meters or less (Young et al., 2020). Bertrand et al. (2019) showed that the mid-latitude N_2 deposits in the northern hemisphere tend to be seasonal, especially those located within depressions. It is unknown whether N_2 exists at mid to high southern latitudes, and, if it does, whether it is perennial or seasonal. For computational expediency, we investigate only static southern distributions too.

Here, the term "static" refers only to the locations of the N_2 ice; N_2 still sublimes from areas of high insolation and condenses onto areas of low insolation, but initially bare locations and initially N_2 ice-covered locations remain so throughout the length of our models. Future work could relax the requirement of a static distribution and time-constant physical parameters, in order to study various feedback effects, such as condensation of N_2 onto winter latitudes (Hansen et al., 2015; Bertrand et al., 2018); runaway albedo feedback (Earle et al., 2018); or the impact of haze on the albedo, emissivity, or thermal inertia.

In addition to the four distributions discussed above, we investigated two others of interest. The first was to exactly mirror the 35-55°N N_2 band in the southern hemisphere, rather than use a uniform fractional abundance for the zonal band. With this distribution, the insolation (and therefore the resulting pressure curves) was nearly indistinguishable from our Southern Zonal Band distribution (which uses a uniform 20% fractional abundance). Since it is unlikely that the southern hemisphere will be exactly identical to the north in that way (due to local topography, existing substrate albedo, etc.), we chose to present the results from the Southern Zonal Band distribution as described above rather than this symmetric version. We also investigated a distribution in which the entire southern hemisphere exactly mirrors the northern hemisphere (as defined in our Reference distribution), except for SP, which was replaced by N_2 ice with a constant fractional abundance of 0.3 (similar to the surrounding N_2; the average fractional abundance of SP is 0.5-0.6). This produces an insolation vs time pattern that is nearly symmetrical around perihelion, and has the peak insolation occurring at perihelion (1990). With this insolation, it is impossible to recreate the doubling/tripling of the atmospheric pressure seen in observations; most (A, Γ, ϵ) cases we investigated had a ratio of predicted 2015 to 1988 pressures of unity, which is outside the 3- range constrained by observations.

2.2.3 Parameter Space Search

For each choice of N_2 distribution, we explore three free parameters: the Bond albedo, A, the emissivity, ϵ, and the thermal inertia, Γ, of the surface N_2 ice. We assume for simplicity that each of

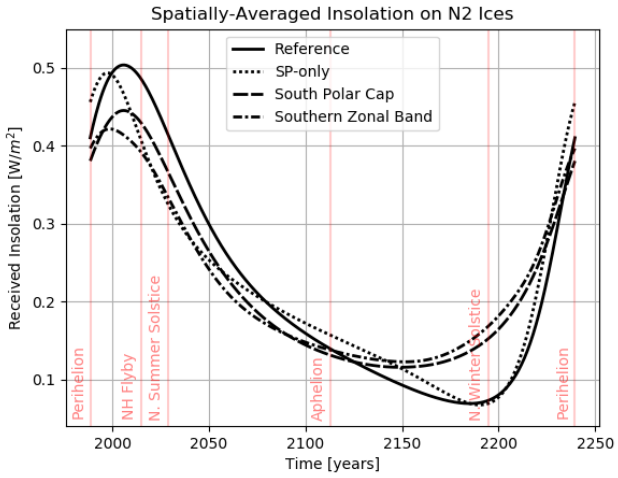

Figure 2.2: Spatially-averaged insolation onto the N_2 ice in each of our four distributions: reference model (solid line), SP-only model (dotted), south polar cap model (dashed), and southern zonal band (dash-dotted). The x-axis shows time in Earth years spanning one Pluto orbit, beginning in 1988.

these parameters is uniform across all of the N_2 ice and constant in time. We perform a grid search of albedo and thermal inertia values, and use the emissivity value that is required to match the New Horizons radio occultation surface pressure of 11.5±0.7 μbar in 2015 (Hinson et al., 2017). To do so, we start with an initial guess at the emissivity, calculate the 2015 surface pressure, and then use a secant method solver to iteratively find the emissivity value which returns a 2015 pressure of 11.5 μbar. We explore the full range of Bond albedos (between 0 and 1), and thermal inertias between 25 and 2000 tiu ($Jm^{-2}K^{-1}s^{-1/2}$). Lellouch et al. (2013) calculates diurnal thermal inertias based on TNO observations on the order of 10 tiu, much lower than the annual values we derive for most cases (by "diurnal thermal inertia", we mean thermal inertia of the material within the diurnal skin depth, while "annual thermal inertia" corresponds to the material within the annual or seasonal skin depth). Spencer and Moore (1992) report thermal inertia values for pure N_2 between 530 and 590 tiu, whether the N_2 is in the α- or β-crystalline phase. On Pluto, the N_2 ices are mixed with some CH_4 and CO, lay above an H_2O ice substrate (Γ = 2100 to 2200 tiu, as reported for Triton in Spencer and Moore (1992)), and could be "fluffy", fractured, or otherwise distinct from a pure lab sample of ice. Thus, we explore a wide range of thermal inertia values in this model. For each A, Γ, ϵ triplet we calculate a surface pressure versus time curve using 500 timesteps per orbit. To ensure convergence, we initialize the numerical VT3D model using the analytic approximation as our initial guess, and we run the model over 20 orbits before selecting the final orbit as our result. Details of the analytic approximation are given in the appendix.

Once we have a grid of pressure curves (one for each A, Γ, ϵ triplet), we apply two constraints to eliminate some regions of this parameter space. The first is to eliminate any cases where the emissivity required to match the 2015 New Horizons pressure is outside of the range $0.3 < \epsilon < 1$. An emissivity greater than unity is unphysical, and we impose a lower bound of 0.3. Stansberry et al. (1996) use Hapke theory to calculate N_2 emissivity as a function of grain size and temperature, and found that the emissivity remains above 0.3 at temperatures between 20 and 60 K for grains larger than 1 cm. Protopapa et al. (2017) found the spectra from most N_2-rich regions, especially those with a high N_2 fractional abundance, were consistent with cm-size or larger grains. The

second constraint is observational. Pluto's atmospheric pressure, as sensed by ground-based stellar occultations, roughly doubled or tripled between the discovery of its atmosphere in 1988 and the New Horizons flyby in 2015. Occultations of Pluto have not probed all the way to the surface, so it is uncertain whether or not the surface pressure experienced the same two- to three-fold increase. If we assume that the surface pressure increase during this time period was the same as the 1205-km altitude pressure increase, then we find $3.14 > P_{2015}/P_{1988} > 1.82$ at the 3-σ level for the surface pressures (Elliot et al., 2003; Hinson et al., 2017). We eliminate any (A,Γ,ϵ) triplets where the ratio of our modeled 2015 and 1988 surface pressures is outside of this range.

2.3 Results

The dependence of the shape and amplitude of the pressure curve on each of the three parameters is explored in Figure 2.3. The leftmost panel holds the thermal inertia and emissivity constant, at 1000 tiu and 0.7, respectively. For a higher albedo, the resulting pressure is lower at every point in time, due to the lower input of solar energy. The middle panel shows the dependence of pressure on emissivity, while holding albedo constant at 0.7 and thermal inertia at 1000 tiu. The dependence is similar to that of albedo; as emissivity increases the pressure curve is lower at every timestep, as the heat is re-radiated away from the surface more efficiently. The rightmost panel shows how the pressure curve depends on thermal inertia, while albedo and emissivity are both constant at 0.7. A lower thermal inertia surface will experience a larger range of pressures over an orbit compared to a higher thermal inertia one, since the lower thermal inertia surface responds more quickly to changes in the input energy. High thermal inertia materials conduct heat towards the surface more efficiently and thus compensate more efficiently for any change in thermal balance at the surface (e.g. the cooling of the surface by thermal emission).

In the following sections, we present the annual pressure versus time curves for the wide range of parameter values we explored, for each of our four possible N_2 distributions, and for both Pluto's current orbital configuration and past "superseasonal" configurations. We begin with our reference model in Section 3.1, which is the reference map and a bare southern hemisphere. Sections 3.2

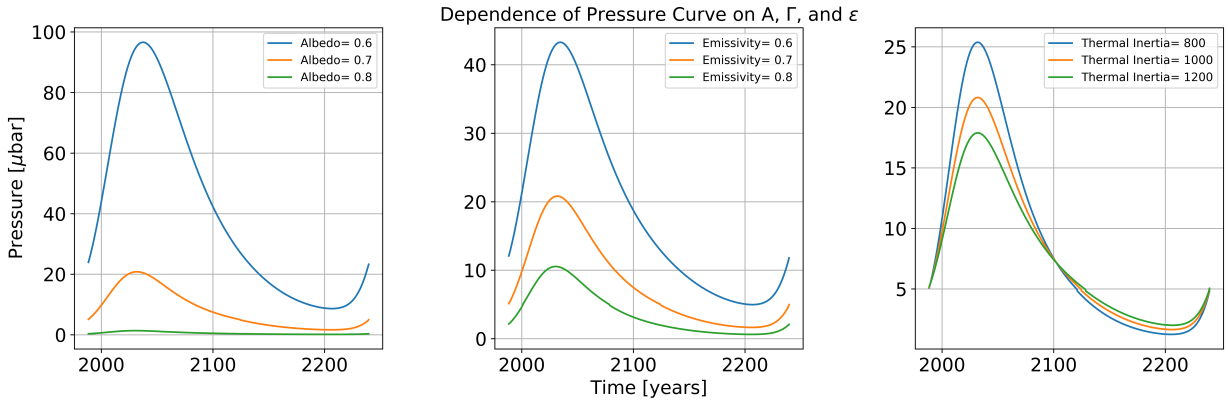

Figure 2.3: Dependence of the shape of the pressure curve on each of the three free parameters. (Left) Dependence on albedo, for constant thermal inertia of 1000 tiu and emissivity of 0.7. (Center) Dependence on emissivity, for constant albedo of 0.7 and thermal inertia of 1000 tiu. (Right) Dependence on thermal inertia, for constant albedo of 0.7 and emissivity of 0.7.

through 3.4 present the results from our alternative models, which are (1) a N_2 distribution map where the surface is assumed to be entirely bare except for the N_2 ice contained in SP, (2) the reference map with a south polar cap, (3) the reference map with a southern zonal band. Section 3.5 presents a sensitivity study using mobile N_2 ice.

2.3.1 Reference Model

We first present the results from Pluto's current orbit using the reference map, along with a bare southern hemisphere.

After applying the constraints as described above for the reference model pressure curves, the remaining allowed parameter space is shown as the grayscale boxes in Figure 2.4. Albedos between 0.6 and 0.9 and thermal inertias above 400 tiu satisfy the constraints, with lower albedos requiring higher thermal inertias. All of the cases that had allowable emissivity values and pressure increases between 1988 and 2015 had minimum pressures between 1 and 3.5 μbar. There are no (A,Γ,ϵ) triplets that drop below the 0.5 μbar haze aggregation limit or the 0.06 μbar local atmosphere limit, or the even lower atmospheric transparency limit for Pluto's current orbit.

The pressure curves for five example cases, chosen to span the full range of allowable parameter space, are shown in Figure 2.5. The thick black line (case A) shows a central case with A = 0.75, Γ = 1225 tiu, and ϵ = 0.593. Case A shows an increase in pressure between perihelion and the peak of pressure shortly after the time of the New Horizons flyby, and then a slow decrease to the minimum pressure near northern winter solstice. The delay between perihelion and the peak of pressure is primarily due to the subsolar latitude dependence. The N_2 ices receive the strongest spatially-averaged insolation near 2008 (see Figure 2.2), which is determined in part from the $1/r^2$ dependence but more strongly depends on the incidence angle of sunlight onto SP. Thermal inertia adds to this delay as well. The jump in pressure near 5 μbar present in all five of the curves is caused by the small numerical discontinuity of 2% at the change in the form of the vapor pressure equation at the α-β transition of N_2, which occurs at 35.6 K (Fray and Schmitt, 2009).

The blue and green curves (cases B and C) are example cases that remain colder (and therefore

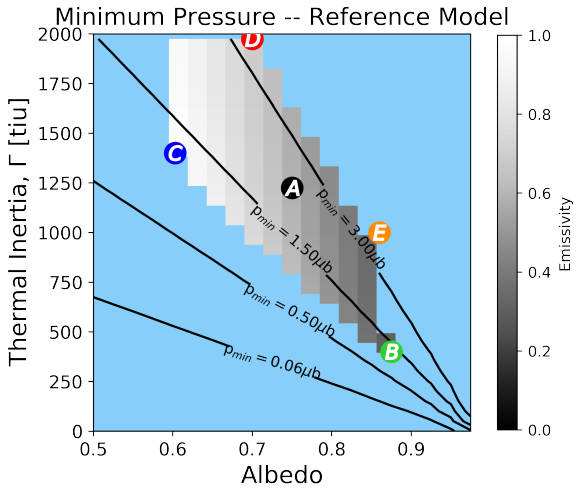

Figure 2.4: Restricted parameter space for Pluto's current orbit and the reference map (bare southern hemisphere) after choosing ϵ to ensure $P_{2015} = 11.5$ μbar, and applying the two further constraints: (1) $1 > \epsilon > 0.3$ (2) $3.14 > P_{2015}/P_{1988} > 1.82$. Grayscale indicates the emissivity required and black diagonal contour lines show the minimum pressure experienced over a Pluto year, for that combination of albedo and thermal inertia values. The lettered circles denote the (A, Γ, ϵ) values of the test cases shown in Figures 2.5, 2.6, and 2.7, using the same color scheme.

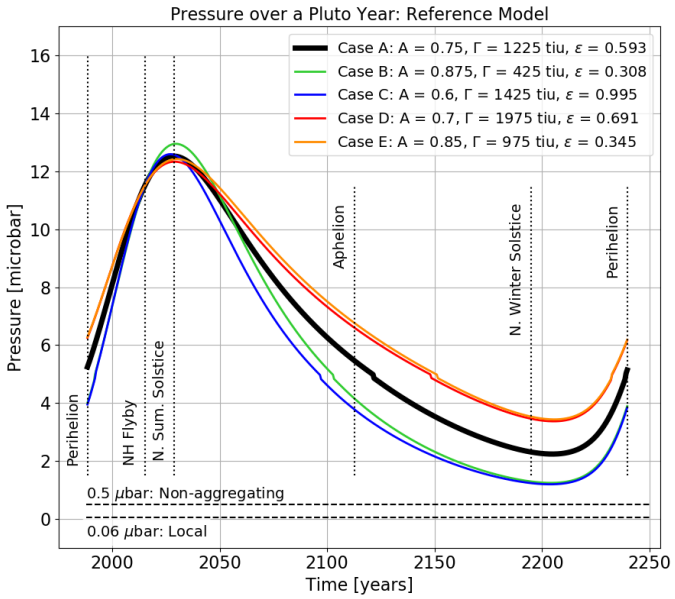

Figure 2.5: Pressure versus time curves for Pluto's current orbit and the reference map (bare southern hemisphere). The 2% discontinuity at 5 μbar reflects the small difference in the calculated pressure at the α-β transition temperature (see text for details).

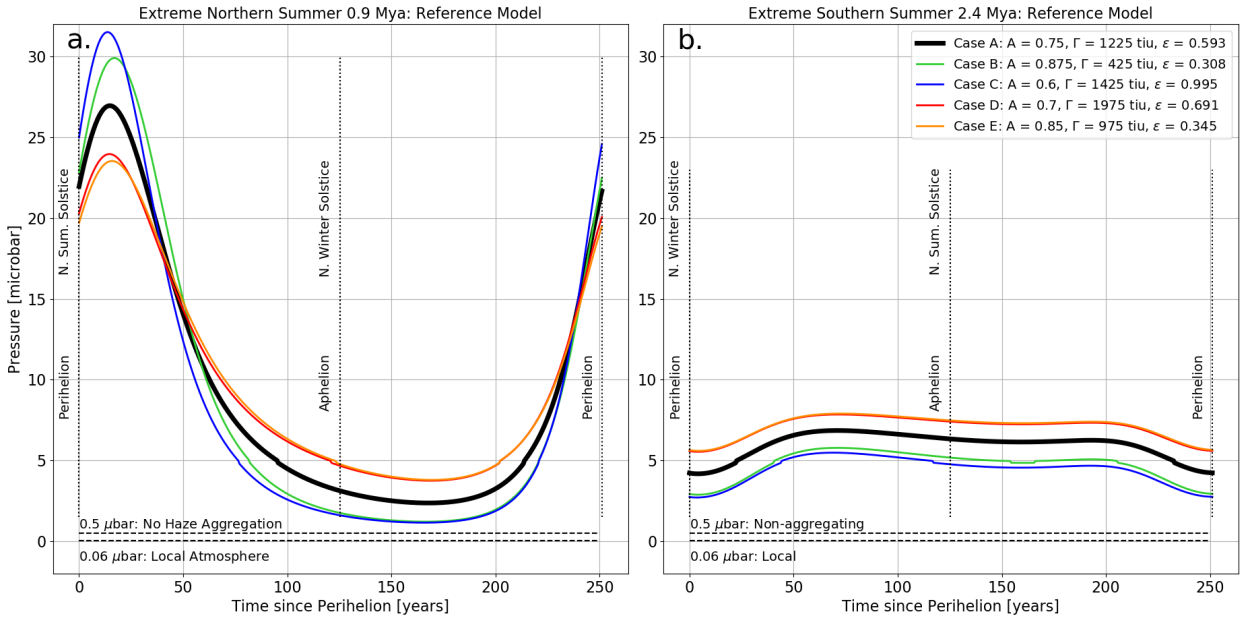

Figure 2.6: (a) Reference model pressure versus time curves for Pluto's orbit 0.9 Mya, when it was experiencing short, intense northern summers. (b) Reference model pressure versus time curves for Pluto's orbit 2.4 Mya, when it was experiencing long, mild northern summers.

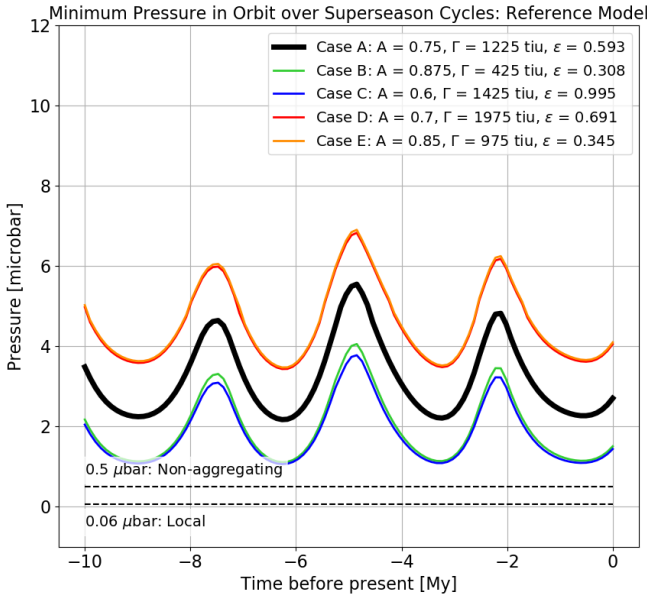

Figure 2.7: Annual minimum pressure experienced at Pluto's surface over the past 10 My for each of the five test cases, using the reference model.

have a lower surface pressure) than case A throughout most of the orbit. The combination of case B's higher albedo and low thermal inertia compensate for the effect of the low emissivity, keeping the surface colder than in case A. Case C has a lower albedo and a higher emissivity (so it effectively reradiates away the insolation), causing it to be consistently colder. The red and orange curves (cases D and E) in Figure 2.5 are example cases that remain warmer than case A throughout most of the orbit. Case D has a similar albedo and emissivity as case A, but experiences a smaller range of pressures due to the higher thermal inertia. Case E has a higher albedo than case A and a lower emissivity, so it is able to remain warmer despite a lower thermal inertia by reradiating the input solar insolation less effectively. None of the test cases predict pressures below any of the haze-important pressures; the atmosphere never becomes non-aggregating, local, nor UV-transparent. This reference model predicts a maximum in the pressure between 2027 and 2030, after which the surface pressure will begin to decrease.

As evident in Figure 2.5, extrema in the surface pressure occur close to solstices, when the primarily-northern N_2 deposits are receiving the most (or least, in the case of winter solstice) direct insolation. If northern summer solstice occurs near perihelion, the N_2 deposits will be receiving the most direct insolation (smallest incidence angle) when they are also receiving the most intense insolation (closest to the Sun), creating a strong but short northern summer. Conversely, if northern summer solstice occurs near aphelion, they will be receiving the most direct insolation (smallest incidence angle) when they are receiving the least intense insolation (farthest from the Sun), creating a mild but long northern summer. In order to investigate Pluto's pressure during these extreme seasons, we used the same five example cases as the current orbit and ran VT3D back 10 My, adjusting the obliquity, eccentricity, and subsolar latitude at perihelion according to Earle et al. (2017). Figure 2.6 shows the pressure versus time curve for the five example cases using our reference model during a period of intense northern summer 0.9 Mya (panel a) and a period of intense southern summer (and hence mild northern summer) 2.4 Mya (panel b). The color scheme and labelling of the cases remains the same as Figures 2.4 and 2.5.

Figure 2.6a shows the extreme summer characteristic of the orbital configuration Pluto was in

0.9 Mya, with a sharp peak just after perihelion and a wide, low minimum in the pressure curve. The pressure varies wildly over an orbit, ranging between 2.5 and 27 μbar for case A. Despite this wide range, none of the example cases drop below any of the pressures important to haze production, so haze would not be affected during this time period. Note that the minimum pressure does not occur simultaneously with aphelion and northern winter solstice, but rather occurs some time afterward due to the effect of thermal inertia.

During the mild northern summer at 2.4 Mya shown in Figure 2.6b, the pressure curves are noticeably flatter than the 0.9 Mya configuration and have a long peak-plateau where the pressure is stable. Since the reference model assumes a bare southern hemisphere (south of 35°S), the southern summer is not particularly extreme; at perihelion/southern summer solstice, the spatially-averaged insolation is very low since no N_2 deposits are receiving direct insolation, which causes the pressure to be low as well. In this configuration, like the current orbit and 0.9 Mya, none of the example cases become cold enough to disrupt haze.

Figure 2.7 shows the minimum pressure experienced over an orbit for the past 10 My (roughly three full obliquity cycles) for the five example cases. None of these curves fall below the 0.5 μbar nor the 0.06 μbar levels, or the even lower atmospheric transparency pressure levels. Depending on the choice of albedo, thermal inertia, and emissivity, this model predicts a minimum pressure over the past 10 My between 1 and 4 μbar. Note that the extreme values in Figure 2.7 do not occur exactly at the superseason epochs 0.9 and 2.4 Mya. This is due to the time offset between winter solstice and the minimum pressure (a seasonal thermal inertia effect).

2.3.2 Sputnik Planitia-only Model

Next, we discuss the results from our alternative models, beginning with a N_2 distribution in which SP is the only source of N_2 on the surface. Figure 2.8 shows the N_2 distribution for this alternative model. Both the band depth map (Schmitt et al., 2017) and the Hapke modeling map (Protopapa et al., 2017) clearly indicate deposits of N_2 ice outside of SP, but by limiting this distribution to SP alone, we can investigate the relative influence of SP on the climate compared

to the other N_2 deposits. SP is 1000 km in diameter (covering 5% of Pluto's total surface area), estimated to be 4 to 10 km thick, and has a fractional N_2 abundance as high as 60%, meaning that as much as 60% by area of each pixel is covered by N_2 (Protopapa et al., 2017). SP is located near the equator, spanning from 20°S to 50°N, so it remains at least partially illuminated for the full range of subsolar latitudes experienced over an orbit. For these reasons, we expect SP to be a strong driver of the atmospheric pressure, and thus expect the SP-only model results to be very similar to the reference model results. This distribution also allows a more direct comparison with Bertrand and Forget (2016), in which N_2 was sequestered into a circular SP-analog basin very similar to this distribution.

Figure 2.9 shows the restricted parameter space for the SP-only model. In comparison with Figure 2.4 for the reference model, lower thermal inertias are required for the SP-only model. Ignoring all of the N_2 ice outside of SP causes the peak in the spatially-averaged insolation to occur sooner after perihelion, and for the difference between the peak value and the perihelion value of the spatially-averaged insolation to be smaller (see Figure 2.2). As a consequence of these two changes to the insolation, lower thermal inertias are needed to compensate, in order to satisfy the constraint on the modeled increase in pressure between 1988 and 2015.

Five example test cases are shown in Figure 2.10 for the SP-only case. Note that due to the different constrained parameter space, these 5 cases are different than the test cases from the reference model, but the color scheme is the same, with red and orange curves being relatively warmer and higher pressure cases, while the blue and green curves are cooler and therefore lower pressure for much of the orbit. In the SP-only model, the peaks in most of the test case pressures occur slightly earlier, before northern summer solstice, and are slightly lower at 11.5 μbar (excluding case B) compared to 12.5 μbar for the reference model test cases. This is again a consequence of the differences in the spatially-averaged insolation between the reference model and the SP-only model. Additionally, the minima in the pressure curves are relatively lower than the reference model case, with the cases B and C dropping below the haze aggregation limit for a period of time near northern winter solstice. This behavior is a consequence of the lower thermal inertias required

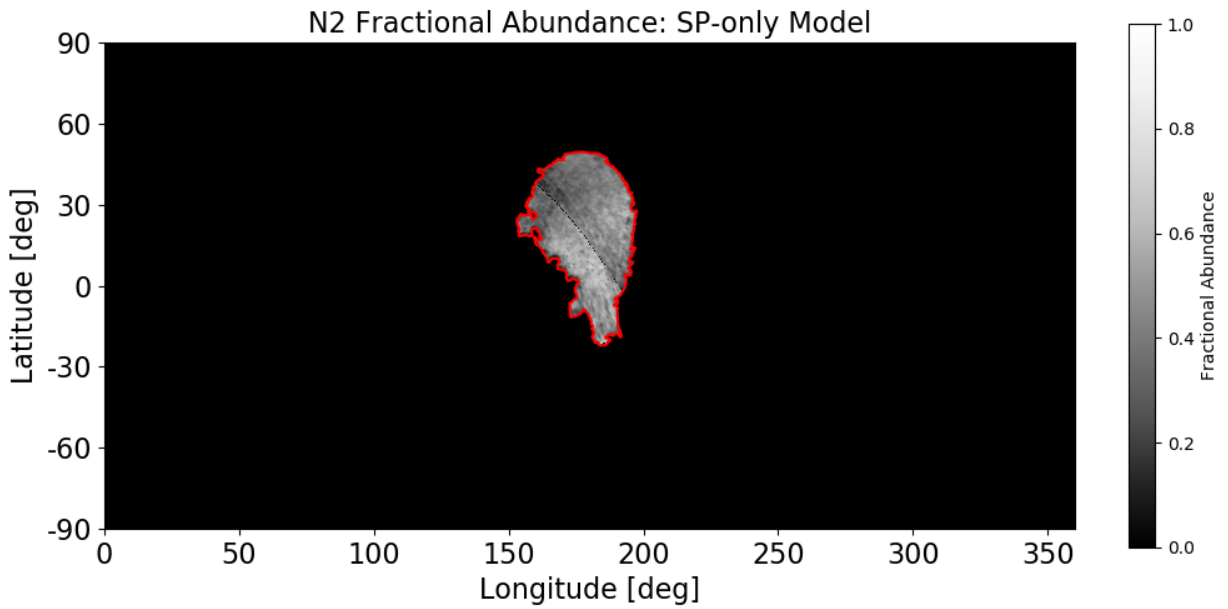

Figure 2.8: Assumed spatial distribution of N_2 ice for the SP-only model. The red outline shows the boundary of SP as defined by White et al. (2017).

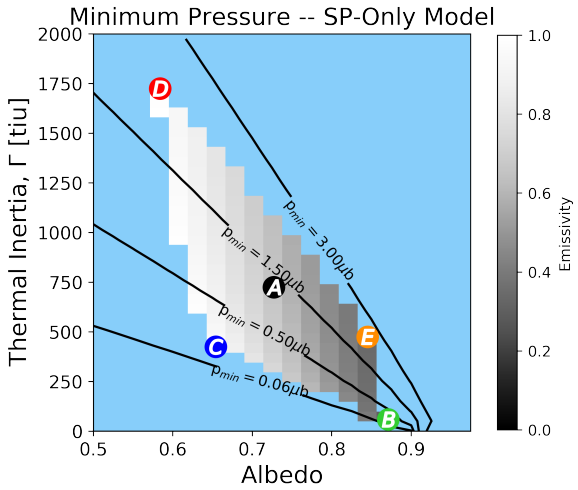

Figure 2.9: Restricted parameter space for Pluto's current orbit assuming SP is the only N_2 ice deposit, after choosing ϵ to ensure $P_{2015} = 11.5$ μbar, and applying the two further constraints: (1) $1 > \epsilon > 0.3$ (2) $3.14 > P_{2015}/P_{1988} > 1.82$. Grayscale indicates the emissivity required and black diagonal contour lines show the minimum pressure experienced over a Pluto year, for that combination of albedo and thermal inertia values. The lettered circles denote the (A, Γ, ϵ) values of the test cases shown in Figures 2.10 and 2.11, using the same color scheme.

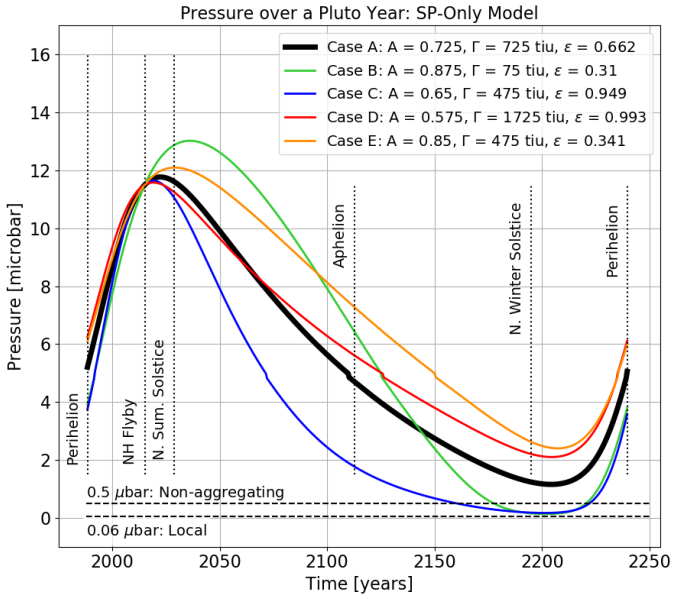

Figure 2.10: Pressure versus time curves for Pluto's current orbit, assuming SP is the only N_2 ice deposit.

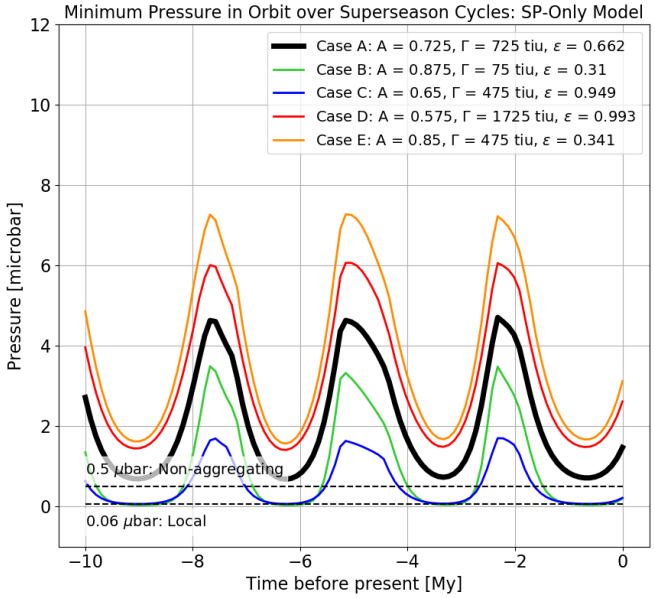

Figure 2.11: Annual minimum pressure experienced at Pluto's surface over the past 10 My for each of the five test cases, assuming SP is the only N_2 ice deposit.

for the SP-only case: lower thermal inertia allows input energy variations to be quickly realized as temperature variations, creating larger temperature and pressure swings. As expected, the general pressure evolution trend is very similar for the SP-only model compared to the reference model, confirming our expectation that SP is a large driver of the seasonal pressure cycle on Pluto. None of the test cases predict a local atmosphere in Pluto's current orbit.

We investigated the long-timescale behavior of the SP-only model as well. Figure 2.11 shows the minimum pressure experienced in each orbit going back 10 My, for the same five test cases. Test case B produced some past atmospheres that could have been non-aggregating and local, predicting minimum pressures that fall just below 0.06 μbar for select orbits over the past 10 My. None of the other test cases ever predict non-aggregating or local atmospheres, meaning the modeled atmospheres with those thermal parameters never collapse over the past 10 My (although case C comes very close with minimum pressure of 0.062 μbar).

2.3.3 South Polar Cap Model

Existing models have shown that perennial polar caps are not likely to form on Pluto, due to the high obliquity which causes the poles to receive more annually-averaged insolation than the equator (Young, 2013; Bertrand et al., 2018, 2019). Prior to the flyby, Young (2013) found that perennial northern volatiles were possible, but that most perennial southern volatile cases could be eliminated based on the modeled pressure increase between 1988 and 2006 not matching the observed increase from occultations. While the simulations of Bertrand et al. (2019) did not produce perennial polar caps of N_2, many of their simulations (representing a range of thermal inertia and albedo values for the N_2 ice, CH_4 ice, and H_2O substrate) resulted in the formation of a seasonal south polar cap that persisted for 80% to 90% of Pluto's orbit. Observations by New Horizons found the north polar region north of 60°N to be relatively N_2-free, with band depths less than 0.005 and fractional abundances less than 30% (Schmitt et al., 2017; Protopapa et al., 2017). The south polar region was experiencing polar night and was thus unobservable.

Hansen and Paige (1996) found that southern polar caps persist for a greater fraction of the orbit than northern caps, due to the fact that northern summer occurs as Pluto is approaching perihelion (causing rapid sublimation of the north polar cap and subsequent rapid condensation on to the cold southern polar cap), while southern summer occurs when Pluto is approaching aphelion (causing slower sublimation of the southern polar cap and slower condensation onto the northern polar cap). Their model assumed a small N_2 inventory (50 kg/m^2), as did Young (2013), while the global equivalent layer implied by the presence of SP alone (5 km deep, 1000 km in diameter) is on the order of 10^5 kg/m^2. A larger N_2 inventory could mean that polar caps grow thick enough to avoid completely sublimating away during the summer, producing perennial polar caps.

Normal reflectance maps produced from Pluto-Charon mutual events in the late 1980s showed a bright south polar cap (Young and Binzel, 1993). This cap was not necessarily composed of N_2 ice (it could have been bright CH_4 ice as well), but it is evidence that at least seasonal southern caps form on Pluto. Additionally, Grundy and Fink (1996) analyzed 15 years of visible-wavelength spectroscopy (1980-1994) and found that the spectra were consistent with a model in which much of the southern hemisphere (from the pole to 50°S) is covered with a N_2-dominated mix of ices, although other solutions could not be conclusively ruled out.

From the above evidence, we do not rule out the possibility of a perennial south polar cap, or a very long-lasting seasonal south polar cap, and choose to investigate it as one of our alternative models. For our south polar cap, we assume a cap of N_2 ice that extends from the pole to 60°S with a uniform fractional abundance of 20%, as shown in Figure 2.12. We investigated polar caps with higher fractional abundances, but found that for larger southern deposits of N_2 ice there were no (A,Γ,ϵ) capable of satisfying our constraints.

The region of allowed parameter space for the south polar cap model is shown in Figure 2.13. Compared the reference model, lower thermal inertias are required. Minimum pressures between 3 μbar and 0.5 μbar are predicted. There are no cases which predict pressures below any of the haze-disruption pressures; aggregation is not interrupted (although case C comes close to a non-aggregating atmosphere with a minimum pressure of 0.506 μbar), the atmosphere remains global,

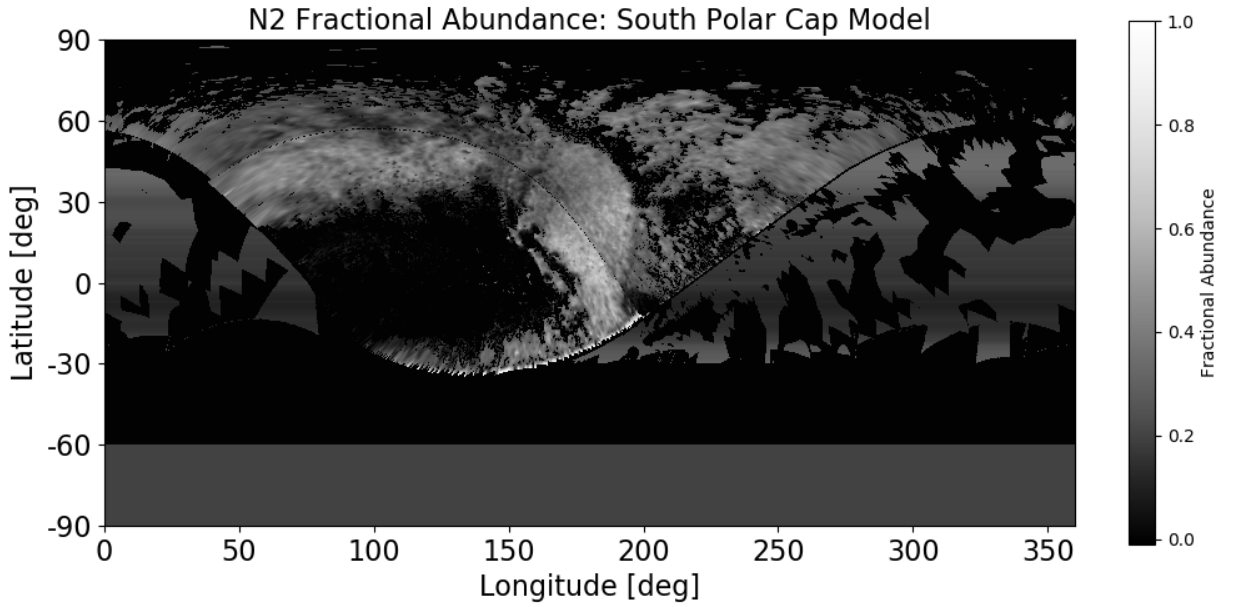

Figure 2.12: Spatial distribution of N_2 ice for the south polar cap model. Assumes a south polar cap is present extending from the pole to 60°S with a fractional abundance of 20%, in addition to the N_2 present in the reference map.

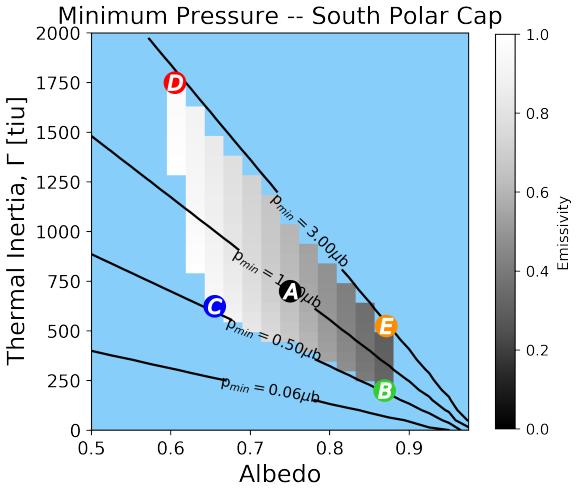

Figure 2.13: Restricted parameter space for Pluto's current orbit and a south polar cap after choosing ϵ to ensure $P_{2015} = 11.5$ μbar, and applying the two further constraints: (1) $1 > \epsilon > 0.3$ (2) $3.14 > P_{2015}/P_{1988} > 1.82$. Grayscale indicates the emissivity required and black diagonal contour lines show the minimum pressure experienced over a Pluto year, for that combination of albedo and thermal inertia values. The lettered circles denote the (A, Γ, ϵ) values of the test cases shown in Figures 2.14 and 2.15, using the same color scheme.

opaque to UV radiation, and does not collapse.

Five test cases from the region of allowed parameter space are shown in Figure 2.14. Overall, the shape and amplitude of the pressure curves are very similar to those from the reference model, with slightly lower maximum and minimum pressures for the south polar cap model. The pressure falls off more quickly in the south polar cap model, leading to a broader minimum extending from aphelion to winter solstice. This behavior, along with the slightly lower maximum and minimum pressures, occurs because the ice in the south polar cap is radiating away energy via thermal emission during the entire orbit (as are the northern hemisphere ices), but is obscured in polar night thus isn't absorbing any solar insolation for part of the orbit.

The superseasonal behavior of the five test cases for the south polar cap model is shown in Figure 2.15. Cases B (green) and C predict pressures that fall below the haze aggregation limit at points in the obliquity cycle despite remaining above the limit in Pluto's current orbital configuration. Near the extreme northern summer period at 0.9 Mya, the minimum pressure over an orbit predicted in Case C drops to 0.41 μbar and Case B drops to just under the limit at 0.497 μbar. In this orbital configuration, the south pole is pointed most directly at the sun at aphelion. The majority of the N_2 ice deposits are not directly illuminated since they are in the northern hemisphere, and despite direct insolation, the N_2 ice at the south pole is not receiving intense insolation due to the high heliocentric distance. Case C has a high emissivity of 0.967, so the unilluminated northern volatiles efficiently reradiate what little solar energy the southern volatiles absorb, causing the low minimum pressure. Case B's high albedo prevents the small amount of northern volatiles from absorbing much energy neear winter solstice, contributing to the low minimum pressure. The other three test cases' combination of albedo, thermal inertia, and emissivity values are able to counteract the orbital configuration's effect on the pressure and their predicted pressures remain above all of the haze-disruption pressures.

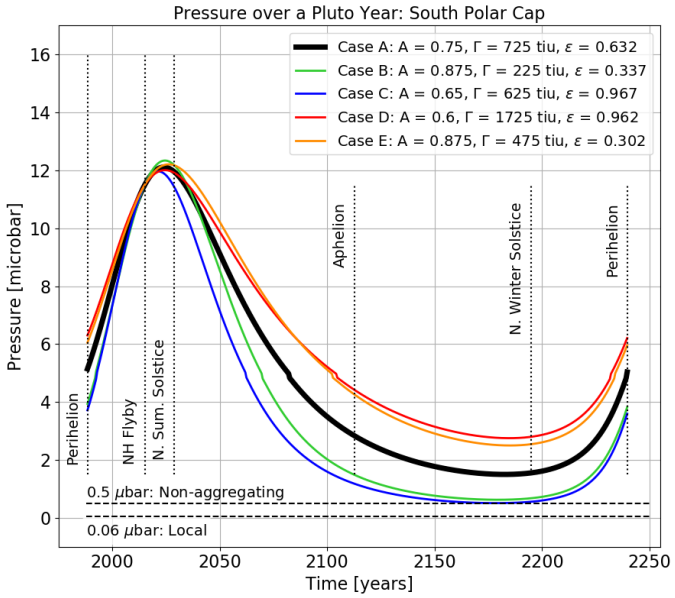

Figure 2.14: Pressure versus time curves for Pluto's current orbit, for the south polar cap model.

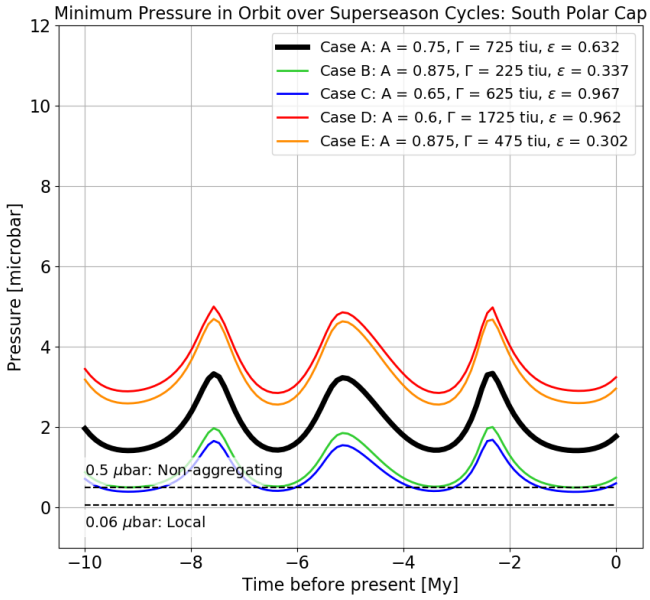

Figure 2.15: Annual minimum pressure experienced at Pluto's surface over the past 10 My for each of the five test cases, for the south polar cap model.

2.3.4 Southern Zonal Band Model

Figure 2.16 shows the N_2 distribution for the final alternative model we investigate, the southern zonal band model. This distribution consists of the reference map plus a zonal band of N_2 between 35°S and 55°S with a fractional abundance of 20%. This location was chosen to be similar to the northern midlatitude distribution; between 35°N and 55°N there is a band of N_2 with an average fractional abundance of roughly 40%, visible in the reference map and also identified in Protopapa et al. (2017). We initially tried a southern zonal band with a fractional abundance of 40% to match the observed northern band, but found there were no (A,Γ,ϵ) triplets capable of satisfying the constraints we imposed. Having such a significant deposit of N_2 ice in the southern hemisphere produced very high spatially-averaged insolation and therefore high pressures in 1988 (near perihelion and equinox). Even with very low thermal inertias (<50 tiu), it was not possible to double or triple the atmospheric pressure between 1988 and 2015 while requiring that the modeled 2015 pressure be 11.5 μbar. This is consistent with results from Meza et al. (2019), who found that small southern N_2 deposits (or no southern N_2 at all) were required to produce reasonable pressure evolution in which the peak of pressure occurs after 2015. Thus, we adopt a fractional abundance of 20% for the southern zonal band. A northern boundary for this band of 35°S places it just out of view of the high resolution encounter hemisphere images. At the time of the New Horizons flyby in 2015, everything south of 40°S was experiencing polar night.

Figure 2.17 shows the region of allowed parameter space for the southern zonal band model. Thermal inertias between 25 and 1000 tiu are able to satisfy our constraints. Minimum pressures range between 1.5 μbar to 0.01 μbar. Many of the (A,Γ,ϵ) triplets produce pressure curves that fall below the haze aggregation limit. Albedos between 0.7 and 0.9 coupled with thermal inertias lower than 200 tiu and nearly the full range of emissivities ($0.3 < \epsilon < 1$) lead to atmospheric collapse.

Five test cases are shown in Figure 2.18 on a linear scale, and in Figure 2.19 on a logarithmic scale to highlight the very low pressures near aphelion and northern winter solstice. All of the example cases have perihelion pressures of around 5 μbar, and then the pressure rapidly increases

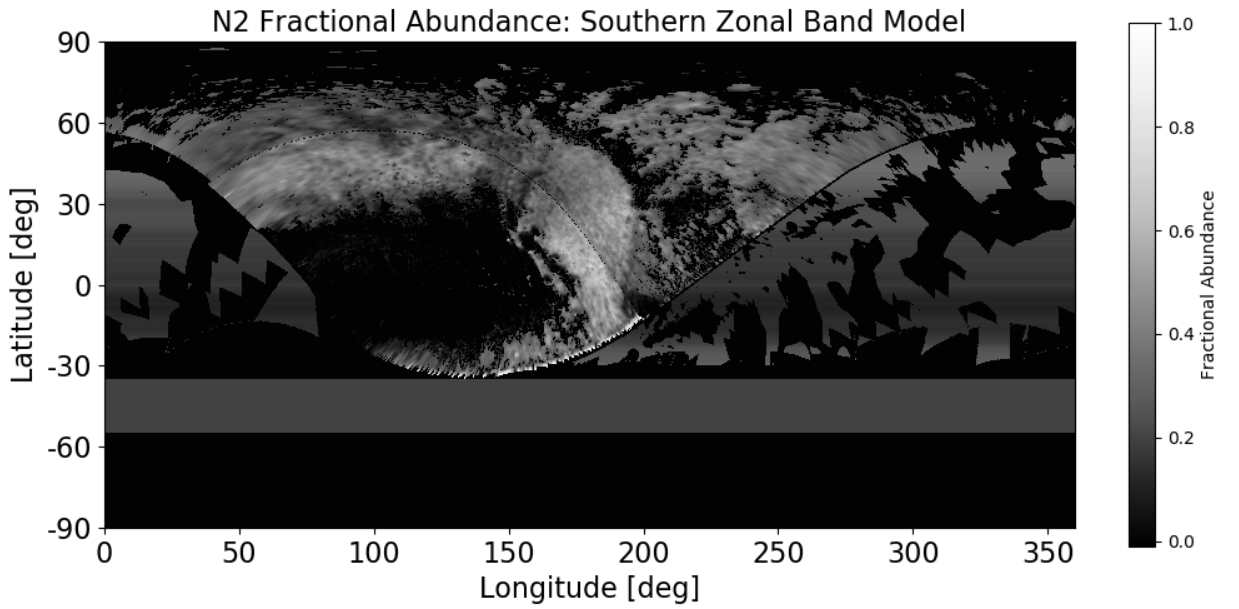

Figure 2.16: Spatial distribution of N_2 ice for the southern zonal band model. Assumes a zonal band of N_2 is present between 35°S and 55°S with a fractional abundance of 20%, in addition to the N_2 present in the reference map.

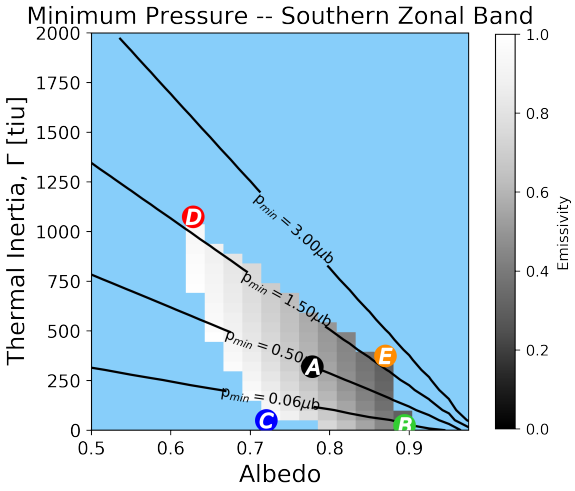

Figure 2.17: Restricted parameter space for Pluto's current orbit and a southern zonal band after choosing ϵ to ensure $P_{2015} = 11.5$ μbar, and applying the two further constraints: (1) $1 > \epsilon > 0.3$ (2) $3.14 > P_{2015}/P_{1988} > 1.82$. Grayscale indicates the emissivity required and black diagonal contour lines show the minimum pressure experienced over a Pluto year, for that combination of albedo and thermal inertia values. The lettered circles denote the (A, Γ, ϵ) values of the test cases shown in Figures 2.18, 2.19, and 2.20, using the same color scheme.

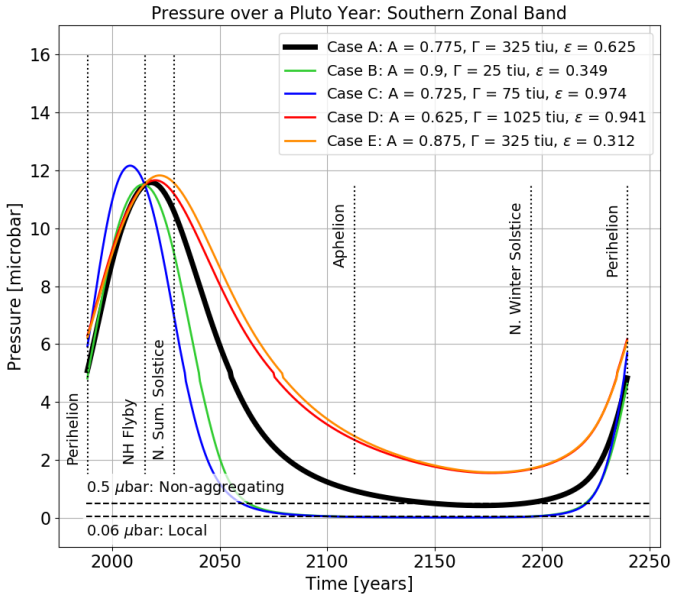

Figure 2.18: Pressure versus time curves for Pluto's current orbit, for the southern zonal band model (linear scale).

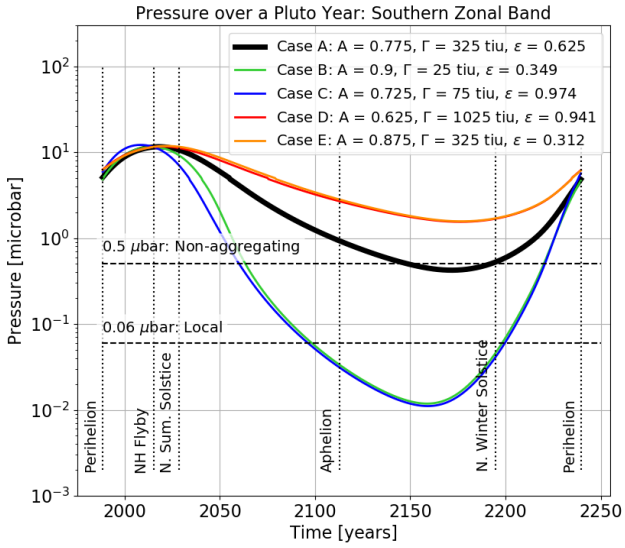

Figure 2.19: Pressure versus time curves for Pluto's current orbit, for the southern zonal band model (log scale). At this scale, Case B is nearly coincident with Case C, and Case D is nearly coincident with Case E.

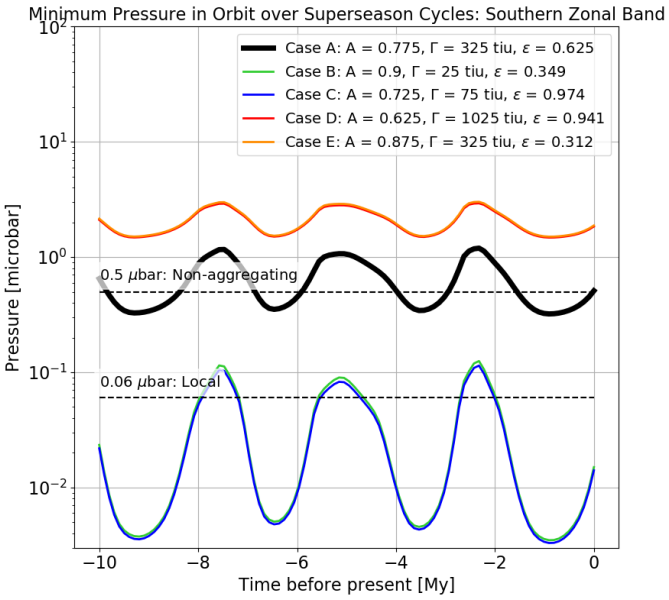

Figure 2.20: Annual minimum pressure experienced at Pluto's surface over the past 10 My for each of the five test cases, for the southern zonal band model (log scale). At this scale, Case B is nearly coincident with Case C, and Case D is nearly coincident with Case E.

to 11.5 μbar in 2015. Compared to the reference model, the peak in the pressure curve is much sharper and the minimum is much broader, due to the lower thermal inertias. The pressure peak occurs earlier in the orbit, around 2016 rather than 2027 for the reference model. This is driven by the spatially-averaged insolation; it is highest near equinox (nearly concurrent with perihelion) when the southern zonal band of N_2 ice and SP are both being directly illuminated, and decreases as the subsolar latitude moves to the north after equinox and the zonal band moves into polar night. The extremely low pressures occur near aphelion and winter solstice, when the spatially-averaged insolation onto the N_2 ices is low, and are due in part to the low thermal inertias which allow for quick temperature and pressure changes.

Figure 2.20 shows the superseasonal behavior for the five test cases in the southern zonal band model. Three of the five cases predict minimum pressures below the haze aggregation limit. Two of those cases, B (green curve) and C (blue curve), predict a minimum pressure below the local atmospheric limit in nearly every orbit for the past 10 My. All of the test cases produce atmospheres that remain opaque to UV radiation throughout the past 10 My.

2.3.5 Mobile Nitrogen Sensitivity Test

A limitation of the results we present earlier in Section 3 is the use of a static N_2 distribution. On Pluto, atmospheric N_2 is able to condense onto previously N_2-free surfaces, a process not accounted for in a static model. We address this limitation here with a sensitivity study. The purpose of this study is to evaluate the effect mobile N_2 has on the minimum pressure over a Pluto orbit, consequently what effect it has on haze production, and under what conditions a static N_2 assumption is valid. A static N_2 distribution has two crucial benefits: (1) computation speed that allows us to explore a wide range of thermal parameters and long timescales and (2) an exact match to the observed N_2 distribution in 2015 (the only time a nearly-global map has been produced).

We simulated the effect of mobile N_2 by establishing the times and locations where the N_2 could condense onto the surface, by identifying when and where the substrate temperature is colder than the perennial N_2 ice's temperature. First, we calculated the bare substrate temperature as a

function of time at each latitude, which depends on the substrate emissivity, albedo, and thermal inertia. We selected a value of 800 tiu for the thermal inertia, 0.9 for the emissivity, and investigate albedos between 0 and 1 in steps of 0.1 (similar to the values of 800 tiu for bare-ground thermal inertia and 1 for emissivity chosen in Bertrand and Forget (2016), Bertrand et al. (2018), Bertrand et al. (2019)). The temperature at each location is also dependent on the incident diurnally-averaged solar insolation, which varies with latitude, time, and albedo. We began by using the Case A N_2 ice temperature from each of the four N_2 distributions presented in Sections 3.1 to 3.4. We assumed that regions of the surface that are colder than the N_2 ice at a given time will become covered by mobile N_2 ice via condensation from the atmosphere, forming a seasonal deposit. This includes regions of bare substrate and also regions with perennial N_2 deposits that have fractional abundances less than 1. For example, if a given area has perennial N_2 with a fractional abundance of 0.25, then the remaining 75% of the area can become covered by seasonal N_2. The resultant seasonal N_2 ice appears with the same thermal parameters as the perennial N_2 and a fractional abundance of 0.5. Using the seasonal N_2 ice distribution as well as the perennial N_2 ice as prescribed by the static N_2 distribution, we recalculated the diurnally- and spatially-averaged insolation onto all of the N_2 ice as described in Section 2.2, and used it to recalculate the temperature and pressure behavior as a function of time using VT3D. If the model didn't predict a 2015 pressure in the range 11.5 ± 0.5 μbar, we adjusted the emissivity and recalculated the perennial-only temperatures, the resulting locations of seasonal deposits, and finally the pressure accounting for both perennial and seasonal deposits. This iterative process was repeated until the 2015 pressures fell in the range 11.5 $\pm$ 0.5 μbar. In general, the modified Case A including mobile N_2 for all four N_2 distributions and all substrate albedos required equivalent or lower emissivities than the corresponding unmodified perennial-only static Case A.

The following figures show the effect of seasonal N_2 on the pressure. We discuss the results in terms of three broad classes divided by substrate Bond albedo: $A_{sub} < 0.3$ (dark substrate), $0.3 < A_{sub} < 0.7$ (intermediate substrate), and $A_{sub} > 0.7$ (bright substrate). In 2015, regions of Pluto's surface with Bond albedos less than 0.3 include the dark maculae near the equator,

while N_2-free regions with Bond albedos higher than 0.7 include the polar region north of 60°N and Eastern Tombaugh Regio (Buratti et al., 2017). We discuss three types of pressure curves: (1) static, which use a static N_2 distribution and were presented earlier in Section 3, (2) mobile, P_{2015}-unconstrained, which have the same thermal parameters as the static cases but allow N_2 mobility causing the pressure in 2015 to be inconsistent with observations, and (3) mobile, P_{2015}-constrained, in which we include seasonal N_2 deposits and modify the emissivity to ensure the pressure in 2015 equals 11.5 μbar as described above. As a specific example, we first present the results from Reference Distribution Case A.

Using Reference Case A ($A_{N2} = 0.75$, $\Gamma = 1225$ tiu, $\epsilon = 0.593$), dark substrate albedos ($A_{sub} < 0.3$) remain warmer than the N_2 ice temperature throughout much of the year. For example, for $A_{sub} = 0.1$, the average substrate temperature is 44 K, while the average N_2 temperature is 36 K. Consequently, there are only small, short-lived seasonal N_2 deposits, or in the darkest albedo cases, no seasonal N_2 deposits at all, as seen in the left panels of Figure 2.21. The minimum pressure is not largely affected, remaining at 2 μbar, so the atmosphere remains haze-aggregating, global, and opaque to UV radiation.

For bright substrate albedos ($A_{sub} > 0.7$), the substrate is typically colder than the N_2 ice temperature for most of the year. In Reference Case A, the N_2 albedo is 0.75, and when $A_{sub} > A_{N2}$ the substrate will absorb less sunlight than neighboring N_2 ice deposits at the same latitude, tending to make the substrate colder than N_2 ice. For example, with $A_{sub} = 0.9$, the average substrate temperature is 26 K, compared to 36 K for the N_2 ice temperature. This results in a "Snowball Pluto" scenario, in which the entire surface is covered by N_2 ice deposits for Pluto's entire orbit, as shown in the right panels of Figure 2.21. Observations of Pluto's surface composition are inconsistent with a surface entirely covered by N_2 ice in 2015 (Schmitt et al., 2017; Protopapa et al., 2017, 2020). The bright substrate cases have the peak in the pressure occurring earlier within Pluto's orbit, closer to perihelion, and the variation in the pressure over the orbit is reduced. Consequently, the ratio of the predicted 2015 to 1988 pressures is below the allowable 3-σ range and the predicted atmosphere is not doubling (or tripling) as Pluto's atmosphere was observed to do in that time

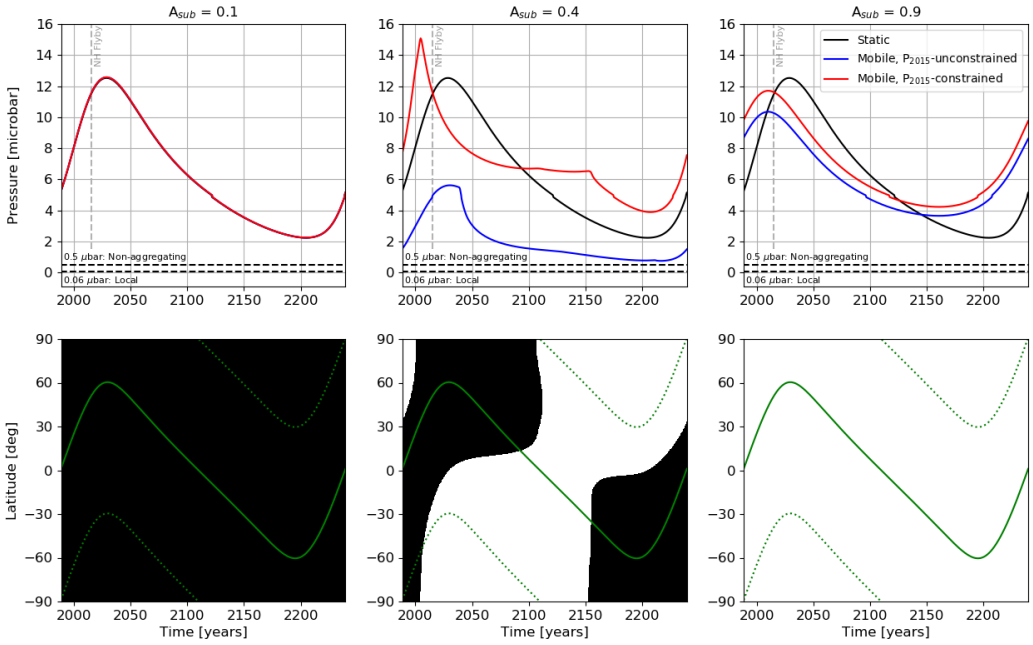

Figure 2.21: (top) Pressure vs. time for Reference Case A with three substrate albedos: A_{sub} = 0.1 (left), 0.4 (middle), and 0.9 (right). The static Reference Case A pressure is shown in black, while the pressure from the mobile, P_{2015}-constrained case is shown in red. The blue line shows the mobile, P_{2015}-unconstrained case, which illustrates the need to adjust the emissivity in order for P_{2015} to equal 11.5 bar, especially for intermediate albedos. For the low A_{sub} case (left), these three lines are the same. For intermediate A_{sub} cases (middle), the mobile, P_{2015}-constrained case produces a sharper, higher, earlier peak in the pressure, and a higher minimum pressure. (bottom) Latitudes of seasonal N_2 deposits as a function of time for the mobile, P_{2015}-constrained Reference Case A with three substrate albedos: A_{sub} = 0.1, 0.4, and 0.9. White indicates seasonal N_2 coverage at that latitude and time, while black indicates bare substrate. While many of these latitudes also contain perennial deposits (see Figure 2.1), only the seasonal deposits are indicated with white. The green solid line shows the subsolar latitude, while the green dotted line marks the edge of the polar night region: any latitudes polewards of the green dotted line experience no daylight. Between 2110 and 2150, the case with A_{sub} = 0.4 predicts that Pluto would be fully covered in N_2, a "Snowball Pluto" scenario, while at other times there exists only a polar cap, at the north pole around the time of northern winter solstice (2195) and at the south pole near southern winter solstice (2029). When A_{sub} = 0.1 (left), no seasonal deposits form at any latitudes and times, and when A_{sub} = 0.9 seasonal deposits form at all latitudes and last for Pluto's entire orbit.

period (see the left panels of Figure 2.22). We would not consider these bright substrate cases to be acceptable models based on this constraint and the surface composition observations.

For intermediate substrate albedos ($0.3 < A_{sub} < 0.7$), seasonal N_2 deposits condense onto and subsequently sublime away from the substrate at various latitudes and times. Figure 2.21 shows an example of this, for a substrate albedo of 0.4. The top panel shows three sets of pressure vs time: (1) the black line shows the static case A with no seasonal N_2, the same as what is shown in Figure 5, (2) the blue line shows the mobile, P_{2015}-unconstrained case A and (3) the red curve shows the mobile, P_{2015}-constrained case A. The blue curve demonstrates the need to adjust the emissivity once mobile N_2 is added; the pressure is uniformly lower for the mobile, P_{2015}-unconstrained case than for the mobile, P_{2015}-constrained case (red). Decreasing the emissivity from 0.593 to 0.395 increases the pressure in 2015 to 11.5 μbar in order to be consistent with the observed pressure. The mobile, P_{2015}-constrained case has a minimum pressure of 4 μbar and a ratio P_{2015}/P_{1988} of 1.5, which is shown in Figure 2.22. The bottom panel of Figure 2.21 shows the latitudes where seasonal N_2 deposits form for the mobile, P_{2015}-constrained case A. While many of these latitudes also contain perennial deposits (see Figure 2.1), only the seasonal deposits are indicated in Figure 2.21. Between 2110 and 2150, this case predicts that Pluto would be fully covered in N_2, a "Snowball Pluto" scenario, while at other times there exists only a polar cap: at the north pole around the time of northern winter solstice (2195) and at the south pole near southern winter solstice (2029). However, for this case, and almost all of the other intermediate albedo cases from the four distributions, the predicted ratio of pressures in 2015 and 1988 is below the allowed 3-σ range. The top panel of Figure 2.21 shows the predicted pressure vs. time has a sharper, higher, and earlier peak in addition to the higher minimum. The peak occurs prior to 2015, so while the atmosphere does double in pressure soon after 1988, the pressure is already decreasing at the time of the New Horizons flyby and the ratio of pressures in 2015 and 1988 is only 1.5. The overturning of pressure prior to 2016 is inconsistent with observations, which show a monotonic increase in pressure through 2016 (Meza et al., 2019). The early peak and inconsistent P_{2015}/P_{1988} ratio were predicted in most of the intermediate albedo cases for the four distributions.

While the previous discussion focused on the reference distribution case A, the general behavior was repeated in our analysis of the other N_2 distributions as well. Figure 2.22 shows the minimum pressure and ratio of 2015 to 1988 pressures as a function of substrate albedo for Case A for each of the four distributions. For substrate albedos less than 0.3, there is little to no seasonal N_2, so the minimum pressure, and consequently the time spent below any of the haze limiting pressures, do not differ greatly from the static cases. For intermediate albedos, seasonal N_2 deposits condense and sublime away at various times. In general, the inclusion of seasonal deposits increases the minimum pressure. For the Southern Zonal Band Case A specifically, the minimum pressure is increased above the haze aggregation limit when $A_{sub} > 0.5$, so the inclusion of seasonal N_2 deposits prevents the atmosphere from becoming non-aggregating. However, for all distributions, cases with $A_{sub} \geq \sim 0.3$ are inconsistent with observations. The peak in pressure occurs too soon after perihelion, contradicting observations of a monotonic increase in surface pressure through 2016 (Meza et al. 2019) and also failing to reproduce the two- to three-fold increase in surface pressure observed between 1988 and 2015 (see the left panels of Figure 2.22). For bright substrate albedos ($A_{sub} > 0.7$), seasonal N_2 deposits would cover Pluto completely, which is inconsistent with surface composition measurements (Schmitt et al., 2017; Protopapa et al., 2017, 2020).

Seasonal N_2 deposits could have different thermal properties than their perennial counterparts, unlike the assumption used here that perennial and seasonal deposits share the same albedo, thermal inertia, and emissivity. Freshly condensed N_2 ice could be brighter than older N_2 ice, which has been processed by incident radiation and could contain contaminants that have fallen onto it. Fresh N_2 ice could be transparent, revealing the albedo of the substrate below (Eluszkiewicz, 1991); the substrate albedo should then be used in energy balance calculations. If the substrate albedo is less than the perennial N_2 ice's albedo, then the effect of transparent seasonal deposits is to warm the N_2 ice and increase the surface pressure (unless the emissivity is also increased in order to keep P_{2015} at 11.5 μbar). If the substrate albedo is greater than the perennial N_2 ice's albedo, then transparent seasonal deposits create a cooler, lower pressure atmosphere, compared to the situation in which the seasonal and perennial deposits have the same albedo. Seasonal N_2 deposits

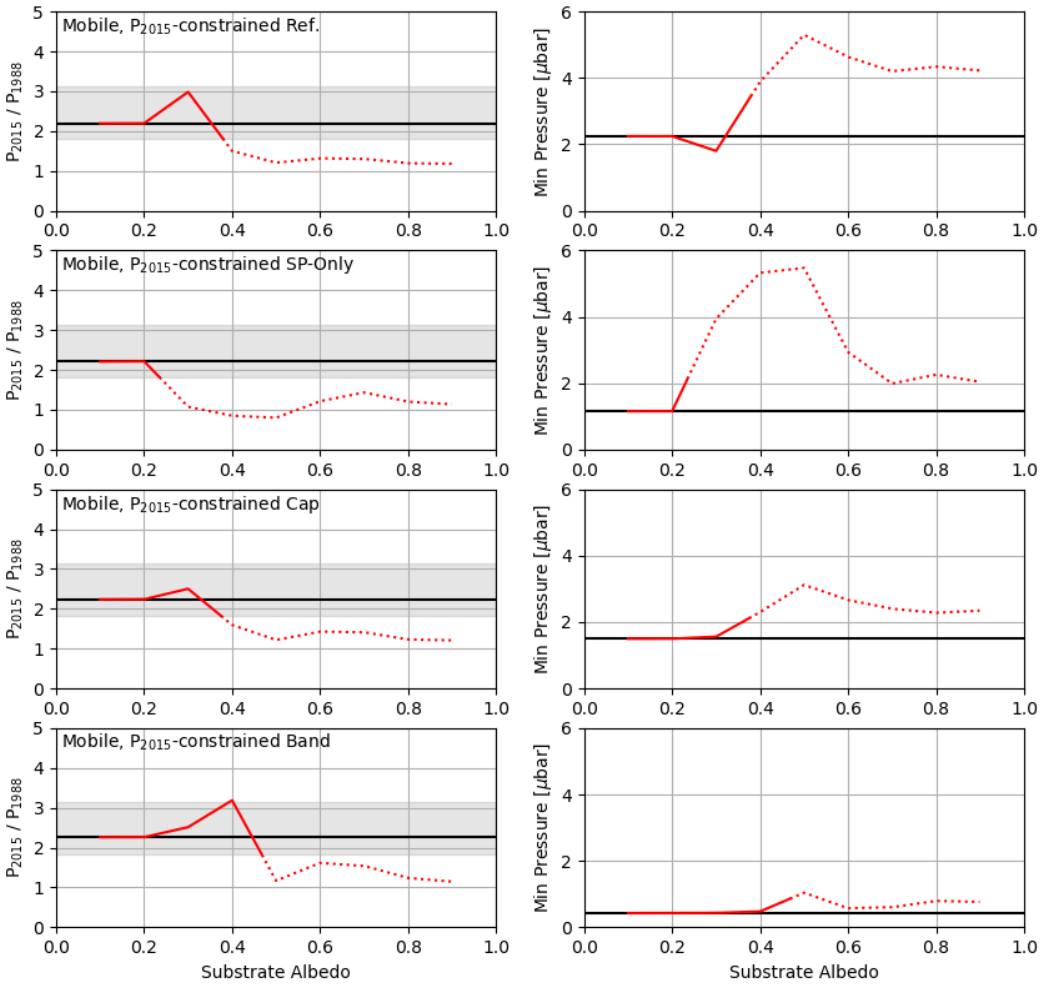

Figure 2.22: Results from the mobile N_2 ice sensitivity test. From top to bottom, they are: the Mobile, P_{2015}-constrained Reference Case A; Mobile, P_{2015}-constrained SP-Only Case A; Mobile, P_{2015}-constrained South Polar Cap Case A; and Mobile, P_{2015}-constrained Southern Zonal Band Case A. The left panels show show the effect of substrate albedo on the ratio of the 2015 pressure to the 1988 pressure, with the horizontal gray shading indicating the 3-σ range from observations (1.82 - 3.14), while the right panels show the effect of substrate albedo on the minimum pressure over the course of an orbit. In all panels, the horizontal black line indicates the value from the respective static pressure curve, with no seasonal N_2. The transition from solid to dotted red lines occurs after the highest A_{sub} with a valid pressure ratio.

will be thinner than perennial deposits which have been built up over many Pluto years. Annual condensation rates were calculated to be on the order of a centimeter by Bertrand et al. (2018). It may therefore be more accurate to use the substrate thermal inertia in energy balance calculations, since the material contained within one thermal skin depth (5 - 50m) will be primarily substrate with just a thin coating of N_2. Freshly condensed N_2 might also have lower emissivity than older N_2 deposits, owing to the smaller grains (older N_2 could sinter together over time into larger grains) (Stansberry et al., 1996). Exploring all of these possibilities introduces considerable complexities to the problem of modeling Pluto's pressure.

What we have shown here is not all-encompassing; we have not explored the full range of thermal parameters for the seasonal N_2 ice, and we have not iterated this process to see if the newly recalculated N_2 temperature behavior reproduces the same seasonal N_2 locations. Including mobile N_2 introduces a plethora of new parameters space to explore (substrate thermal properties, seasonal N_2 deposit thermal properties and fractional abundance), which add complexity to the problem of matching the New Horizons observations, such as the pressure and the nitrogen distribution in 2015. Exploring all of these possibilities is outside the scope of this paper. By providing this sensitivity section, we hope to motivate our assumption of static, perennial N_2. For seasonal N_2 deposits with the same properties as their perennial counterparts, we found no cases which produced widespread seasonal deposits and simultaneously matched observations of the 2015 pressure and reproduced the two- to three-fold increase in pressure between 1988 and 2015. For substrate albedos less than 0.3, the substrate is too warm for N_2 condensation. For intermediate substrate albedos, the predicted pressure variations between 1988 and 2016 are inconsistent with observations from occultations. For bright substrate albedos, the resulting surface composition and the pressure behavior are both inconsistent with observations and can thus be ruled out.

From this sensitivity study we conclude the following:

(1) The inclusion of mobile N_2 tends to raise the minimum pressure, because the emissivity must be decreased in order to match the observed 2015 pressure. This restricts the section

of parameter space that leads to haze disruption or atmospheric collapse.

(2) There is likely not a large amount of N_2 in the unobserved southern hemisphere. Most cases that have expansive and/or long-lived seasonal deposits in the southern hemisphere failed to match observations of the change in surface pressure between 1988 and the present. We concluded this from our static-N_2 models as well; the South Polar Cap and Southern Zonal Band distributions required very low N_2 fractional abundances (less than 0.2) to match observations. Meza et al. 2019 reached a similar conclusion from their modeling results as well.

(3) Our conclusions about haze interruption based on static N_2 distributions are not likely to be changed based on the inclusion of mobile N_2.

2.4 Haze Implications

In Pluto's current orbit, our reference model does not produce any case where the pressure drops low enough to interrupt haze. There are no combinations of parameters, namely Bond albedo, thermal inertia, and emissivity, which are simultaneously capable of reproducing the observed 2015 flyby pressure and having a minimum pressure below any of the haze-disruption pressures, in the current orbit. Additionally, on long timescales, none of the five test cases in our reference model produce pressures that fall below the haze-disruption pressures. The modeled atmosphere remains haze-aggregating, global, and opaque to UV radiation during the 10 My period we investigated.

Southern N_2 is necessary for haze to be interrupted. Our south polar cap and southern zonal band models both predict that haze aggregation could stop at some point during the orbit, although in the case of our polar cap this is only possible for special orbital configurations when northern summer solstice and perihelion occur at the same time, and then only for low-albedo, low-thermal inertia cases. In the case of the southern zonal band model, haze aggregation is stopped between aphelion and northern winter solstice in Pluto's current orbit and in many past orbits going back 10 My, for most cases in the allowed parameter space. Stopping haze aggregation for a portion of the

orbit could cause the appearance and size of the haze particles being deposited to vary seasonally. The haze was observed globally at the time of the New Horizons flyby, but it was brighter towards the north, probably indicating greater haze mass (Cheng et al., 2017). Deposition rates could be dependent on the brightness, which could vary seasonally. Thus, locations on the surface with a higher deposition rate could be covered with more monomer haze particles than others, explaining the heterogeneity. As demonstrated in Bertrand and Forget (2017), haze production rates as a function of latitude and time can be determined based on the assumed UV flux at the top of Pluto's atmosphere and the opacity of the atmosphere. This same technique could be applied to our results, in order to determine which latitudes would experience the largest decrease in haze production resulting from atmospheric collapse. If meridional circulation is weak, these latitudes would also experience the largest decrease in haze deposition.

The atmosphere resulting from the southern zonal band model becomes local between aphelion and northern winter solstice, but only for the lowest thermal inertias. When the atmosphere becomes local, the sublimation winds are equal in magnitude to the atmosphere's sound speed, and thus there will be large pressure variations across the surface (Trafton and Stern, 1983). As a result, the atmosphere becomes patchy and Io-like, extending only over the warmest patches of the surface. Any haze deposition would be restricted to these patches, which could build up surface contrasts. It could also reinforce existing contrasts. All else being equal, the darkest N_2 surfaces will be the warmest and could maintain an atmosphere above them. If the deposition of haze particles darkens the surface further, it would create a positive feedback that enhances existing surface contrasts. Conversely, a local atmosphere could shield the underlying surface from UV light, preventing ice-phase photolysis. Whether this would lead to positive or negative feedback depends on the relative albedo of the gas-phase and ice-phase photolysis products, and their rates of production.

A complication we have not considered here is a time-variable CH_4 mixing ratio in the atmosphere. The pressures we investigate here as being relevant to haze production (0.5 μbar haze aggregation limit, 0.06 μbar local atmosphere limit, and the 10^{-3} to 10^{-4} μbar atmospheric

transparency limit) are determined from the atmospheric structure as observed in 2015 by New Horizons. Over time however, the mixing ratio of CH_4 could vary, changing the altitude at which the photochemical reactions producing the haze occur. A variable CH_4 mixing ratio would have implications for haze chemistry, changing the color and composition, as well as the production rate. For example, if the mixing ratio was about 10^{-3} times less than it is currently, the atmospheric transparency limit would be 10^3 times higher, at about 1 μbar, and many of our cases would become transparent to UV radiation. However, models with variable mixing ratios of CH_4 show much less variation than that, on the order of a factor of 10 to 20 (Bertrand et al., 2019), and the CH_4 mixing ratio tends to be higher when the surface pressure is lowest (Bertrand and Forget, 2016). This suggests that, while a variable CH_4 mixing ratio may effect the photochemical products in Pluto's atmosphere, it does not lead to Pluto's atmosphere becoming UV-transparent.

Grundy et al. (2018) and Bertrand et al. (2020) describe other methods that could explain the observed surface heterogeneity, which we briefly summarize here. One mechanism could be differing thermal processing of the haze particles as they settle through the atmosphere, perhaps due to latitudinal or seasonal changes in the amount or type of hydrocarbons available to stick onto the haze monomers. If the haze particles are not all uniform but instead follow a distribution of characteristics such as size or albedo, then different parts of the distribution could respond differently in various surface environments. Another possible mechanism is cyclical burial and exhuming of haze particles, where the different surface appearances could represent freshly fallen hazes versus exhumed, previously buried haze particles. Over SP, katabatic winds blowing downslope could concentrate haze particles on the ice sheet, counteracting the sublimation winds' tendency to blow haze particles off of it (Bertrand et al., 2020); aeolian processes could be important at the locations of other N_2 deposits as well. Protopapa et al. (2020) suggest that a single coloring agent, very similar to the Titan-like tholin of Khare et al. (1984), can account for all of Pluto's colors (from red to yellow). They suggest that Pluto's coloration is the result of photochemical products mostly produced in the atmosphere, concurring with Grundy et al. (2018). Variations in color are to be attributed to variations in abundance and grain size of the haze particles.

Table 2.3: Summary of the haze disruption results for each of the spatial N_2 distributions we investigate.

		Non-Aggregating	**Local**	**UV-Transparent**
		<0.5 μbar	<0.06 μbar	$<10^{-3}$ to $<10^{-4}$ μbar
Reference Model	Current	-	-	-
	Superseasons	-	-	-
Sputnik Planitia - Only	Current	possible	-	-
	Superseasons	possible	possible	-
South Polar Cap	Current	-	-	-
	Superseasons	possible	-	-
Southern Zonal Band	Current	probable	possible	-
	Superseasons	probable	possible	-

2.5 Conclusions

Table 2.3 summarizes the results for each of the four N_2 distributions we investigate here, for Pluto's current orbit and configurations experienced over the past 10 My. 'Possible' indicates that a particular model predicts pressures for 1 or 2 of the test cases indicative of an atmosphere with the given characteristic (non-aggregating, local or UV transparent) for some portion of the orbit, while 'probable' indicates that 3 or more of the test cases predicted atmospheres with that characteristic. Table 2.3 is based on the five test cases for each N_2 distribution, but since the test cases were chosen to span the allowed parameter ranges, they are indicative of the whole parameter space. For the reference model, which has a bare southern hemisphere, haze production is not predicted to be interrupted at all, and the atmosphere will not collapse, neither in the current orbit nor over the past 10 My. Non-aggregating and local atmospheres are possible using the SP-Only distribution, but this distribution was included for comparison purposes only and is not realistic. Therefore, southern N_2 in some form is required to produce pressures below any of the haze-disruption pressures we considered. We investigated two example southern N_2 distributions: a south polar cap extending from the pole to 60°S with a fractional abundance of 20% and a southern zonal band between 35°S and 55°S, also with a fractional abundance of 20%. Other southern distributions are of course possible, but we chose these two to be representative of some of the possibilities. Atmospheric collapse, when the pressure becomes too low to support a global atmosphere, only occurs in our

southern zonal band model, and only for low thermal inertias (<200 tiu). Across all realistic N_2 distributions and cases considered here, the minimum pressure is predicted to be between 0.01 - 3 μbar in Pluto's current orbit, and the pressure has remained above 0.004 μbar over the past 10 My.

In general, the N_2 ices on the surface collectively re-radiate the insolation absorbed by only the illuminated ices. If more ice coverage is added to the southern hemisphere, currently in polar night, then these unilluminated ices will not absorb solar energy, but they will emit energy. Thus, the presence of obscured southern N_2 ices can lower the minimum pressure experienced over an orbit. However, in order to satisfy the constraints (doubling of the surface pressure since 1988 and an 11.5 μbar pressure in 2015), we found that N_2 distributions including southern N_2 required much lower thermal inertias. From the mobile N_2 sensitivity study, we concluded that the addition of mobile N_2 tends to increase the minimum pressure experienced during Pluto's orbit, because the emissivity of the N_2 ice must be decreased in order to match the observed pressure in 2015. Thus, N_2 mobility decreases the likelihood of haze disruption or atmospheric collapse.

The amount of the southern hemisphere that is obscured in polar night will not decrease until after solstice occurs in 2029, and the entire southern hemisphere won't be visible until equinox occurs 100 years after that. The southern hemisphere could be thermally mapped when it is in polar night, providing a means to determine the spatial distribution of N_2 in the near future rather than a century from now. Our model predicts that there can only be small perennial southern deposits, since we were unable to match observable constraints for southern zonal bands or south polar caps with fractional abundances above 20%, or large, seasonal southern deposits. Another possible scenario is that the southern deposits could have different properties (e.g. a larger deposit with a lower fractional abundance, or different thermal properties) than the northern deposits, which we have not explored here.

Recent analysis of ground-based stellar occultations report a monotonic increase in Pluto's pressure between 1988 and 2016 (Meza et al., 2019). This is consistent with nearly all of our static models, with the exception of test case C from the southern zonal band distribution, which predicts a turnover in pressure in 2008 and test case B from the southern zonal band distribution,

which is approximately flat in pressure in the 2010s. Arimatsu et al. (2020) observed a single-chord occultation in 2019 which showed a large drop in surface pressure, from 11.5 μbar in 2015 to $9.56^{+0.52}_{-0.34}$ μbar in 2019. This pressure decrease is marginally significant at the 2.4-σ level; if real, it represents an earlier and more rapid decrease than all of the models we present here, with the exception of the Southern Zonal Band cases B and C (however, the pressure peak in case B occurs in 2008, inconsistent with Meza et al. (2019) occultation results). All of our models predict a turnover in the pressure by the 2030s, when the surface pressure will begin to decrease as Pluto moves toward aphelion and the subsolar latitude retreats to the southern hemisphere. However, the date of the turnover and the rate of the decline in pressure varies between distribution and chosen parameters in our model. Observations of the atmospheric pressure in the next few decades will thus be crucial for determining which N_2 distributions and which (A,Γ,ϵ) triplets best represent Pluto.

Acknowledgments

This work was supported in part by NASA ROSES SSW grant NNX15AH35G and by NASA's New Horizons mission to the Pluto system. The authors would like to thank Tanguy Bertrand for illuminating discussions and feedback, as well as James Keane, Amanda Sickafoose, and Anja Genade for reviewing early versions of the appendix. We would also like to thank two anonymous reviewers, for greatly improving this paper with their feedback.

Chapter 3

New Constraints on Pluto's Sputnik Planitia Ice Sheet from a Coupled Reorientation-Climate Model

This chapter was originally published in the Planetary Science Journal (Johnson et al., 2021a).

Abstract: We present a coupled reorientation and climate model, to understand how true polar wander (TPW) and atmospheric condensation worked together to create the Sputnik Planitia (SP) ice sheet and reorient it to its present-day location on Pluto. SP is located at 18°N, 178°E, very close to the anti-Charon point, and it has been previously shown that this location can be explained by TPW reorientation of an impact basin as it fills with N_2 ice. We readdress that hypothesis while including a more accurate treatment of Pluto's climate and orbital obliquity cycle. Our model again finds that TPW is a viable mechanism for the formation and present-day location of SP. We find that the initial impact basin could have been located north of the present-day location, at latitudes between 35°N and 50°N. The empty basin is constrained to be 2.5 – 3 km deep, with enough N_2 available to form at most a 1 – 2 km thick ice sheet. Larger N_2 inventories reorient too close to the anti-Charon point. After reaching the final location, the ice sheet undergoes short periods of sublimation and re-condensation on the order of ten meters of ice, due Pluto's variable obliquity cycle, which drives short periods of reorientation of a few km. The obliquity cycle also has a role in the onset of infilling; some initial basin locations are only able to begin accumulating N_2 ice at certain points during the obliquity cycle. We also explore the sensitivity of the coupled model to albedo, initial obliquity, and Pluto's orbit.

3.1 Introduction

Sputnik Planitia (SP), the western half of Pluto's "heart," is a 1000 km-wide, several km-thick ice sheet made of nitrogen, methane, and carbon monoxide ices, located very close to the anti-Charon point on Pluto's surface (Stern et al., 2015). The volatile ice sheet partially fills a topographic depression in Pluto's water-ice crust. The ice sheet encompasses 870,000 km^2 ($\sim$ 4% of Pluto's surface area) and lie 2 km below the average surface elevation (Schenk et al., 2018). Due to the topographic low and elliptical shape, the ice sheet is thought to lie within an ancient impact basin (Stern et al., 2015; Moore et al., 2016; Johnson et al., 2016). Based on spectral modeling of the surface, the ice sheet is thought to be $\sim$ 50% N_2 ice (Protopapa et al., 2017), but the relative amounts of the various other ices (CH_4, CO) at depth is not well known. The presence of water ice blocks that appear to be floating on the edge of the ice sheet suggests that N_2 is the dominant species at depth, since methane's low density ($\sim$ half that of water ice) would not allow water ice blocks to float (McKinnon et al., 2016).

While SP contains a large amount of Pluto's N_2, there are also smaller ice deposits elsewhere on the surface, and the atmosphere contains some N_2 as well. Glein and Waite (2018) estimate that in Pluto's present-day atmosphere, the surface N_2 ice deposits contain five orders of magnitude more N_2 than the atmosphere. The amount of surface N_2 ice outside of SP is hard to estimate, because the depths of the observed deposits are unknown. Modelling by Bertrand et al. (2019) found that perennial deposits of N_2 could be around 1 - 10 m thick. Additionally, the non-SP deposits must be thick enough to be observed spectroscopically. SP covers 870,000 km^2, and New Horizons observed another 6,200,000 km^2 to be N_2-covered. Since SP is estimated to be a few km thick, if the average thickness of the non-SP deposits is less than 0.5 km, then SP would be the dominant source of N_2, volumetrically.

The surface of the ice sheet is characterized by a polygonal pattern, thought to be evidence of active solid-state convection (Moore et al., 2016). The cells are a few tens of km in diameter, and the centers of the cells rise as much as 50 m above their edges. Convection modeling has shown that

nitrogen ice sheets thicker than 1 km should undergo convection on Pluto, and that ice thicknesses of 3-6 km are necessary to explain the cell diameters, although the uncertain rheology of nitrogen ice introduces large uncertainties (McKinnon et al., 2016). The convection models of Trowbridge et al. (2016) calculate a slightly larger thickness of 10 km. McKinnon et al. (2016) estimate that the basin itself should not be deeper than ∼10 km.

Based on the lack of observed craters, an upper limit of 30 - 50 My is estimated for the crater-retention age of SP's surface (Singer et al., 2021). However, the convective overturning motions of the ice sheet could refresh the surface in only 500,000 years (McKinnon et al., 2016; Buhler and Ingersoll, 2018), so the ice sheet's surface is very young. Conversely, the age of the basin itself is very old, likely older than 4 Gy (Singer et al., 2021), indicating that the infilling of the impact basin with N_2 ice could have occurred very early in Pluto's history. We show in this work that modeled basins collect all available N_2 very quickly, within 10 My typically, so infill likely occurred very soon after the impact, provided that there was sufficient available mobile N_2 on the surface.

SP is centered around 18°N, 178°E, which places it very close to the anti-Charon point. Nimmo et al. (2016) calculate that there is only a 5% chance of the basin forming that close to the anti-Charon point, and instead suggest that the basin likely migrated there as a result of true polar wander (TPW), a hypothesis shared by Keane et al. (2016) as well. For this hypothesis to be true, the impact basin and ice sheet combination needs to be a positive gravity anomaly, since positive gravity anomalies reorient towards the equator to maintain a minimum energy state of principal axis rotation (Matsuyama et al., 2014). Negative gravity anomalies, which one might expect an empty impact basin to be, reorient to one of the rotation poles for the same reason. However, large impact basins throughout the solar system are not predominantly negative gravity anomalies, but instead can be positive or negative anomalies based on various factors (Keane et al., 2016).

Keane et al. (2016) find that a N_2 ice sheet alone is not able to explain SP's present-day location; an unreasonable amount of ice (enough to form a 100+ km-thick ice sheet) would be required to increase the empty basin's gravity anomaly enough to reorient it to the present-day location. Nimmo et al. (2016) reach a similar conclusion, that the present-day location cannot be

explained by TPW from N_2 infilling alone. Instead, the authors suggest that an ejecta blanket from the impact or subsequent uplift from a subsurface liquid ocean, or a combination of both, contribute to the positive gravity anomaly of the basin, in addition to the ice sheet.

Keane et al. (2016) compared the observed faults on Pluto to modeled faults resulting from reorientation stresses, and found that their large reorientation solutions (in which the impact basin starts northwest of SP's present-day location) produced faults most consistent with the observed pattern. The small true polar wander solutions (in which the impact basin starts north of SP's present-day location) were also consistent, but less so. This consistency strengthens the argument that TPW is responsible for the present-day location of SP.

Hamilton et al. (2016) suggest an alternative to the impact basin formation theory for SP. They suggest that N_2 ice will naturally accumulate at latitudes near 30°, because, when averaged over Pluto's orbit, that region is the coldest part of the surface. The runaway albedo affect can concentrate the ice into a single cap at 30°N within 1 My after the Charon-forming impact, and the subsequent orbital evolution locks the mass anomaly of this cap onto the anti-Charon side, as is observed. Finally, the weight of the many km-thick accumulation of ice causes the underlying crust to slump, creating the observed topographic depression. This hypothesis requires that latitudes near SP's present-day latitude are the coldest region on the surface, which is true for some, but not all orbital obliquities in Pluto's present-day obliquity cycle, as shown in Figure 3.1. Hamilton et al. (2016) did not consider the expected global tectonic pattern in this scenario. The quasi-radial fractures proximal to SP can be explained by N_2 loading (Keane et al., 2016; McGovern et al., 2021). However, the quasi-azimuthal faults distal to SP require TPW stresses (Keane et al., 2016).

Pluto's obliquity (the angle between the spin axis and the heliocentric orbital axis) varies over time due to perturbations from the rest of the solar system bodies (Dobrovolskis and Harris, 1983). Dobrovolskis et al. (1997) calculated that the obliquity would vary between 103° and 128° over a 2.7 My period. Pluto's spin is retrograde, so the obliquity value is reported as >90°, and higher values indicate smaller absolute angles between the spin and orbit axes (less "tilting"). Pluto's obliquity is currently 120° and increasing with time. The obliquity of the orbit affects the

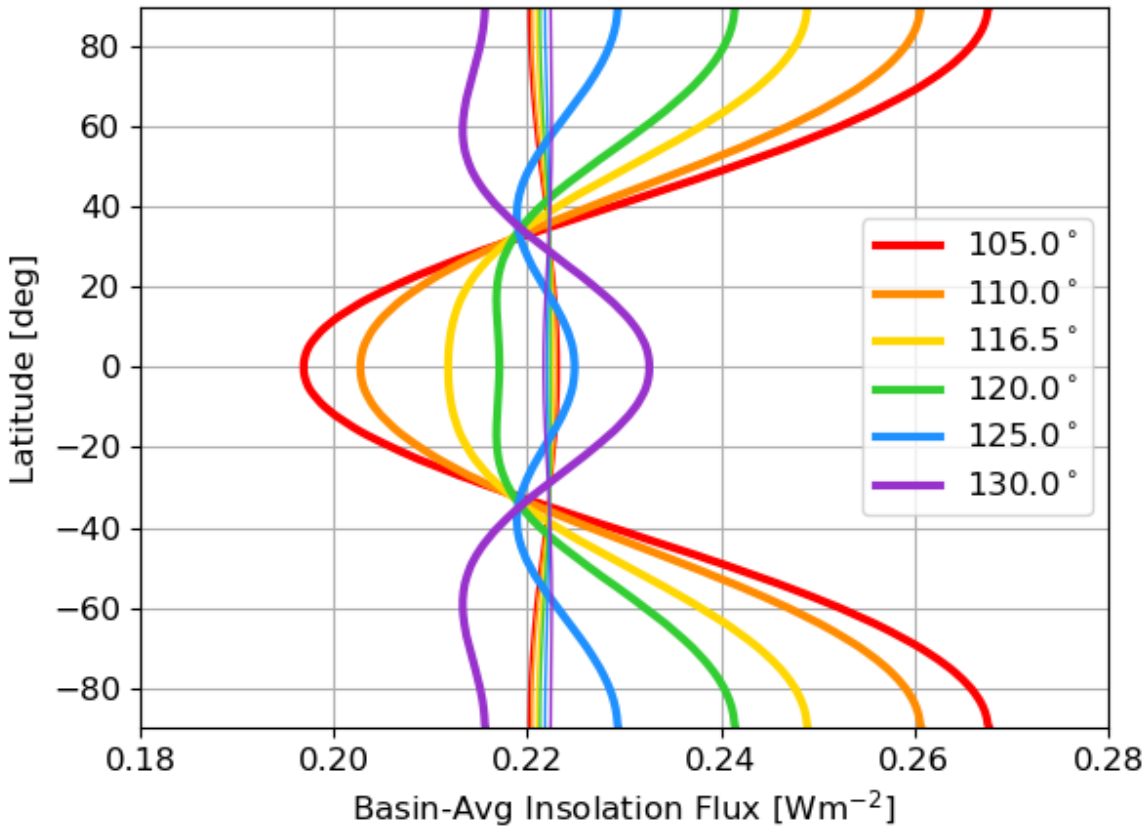

Figure 3.1: Orbit-averaged insolation onto a 24°-radius circular basin centered at each latitude for 6 example obliquities, chosen to span Pluto's obliquity cycle. Pluto's current obliquity is 120° (green curve) and increasing towards the maximum obliquity of 128°. The thin lines with little variation represent the spatially-averaged insolation onto the rest of the surface, excluding the basin, for each obliquity. If the effect of depth is ignored, a basin will fill with N_2 ice when the basin-averaged insolation is less than the surface-averaged insolation.

latitudinal distribution of incident insolation, as shown in Figure 3.1. To speedily calculate the orbital-averaged insolation, we implement the sixth order Legendre approximation from Nadeau and McGehee (2017). Figure 3.1 shows the orbit-averaged incident insolation onto the surface, averaged over the area inside the modeled 24°-radius basin. For the local (not basin-averaged) insolation, see Fig. 1 in Hamilton et al. (2016), for example. Averaging over the area of the basin has the effect of flattening the insolation curves, and we perform this averaging because the model used here calculates the average infill rate into the basin, which depends on the average insolation. Higher obliquity values (indicating less tilted orbits) have a more uniform distribution (e.g. the purple curve), while lower values exhibit extreme contrasts between the annual average insolation at the poles vs. at the equator (e.g. the red curve). Thus, the obliquity cycle has significant consequences for an impact basin's ability to fill in with N_2 ice from atmospheric condensation. At a time of low obliquity, a high-latitude basin might receive more insolation than the rest of the surface, so condensation does not occur, but sometime later in the obliquity cycle the basin will receive equal or less insolation than the rest of the surface. Lower insolation, or equal insolation coupled with the depth of the basin, leads to condensation of N_2 ice onto the basin floor.

The model presented here couples TPW with climate for the first time, to understand if, and how, these processes interact to place SP at its present-day location. This work seeks to determine for which initial conditions (basin depth, N_2 inventory, and basin location) is the present-day location of SP consistent with infill of an impact basin via atmospheric condensation (accounting for a cyclic obliquity) and subsequent reorientation via TPW. The methodology is explained in Section 3.2, and the infill and reorientation results for a wide variety of initial locations and basin depths are shown in Section 3.3. Sections 3.3.2 – 3.3.5 contain more details about the effect of initial obliquity, crustal deformation, albedo, and orbital semi-major axis on the results. The conclusions are summarized in Section 3.4.

3.2 Model

3.2.1 Volatile Infill Model

The model is initialized in a "snowball" Pluto state, in which the available N_2 ice is spread uniformly over the entire surface. The model tracks the average thickness of N_2 ice in two regions: inside of a 24°-radius circular basin (subscript "basin") and outside of this basin on the rest of Pluto's surface (subscript "surface"). It is assumed that any ice that sublimes from one region immediately condenses uniformly over the other region. This assumption of instantaneous mixing of nitrogen in the atmosphere was also used by Bertrand and Forget (2016). We do not account for a variable atmospheric mass, although we do assume that there is always sufficient N_2 mass in the atmosphere to maintain a global atmosphere in which temperature is independent of latitude and longitude (but temperature does depend on altitude). Modeling by Johnson et al. (2021b) showed that Pluto's atmosphere remains global over the past 3 My for most realistic scenarios. The two regions have equivalent Bond albedos of 0.75, and the albedo is constant in time throughout the model run, so we do not account for an albedo that varies based on the abundance of N_2 on the surface, for example. We explore the effect of different albedos in Section 3.3.4.

The infilling rate $\dot{m}$ (in kg s^{-1} m^{-2}) is calculated by assuming energy balance and global mass conservation between the two regions. In each region, the difference between absorbed insolation and thermal emission gives the latent heat energy of the condensed material:

$$\Omega_{surface}\epsilon\sigma T_{surface}^4 - \Omega_{surface}(1-A)S_{surface} = \Omega_{surface}L\dot{m}_{surface} \tag{3.1}$$

$$\Omega_{basin}\epsilon\sigma T_{basin}^4 - \Omega_{basin}(1-A)S_{basin} = \Omega_{basin}L\dot{m}_{basin} \tag{3.2}$$

Ω is the angular area of the region, ϵ is the emissivity, σ is the Stefan-Boltzmann constant, T is the N_2 ice temperature, S is the absorbed insolation (averaged over the region and averaged over one Pluto orbit), and L=2.5 x 10^5 J kg^{-1} is the latent heat of N_2. We have not cancelled the Ω factors in Equations 1 and 2 to make it clear that $\dot{m}$ is a per-area quantity.

Global mass balance is also enforced, requiring that any N_2 sublimed from one region condenses onto the other region:

$$\Omega_{surface}\dot{m}_{surface} = -\Omega_{basin}\dot{m}_{basin} \tag{3.3}$$

In reality, some of the sublimed N_2 stays in the atmosphere, rather than immediately condensing onto the other region. However, the atmospheric mass is several orders of magnitude smaller than the mass of N_2 on the surface, so these seasonal variations in atmospheric mass are negligible to the total N_2 inventory (Glein and Waite, 2018). For example, the atmospheric pressure above a N_2-covered surface at 34.3 K (the surface temperature for most of our modeled scenarios) is about 1.8 μbar, which implies an atmospheric mass of 5 x 10^{12} kg. 40 - 80 m GEL, the range of N_2 inventories we consider here, is equivalent to 0.7 - 1.4 x 10^{18} kg of N_2 ice.

To arrive at an equation for the infilling rate, we need to relate the two N_2 ice temperatures. The pressure at the top of the ice sheet is larger than at the non-basin surface because of hydrostatic equilibrium, and the equilibrium temperature is consequently higher at the top of the ice sheet via the Clausius-Clapeyron relation. We have defined the ratio of the temperature at the top of the ice sheet $T_{basin}/T_{surface}$ by a factor a. If we assume that the atmospheric temperature is in equilibrium with the pressure at every at altitude (that is, the gradient follows the wet adiabat of the primary gas), then

$$a = e^{gd/L} \tag{3.4}$$

where d is the depth to the top of the ice sheet and $g = 0.62$ ms^{-2} is Pluto's gravitational acceleration. For T_{basin}=37 K and d=3 km, a=1.0075. Since the depths are small compared to a scale height, a depends only slightly on the thermal structure of the atmosphere above the top of the ice sheet. For example, if the atmosphere were isothermal above the ice sheet, then $a = 1 + gd/L$, which alters T_{basin} by of order 1 mK.

Combining equations 1 through 4 leads to the following equation for the rate of infill into the basin:

$$\dot{m}_{basin} = (1 - A)\frac{\Omega_{surface}}{\Omega_{surface} + a^4\Omega_{basin}} \left(a^4 S_{surface} - S_{basin}\right) \frac{1}{L} \tag{3.5}$$

At each timestep, the model calculates the average insolation onto each region and uses the current ice sheet depth to calculate the rate of condensation onto (or sublimation from) the top of the ice sheet. This added ice mass is used to update the gravity anomaly of the basin and calculate the corresponding reorientation of Pluto.

l

3.2.2 True Polar Wander (TPW) Model

The TPW part of the model closely follows the method used in Keane et al. (2016), which we summarize here. We created a simple dynamical model of Pluto, where the total inertia tensor of Pluto, $\mathbf{I}_{Pluto}$, is written as the sum of two components: the remnant figure, $\mathbf{I}_{RF}$, and the contribution from SP, $\mathbf{I}_{SP}$:

$$\mathbf{I}_{Pluto} = \mathbf{I}_{RF} + \mathbf{I}_{SP} \tag{3.6}$$

where bold symbols indicate tensors. Only the non-spherically symmetric contribution to the inertia tensors plays a role in determining the amount of TPW because the spherically symmetric contribution does not modify the principal axes of inertia. We take into account deformation of Pluto in response to both the changing tidal/rotational potential and response due to volatile loading of SP using Love number theory (e.g. Sabadini et al., 2016). Given the long ∼Myr timescales involved, we use the long-term Love numbers describing long-term deformations.

The remnant figure, $\mathbf{I}_{RF}$, represents Pluto's non-hydrostatic, elastically supported tidal-rotational bulge. This bulge is preserved no matter how Pluto reorients. At present, no bulge has been observed at Pluto, although Nimmo et al. (2017) report an upper limit of 0.6% for Pluto's oblateness. Thus, we construct a theoretical remnant figure using Love numbers (e.g. Matsuyama et al., 2014). We assume the nominal four-layer interior structure of Pluto from Keane et al. (2016) consisting of a silicate-rich core, liquid water ocean, and a two-layer water ice shell with a weak

lower crust and upper, 50 km thick elastic lithosphere with a rigidity of 3.5 GPa. The remnant figure arises due to deformation in response to rotation and the present-day tides of Charon, and is supported entirely in the elastic lithosphere. The remnant figure could relax over time, but the timescale for this relaxation is unknown. If we consider a thinner elastic lithosphere, there will be more compensation to the ice load, which leads to smaller TPW reorientations. However, a thinner lithosphere also leads to a smaller remnant figure, which has a stabilizing effect and makes TPW reorientations larger. Therefore, the relaxation of the remnant figure may not have a significant effect on the results presented here. A detailed study of the effect that the magnitude of the remnant figure has on SP's initial location and the ice thickness is beyond the scope of this work, so we only use our nominal value of 50 km for the elastic thickness.

The inertia tensor from SP, $\mathbf{I}_{SP}$, represents the total inertia tensor perturbation arising from SP, which we subdivide further into the inertia tensor arising from the underlying impact basin and the ice sheet:

$$\mathbf{I}_{SP} = \mathbf{I}_{basin} + \mathbf{I}_{ice\ sheet} \tag{3.7}$$

The inertia tensor from the underlying basin is unknown. In the absence of data, we agnostically assume that the basin was initially fully compensated ($\mathbf{I}_{basin} = 0$), which is a reasonable assumption if SP has an underlying ocean uplift or surrounding ejecta blanket (Keane et al., 2016; Nimmo et al., 2016). With this assumption, the only contribution to $\mathbf{I}_{SP}$ is from the ice sheet, which we describe as a spherical cap of uniform thickness. For the case of SP located on the north pole of Pluto, the uncompensated ice sheet contribution can be written:

$$\mathbf{I}'_{ice\ sheet} = \frac{\pi\sigma r^4(4-3\cos\gamma)}{3}\begin{bmatrix}1&0&0\\0&1&0\\0&0&1\end{bmatrix} + \frac{\pi\sigma r^4\cos\gamma}{3}\begin{bmatrix}-\cos^2\gamma&0&0\\0&-\cos^2\gamma&0\\0&0&2\cos^2\gamma-3\end{bmatrix} \tag{3.8}$$

where σ is the surface density (mass per unit area, i.e., kg m^{-2}) of the ice sheet, γ is the angular radius of the ice sheet, and r is the radius of Pluto (1187 km). $\mathbf{I}'_{ice\ sheet} = 0$ when $\gamma = 0$, as expected.

The first term in Eq. (3.8) does not play a role in inducing TPW because it is spherically symmetric, and therefore it is ignored hereafter. Taking compensation into account, the non-symmetric ice sheet contribution can be written:

$$\mathbf{I}_{ice\ sheet} = (1 + k_2^L)\frac{\pi\sigma r^4 \cos\gamma}{3}\begin{bmatrix} -\cos^2\gamma & 0 & 0 \\ 0 & -\cos^2\gamma & 0 \\ 0 & 0 & 2\cos^2\gamma - 3 \end{bmatrix} \tag{3.9}$$

where k_2^L is a degree two load Love number describing the long-term deformation in response to ice loading. Without an elastic lithosphere, the ice sheet would be fully compensated ($k_2^L = -1$) and would not contribute to the inertia tensor. Conversely, in the limit case of an infinite rigidity elastic lithosphere, Pluto would not deform in response to ice loading ($k_2^L = 0$). For the assumed nominal four-layer interior structure containing a 50 km thick elastic lithosphere with a rigidity of 3.5 GPa, $k_2^L = -0.55$. While Eq. (3.9) describes the case for the ice sheet located on the north pole, it can be rotated to anywhere on the globe using standard rotation matrices.

3.2.3 The Combined Model

The reorientation is calculated iteratively. We start first with Pluto's remnant figure, and consider an arbitrary initial location, and in each subsequent timestep, we calculate how much mass is added to (or lost from) the ice sheet. After each step, we diagonalize the resulting inertia tensor, and define the new rotation axis and tidal axis as the maximum and minimum principal axes of inertia, respectively. This is equivalent to keeping Pluto in a minimum energy (principal axis) rotation state—which implicitly assumes that Pluto can rapidly adjust to applied forces. The angles between the new and old principal axes of inertia give the reorientation of the surface and determine the new latitude and longitude of the basin and ice sheet.

As the ice sheet grows in mass, the underlying basin and surrounding area deforms, with the basin floor sinking in elevation and the area immediately surrounding the basin rising slightly. We assume a spherical cap with an angular radius of 24° for the ice sheet and compute the corresponding

radial deformation using displacement Love numbers. The deformation is larger near the basin center with an amplitude and profile similar to the one found by McGovern et al. (2021) using a finite element method. In order to find the average deformation, we convert the modelled bowl-shaped deformation profile to a flat-bottomed, cylindrical profile. We do this by finding the volume of ice contained within the 24°-radius deformed ice sheet and equating it to the volume of a flat-bottomed, cylindrical idealized ice sheet of some thickness. The bottom elevation of the ice sheet implied by this thickness gives the average deformation. For every 1 km of N_2 ice in the basin, the basin floor sinks by roughly 0.5 km, comparable to the average deformation in McGovern et al. (2021) (sinking an average of 1.27 km for every 2.27 km of N_2 ice, a deformation-to-load ratio of 0.56 to our ratio of 0.5). This affects the model in two ways: it reduces the contribution of the ice sheet load to the overall inertia tensor, and it increases the infill rate by lowering the elevation of the condensation surface at the top of the ice sheet. Section 3.3.3 explores the effect of ignoring basin floor deformation.

As Pluto reorients, the basin and nascent ice sheet are moved to different latitudes and therefore receive different amounts of average insolation. The model accounts for Pluto's varying obliquity, which also varies the insolation onto the basin as a function of time. Pluto's obliquity currently varies on a 2.7 My cycle, between 105° and 129° (Earle et al., 2017). It is not clear what Pluto's obliquity would have been at the time of the impact that formed the basin and/or at the time of the infilling, but the model assumes the current-day obliquity cycle.

For this work, we investigated initial basin latitudes between 5° and 85° latitude and 95° and 175° longitude, in increments of 5° (the initial location of SP is limited to this single octant of the surface). The model timestep was 300 Pluto orbits, about 75,000 years. The reorientation and the glacial flow needed to level the surface of the ice sheet were both assumed to happen within a single timestep. The models ran for 268 timesteps, giving a total run time of 20 My, at which point the modelled ice sheet had reached a semi-stable final location and thickness. The basin was circular in cross section, flat-bottomed, and covered 4% of Pluto's surface, the equivalent of present-day SP's extent. We used Pluto's current orbital parameters in the model, although alternative orbits, such

as a smaller semi-axis orbit, are discussed in Section 3.3.5.

The top of SP is 2 km below the surface's average elevation (Schenk et al., 2018). Thus, we only considered initial basin depth and N_2 inventory combinations that result in this configuration. In the following section, we present the results from initial basin depths of 2.5 and 3 km, paired with final ice thicknesses of 1 and 2 km, respectively. These correspond to N_2 inventories of 0.7 x 10^{18} kg and 1.4 x 10^{18} kg, and global equivalent layers (GEL) of 40 - 80 m. Deeper initial basins require larger N_2 inventories, which cause too much reorientation and place the basin too close to the sub-Charon point.

3.3 Results

Runs are considered successful if the basin's final semi-stable location lies within $\pm 5^\circ$ of the present-day center of SP. SP's center can be defined in several ways: the centroid of the ice sheet as defined from geologic maps (White et al., 2017), the centroid of the larger topographic low that the ice sheet lies within, or the averaged latitude and longitude of the ice sheet region weighted by the surface area. We adopt an average of these three values as the center of SP: 17.7°N, 178.2°E. The model runs for 20 My, which is long enough for all cases to reach a final semi-stable state. The model ends at Pluto's present-day obliquity value of 120°. We only explore initial locations within one octant of Pluto's surface (the northeastern part of the western hemisphere: 0°N - 90°N, 90°E - 180°E), because TPW will not cause basins to cross the equator or the 90°E and 180°E longitudes. Since the present-day location of SP is within this octant, the initial location must be as well.

Figure 3.2 shows the paths that basins take in an instantaneous reference frame defined by the current timestep's principal axes, in which the latitude and longitude of surface features change over time. As an example, Figure 3.2 shows the paths resulting from a 3 km deep basin with an available N_2 inventory of 80 m GEL.

Basins that begin near the pole, at latitudes $\gtrsim 50^\circ$, never infill completely. An example of the corresponding reorientation is shown by the red line labeled as 1 in Figure 3.2. For most obliquity values, the poles receive higher insolation than lower latitudes, so ice sheets near the pole receive

more sunlight than the N_2 deposits elsewhere on the surface and tend to sublime away. However, at certain points during the obliquity cycle, the obliquity is high enough, that when combined with the depth of the basin, the infill rate becomes positive and some condensation occurs. As a result, the basin reorients slightly, moving down in latitude. However, when the obliquity increases again, all of the condensed ice sublimes away and the basin reorients back to its initial location.

Basins that start near the equator, at latitudes $\lesssim 35°$, collect all of the available N_2 inventory, but subsequently reorient too close to the sub-Charon point instead of stopping at a semi-stable final location close to the present-day center of SP. An example reorientation path is shown by the orange line labeled as 2 in Figure 3.2. Similarly, basins that begin at intermediate latitudes and longitudes, approximately 130°E to 150°E and 45°N to 50°N (see Region 3 in Figure 3.5), infill completely and collect all available N_2, but the resulting reorientation leaves the final basin too far west of the anti-Charon longitude. An example reorientation path is shown by the yellow line labeled 3 in Figure 3.2.

There are three regions of Pluto's surface that lead to successful reorientations. First, basins that begin at intermediate latitudes ($\sim$35° N - 50° N) directly north of the present-day location infill with all available N_2 and reorient to final locations within $\pm 5°$ of the present-day location of SP. The green line labeled 4 in Figure 3.2 shows an example path, analogous to the "small-TPW" solutions described in Keane et al. (2016). Additionally, basins that begin at low initial longitudes and intermediate latitudes also reorient to final locations within $\pm 5°$ of the present-day center of SP. An example reorientation path is shown by the blue line labeled 5 in Figure 3.2, analogous to the "large-TPW" solutions described in Keane et al. (2016). Basins that begin at intermediate longitudes in a narrow range of intermediate latitudes (see Region 6 in Figure 3.5) reorient to final locations within $\pm 5°$ of the present-day center of SP. An example reorientation path is shown by the purple line labeled 6 in Figure 3.2.

Figure 3.3 shows the temporal behavior of Pluto's obliquity, the basin's location, and the ice thickness for each path drawn in Figure 3.2. The behavior can be classified into three phases: (S) Stationary, (I) Infilling, and (C) Cyclic, which are labelled in the fourth panel of Figure 3.3. A

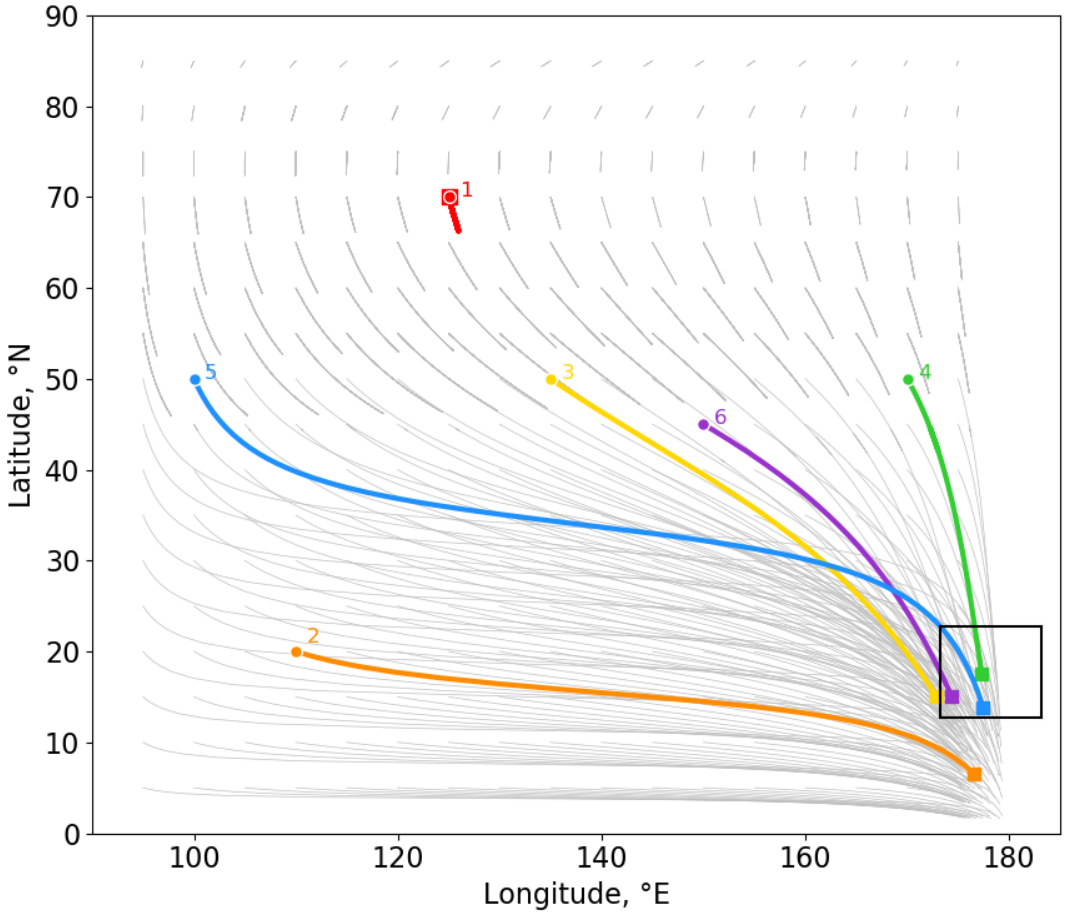

Figure 3.2: Reorientation paths for 3-km deep basins at all initial locations with 80 m GEL of available N_2 (faded lines). The solid black box marks the region within ±5° of the present-day center of SP. A few example paths are highlighted: (1, red) an initially high-latitude basin's path; (2, orange) an initially low-latitude basin's path; (3, yellow) the path of an initially intermediate-latitude basin that ends too far west; (4, green) the path of an initially intermediate-latitude and high-longitude basin that ends within ±5° of the present-day center of SP; (5, blue) the path of an initially intermediate-latitude and low-longitude basin that ends within ±5° of the present-day center of SP; (6, purple) the path of an initially intermediate-latitude and intermediate-longitude basin that ends within ±5° of the present-day center of SP. Small circles denote the initial location of the basin and small squares denote the final location. Note that for path 1, the initial and final locations are the same. The color scheme in subsequent figures (excluding Figure 3.4) corresponds to the labeled paths in this figure.

given basin may experience all three phases, or it may only experience one or two of the phases. The phases can be experienced in any order and can be experienced more than once. For example, Path 1 moves straight from the stationary phase to the cyclic phase, while Path 4 starts out in the infilling phase, briefly enters the stationary phase, and then returns to infilling before finally entering the cyclic phase.

In the case of the blue path labeled 5 (initially intermediate latitude and low longitude basin), the basin first moves primarily south, then east, and then south again. The basin is stable at the initial location for ~ 2 My (Stationary Phase), and then gradually gains ice mass and reorients over a period of about 6.5 My (Infilling Phase) once the obliquity reaches a high value and the insolation onto the basin is less than that onto the rest of the surface. When the obliquity is at high values (note that Pluto's obliquity is $>90°$ due to its retrograde rotation, so a high obliquity value indicates a smaller angle between the spin pole and the orbit plane), the difference in insolation between the equator and poles is at a minimum. The basin remains semi-stable at the new location and ice thickness, only experiencing small deviations on the order of one tenth of a degree in latitude and longitude and tens of meters in ice thickness as the obliquity cycles (Cyclic Phase). These small excursions in location and ice thickness occur for basins at all initial locations, but vary in magnitude, with the initially high-latitude basins exhibiting the largest oscillations on the order of 5° latitude and 180 m in ice thickness. This is discussed more in Section 3.3.1.

The preceding discussion used an initially 3-km deep basin with 80 m GEL available N_2 inventory (enough to create a 2 km thick ice sheet in the basin and a final basin depth of 4 km), but we explored other initial basin depths and N_2 inventory combinations as well. Combinations that create a final ice sheet at an elevation of -2 km are as follows: 2.5 km initial depth with a 1 km ice sheet, 3 km initial depth with a 2 km ice sheet, 3.5 km initial depth with a 3 km ice sheet, and so on. We found that ice sheets thicker than 2 km reoriented too close to the anti-Charon point for all initial basin locations that experienced an Infilling Phase. This result is subject to our assumption of the lithosphere's elastic thickness of 50 km. The effective size of a mass load inducing TPW is given by the ratio between the degree-2 gravity coefficients of the compensated

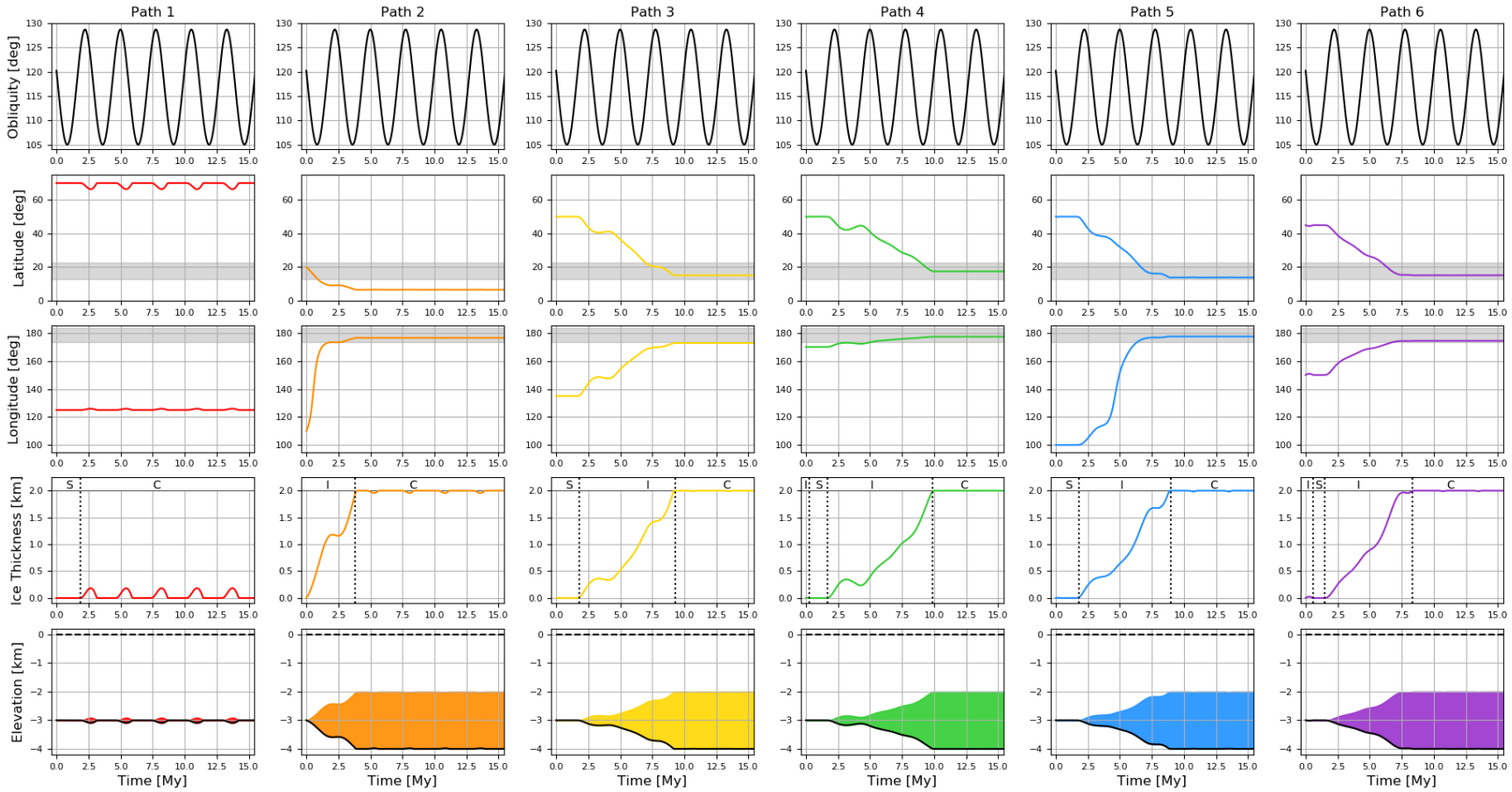

Figure 3.3: Temporal behavior for Pluto's obliquity, the basin's latitude and longitude, ice thickness, and the cross-section of the basin for each path. For the latitude and longitude rows, the shaded region is ±5° from the latitude or longitude of SP's present-day location. Obliquity is shown in black because it is the same for all paths; it is repeated in each column for ease of comparison. In the ice thickness plots (second to bottom row), three phases of behavior are labeled: (S) Stationary, (I) Infilling, and (C) Cyclic. The bottom row shows a cross section of the basin in time, with the basin floor shown as a solid black line, the surface shown as a dotted black line at 0 km elevation, and the ice sheet shown as solid color fill. The color scheme is the same as that used in Figure 3.2.

load and the remnant figure (Matsuyama et al., 2014, Eq. (20)). For a thicker elastic lithosphere, the compensated load increases, increasing TPW, and the remnant figure increases, decreasing TPW. These two effects balance each other, resulting in a weak dependence on the assumed elastic lithosphere thickness (e.g. Keane et al., 2016, Extended Data Figure 5k).

Figure 3.4 shows those initial basin locations for each initial basin depth that reoriented so that the final basin location was within $\pm 5^\circ$ of the present-day location of SP, for the 2.5 and 3 km initial depth basins. The initial longitude of the basin is denoted with color in Figure 3.4, with the color transitioning from red to white to blue as longitude increases. For the 3 km initial depth (right panel), basins that start far to the west of SP's present-day location (red circles) undergo large reorientations and tend to end up south of SP's present-day location (cluster in the bottom of the success box). Basins that start at intermediate longitudes (pale red to pale blue colors) end up west or southwest of SP's present day location, and basins that start directly north (blue circles) tend to have final locations that are the closest of the present-day location of SP, but there is significant spread in the final location. The initially 2.5 km deep basins have even more significant spread in their final locations.

Figure 3.5 summarizes the final location of the basin as a function of initial latitude and longitude. The color scheme is the same as Figure 3.2. The latitude and longitude boundaries of the regions are approximate, in order to be representative of various initial basin depths.

3.3.1 Obliquity Cycle Excursions

After some time in either the Stationary or Infilling Phases (or both), usually within 10 My, basins from all initial locations reach a semi-stable final location and ice thickness. However, they still experience short, small excursions from this location and thickness at certain parts of the obliquity cycle. Keane et al. (2016) considered "seasonal wobbles" owing to the transport of volatiles on annual timescales; the obliquity cycle excursions discussed here are the analogous "superseasonal wobbles." If the depth to the top of the ice sheet is zero (e.g. ice thickness equals basin depth), then the infill rate is proportional to the difference between the average insolation onto

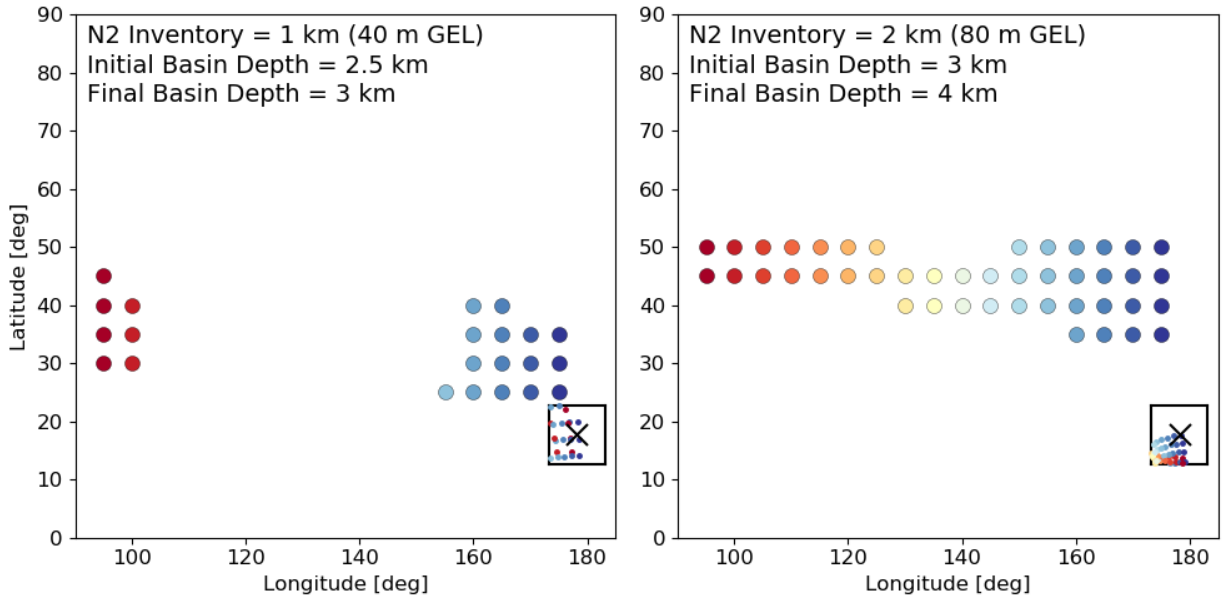

Figure 3.4: Initial locations for the impact basin that reorient to place the basin within 5 degrees of SP's current location are shown as small circles. The left panel shows the case for an initially 2.5 km deep basin and the right panel shows the case of an initially 3 km deep basin. The black cross and surrounding box show the present-day center of SP and the region $\pm 5^\circ$ from the center. The final locations are also shown as small circles, and they tend to cluster in the southwest corner of the boxed success region. The initial longitude of the basins are shown via color: the western basins are red, intermediate-longitude basins are white, and eastern basins are blue.

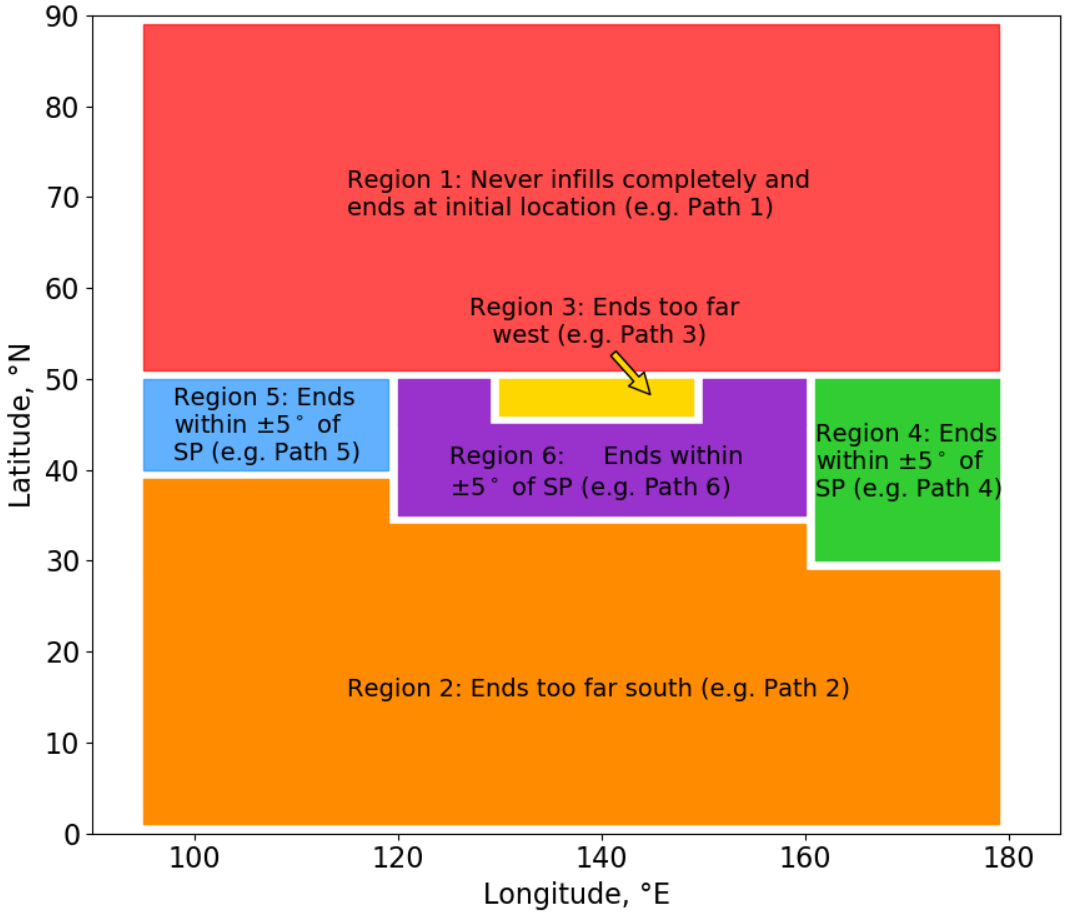

Figure 3.5: Graphical summary of the final location of the basin as a function of initial latitude and longitude, using the same color scheme as Figure 3.2. Initial basins that begin within each colored region will have final locations as described by the text within the region.

the basin/ice sheet and the average insolation onto the rest of the surface; if the basin receives more insolation, N_2 ice will sublime away from the ice sheet while if the basin receives less insolation, N_2 will condense onto the ice sheet. Ice sheets set inside deep basins can receive slightly more insolation than the average of the rest of the surface (up to $e^{4gd/L}S_{surface}$) and still experience condensation. The relative insolation depends on the latitude of the basin and also on the current obliquity (since that controls the latitudinal distribution of insolation, see Figure 3.1). Even when a basin has reached a semi-stable location and ice thickness, the obliquity cycle causes variations in the relative insolation onto the basin and thus small excursions in latitude, longitude, and ice thickness occur.

Figure 3.6 explains the time series behavior leading to latitude and ice thickness excursions for two examples basin paths: the paths labelled 1 (red, left panel) and 5 (blue, right panel) from Figure 3.2. The left panel shows an initially high-latitude basin, which never infills completely and instead oscillates back and forth between a lower latitude and its initial location. At its initial high latitude, the basin is receiving more insolation than the average of the rest of the surface, so the infill rate is negative. However, there is not yet any N_2 ice to sublime away, since the basin starts out empty, so the basin remains as is and no reorientation occurs. Eventually, when the obliquity is high, the basin insolation is lower than the rest of the surface, so the infill rate becomes positive and condensation occurs. This infill period is indicated by the gray shading. As the basin fills, the increase in mass causes an equatorward reorientation. Eventually, the combination of a lower latitude, thicker ice sheet, and lower obliquity cause the infill rate to drop below zero once again. This time, there is N_2 ice to sublime away ($\sim$180 m in this case), so the ice thickness decreases and the resulting reorientation returns the basin to its original location. This process repeats when the obliquity cycles back to high values.

Basins that infill with all available N_2, such as the blue path labeled 5 in Figure 3.2, also experience cyclic excursions from their final semi-stable location and ice thickness, as seen in the right panel and insets of Figure 3.6. In this case, the initially mid-latitude basin begins the Infilling Phase after 2 My, when the obliquity is high enough, and eventually collects all of the available

Table 3.1: Amplitude of location and ice thickness excursions

	Latitude Excursion	**Longitude Excursion**	**Ice Thickness Excursion**
	°	°	**m**
Path 1	-3.7	0.96	183
Path 2	0.1	-0.09	-44.9
Path 3	0.07	-0.04	-10.8
Path 4	0.02	-0.002	-2.3
Path 5	0.1	-0.03	-16.3
Path 6	0.07	-0.03	-10.8

N_2 and reorients over another 6.5 My, reaching its final semi-stable latitude of 13.8°N and final ice thickness of 2 km. When the obliquity returns to high values, >127°, the basin receives slightly more insolation than the average of the rest of the surface so a short period of sublimation and poleward reorientation occurs. 16.8 m is ice is sublimed, which causes a 0.1° reorientation in latitude. However, the combination of increasing the latitude and decreasing the obliquity causes the infill rate to return to positive values and the ice sheet returns to the maximum 2 km thickness, returning the basin to its previous semi-stable location.

These excursions have consequences for present-day Pluto. Currently, Pluto's obliquity is 120° and increasing. If SP follows the blue curve in Figure 3.6, for example, then it could undergo a small excursion, reorienting a few tenths of a degree in latitude and losing a few tens of meters of N_2 ice in the next 0.4 My or so. This period of reorientation would last for 0.3 My. The previous excursion began around 2.4 My ago, and there could be geologic evidence of it on Pluto's present-day surface. Bertrand et al. (2018) discuss the effect of N_2 condensation on geology in more detail. These excursions could also be responsible for refreshing the surface and helping to remove impact craters, along with glacial flow and convective overturning.

Table 3.1 shows the amplitude of the location and thickness excursions for each of the paths.

3.3.2 Effect of Initial Obliquity

All of the results shown above are initialized with Pluto's present-day obliquity of 120°. However, the initial obliquity at the time of ice sheet formation is unknown. Additionally, the

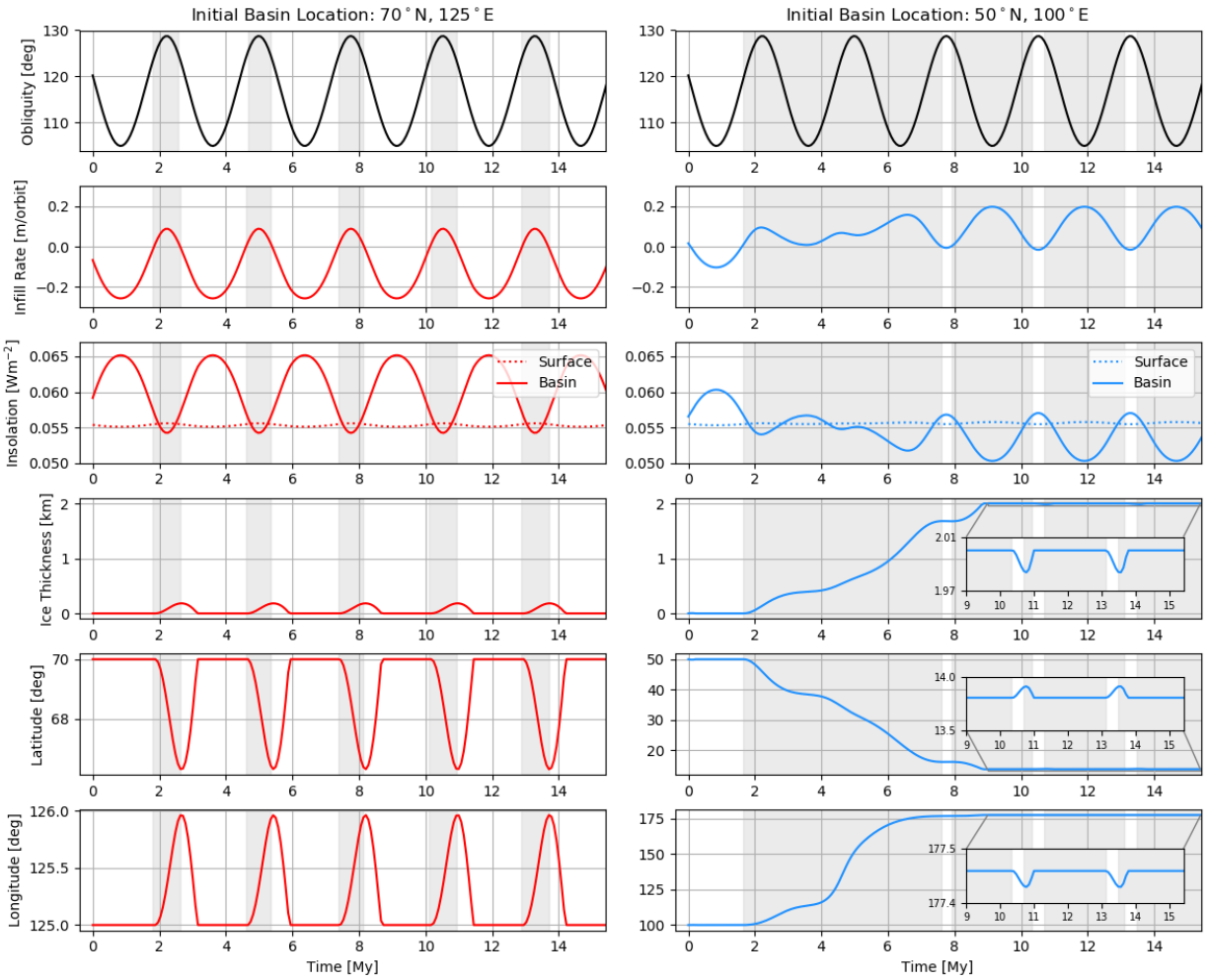

Figure 3.6: Time series of two example basins, highlighting the location and thickness excursions as a result of the obliquity cycle. The gray shading across all panels indicates time periods of positive infill rate. The red curves in the left panel correspond to the red path labeled 1 in Figure 3.2, and the blue curves in the right panel correspond to the blue path labeled 5. In the third panel from the top, the solid line is the orbit-averaged insolation onto the basin, and the dashed line is the orbit-averaged insolation on the remainder of the surface. The insets on the right side zoom in to show the excursions in more detail.

period and magnitude of the obliquity cycle at the time of the ice sheet formation is also unknown, which is discussed more in Section 3.3.5. Here, we explore the effect of varying the initial obliquity on the final location of the basin, final thickness of the ice sheet, and the timing of the infill and subsequent excursions.

Figure 3.7 shows that changing the initial obliquity only affects the timing of events and not the final location, final ice thickness, nor the magnitude of the location or thickness excursions. It shows the location and ice thickness over time for a 3-km basin with an 80 m GEL N_2 inventory beginning at either 20°N, 110°E or beginning at 50°N, 135°E with initial obliquities of 120° (the present-day value), 105° (the minimum of the obliquity cycle), and 128° (the maximum of the obliquity cycle). The 120° run starts at time t = 0, and the 105° and 128° runs begin 0.8 and 2.3 My later, respectively, when the phase of the obliquity cycle reaches the specified value.

In all cases, the three line colors, representing different initial obliquities, all eventually converge. As seen in the left panel of Figure 3.7, the different initial obliquity model runs converge to the same location and ice thickness after about 6 My for this initially low-latitude basin, while the initially intermediate-latitude basin, shown in the right panel, takes 12 My to converge. If in the 120° case, the basin enters the Infilling Phase before the obliquity cycle reaches 105° or 128°, then the 105° and 128° initial obliquity curves have to spend time "catching up" to the 120° case, delaying their infill and time to reach their final location. This is seen for both the 105° and 128° initial obliquity curves in the left panel, and the 128° initial obliquity curve in the right panel. However, since the initially-intermediate latitude basin in the right panel begins with a 2 My Stationary Phase period, in which it is waiting for a favorable obliquity for infill to begin, the 105° initial obliquity curve lies exactly on top of the 120° curve as soon as it begins (0.8 My after the 120° curve).

3.3.3 Effect of Basin Deformation

As the ice sheet grows, the mass of N_2 ice deforms the underlying crust, causing the ice sheet to sink lower into the surface. However, the magnitude for the deformation is dependent on

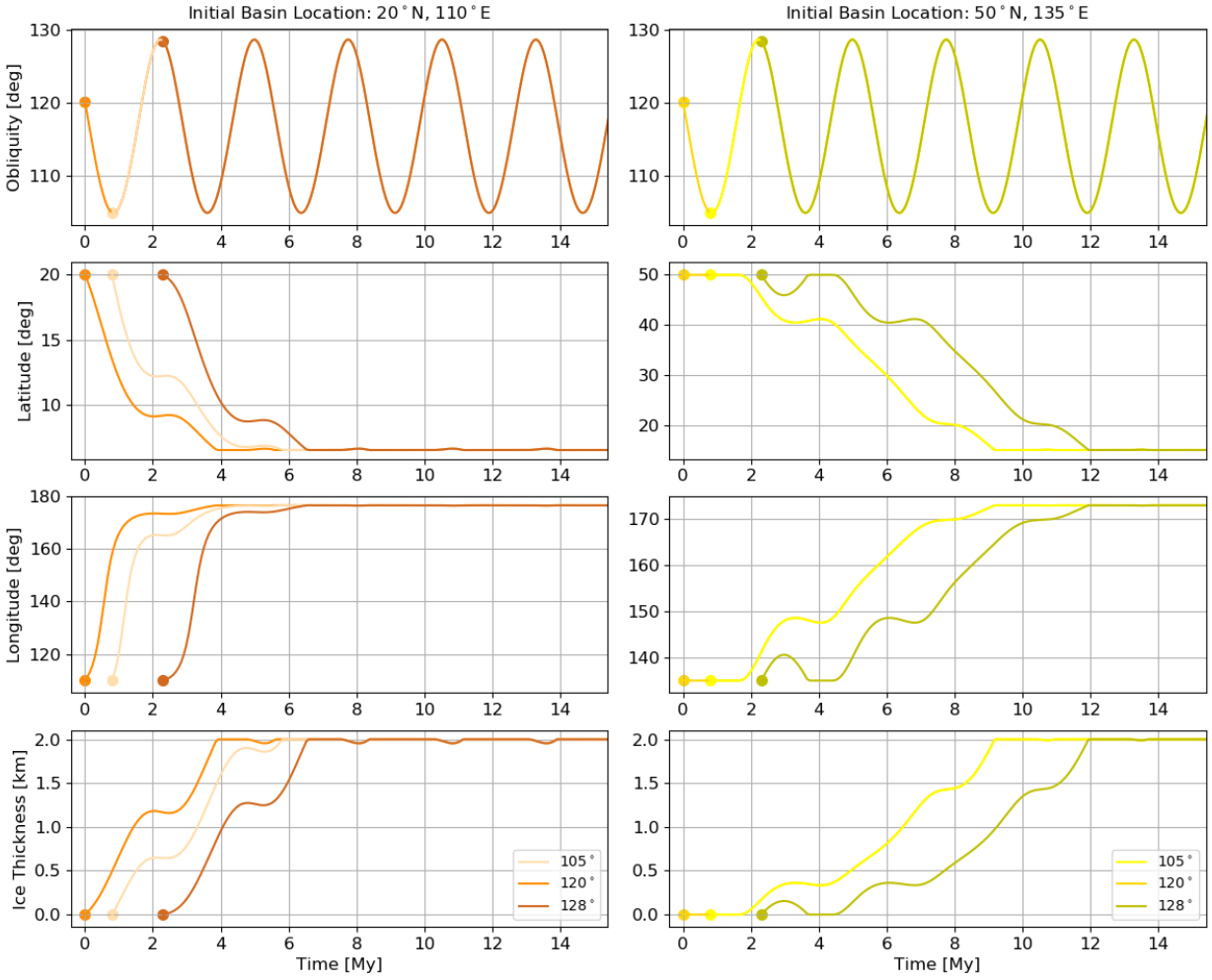

Figure 3.7: Time series of the obliquity, latitude and longitude of the basin, and thickness of the ice sheet for a 3-km basin with an 80 m GEL N_2 inventory beginning at 20°N, 110°E (left, corresponding to the orange path labeled 2 in Figure 3.2) and beginning at 50°N, 135°E (right, corresponding to the yellow path labeled 3 in Figure 3.2). The line shade indicates the initial obliquity: light orange and yellow have an initial obliquity of 105°, medium orange and yellow are 120°, and dark orange and yellow are 128°. Note that, in the right panel, the 105° curve lies directly on top of the 120° curve. The initial obliquity only affects the timing of events and not the final location, final ice thickness, nor the magnitude of the location or thickness excursions.

assumptions about the interior structure of Pluto. Here, we investigate the effect of deformation by comparing our nominal model to a model that ignores the effect of deformation entirely, equivalent to a perfectly rigid lithosphere with no elastic layer.

Our model accounts for the deformation by varying the elevation of the basin floor (underneath the N_2 ice sheet) as a function of ice thickness. We solve for this deformation self consistently with the viscoelastic Love number interior structure model described in Section 3.2. In short, for a 50 km thick elastic lithosphere, for every 1 km of N_2 ice in the basin, the basin floor sinks by 0.5 km. As the basin floor sinks, the top of the ice sheet sinks with it, so consequently the condensation surface is deeper and the infill rate is higher than it would be if the crust was not deformable. Figure 3.8 compares the temporal behavior of the model including crustal deformation with a variation of the model that does not allow the crust to deform. When crustal deformation is ignored, the basins reorient further in a shorter amount of time relative to when crustal deformation is included. As a consequence of crustal deformation, the present-day depth of the SP basin floor is deeper than the depth of the original, unfilled impact basin's floor.

3.3.4 Effect of Albedo

In the preceding sections, the modeled surface, basin floor, and ice sheet all have an albedo of 0.75. However, the infilling rate $\dot{m}$ is directly proportional to $(1 - A)$, so reducing the albedo increases the infilling rate, and vice versa. This section explores the effect this has on the final basin locations, depths, and ice thicknesses.

The principal effect of albedo is on timing. Increasing the albedo reduces the infilling rate, so the basins infill more slowly, all else being equal. With an albedo of zero, basins at all initial locations reached their final semi-stable locations within 6 My or so, while with an albedo of 0.75, many basins required 10 My to reach their final locations and enter the Cyclic Phase.

Slower infill also has an indirect consequence on the initial locations that reorient to within $\pm 5^\circ$ of the present-day location of SP. Initially high-latitude basins undergo only brief periods of positive infill rates, and when they accumulate enough N_2 ice during one of these periods, the

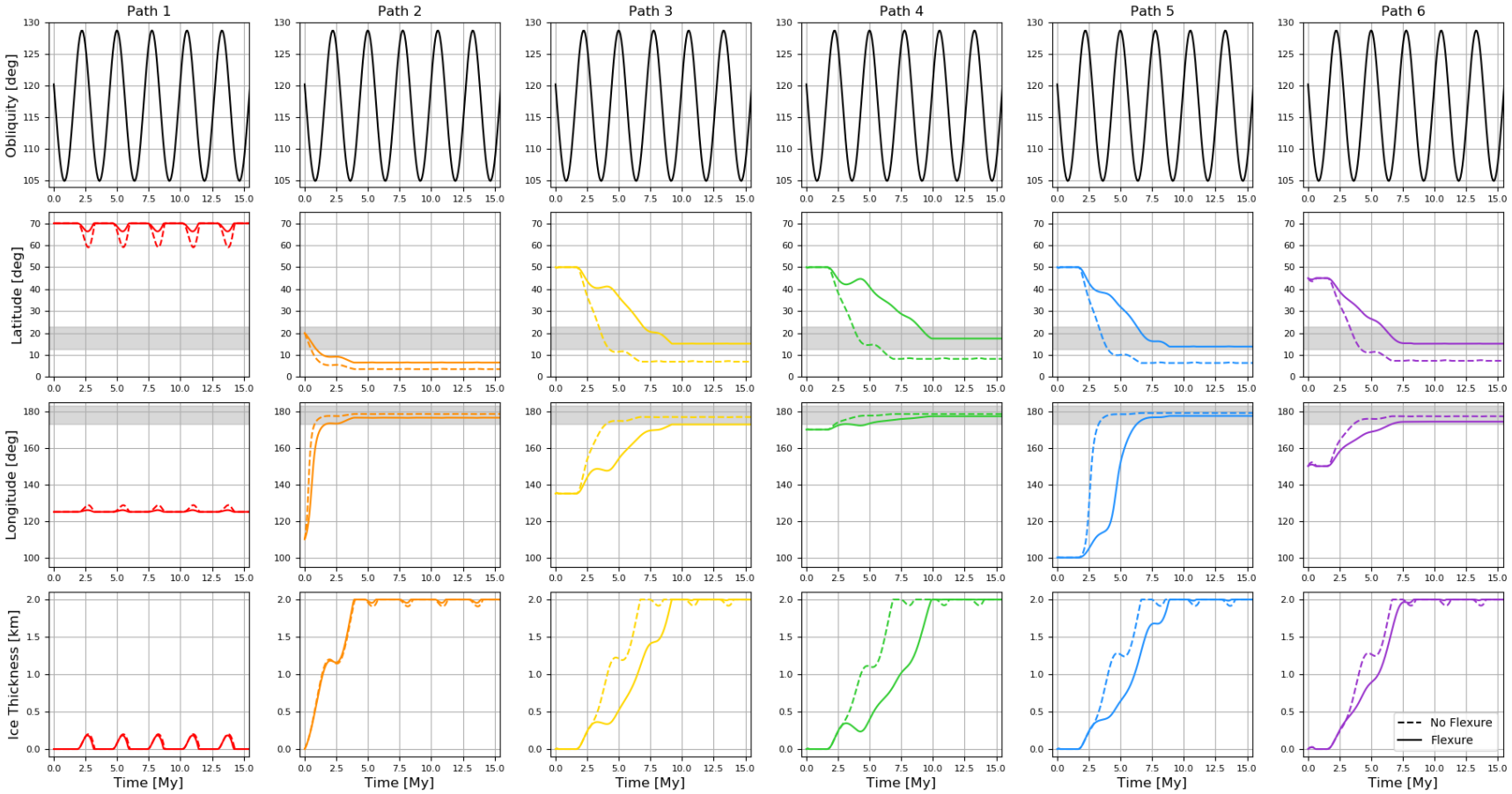

Figure 3.8: Comparison of the temporal behavior for Pluto's obliquity, the basin's latitude and longitude, and ice thickness for each path for the nominal model (including crustal deformation, solid line) and without crustal deformation (dashed line). For the latitude and longitude rows, the shaded region is $\pm 5°$ from the latitude or longitude of SP's present-day location. Obliquity is shown in black because it is the same for all paths; it is repeated in each column for ease of comparison. The color scheme is the same as that used in Figure 3.2.

subsequent reorientation to lower latitudes leads to a runaway process in which the basins infill completely and collect all available N_2. If the infill rate is lower, due to a higher albedo for example, it becomes more difficult to accumulate enough ice during the favorable-obliquity period, and the basins instead exhibit a back-and-forth reorientation where they never infill completely (in fact they never enter the Infilling Phase) and always return back to their initial location (e.g. the red path labeled 1 in Figure 3.2). Figure 3.9 shows how the transition latitude between back-and-forth paths and runaway infill paths depends on albedo. The latitude decreases from 80° N at an albedo of zero to 55° for an albedo of 0.9. This means that, if the albedo is 0.9, no basins starting at or north of 55° will have final locations within ±5° of the present-day location of SP. In terms of the regions defined in Figure 3.5, the lower boundary of Region 1 is defined by this the transition latitude, 55° for the A = 0.9 scenario.

Figure 3.10 shows the fraction of the surface where the initial basin could be in order to reorient to within ±5° of the present-day location of SP. This is the fraction relative to the octant of interest (0°N to 90°N and 90°E to 180°E); to find the fraction relative to Pluto's entire globe, the values in Figure 3.10 need to be divided by 8. Higher albedo surfaces have smaller initial areas that reorient to be within ±5° of the present-day location of SP, in part due to the lower transition latitude between back-and-forth and runaway-infill reorientations discussed above. Figure 3.10 shows that, if the basin was formed by an impact as suggested, impacts onto 15-25% of the surface, mostly at intermediate latitudes, would be capable of reorienting to produce the observed present-day location of SP.

3.3.5 Effect of Pluto's Early Orbit

For the results presented above, we used Pluto's present-day orbital parameters: namely a semi-major axis of 40 AU and an eccentricity of 0.254. However, at the time of the ice sheet formation, which could be as long ago as 4 Gy, Pluto could have been in a much different orbit, potentially much closer to the Sun. For example, Nesvorný (2015) modeled the orbital evolution of many Plutinos (other objects in the 3:2 resonance with Neptune) and found that Plutinos can

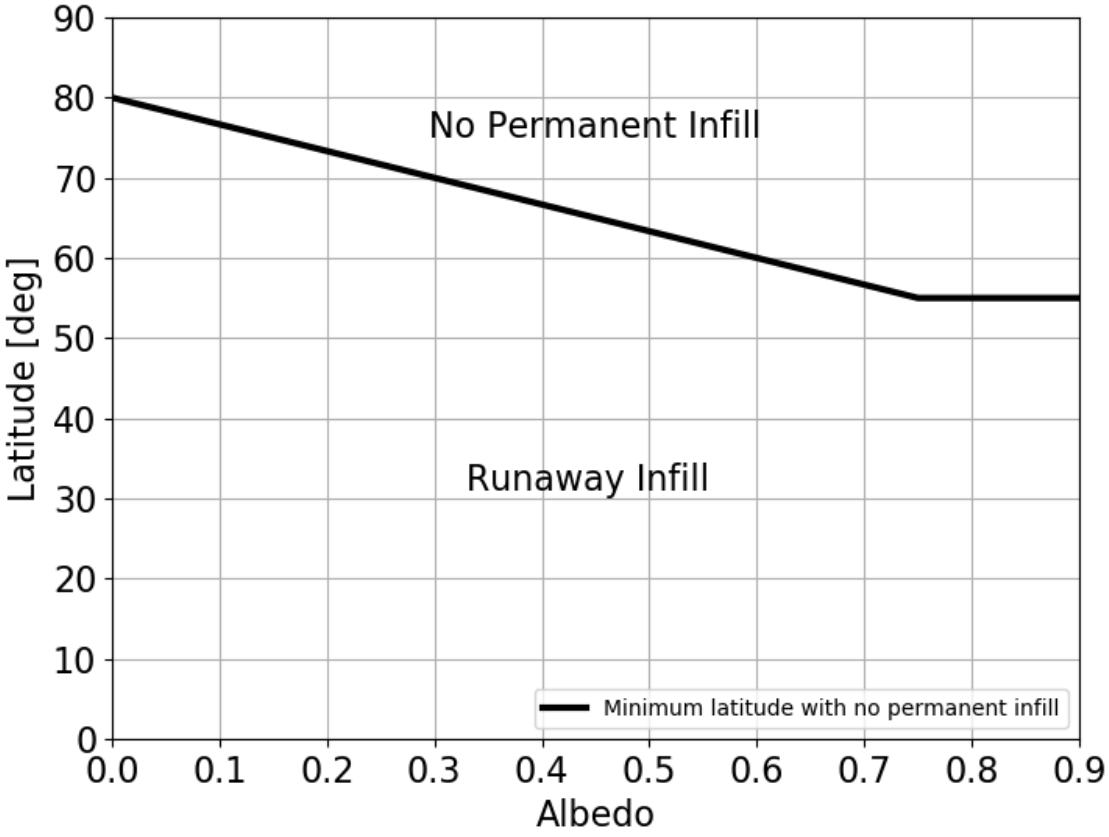

Figure 3.9: Dependence of the transition latitude between back-and-forth paths and runaway infill paths on albedo. Note that the latitude here is the lowest latitude at any longitude that exhibits back-and-forth reorientation; some basins at that latitude may exhibit runaway reorientation depending on their longitude.

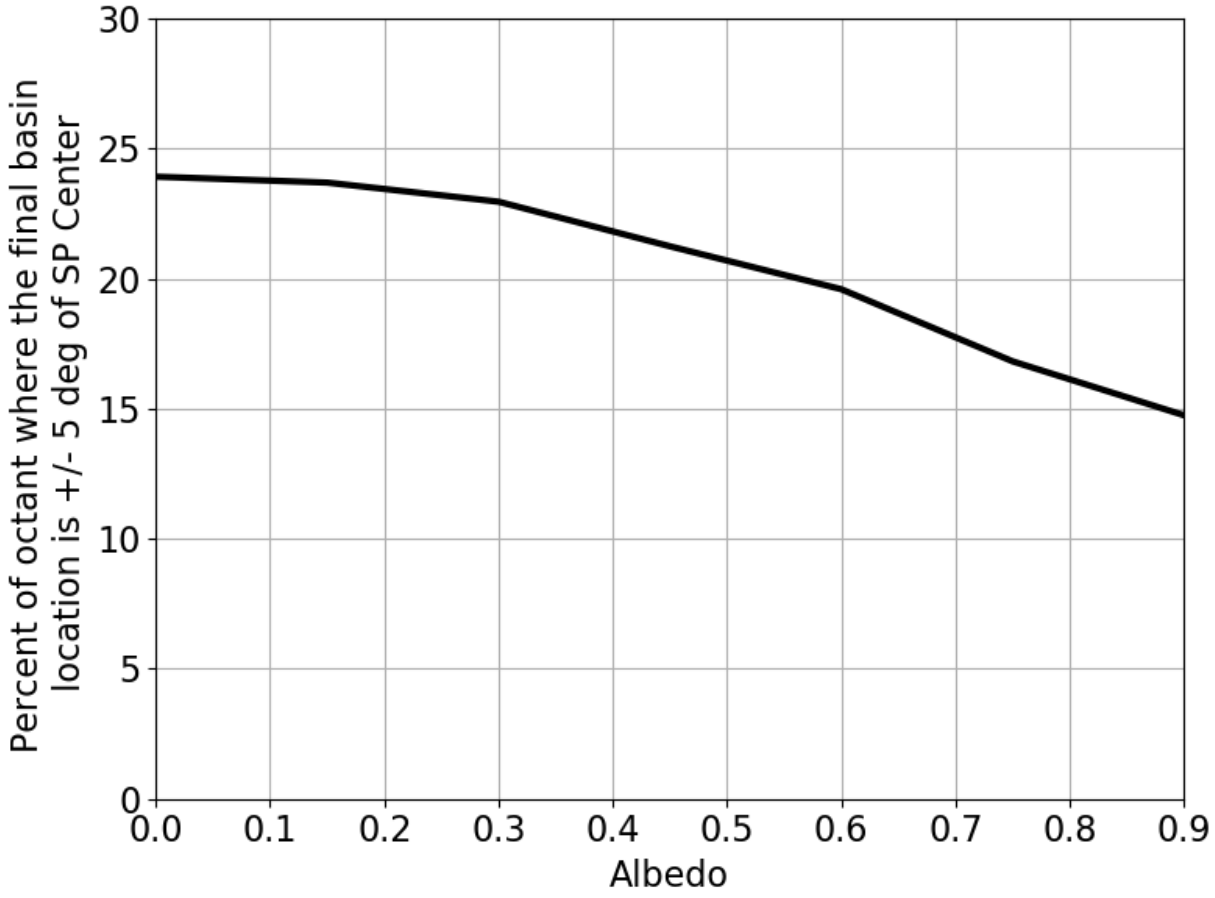

Figure 3.10: Fraction of the surface where the initial basin could be in order to reorient to within $\pm 5^\circ$ of the present-day location of SP as a function of albedo. Note that this is the fraction relative to the region of interest (0°N to 90°N and 90°E to 180°E); to find the fraction relative to Pluto's entire globe, the values in this figure need to be divided by 8.

spend significant time in orbits with semi-major axes less than 30 AU. As a simple test of how a reduction in semi-major axis affects our results, we repeated the analysis shown in Figure 3.4 for a 3-km deep basin and 80 m GEL N_2 inventory with a semi-major axis of 20 AU instead of 40 AU. We found that there were more initial basin locations which reorient to within $\pm 5^\circ$ of SP's present-day location for the 20 AU semi-major axis orbit compared to the 40 AU case. Regions 3, 4, and 5 (see Figure 3.5) extended to higher latitude (70°N). Reducing the semi-major axis has a similar affect to reducing the albedo; both changes increase the absorbed insolation and therefore increase the infill rate.

Figure 3.11 shows a comparison of results for a 20 AU and 40 AU orbit. In this figure, the basin is 3-km deep and there is 80 m GEL of available N_2 ice, and the basin's initial location is either 70°N, 125°E (left panel, red curves) or 50°N, 170°E (right panel, green curves). The differences between the 20 AU and 40 AU runs shown in the right panel are indicative of most initial basin locations. The final location and final ice thickness are not affected by reducing the semi-major axis in most cases, since a reduction in semi-major axis affects the $S_{surface}$ and S_{basin} terms in Equation 3 proportionally. The surface pressure and temperature affect infill rates only through the latent heat, which changes slowly with temperature. The overall infill rate is quadrupled, so the 20 AU basins infill four times faster than the 40 AU basins. However, in some cases, the infill rate is high enough at 20 AU to allow complete infill, while at 40 AU the same basin never accumulated much ice and doesn't enter the Infilling Phase. The left panel of Figure 3.11 shows an example of this, in which the 20 AU basin (dark red) forms a 2-km thick ice sheet and reorients close to the anti-Charon point, while the 40 AU basin (lighter red) never forms an ice sheet thicker than 0.25 km and cyclically reorients away from and back to its initial location.

Figure 3.11 assumes the same obliquity cycle as used throughout this work: a 2.7 My periodic cycle oscillating between 105° and 128°. However, since this cycle is determined by perturbations from other solar system bodies, the period and amplitude are likely to change if the orbit's semi-major axis is reduced from 40 AU to 20 AU. Additionally, the solar output from the Sun 4 Gy ago is potentially quite different from the present-day value. A more detailed analysis of a "closer-in"

version of Pluto's orbit, accounting for these variables, is left for future work.

3.4 Conclusions

We present, for the first time, a coupled reorientation and climate model that can calculate the atmospheric condensation onto a ice sheet in a depression as a function of time, accounting for Pluto's varying obliquity and the possibility of true polar wander (TPW) as the mass contained within the basin grows. By stipulating that the final basin location must be within ±5° of the present-day center of SP at 17.7°N, 178.2°E and that the top of the final ice sheet must be at an elevation of -2 km, we find that the final thickness of the ice sheet in the basin cannot be larger than 2 km, which is equivalent to a total mass of 1.4 x 10^{18} kg or an 80 m global equivalent layer. More massive ice sheets cause too large of reorientations and the final basin ends up closer to the anti-Charon point than SP is observed to be. Based on the observed topography, the top of the ice sheet needs to be 2 km below the surrounding terrain, requiring that the initial basin depth be 2.5–3 km (final basin depth of 3–4 km) with a 1–2 km thick final ice sheet. The final ice thickness is subject to our assumption of the elastic thickness of the lithosphere; although as discussed earlier the effect is likely to be small due to the opposing effects of a larger remnant figure and less load compensation that result from thinner elastic lithospheres. With these requirements, our model finds that the basin most likely formed at an intermediate latitude, between 35°N and 50°N.

- Mean Ice Thickness: 1–2 km
- Initial Basin Depth: 2.5–3 km
- Present-Day Basin Depth: 3–4 km
- Initial Location: intermediate latitudes ($\sim$ 35°N – 50°N).

The constraints presented in Section 3.3 and summarized above, 1–2 km for the maximum ice thickness and 3 or 4 km for the present-day depth of the basin, are both slightly smaller than previous estimates for those quantities. Convection models (McKinnon et al., 2016; Trowbridge

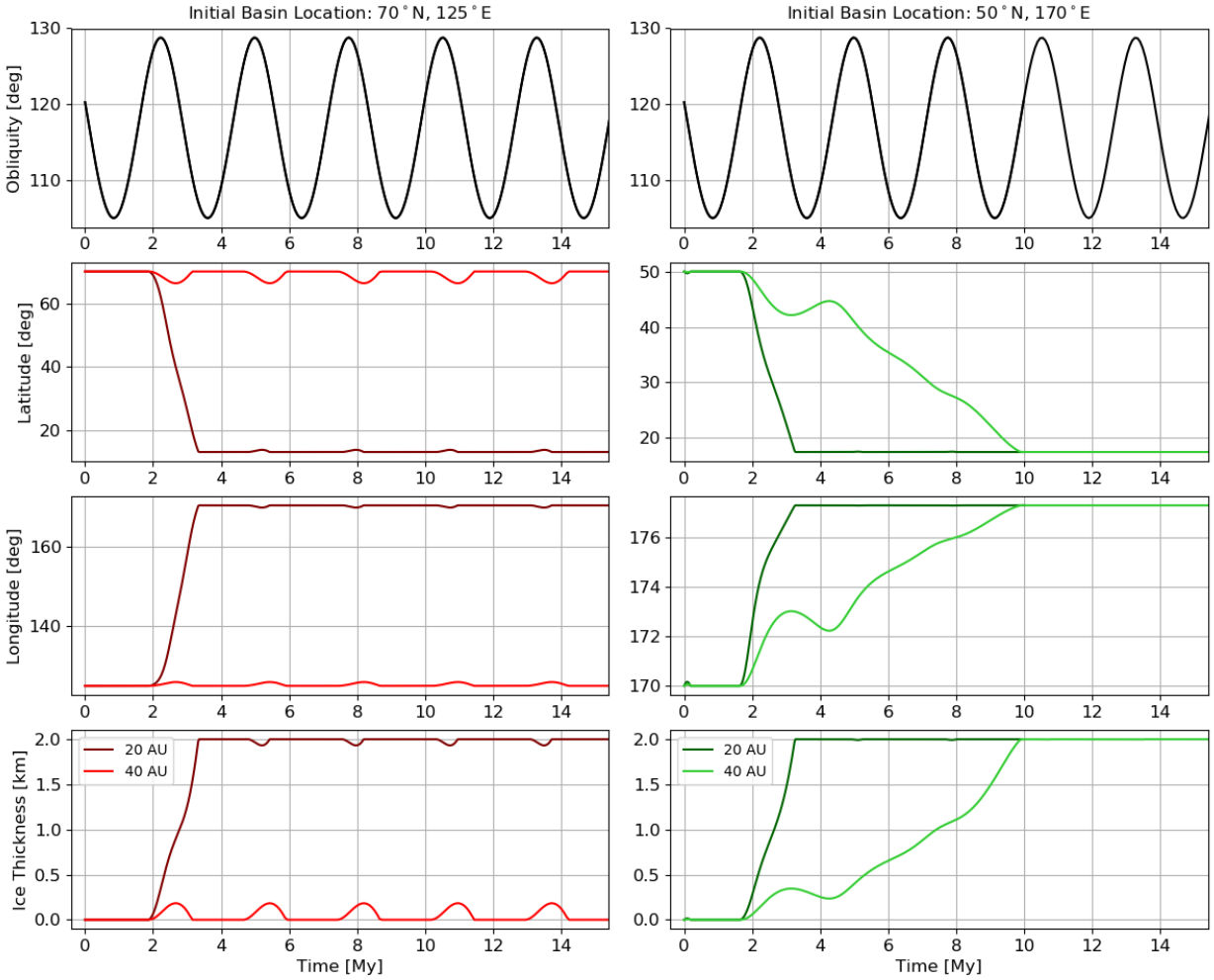

Figure 3.11: Time series of the obliquity, latitude and longitude of the basin, and thickness of the ice sheet for a 3-km basin with an 80 m GEL N_2 inventory beginning at 70°N, 125°E (left panel, corresponding to the red path labeled 1 in Figure 3.2) and 50°N, 170°E (right panel, corresponding to the green path labeled 4 in Figure 3.2). The line color indicates the orbit's semi-major axis: lighter colors are Pluto's present-day semi-major axis of 40 AU, and darker colors are a hypothetical past orbit's semi-major axis of 20 AU.

et al., 2016) imply an ice thickness of 3-10 km, but they are dependent on the unknown N_2 ice rheology. McKinnon et al. (2016) estimate that ice sheets thicker than 1 km will undergo convection, so the ice sheets in this model would be able to support active convection. The depth of the basin itself is also not well known, besides needing to be 2 km deeper than the thickness of the ice sheet, to account for the observed elevation difference between the top of the ice sheet and the level of the average terrain. Earlier estimates placed the depth to the top of the ice sheet at 3–4 km (i.e. Moore et al. (2016)), larger than the 2 km we use here. This is due in part to improvements to the global stereo topography model (Schenk et al., 2018). Also, the -2 km elevation estimate is made relative to the average surface elevation, rather than to the topographically-high rim surrounding the basin. McKinnon et al. (2016) argue that the depth of the original empty basin was likely less than 10 km, and the impact models from Johnson et al. (2016) produce final compensated basins on the order of 5-10 km deep. Our assumptions about the initial gravity anomaly of the empty basin affects the final ice thickness and basin depth, and can be easily adjusted to reflect new information about Pluto's interior as it becomes available.

These constraints on the basin depth, ice thickness, and initial location are somewhat dependent on the assumptions made in the model, which are explained below.

(1) We assume that the empty basin has a net-zero gravity anomaly, implying that there is some form of compensation, like subsurface ocean uplift or an ejecta blanket (Nimmo et al., 2016; Keane et al., 2016). If the empty basin instead had a negative gravity anomaly (e.g. not fully compensated), the final ice thickness would be larger than 2 km.

(2) We also make assumptions about Pluto's interior structure, which determines the deformation in response to ice loading, and the rotational and tidal deformation preserved by a fossil figure. A weaker interior (e.g. due to a thinner elastic lithosphere or a smaller rigidity) results in more ice sheet compensation, which decreases TPW, and a smaller fossil figure, which increases TPW. These two effects nearly cancel each other, making the results presented here insensitive to the assumed interior structure.

(3) The topography of the basin floor, underneath the ice sheet, is unknown. We assume a flat bottom. If the basin floor instead is curved such that the ice sheet is thickest in the center and thinner at the edges, then our model's estimate of the ice thickness (where this is now measured at the center of the basin) would be slightly larger. For basins containing equal-mass ice sheets, curved-bottom basins will have deeper centers than flat-bottomed basins.

(4) We assume that Pluto reorients instantaneously in response to movements of volatiles across the surface. If Pluto does not respond this fast, then volatile transport may result in small-scale non-principal axis rotation, which would result in more complicated couplings between rotational dynamics and volatile transport.

This TPW model accounts for the time variability of Pluto's climate and accounts for how reorientation changes the infill rate into the basin, unlike previous models. We find that most ice sheets form completely within 5–10 My, subject to the assumption of instantaneous reorientation after each timestep, but that this formation is not monotonic. The modelled basins do not infill at a constant rate from start to finish; instead the rate varies based on the current obliquity and the current latitude of the basin (which control the relative insolation onto the ice sheet) and also on the current depth to the top of the ice sheet. In some cases, the ice sheet begins to form, but then partially or completely sublimes away due to a change in obliquity. Even after reaching a final semi-stable state (e.g. collecting all of the available N_2 inventory), changes in the obliquity drive changes in the ice thickness and basin location every 2.7 My, on the order of 10 m in thickness and 0.1° in latitude. This cyclic TPW would continue to be active on present-day Pluto, with the next sublimation period expected to occur in 0.4 My, and the previous one ending 2 My ago.

The origin of Pluto's Sputnik Planitia basin and ice sheet is a rich problem. This work adds to previously presented work (Keane et al., 2016; Nimmo et al., 2016) that suggested that TPW is the mechanism that reoriented an impact basin to the present-day location of Sputnik Planitia. This work shows that the TPW hypothesis can and should be coupled with Pluto's climate and orbital

evolution, and that this coupled model is also consistent with the observed features of Sputnik Planitia. Further understanding of the details of Pluto's orbit and climate early in the history of the solar system and how that affects the ice sheet's formation is warranted.

Acknowledgments

This work was supported by NASA ROSES SSW grant NNX15AH35G. A portion of this research was carried out at the Jet Propulsion Laboratory, California Institute of Technology, under a contract with the National Aeronautics and Space Administration (80NM0018D0004). A portion of this research was supported by the California Institute of Technology Joint Center for Planetary Astronomy postdoctoral fellowship. A portion of this work was supported by the National Aeronautics and Space Administration (80NSSC17K0724). Discussions with Pat McGovern helped frame the context. The authors would also like to express their appreciation of the New Horizons mission and its team for their exceptional work.

Chapter 4

Nitrogen Loss from Pluto's Birth to the Present Day via Atmospheric Escape, Photochemical Destruction, and Impact Erosion

This chapter was prepared with the intent to be published in the Planetary Science Journal (Johnson et al., 2023).

Abstract: We estimate the loss of nitrogen Pluto experienced over its entire lifetime, including its chaotic and uncertain youth during the time period of the giant planet instability early in solar system history, which we term the "Wild Years." To do so, we analyze the orbital migration of an ensemble of simulated Plutinos, which are Kuiper belt objects that, like Pluto, were caught in the 3:2 mean motion resonance with Neptune during the giant planet instability. This orbital migration brought the Plutinos from their birth location near 20 - 30 AU to their present-day orbits near 40 AU, along a very non-linear, chaotic path that reached orbits with semi-major axes as small as 10 AU and as large as 100 AU. We model the thermal history that results from this orbital migration, and estimate the escape and photochemical destruction rates from an atmosphere subject to the ever-changing thermal environment. Due to the early Sun's enhanced UV output, the photochemical destruction rate during the Wild Years was a factor of 100 higher than the present day rate, but this still only results in a loss of $\sim$ 10 m Global Equivalent Layer (GEL) over the age of the solar system. The enhanced Jeans escape rate varies wildly during this time, and a net loss of $\sim$ 100 cm GEL is predicted. Additionally, we model the impact history during the orbital migration, in order to determine the net loss or gain of volatile compounds from impactors onto the Plutinos' surfaces, and find that impacts are a net source, rather than loss, of N_2 for Pluto,

contributing $\sim$ 100 cm GEL over the age of the solar system. 100 cm GEL amount is just 0.1% of the observed amount of N_2 in Sputnik Planitia. We therefore conclude that Pluto did not lose an inordinate amount of volatiles during the Wild Years, and its primordial volatile inventory can thus be approximated as its present-day inventory. However, significant fractions of these total values of photochemical destruction, escape, and impact delivery occurred during the Wild Years, so estimates made using present-day rates will be underestimates of the total loss of N_2 via each mechanism.

4.1 Introduction

Pluto's atmosphere is more than 99% nitrogen (Stern et al., 2015), and much of the observed surface is covered with nitrogen ice, most notably the 1000-km-wide ice sheet known as Sputnik Planitia. Observations from the *New Horizons* mission provide estimates of the present-day nitrogen inventory, which is dominated by the ice in Sputnik Planitia. However, over the course of Pluto's 4.5 Gy lifetime, various loss mechanisms have been active and thus Pluto's primordial inventory may have been very different from it's present day inventory.

Modeling the loss of volatiles, specifically N_2, from Pluto's surface over the age of the solar system allows estimation of its primordial volatile inventory by calculating the amount lost via escape, impact erosion, and photochemical destruction. These models must account for the formation location and subsequent orbital evolution of Pluto. Pluto is thought to have formed not at 40 AU but instead likely closer to the Sun and was pushed outwards by interactions with Neptune during giant planet migration, ultimately being captured into the 3:2 mean motion resonance with Neptune. Models of volatile loss must also account for the variable behavior of the Sun over its lifetime. When the Sun entered the main sequence and officially became a star, its output in ultraviolet (UV) wavelengths, which are important for escape, was orders of magnitude larger than the present-day value. Additionally, the timing of Pluto's differentiation is important for understanding when there were or were not significant deposits of N_2 on the surface available to form an atmosphere and be subject to loss mechanisms. In this section, these topics are summarized as

they relate to our model of volatile loss from early Pluto.

Pluto likely formed closer to the Sun than its current orbit (Canup et al., 2021, and references therein). Its location in the 3:2 mean motion resonance with Neptune (meaning Pluto completes two orbits about the Sun for every three that Neptune completes) is evidence for this. As Neptune's orbit expanded, the heliocentric distance corresponding to resonances with its orbit swept out through the solar system as well. Objects originally on orbits unrelated to Neptune could have be "picked-up" into the resonance and then continued to evolve in step with Neptune such that they remained in the resonance as it expanded outwards from the Sun (Malhotra, 1993). The discovery of other objects in Neptune's 3:2 resonance (the so-called "Plutinos") has strengthened this argument (e.g. Yu and Tremaine (1999)). Many authors have modeled the giant planet migration. For this work, we use the output from the model of Nesvorný (2015), which constrained the migration of giant planet Neptune specifically based on orbital properties of the Kuiper Belt. From Nesvorný (2015), we have orbital evolution paths for 53 Plutinos, covering a period of 100 My in the early part of the solar system. These paths start at the time of the giant planet instability, which probably occurred within the first few tens of millions of years after the protoplanetary disk dispersed. We discuss the exact timing further, below.

The sun is thought to have formed in a giant molecular cloud around 4.6 Gy ago. The protosun grew in mass as it gained material from the surrounding cloud. Once the protosun stopped gaining mass, it transitioned into what is called a "pre-main sequence" star. During this stage, the sun's luminosity was powered by gravitational collapse. For the first part of the stage, known as the T-Tauri phase, there was a thick protoplanetary gas disk and strong stellar winds. Sometime later, the Sun condensed enough under its own gravity for hydrogen burning to begin. This point is known as the Zero-Age-Main-Sequence (ZAMS) as it is the beginning of the Sun's time on the main sequence of the H-R diagram. According to the solar evolution model we use here, the pre-main sequence stage lasted for approximately 40 My (Bressan et al., 2012).

When the Sun was only a few tens of My old, its radiation output was very different from present-day values. 4.6 Gy ago, the bolometric luminosity of the "Faint Young Sun" was just

70% of the present-day value (Bressan et al., 2012). However, at UV wavelengths, the young Sun was actually significantly brighter than it is today. Ribas et al. (2005) measured UV fluxes from 6 solar analogs of various ages (0.1 - 7 Gy) and created a solar evolution model for wavelengths between 1 to 1200 Å, as well as various line fluxes, including Lyman alpha at 1216 Å. Lyman alpha contributed 20% of the total flux between 1-1700 Å when the Sun was 0.1 My old. Considering the combination of the 1-1200 Å flux plus the Lyman alpha flux, the Sun was 50 times brighter at 0.1 Gy old than it is currently at 4.56 Gy old.

While the early Sun was evolving as described above, the solar system was forming as well. Calcium–Aluminum-rich Inclusions (CAIs) are small inclusions found inside of carbonaceous chondrite meteorites. They are thought to be among the oldest solid materials in the solar system, and are commonly used to determine the solar system's age. Four CAIs from meteorites have been radiometrically dated, yielding an age of 4567.30 ± 0.16 Myr (Connelly et al., 2012). CAIs are likely to have condensed around the time the protosun was transitioning into its pre-main sequence stage, so we assume these two events were concurrent in this work.

The lifetime of protoplanetary disks is needed in order to pin down when the giant planet instability occurred relative to the age of the Sun. In their observational L-band study of young to intermediate-age (0.3 - 30 My) stellar clusters, Haisch et al. (2001) found an overall disk lifetime for stars in the clusters they studied of 6 My (meaning all of the stars older than 6 My did not have disks), and found that half of the stars lost their disks by an age of 3 My. The review by Williams and Cieza (2011) establishes an upper limit of 10 My for disk lifetimes based on a variety of Spitzer observation programs. The Sun's protoplanetary gas disk had thus likely dissipated fully by 4.557 Ga (10 My after CAI condensation). Lisse et al. (2021) discusses the shadowing and therefore cooling effect that the protoplanetary disk had on the Kuiper Belt early in Solar System history, but given that the disk disperses before the time period relevant to this work, we don't need to account for this effect.

When originally proposed, a late giant planet instability, occurring ∼700 My after the solar system formed, was favored in order to explain the Late Heavy Bombardment suggested by large

lunar impact basins (Gomes et al., 2005). However, more recent work argues that the instability occurred much earlier, within 100 My of solar system formation. In order to prevent dynamically overexciting the terrestrial planet orbits, the giant planet instability needs to occur within 50 My of solar system formation (Nesvorný, 2018). For this work, we assume the giant planet instability occurred 30 My after solar system formation, defined as the condensation time of CAIs.

Finally, we need to know when Pluto's N_2 inventory reached the surface and became available to loss mechanisms. Differentiation would bring the lighter volatiles to the surface while the heavier rocky material forms a core. Based on the composition and formation models for Charon, it is likely that the Pluto and Charon progenitors were at least partially differentiated at the time of the Charon-forming impact, if not fully differentiated (Canup et al., 2021). Heat from the impact or subsequent tidal heating from the newly-formed Charon could finish differentiating Pluto and bring its volatiles, including N_2, to the surface (McKinnon et al., 2016). Tidal heating would be limited to within 1-10 My of the Charon-forming impact, after which the orbits would have been circularized (Canup et al., 2021; McKinnon et al., 2021). In order to form Charon from a mostly-intact progenitor as is suggested, the impact velocity needs to be slow, roughly less than 1.2 times the escape velocity. This constraint is best met after the dispersal of the protoplanetary gas disk but before the onset of Neptune migration. Thus we can conclude that Pluto's N_2 inventory was at the surface and subjected to loss mechanisms during the time of Neptune migration.

Figure 4.1 summarizes the preceding discussion about the relative and absolute timing of events in the early solar system, and indicates the assumptions made for this work.

Section 4.2 goes into more detail about the models of the early Sun, solar system, and Pluto. In Section 4.3, we present results about the orbital migration itself and the general climates experienced by migrating Plutinos. Sections 4.4, 4.5, and 4.6 present first our models for each loss mechanism and then the results from volatile loss due to photochemical destruction, impact erosion, and atmospheric escape, respectively. Finally, in Section 4.7, we discuss what these results imply for Pluto's formation and hypothesized epochs of ancient glaciation.

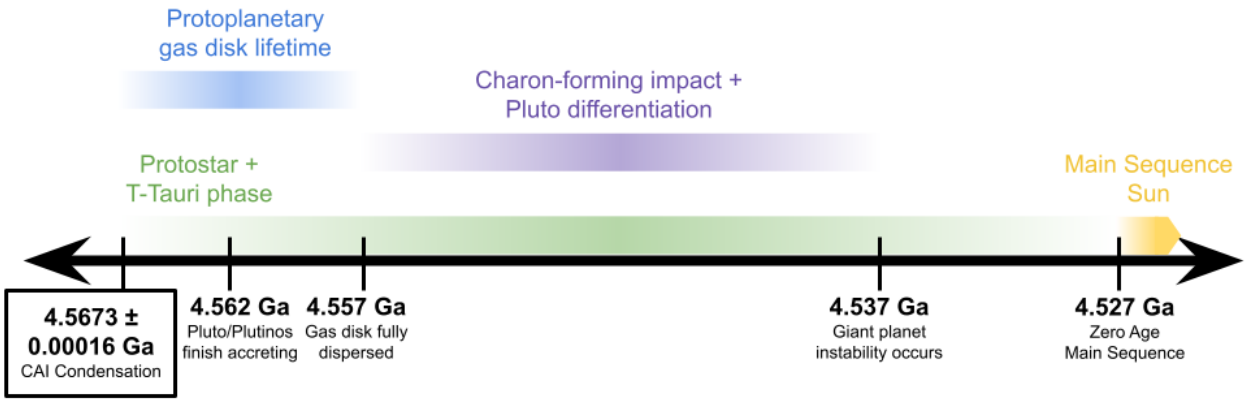

Figure 4.1: Timeline of the early solar system. The CAI condensation time of 4.5673 ± 0.00016 Ga (boxed) is well-known via radiometric dating (Connelly et al., 2012). The other times shown on the timeline are more uncertain, and represent our assumptions based on the arguments presented in the text.

4.2 Early Solar System, Sun, and Pluto Models

4.2.1 Orbital Migration

As an input to the model, we use the output Plutino orbital evolutions from the dynamical model presented in Nesvorný (2015). In this model, Neptune begins on an orbit with semi-major between 20 and 30 AU, and a disk of planetesimals extends from the orbit of Neptune to 30 AU. As Neptune migrates, some of the planetesimals are swept up into the 3:2 mean motion resonance with Neptune, forming the Plutino population. For an ensemble of 53 of these simulated Plutinos, we have their semi-major axis, orbital eccentricity, and inclination at 10000 year timesteps for a total run time of 100 My, covering a period of time we term the "Wild Years." For more details on the creation of these orbits, see Nesvorný (2015). It is important to note that we use these Plutino migrations as proxy for the possible migration that Pluto specifically underwent, and use the physical properties of Pluto throughout this work. Figure 4.2 shows the eccentricity vs semi-major axis migration for all 53 of the Plutinos in our sample. The Plutino labeled 47 is used as an example throughout this paper.

4.2.2 Solar Luminosity and UV Flux

The sun was less bright overall when it was young. At the time of the Wild Years, the sun's luminosity was about 70% of the present-day value, and it has steadily increased since then. We use the PARSEC model from Bressan et al. (2012) and the updates from Chen et al. (2014) to calculate the Sun's bolometric luminosity as a function of time, shown in the top panel of Figure 4.3. The PARSEC model includes the sun's luminosity behavior during its pre-main sequence phase, which we assume begins concurrently with CAI condensation and lasts for around 44 My. At the ZAMS (44 My after CAI condensation), the solar luminosity predicted by the model is 2.7×10^{26} W, which is 70% of the present day value of 3.828×10^{26} W.

While bolometrically the sun was fainter during the wild years, the UV flux of the sun was far stronger during this time period, relative to the present day. We use the solar evolution model of

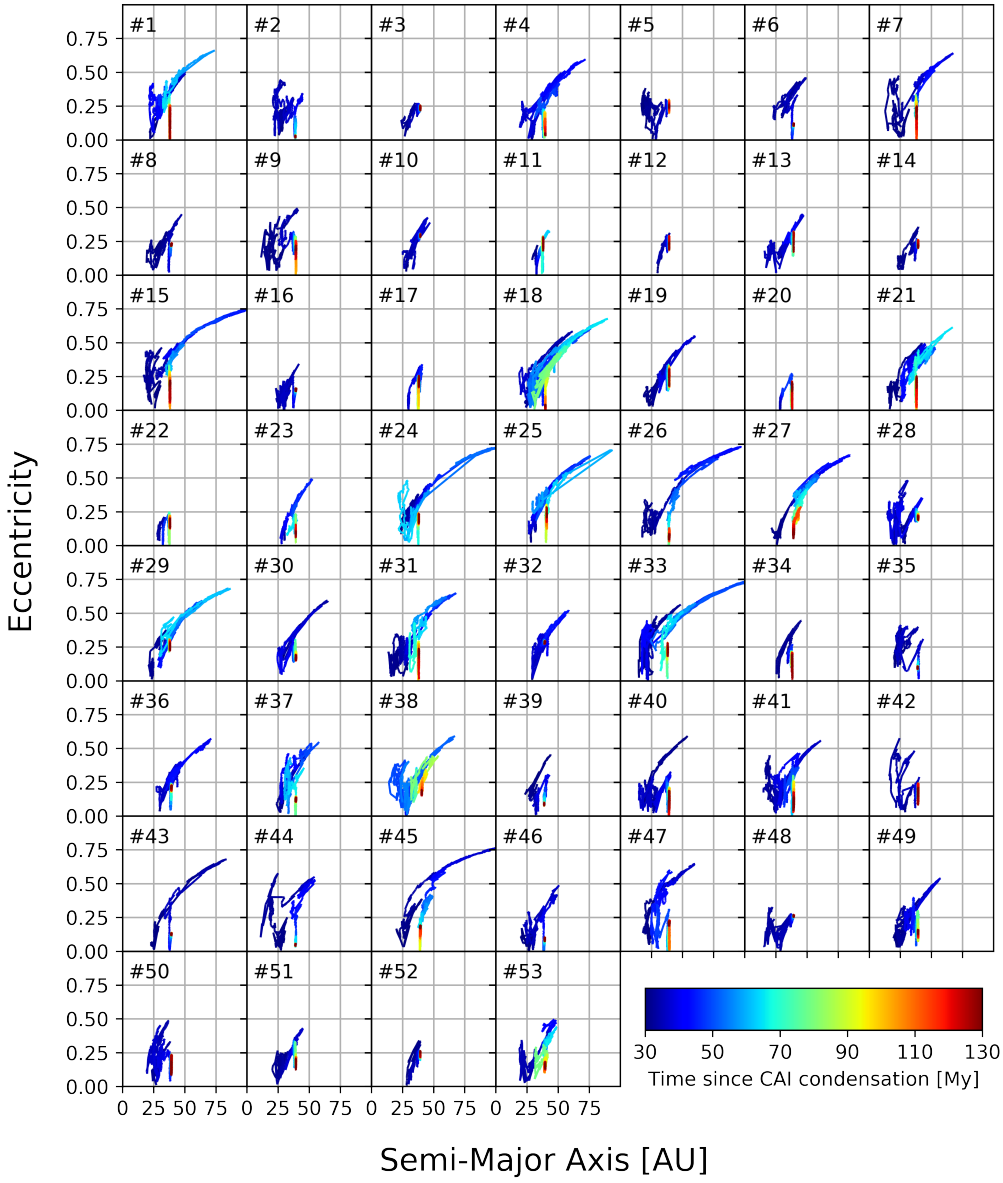

Figure 4.2: Eccentricity vs semi-major axis evolution for all 53 of the Plutinos in the sample. The colorscale indicates time since CAI condensation.

Ribas et al. (2005) to estimate the UV flux from the early Sun. The Ribas et al. (2005) model uses observations of 7 solar-type stars (including the Sun) of varying ages to create power-law model fits of the stellar flux in various wavelength bands as a function of time.

For part of this work, we are interested in photochemical destruction of N_2 molecules in the atmosphere by UV radiation. Radiation at wavelengths between roughly 100 and 1000 Å is capable of breaking the N_2 triple bond. We use three model fits from Ribas et al. (2005) in order to cover this wavelength range:

$$F_1(t) = 13.5t^{-1.2} \quad \text{100 to 360 Å} \tag{4.1}$$

$$F_2(t) = 4.56t^{-1} \quad \text{360 to 920 Å} \tag{4.2}$$

$$F_3(t) = 2.53t^{-0.85} \quad \text{920 to 1180 Å} \tag{4.3}$$

The time t is the solar age in Gy, relative to the CAI condensation time, and the resulting fluxes $F_{1,2,3}$ (at 1 AU) are in units of mW/m^2. We calculate the UV flux enhancement relative to the present-day solar UV flux at a given time with the following:

$$E_{UV}(t) = \frac{F_1(t) + F_2(t) + F_3(t)}{F_1(t_{present}) + F_2(t_{present}) + F_3(t_{present})} \tag{4.4}$$

Additionally, for the energy-limited escape discussed in Section 4.6.1.1, the early Sun's Lyman-α flux is also needed. From Ribas et al. (2005), the Sun's Lyman-α flux as a function of time can be estimated using

$$F_{Ly\alpha} = 19.2t^{-0.72} \tag{4.5}$$

where once again t is in Gy and the resulting flux at 1 AU is in mW/m^2. The corresponding enhancement, due to both 100 - 1180 Å and Lyman-α radiation, is shown in the middle panel of Figure 4.3 and given by:

$$E_{UV+Ly\alpha} = \frac{F_1(t) + F_2(t) + F_3(t) + F_{Ly\alpha}(t)}{F_1(t_{present}) + F_2(t_{present}) + F_3(t_{present}) + F_{Ly\alpha}(t_{present})} \tag{4.6}$$

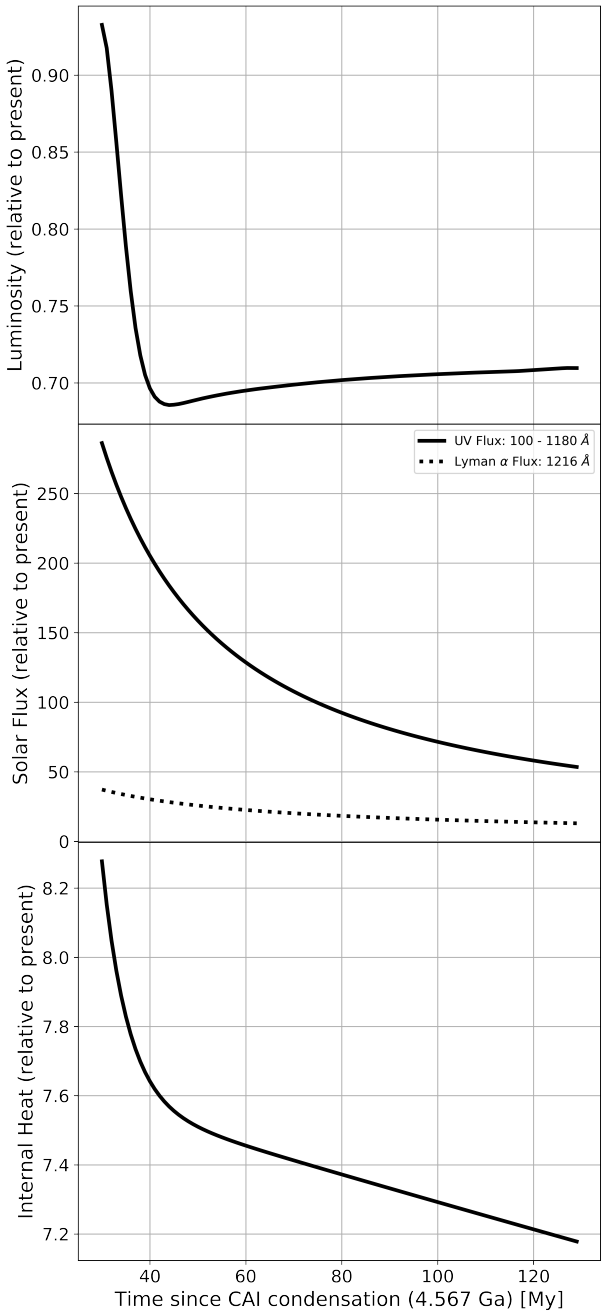

Figure 4.3: (top) Bolometric luminosity of the Sun during the orbital migration period, relative to the present day luminosity. (middle) UV and Lyman-α flux of the Sun during the orbital migration period, relative to the present day UV and Lyman-α fluxes. (bottom) Radiogenic internal heat flux of Pluto during the orbital migration period, relative to the present day rate.

Table 4.1: Values for the abundance C, heat release H, and half-life τ of each of the 7 isotopes used to calculate radiogenic internal heating. The long-lived isotope values are from Robuchon and Nimmo (2011), and the short-lived isotope values are from Castillo-Rogez et al. (2007).

Isotope		C	$\mathcal{H}$	τ
		ppb	W/kg	My
Long-Lived Isotopes	^{238}**U**	19.9	94.65 x 10^{-6}	4468
	^{235}**U**	5.4	568.7 x 10^{-6}	703.81
	^{232}**Th**	38.7	26.38 x 10^{-6}	14030
	^{40}**K**	738	29.17 x 10^{-6}	1277
Short-Lived Isotopes	^{26}**Al**	600	0.146	0.73
	^{60}**Fe**	225	0.074	1.5
	^{53}**Mn**	25.7	0.027	3.7

4.2.3 Radiogenic Internal Heat

Pluto's radiogenic internal heat flux was also different during the time period of the Wild Years. We implement the model of Hussmann et al. (2010) to calculate radiogenic heat production rates as a function of time t:

$$F_{internal} = \frac{M_{core}}{4\pi R_{pluto}^2} \sum_{i=1}^{4} C_i \mathcal{H}_i e^{-ln(2)t/\tau_i} \tag{4.7}$$

where $M_{core} = 8.89$ x 10^{21} kg is the mass of Pluto's core (assuming a radius of 858 km and a density of 3360 kg/m^3) (Keane et al., 2016), $R_{pluto} = 1189$ km is the radius of Pluto, C_i is the abundance of the given isotope based on carbonaceous chondrites, $\mathcal{H}_i$ is the heat release, and τ_i is the half-life for each isotope. The values we assume for this work are shown in Table 4.1.

In Equation 4.7, we divide by the total surface area of Pluto and multiply by the mass of Pluto's core because we assume that all of the heat produced from radioactive decay in the core exits the body as a surface heat flux and none of the heat remains in the body to change its temperature. In this way, the surface heat flux we use is an upper limit to the true heat flux that could result from this radioactive decay. The bottom panel of Figure 4.3 shows the resulting surface heat flux as a function of time, which varies from ∼90 mW/m^2 at the earliest times to 18 mW/m^2 at the end of the Wild Years. The present-day surface heat flux is estimated to be a few mW/m^2

(McKinnon et al., 2016).

4.2.4 Climate Model

To calculate the surface temperature as a function of time, we use the VT3D Model (Young (2012),Young (2017)). Here we summarize the relevant parts of VT3D to this work. VT3D is an energy balance model, finding the temperature that results from the balance between thermal emission, solar insolation, internal heat, thermal conduction, and latent heat of sublimation. For this work, we assume that Pluto is in a "snowball" state: uniformly covered by N_2 ice for the duration of the Wild Years. The timing is highly uncertain for the impact that created Sputnik Planitia, and by assuming uniform N_2 ice coverage we implicitly assume it occurred after the Wild Years ended. We assume the ice has an albedo of 0.8, a thermal inertia of 1225 tiu ("thermal inertia units," equivalent to $\mathrm{Jm^{-2}\ K^{-1}\ s^{1/2}}$), and an emissivity of 0.6 (these values are similar to Reference Case A from Johnson et al. (2021b)). Sputnik Planitia has a Bond albedo of 0.8 - 1 (Buratti et al., 2017), which we took to be a typical albedo for thick N_2 ice deposits. The orbital migrations from Nesvorný (2015) are spaced every 10,000 years. We use the analytic form of VT3D to calculate the nitrogen ice temperature at 20 equally-spaced timesteps in each of these distinct orbits. We found that 20 timesteps was sufficient to resolve the extrema of the orbit, while minimizing computation time. Using the current orbit's semi-major axis and eccentricity, we calculate the absorbed solar insolation at each timestep, subject to the "Faint Young Sun" behavior discussed above, as well as the internal heat flux at the given time. This annual temperature behavior is repeated for as many orbits as can be completed in the 10,000 year macro-timestep, given the current orbital period.

4.3 Migration and Climate Results

4.3.1 Orbital Migration During the Wild Years

Figure 4.4 shows a typical Plutino's path throughout the solar system during the Wild Years, both in eccentricity vs. semi-major axis space (left panel) and in semi-major axis, perihelion,

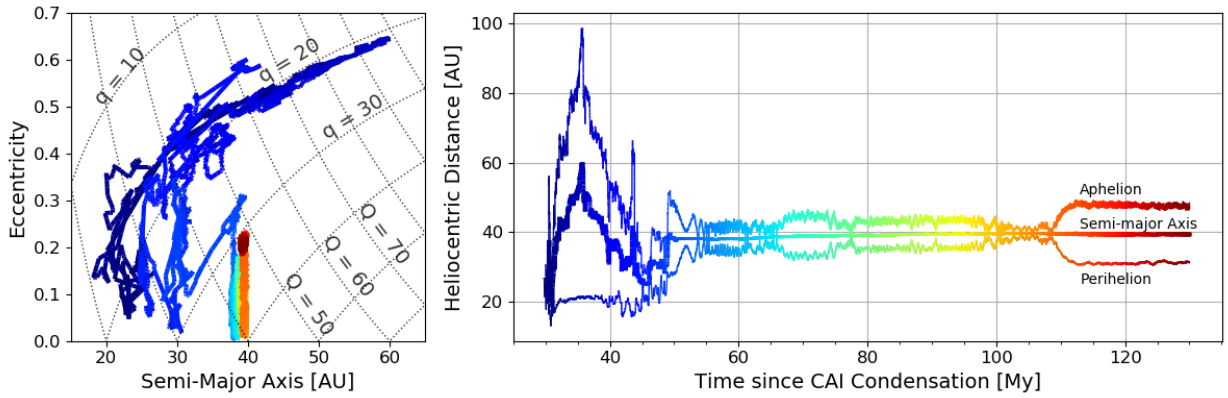

Figure 4.4: Orbital migration for an example Plutino. (left) Eccentricity vs. semi-major axis, with color indicating the time since simulation start (see the right panel for colorscale). Several lines of constant perihelion q and aphelion Q are labeled. (right) Aphelion and perihelion distances vs. time since simulation start.

and aphelion distances as a function of time (right). Typical Plutinos reach minimum heliocentric distances of 15 AU and maximum heliocentric distances of 80 AU, although distances grater than 150 AU are possible for certain Plutinos for short periods of time ($<$ 50,000 years). This chaotic period of rapid orbital evolution is short-lived, typically lasting only 30 My or so, before the Plutino settles down into an orbit near Pluto's present-day orbit. Figure 4.5 shows a whisker plot of time spent in each heliocentric distance bin, showing that the bulk of time (80 My out of the total 100 My simulation) is spent in heliocentric distances between 30 and 50 AU (Pluto's present-day heliocentric distance range). For the remainder of simulation time that the average Plutino spends outside of the 30 - 50 AU range, most of it is spent closer to the Sun. The average Plutino spends 9 My at heliocentric distances less than 30 AU and 1.5 My at heliocentric distances larger than 50 AU.

4.3.2 Climate During the Wild Years

Before discussing volatile loss rates, we start by showing the surface temperature and surface atmospheric pressure experienced by the Plutinos during their orbital migration, to give an idea of the range in general climate characteristics. Figure 4.6B shows the temperature evolution of an

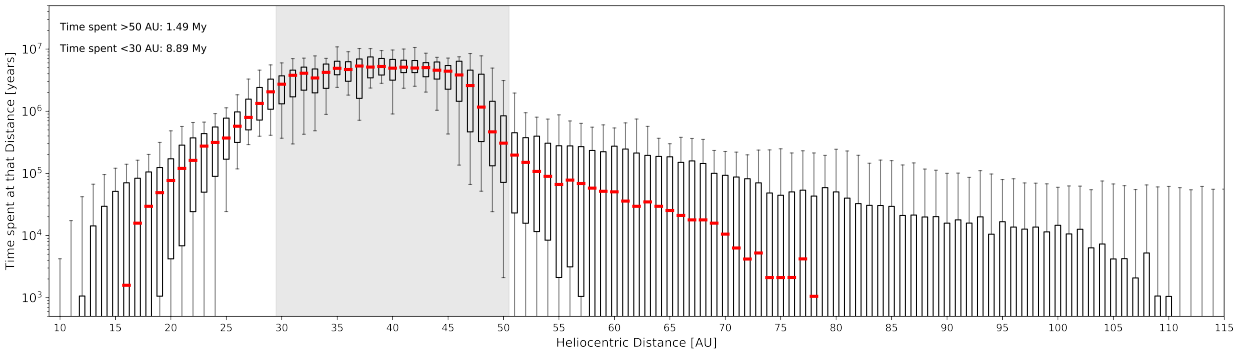

Figure 4.5: Whisker plot showing the time spent at a given heliocentric distance for the ensemble of Plutinos. The red lines are the median value, the boxes encompass the 25th to 75th percentiles, and the whiskers are the 5th and 95th percentiles. For the average Plutino, 80 My out of the 100 My simulation is spent at heliocentric distances between 30 and 50 AU (shaded region), which is Pluto's present-day orbital range.

example Plutino (the same Plutino from Figure 4.4). The surface temperature of the Plutino is calculated using the VT3D model (as discussed above) with uniform spatial coverage of nitrogen ice with an albedo of 0.8, a thermal inertia of 1225 tiu, and an emissivity of 0.6. This particular Plutino begins in an orbit with semi-major axis of 24 AU, but its orbit quickly expands to a semi-major axis near 60 AU, and an eccentricity as high as 0.65, leading to aphelion values near 100 AU. As this orbit expansion occurs, the surface temperature falls from initial values as high as 53 K, to minimum values of 32 K. Subsequently, this Plutino's orbit slowly re-contracts to a final semi-major axis of 39.5 AU (after overshooting slightly), and the surface warms accordingly to a final surface temperature of 35-36 K. This final surface temperature is roughly 1 K cooler than the present-day surface temperature of a Pluto-like object in this orbit with these thermal parameters would be, due primarily to the Faint Young Sun luminosity (see Figure 4.3). The internal heat is higher during this time period relative to the present-day, but the solar luminosity has a larger effect on temperature, because the absorbed insolation at the present day is 57 mW/m^2 versus the present-day internal heat flux of only 2 mW/m^2.

Figure 4.7 shows histograms of the time spent at each temperature for the suite of Plutinos. The red lines indicate the median time spent at that temperature, the boxes encompass the 25th through 75th percentiles, and the whiskers indicate the 5th and 95th percentiles. The shaded region (35-36 K) highlights the temperature range of Plutinos once they reach their final orbit near 40 AU; all the Plutinos spend the majority of the simulation time (tens of My) in this temperature range. For context, models suggest that Pluto's surface temperature might seasonally vary between 33 and 37 K in its present day orbit, depending on assumptions about its present-day nitrogen distribution (Johnson et al., 2021b). If Pluto is assumed to be uniformly-covered in N_2 ice in order to match the assumption made here, its surface temperature would vary between 36 - 37 K over its present-day orbit.

The lowest temperature reached is ∼28 K, typically for less than 10,000 years. The surface pressure in equilibrium with nitrogen ice at 28 K is 4.4 nanobar (Fray and Schmitt, 2009). Johnson et al. (2015) calculated that for a nitrogen atmosphere to have an optical depth of one in UV wave-

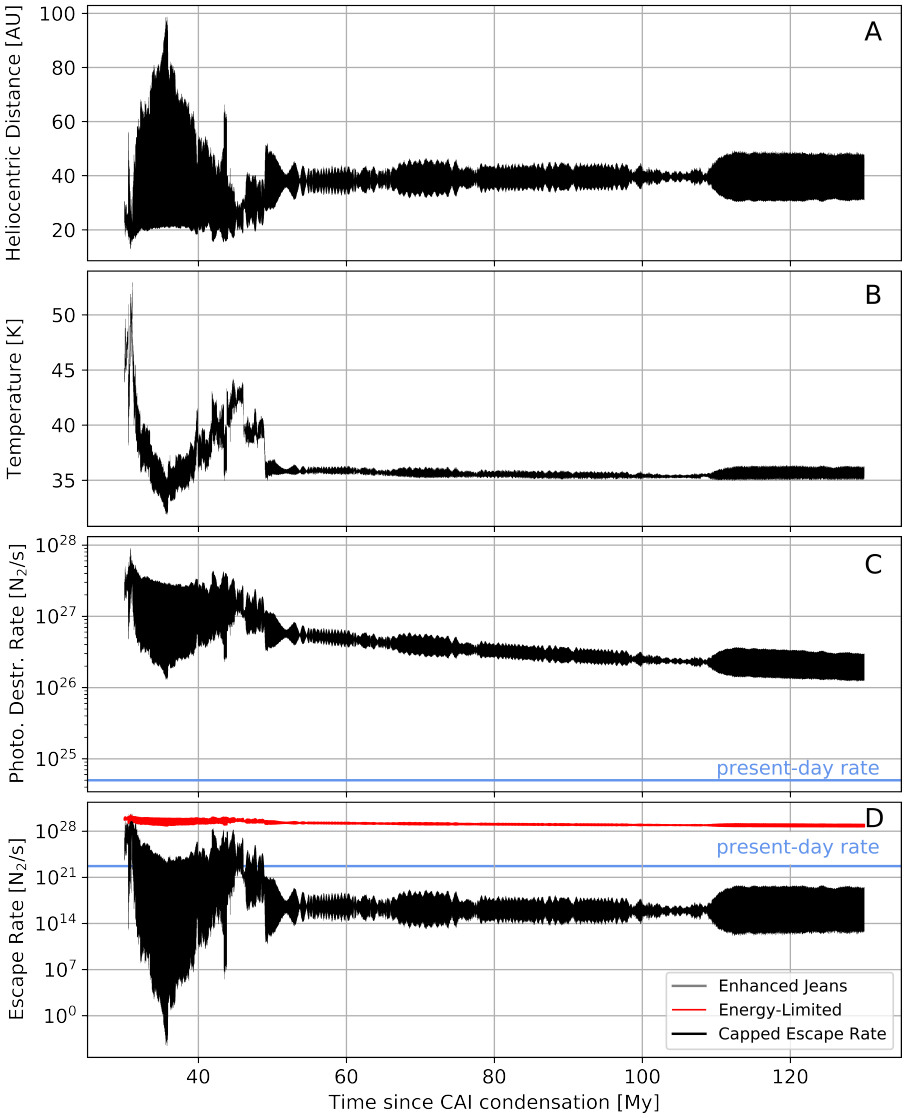

Figure 4.6: **Panel A:** Heliocentric Distance as a function of time for the example Plutino during its orbital migration. See Figure 4.4 for the orbital parameters of this Plutino as a function of time. **Panel B:** Temperature vs. time for an example Plutino during its orbital migration. By $\sim$ 50 My after CAI condensation, the Plutino has been captured into resonance with Neptune and the subsequent orbit changes are minimal, so the surface temperature is nearly constant in time. Seasonal temperature changes are on the order of 1 K, and contribute to the apparent thickness of the line. **Panel C:** Photochemical destruction rate as a function of time for the example Plutino. The present-day photochemical destruction rate from Krasnopolsky (2020) is shown as the horizontal blue line. The general decreasing trend is attributed to the decrease in solar UV output over time, which falls from 250 times the present-day value to only 50 times the present-day value over this time period (Ribas et al., 2005). **Panel D:** Escape rate as a function of time for the example Plutino. The red line shows the energy-limited escape rate. The enhanced Jeans escape rate exceeds the energy-limited value near the start of the Wild years, and only barely. The present-day escape rate (Strobel, 2021) is shown in blue.

lengths, a minimum column abundance N_C = 2 x 10^{18} cm^{-2} is required. This column abundance implies a surface pressure of N_C x m_{N2} x g_{surf} = 5.8 nanobar (implying a surface temperature of 28.2 K, assuming vapor pressure equilibrium), shown as the blue dotted line in Figure 4.7. So at the very lowest temperatures, it is possible for UV rays to reach all the way to the surface of the Plutinos, albeit only for 10,000 or fewer years cumulative during the Wild Years period.

The highest temperature reached by the median Plutino is around 48 K, corresponding to a Mars-like surface pressure of 2.1 millibar. The Plutinos are at this temperature for less than 10^5 years, typically. The triple point for N_2 is 63 K (Fray and Schmitt, 2009), so liquid N_2 is never stable on Pluto's surface even at the hottest points during the Wild Years. Stern et al. (2017) proposed that the observed dendritic valleys on Pluto could have been carved by liquids, and identifies Alconis Lacus has a potential paleo-lake, but our results show that temperatures likely do not get high enough to support these hypotheses. We discuss the alternative possibility that glaciers could have carved the valleys in Section 4.7.

4.4 Photochemical Destruction

One loss mechanism for nitrogen from Pluto's atmosphere is the irreversible photochemical destruction of N_2 in the atmosphere, which primarily creates solid-phase daughter products that fall out of the atmosphere onto the surface , although some escape to space is possible as well. Krasnopolsky (2020) used a photochemical model to calculate the loss of atmospheric N_2 due to photochemical destruction at the time of the *New Horizons* flyby of 37 g cm^{-2} Gy^{-1}, equivalent to 5 x 10^{24} N_2/s, which is roughly 100 times greater than the atmospheric escape rate at the time of the flyby (Strobel, 2021). The dominant daughter product is HCN.

4.4.1 Photochemical Destruction Model

In order to estimate the photochemical destruction rate during the Wild Years, we scale the present-day rate from Krasnopolsky (2020) based on both solar output and heliocentric distance. The "present-day" rate is based on the *New Horizons* flyby conditions, which occurred when Pluto

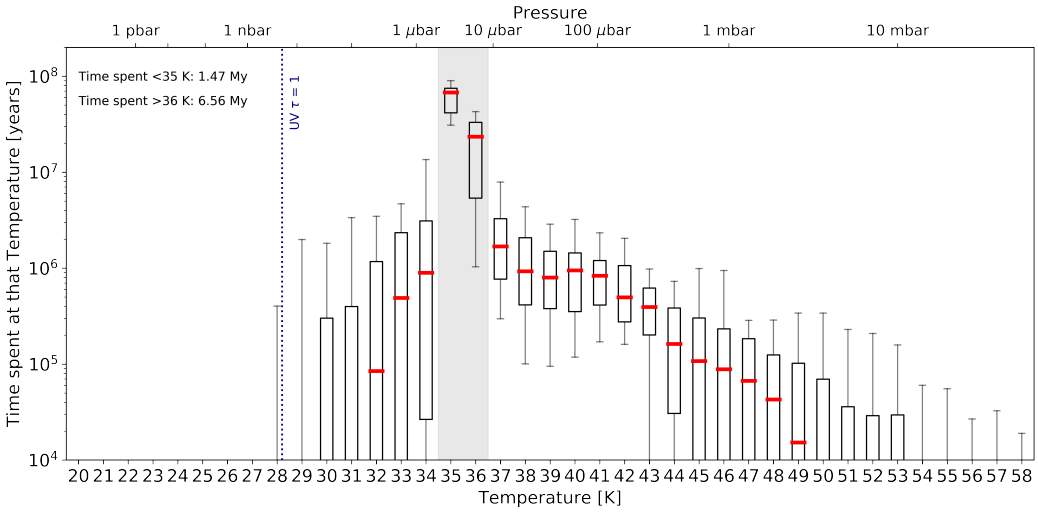

Figure 4.7: Histograms of the time spent at a given temperature. The red lines are the median value, the boxes encompass the 25th to 75th percentiles, and the whiskers are the 5th and 95th percentiles. For temperature with no red median line, the median Plutino spend zero time at that temperature. The shaded region (35-36 K) indicates the temperatures that Plutinos are at once they reach their final orbits near 40 AU. The top axes shows the vapor pressure that is in equilibrium with nitrogen ice at the given temperature. All the Plutinos spend the bulk of their time (tens of My) at 35-36 K.

was at a heliocentric distance of 32.9 AU. The photochemical destruction rate $F_{photochem}$ should depend on inverse square of heliocentric distance h, thus we can write the relation:

$$F_{photochem}(t,h) \propto \left(\frac{32.9AU}{h}\right)^2 \tag{4.8}$$

Additionally, the photochemical destruction rate will depend on the solar output at the given time. As discussed above, the solar output was very different during the Wild Years as compared to the present-day output. N_2 is photochemically destroyed by radiation at UV wavelengths, so we scale the present-day rate based on the Ribas et al. (2005) model of early stellar output. For the dependence on solar output, we can write the following relation:

$$F_{photochem}(t,h) \propto E_{UV}(t) \tag{4.9}$$

where $E_{UV}(t)$ is the UV enhancement at a given time (relative to the present-day solar output) and is calculated using Equation 4.4 from Section 4.2. Lyman-α is not energetic enough to break the bond in a molecule of N_2, so we do not account for the early Sun enhancement in Lyman-α for the photochemical destruction.

By combining the two preceding relationships, we can write an equation for the photochemical destruction rate of N_2 in Pluto's atmosphere as a function of both time and heliocentric distance during the Wild Years:

$$F_{photochem}(t,h) = E_{UV}(t)\left(\frac{32.9AU}{h}\right)^2 F_{photochem}(t_{present}, 32.9AU) \tag{4.10}$$

where $F_{photochem}(t_{present}, 32.9AU) = 5$ x 10^{24} N_2/s is the photochemical destruction rate calculated for Pluto's conditions at the time of the *New Horizons* flyby in 2015 (Krasnopolsky, 2020).

4.4.2 Photochemical Destruction Results

Panel C in Figure 4.6 shows the calculated photochemical destruction rate as a function of time for the example Plutino. For reference, the present-day photochemical destruction rate

(Krasnopolsky, 2020) is shown as the blue line; note that the calculated photochemical destruction rate during the Wild Years is always at least an order of magnitude higher than the present-day rate, primarily due to the enhanced early solar UV output. The photochemical destruction rate generally decreases with time, following the decreasing trend of the solar UV flux. The solar UV output falls from over 250 times the present-day value to just 50 times the present-day value during the Wild Years. The photochemical destruction rate is near 3 x 10^{27} N_2/s at the start of the simulation time, and falls by an order of magnitude to 2 x 10^{26} N_2/s by the end of the simulation, due to the decreasing solar UV output and also due to the orbital migration from an orbit with a semi-major axis of 24 AU to one with a semi-major axis of 39 AU.

The total photochemical destruction of N_2 during the Wild Years for this example Plutino amounts to 387 cm GEL, and the remainder of the age of the solar system adds another 857 cm GEL. The median values for the entire ensemble are shown in Table 4.2, which are very similar to this example Plutino's amounts. The Wild Years are only 100 My long, accounting for only 2% of the age of the solar system, but we calculate that roughly 30% of the total photochemical destruction of N_2 occurred during the Wild Years. This can primarily be attributed to the highly enhanced solar UV output early in solar system history. Pluto's present-day atmosphere, if condensed onto the surface, amounts to 0.2 cm GEL, and the ice sheet inside of Sputnik Planitia basin is estimated to contain 44-440 m GEL of nitrogen ice (McKinnon et al., 2016; Trowbridge et al., 2016; Johnson et al., 2021a). The photochemical destruction amounts we calculate here fall in between these two values, equivalent to the destruction of more than 6000 present-day Pluto atmospheres worth of N_2, which is 3 - 30 % of the amount of nitrogen contained within Sputnik Planitia.

4.5 Impact Delivery and Erosion

The next loss mechanism for nitrogen that we investigate here is impact delivery and removal. Impacts can deliver volatiles to Pluto's surface (or Plutinos' surfaces) if the impactors contain volatiles and those volatiles are retained after the impact, either as fragments on the surface or as gas in the atmosphere. However, impacts can also remove volatiles, by injecting energy into the

atmosphere which allows particles to escape. The size and frequency of impactors determines which of these processes win, and if impactors are a net source or a net loss of volatiles from a body.

Planetary surfaces record their impact history in the form of craters. There are complications, including that new craters can 'erase' or overprint old craters on heavily-cratered surfaces, geologic activity, such as volcanism, can obscure existing craters by resurfacing, and impacts can occur before a planetary surface has solidified and become capable of recording craters. Morbidelli et al. (2021) combine crater counting techniques and a dynamical model of the solar system in order to estimate the total number of impacts onto Pluto throughout its history, accounting for these complicating factors. They define 1 ICR ("Integrated Current impact Rate") to be the total number of impactors calculated assuming the present-day impact rate applied for the past 4.5 Gy. However, the impact rate was higher in the past, such that Pluto actually experienced 4 ICRs worth of impactors in the past 4.5 Gy according to Morbidelli et al. (2021). Assuming a size frequency distribution of $N(> d) \propto d^{-2.1}$ (as in Morbidelli et al. (2021)), where d is the impactor diameter, and an impactor density of 1000 kg m^{-3}, 4 ICRs corresponds to 1.16 x 10^{18} kg of material delivered to Pluto. There is some evidence that large KBOs (>50 km) may follow a steeper size frequency distribution Fraser et al. (e.g., 2014). However, as seen in the bottom panel of Figure 4.8, impacts that large are already rare in our random sample; a steeper slope would reduce the likelihood of one occurring even further. Additionally, as seen in the top panel, impacts of that size contribute a net delivery of volatiles, but remove the same amount as a smaller impactor, since all impactors with $r_{cap} < r < r_{gi}$ remove the same amount of atmosphere. Thus, the exact size frequency distribution slope used for large KBOs does not have a significant impact on the results discussed here.

We assume that all of the impactor mass is retained by Pluto after the impact. Considering only nitrogen, and assuming each impactor is 2% nitrogen in all forms by mass (Mumma and Charnley, 2011; Singer and Stern, 2015), the total delivery of nitrogen is 2.32 x 10^{16} kg, equivalent to 1000 times the mass of Pluto's present-day atmosphere or 1% of the mass of nitrogen thought to be contained in Sputnik Planitia.

There are many models of how impacts remove gas from an atmosphere. In this work, we

follow the framework of Schlichting et al. (2015), but adapt their models from Earth to Pluto parameters. Schlichting et al. (2015) define four impactor size regimes:

(1) $r < r_{min}$: Impactors that are too small to remove any atmosphere

(2) $r_{min} < r < r_{cap}$: Impactors that can remove some of the atmosphere local to the impact site

(3) $r_{cap} < r < r_{gi}$: Impactors that remove all of the atmosphere local to the impact site, meaning all of the atmosphere above the tangent plane to the impact site

(4) $r > r_{gi}$: Giant Impactors capable of removing all of the local atmosphere and some (or all) of the non-local atmosphere material through ground-shocks

The equations for the impactor radii r_{min}, r_{cap}, and r_{gi} are given below:

$$r_{min} = \left(\frac{3\rho_{atmo}}{\rho_{imp}}\right)^{1/3} H \tag{4.11}$$

$$r_{cap} = \left(\frac{3\sqrt{2\pi}\rho_{atmo}}{4\rho_{imp}}\right)^{1/3} \sqrt{HR_{pluto}} \tag{4.12}$$

$$r_{gi} = \left(2HR_{pluto}^2\right)^{1/3} \tag{4.13}$$

where ρ_{atmo} is the density of Pluto's atmosphere at the surface, $\rho_{imp} = 1000$ kg/m^3 is the impactor density, H is the atmosphere scale height at the surface, and $R_{pluto} = 1189$ km is Pluto's radius. For Pluto's present-day atmosphere, where ρ_{atmo} is 10^{-4} kg/m^3, $H = 20$ km, and $T_u = 65$ K, these impactor size regimes are $r_{min} = 0.13$ km, $r_{cap} = 0.88$ km, and $r_{gi} = 384$ km.

4.5.1 Impact Delivery and Erosion Model

In order to calculate the net delivery (or removal) of N_2 from impacts, we do the following steps:

(1) Generate an impactor with a randomly-distributed radius r, following a size frequency distribution proportional to $r^{-2.1}$.

(2) Calculate the N_2 mass delivered by the impactor:

$$m_{deliv} = \frac{4}{3}\pi r^3 \rho_{imp} f_{N2} \tag{4.14}$$

where f_{N2} is the N_2 mass fraction of the impactor, assumed to be 2%. There is an implicit assumption that all of the N_2 is retained on Pluto's surface after the impact.

(3) Calculate the atmospheric N_2 mass removed by the impactor, which is dependent on its size r and also the parameters of Pluto's atmosphere at the given time.

$$m_{remov} = \left\{ \begin{array}{cc} 0 & \text{if } r < r_{min} \\ \frac{m_{imp} r_{min}}{2r}(1 - (\frac{r_{min}}{r})^2) & \text{if } r_{min} \leq r < r_{cap} \\ 2\pi \rho_{atmo} H^2 R_{pluto} & \text{if } r_{cap} \leq r < r_{gi} \\ (0.4x + 1.4x^2 - 0.8x^3) M_{atmo} & \text{if } r \geq r_{gi} \end{array} \right\} \tag{4.15}$$

$$\text{where} \quad x = \frac{v_{imp} m_{imp}}{v_{esc} M_{pluto}} \tag{4.16}$$

where v_{imp} and v_{esc} are the impact velocity and Pluto's escape velocity, and m_{imp}, M_{pluto}, and M_{atmo} are the impactor mass, Pluto's mass, and the mass of the atmosphere. We use an impactor velocity of 2 km/s (Zahnle et al., 2003; Dell'Oro et al., 2013). The escape velocity from Pluto's surface can be calculated $v_{esc} = \sqrt{2gR_{pluto}} = 1.2$ km/s. The mass of Pluto is 1.31 x 10^{22} kg.

We then repeat this process of generating randomly-sized impactors and track amount of N_2 they deliver and remove until the total mass of impactors reaches 2 ICRs. Given the random nature of the impactor sizes, we repeat this entire process 100 times and analyze the resulting distribution.

4.5.2 Impact Delivery and Erosion Results

According to Morbidelli et al. (2021), Pluto should have received 2 ICRs worth of impacting material in the past 4 Gy, during which time Pluto was in its current orbit and its atmosphere was likely approximately equivalent to the present-day atmosphere. At 4 Ga, the Sun's bolometric luminosity was roughly 75% of the present-day value (Bressan et al., 2012), so Pluto's atmosphere

would have been slightly cooler and more compact during this time period, but we assume the atmosphere was constant in time. Using Pluto's present-day atmospheric parameters ($\rho_{atmo} = 10^{-4}$ kg/m^3 and $H = 20$ km), we estimate that 2 ICRs (equivalent to 5.8 x 10^{17} kg of impacting material) will deliver -70 cm GEL, but they will also remove 12 cm GEL of atmosphere, resulting in a net delivery of -58 cm GEL of N_2. Note that, throughout this section, a negative sign means a net delivery of N_2, while a positive sign is reserved for a net removal or loss of N_2, to be consistent with the loss mechanisms discussed elsewhere in the paper.

Figure 4.8 shows the mass of N_2 delivered and removed by an impactor of a given size. From this, one can see that there is only a narrow size range in which an impactor is capable of removing more N_2 than it delivers. For an atmosphere like Pluto's present-day one, impactors between roughly 100 m and 2 km remove more atmospheric N_2 than they deliver. Impactors larger than 2 km, although significantly less likely to hit Pluto, deliver orders of magnitude more N_2 than they remove. The net effect is that impact delivery outstrips impact removal of N_2, resulting in a net delivery of -29 cm GEL per ICR, for a present-day Pluto-like atmosphere.

For the time period between the start of the giant planet instability and 4 Ga, Morbidelli et al. (2021) estimate that the Pluto system received 2 ICRs of impacting material as well, for a total of 4 ICRs between the start of the instability and the present-day. This is a cumulative, integrated estimation, and the exact timing of when an impact of a given size would have occurred is not known. Thus, the atmospheric parameters at the time of each impact are also not known. Instead, we analyze three limiting cases of possible atmospheres during this time period: (1) the present-day atmosphere, (2) the coldest atmosphere experienced by the example Plutino, with $\rho_{atmo} = 10^{-6}$ kg/m^3, $H = 13$ km, and $T_u = 27$ K, and (3) the warmest atmosphere experienced by the example Plutino, with $\rho_{atmo} = 10^{-2}$ kg/m^3, $H = 60$ km, and $T_u = 124$ K. We assume these atmosphere parameters are constant during the entire time period between the start of the giant planet instability and 4 Ga.

In scenario (1), Pluto experiences 4 ICRs of impacts with its present-day atmosphere. According to our model, these impacts deliver -105 cm GEL of N_2 and remove 24 cm GEL, for a net

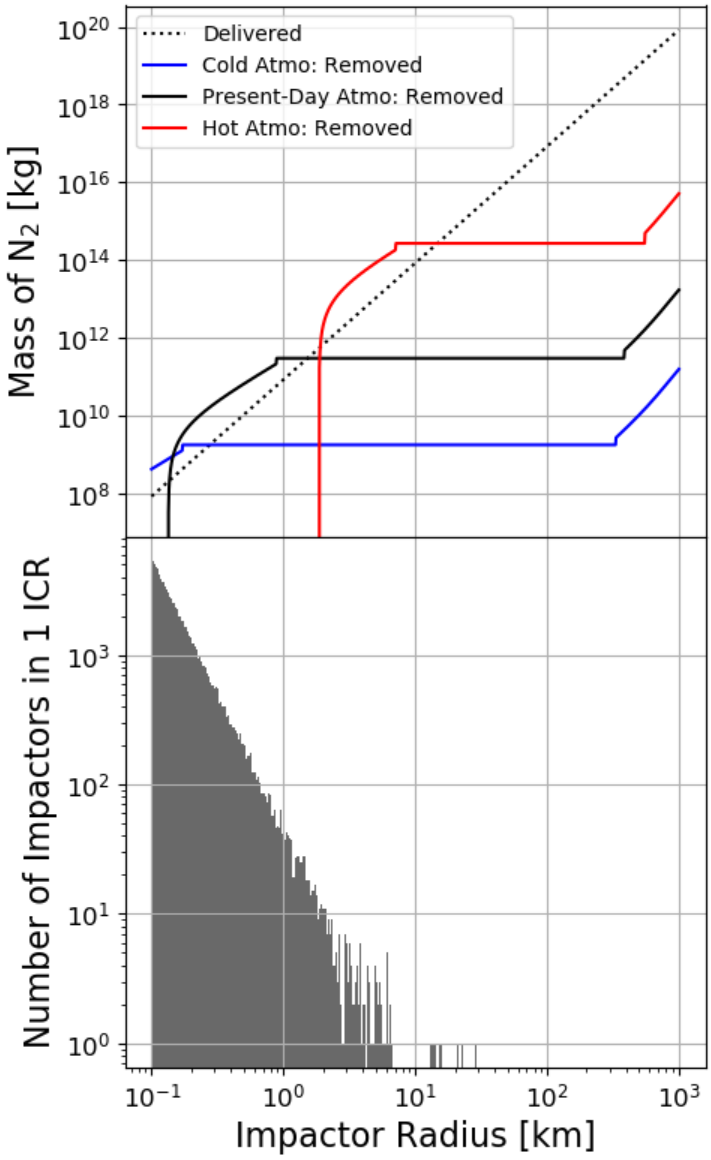

Figure 4.8: (top) Mass delivered (dotted line) or removed (solid line) by a single impactor as a function of impactor size. The red line corresponds to the amount removed from a hot atmosphere (T_u = 124 K, H_{surf} = 60 km, ρ_{surf} = 10^{-2} kg/m^3), black to Pluto's present-day atmosphere (T_u = 65 K, H_{surf} = 20 km, ρ_{surf} = 10^{-4} kg/m^3), and blue to a cold atmosphere (T_u = 27 K, H_{surf} = 13 km, ρ_{surf} = 10^{-6} kg/m^3). (bottom) Histogram showing the number of impactors of a given size in a random sample equivalent to 1 ICR.

change of -81 cm GEL. 30% of this amount occurs in the past 4 Gy, with the remainder being delivered in the much shorter period of time between the start of the instability 4.537 Gy ago and 4 Gy ago.

In scenario (2), we assume Pluto had a colder, more compact atmosphere between 4.537 and 4 Gy ago and received 2 ICRs, and then had its present-day atmosphere from 4 Gy ago to the present and received 2 ICRs of impacts, for a total of 4 ICRs. We predict a net change of about -92 cm GEL of N_2, split into -69 cm GEL during the cold period and -23 cm GEL during the present-day atmosphere period. As shown by the blue curve Figure 4.8, impactors greater than $\sim$ 0.3 km radius will deliver more N_2 than they remove. In fact, 2 ICRs worth of impactors only remove a few cm GEL of atmospheric material. In the present-day atmosphere and in the cold, compact atmosphere, impact delivery always exceeds impact removal.

In scenario (3), in which we assume Pluto had a very warm extended atmosphere between 4.537 and 4 Gy ago, we predict a net change of -8 cm GEL N_2 delivered between 4.537 Gy ago and the present. In the warm, extended atmosphere, it is relatively easier for impacts to remove more atmosphere than they deliver, compared to the colder atmospheres discussed above. It is possible for there to be a net removal (rather than a net delivery) for the time period immediately after the giant planet instability in the hot atmosphere case, with the median value being 15 cm GEL removed. However, over the full time range, the net effect is still a delivery of N_2 of -8 cm GEL.

Due to the higher rate of impacts in the aftermath of the giant planet instability, a significant fraction of the impact delivery and erosion occurs during the relatively short 100 My Wild Years. Estimates of volatile delivery or related quantities that use the present-day impact rate on Pluto and ignore the Wild Years time period will be significant underestimates as a result.

4.6 Atmospheric Jeans Escape

The final loss mechanism for N_2 investigated here is atmospheric escape, via an enhanced Jeans escape process. At the time of the *New Horizons* flyby, Pluto's atmospheric structure implied an escape rate for N_2 of 3 - 8 x 10^{22} molecules/s, while CH_4 escaped faster at 4 - 8 x 10^{25} molecules/s

(Young et al., 2018). These escape rates were orders of magnitude lower than pre-flyby estimates.

Particles escape from a level of the atmosphere known as the exobase. Well below the exobase, the atmosphere can be treated as a fluid, but above a transition region near the exobase, the atmosphere becomes collision-less andvt the mean-free-path of a particle exceeds the scale height. This means that if a particle is travelling upwards at the escape velocity from the body, then at the exobase it is as likely to escape from the atmosphere as it is to collide with another particle. In the following section, we describe our scheme for estimating the atmospheric structure, including the height of the exobase, of Pluto's atmosphere during the Wild Years in order to estimate the escape rate.

4.6.1 Enhanced Jeans Escape Model

We use an enhanced-Jeans escape framework (Zhu et al., 2014; Strobel, 2021), as follows:

(1) We begin by estimating the upper atmospheric temperature. During the *New Horizons* flyby when Pluto was at 32.9 AU, the upper atmosphere, above the 10^{-5}Pa level, was roughly isothermal at T_{upper} = 65 K, due to efficient thermal conduction. Additionally, below the 10^{-5} Pa pressure level in Pluto's current atmosphere, it was proposed that the haze radiative heating and cooling dominate the energy balance and control the temperature profile (Zhang et al., 2017; Wan et al., 2021). For simplicity, we assume the haze particles in the atmosphere also control the temperature below this pressure level throughout Pluto's history. We further assume that both haze heating and cooling rates roughly scale with the haze mixing ratio, thus the temperature in the haze-dominant lower region is not very sensitive to the haze mixing ratio nor the surface methane mixing ratio. Thus, in our escape model we approximate the atmosphere as fully isothermal, from just above the surface through to the exobase.

(2) To estimate how T_{upper} varies with heliocentric distance, we create a scaling from Titan, which also has a hazy, nitrogen-dominated atmosphere. Using Titan's atmospheric tem-

perature of 160 K at the 10^{-5} Pa level (Fulchignoni et al., 2005) and its semi-major axis of 9.5 AU in addition to the values for Pluto, we derive a power law of $T_{upper} \propto h^{-0.725}$, where h is the heliocentric distance.

(3) The relation for T_{upper} and heliocentric distance derived above needs to be adjusted to account for the variable output of the early Sun. Incident solar flux drops off as heliocentric distance to the inverse square power. This is equivalent to saying the heliocentric distance is proportional to the incident flux to the -1/2 power. Thus, we can relate T_{upper} to the incident solar flux as:

$$T_{upper} \propto h^{-0.725} = (F_{bolo}^{-1/2})^{-0.725} = F^{0.3625} \tag{4.17}$$

where F_{bolo} is incident bolometric solar flux at a given heliocentric distance. In using the bolometric flux here, we are assuming that the atmospheric heating, namely the haze heating and cooling, is dominated by visible wavelength solar radiation. In the present-day Sun's output, the bolometric flux is 13,000 times higher than the UV flux (100 - 1180 Å) alone, so any UV haze heating is negligible. During the Wild Years this drops to only 100 times higher, so UV heating could possibly be non-negligible. However, laboratory studies of Pluto's haze do not extend into UV wavelengths, so rather than make an unconstrained guess as to the haze absorption in UV wavelengths, we assume that haze UV heating and cooling is negligible even during the enhanced early Sun. Thus, we estimate T_{upper} at any time and heliocentric distance as follows:

$$T_{upper}(t,h) = T_{upper,present}\left(\frac{F_{bolo}(t,h)}{F(t_{present}, 32.9AU)}\right)^{0.3625} \tag{4.18}$$

where $F_{bolo}(t,h)$ is calculated using the PARSEC model described above.

(4) The next step is to estimate the altitude z_{upper} of the 10^{-5} Pa level. The atmosphere is assumed to be isothermal and hydrostatic, but the gravitational acceleration is not constant with altitude (it varies by a factor of 2 or more between the surface and the upper

atmosphere). Thus, the altitude z of a given pressure level P and temperature T is:

$$z = R_{pluto}\left(\frac{k_B T}{m_{N2} g_{surf} R_{pluto}} \log\left(\frac{P}{P_{surf}}\right) + 1\right)^{-1} - R_{pluto} \tag{4.19}$$

where g_{surf} and P_{surf} are the gravitational acceleration and atmospheric pressure at the surface, k_B is Boltzmann's constant, and m_{N2} is the mass of a nitrogen molecule. For the atmospheric conditions at the time of the flyby, assuming an isothermal atmosphere leads to a prediction of 630 km altitude for z_u, compared with the observed altitude of 700 km for the 10^{-5} Pa level.

(5) Given P_{upper} and T_{upper}, we use the ideal gas law to calculate the column density N_{upper} at altitude z_{upper}. Then, we find the column density profile at $z > z_{upper}$ assuming the atmosphere is isothermal above this altitude and again including an altitude-dependent gravitational acceleration $g(z_{upper})$:

$$N(z) = N_{upper} exp\left(\frac{m_{N2} g(z_{upper})(R_{pluto} + z_{upper})}{k_B T_{upper}} \frac{z - z_{upper}}{R_{pluto} + z}\right), \quad z > z_{upper} \tag{4.20}$$

Using this column density, we calculate the mean free path of a nitrogen molecule:

$$l_{mfp}(z) = \frac{1}{N(z)\sigma} \tag{4.21}$$

where σ is the collisional cross section of a nitrogen molecule. We use σ = 3 x 10^{-19} m^2 Strobel (2021). The exobase is classically defined as the altitude where the mean free path and the scale height are equal (Strobel, 2021). The scale height is given by:

$$H(z) = \frac{k_B T_{upper}}{m_{N2} g(z)} \tag{4.22}$$

To find the exobase altitude z_{exo}, we set $l_{mfp}(z_{exo}) = H(z_{exo})$.

(6) Next we calculate the Jeans escape rate at the exobase:

$$F_{Jeans} = 4\pi(R_{pluto} + z_{exo})^2 N(z_{exo}) \sqrt{\frac{k_B T_{upper}}{2\pi m_{N2}}} e^{-\lambda_{exo}}(1 + \lambda_{exo}) \tag{4.23}$$

where λ_{exo} is the Jeans parameter at the exobase, given by

$$\lambda_{exo} = \frac{G M_{pluto} m_{N2}}{k_B T_{upper}(R_{pluto} + z_{exo})} \tag{4.24}$$

where G is the universal gravitational constant and M_{pluto} = 1.31 x 10^{22} kg is the mass of Pluto. Recent numerical models have shown that molecules actually escape at a slightly different rate relative to the Jeans rate at the exobase. We adopt the enhancement model presented in Strobel (2021) based on the work of Zhu et al. (2014):

$$\Gamma(\lambda_{exo}) = e^{4.086446916-0.870018743\lambda_{exo}} + e^{0.63554463-0.019922313\lambda_{exo}} \tag{4.25}$$

where we have corrected a small typo in the equation from Strobel (2021). For the range of Jeans parameters experienced by the Plutinos ($\lambda_{exo} \sim$ 9 - 37), the enhancement factor Γ ranges from 1.6 to 0.9. The net escape rate is then

$$F_{esc} = \Gamma(\lambda_{exo}) F_{jeans} \tag{4.26}$$

4.6.1.1 Energy-Limited Escape Model

Particles cannot escape at a rate faster than the incident energy driving their escape arrives at the atmosphere. Thus, the maximum realistic escape rate is limited by the incident energy. To estimate this energy-limited escape rate, we use the model of Johnson et al. (2015). While it was developed to estimate escape rates from various KBOs by scaling from Pluto, we modify it to calculate escape rates from Pluto (or Plutinos) at various times throughout the history of the solar system. The relationship we use is as follows:

$$F_{esc}(h,t) = E_{UV+Ly\alpha} \left[\left(\frac{32.9AU}{h} \right)^2 + 0.09 \right] F_{esc,present} \tag{4.27}$$

where $E_{UV+Ly\alpha}$ is the flux enhancement, accounting for both 100 - 1180 ÅUV radiation and also Lyman-α radiation, h is the heliocentric distance (in AU) at time t, and $F_{esc,present}$ is the present-day energy-limited escape rate from Pluto, 2.6 x 10^{27} N_2/s (Johnson et al., 2015). The 0.09 term in the parentheses is due to the background flux from other stars.

For each Plutino migration from Nesvorný (2015), we know the orbital parameters at timesteps of 10,000 years. For each of these unique sets of orbital parameters, we calculate the heliocentric distance at 20 points per period, which is enough timesteps to resolve the perihelion and aphelion. We then repeat this heliocentric distance as a function of time array for as many orbits as

the Plutino completes in 10,000 years. We assume the Plutino restarts at perihelion each time the orbital parameters change. This technique gives us heliocentric distance as a function of time (albeit unevenly-spaced in time) for the Plutino during its 100 My migration ('Wild Years'). Using this and the solar evolution model, we can calculate escape rate as a function of time or the total amount of N_2 that escapes during the Wild Years and throughout the entire 4.56 Gy history of the solar system.

4.6.2 Atmospheric Jeans Escape Results

Figure 4.6D shows the estimated escape rate as a function of time for the example Plutino. At times when the calculated enhanced Jeans escape rate is greater than the energy-limited escape rate, we cap the escape rate at the energy-limited value (red line), although this rarely occurs. Integrating this capped escape rate over the length of the Wild Years yields a total nitrogen loss of 757 cm GEL for this Plutino, and the median loss of nitrogen from the ensemble of 53 Plutinos is 98 cm GEL (see Table 4.2). The range of escape losses is much larger than the range for the other loss mechanisms studied here. The middle 50% of the ensemble of Plutinos loses between 1 and 1000 cm GEL of N_2, as shown in Figure 4.9. The enhanced Jeans escape rate is highly dependent on the incident flux, so even a short period of time spent closer to the Sun than the average Plutino can have a large effect on the total N_2 loss.

In Figure 4.6, it is clear that at the end of the simulated time period, the escape rate is still far lower than the present-day rate. The solar luminosity is 71% of the present-day value at the end of the Wild Years, resulting in an atmosphere that is colder and more compact than Pluto's present-day atmosphere. The upper atmosphere temperature T_u is 47 K, versus 65 K for present-day Pluto, and the exobase altitude z_{exo} is 550 km, compared with 1700 km. As a result, the Jeans parameter (that is, the ratio of gravitational potential energy to thermal kinetic energy) at the exobase is 35 at the end of the Wild Years, versus 16 for present-day Pluto, meaning that the atmosphere is much more tightly bound to Pluto and thus escape is much slower.

Using this same framework for estimating atmospheric escape, we calculate that the total

nitrogen loss during the time from the end of the Wild Years to the present day is 2.35 cm GEL. Thus, the total nitrogen loss due to atmospheric Jeans escape is on the order of 100 cm GEL, which is a negligible amount relative to the observed nitrogen inventory on Pluto in the present-day (i.e. the 44 - 440 m GEL of nitrogen contained within Sputnik Planitia). Thus, atmospheric escape via the enhanced Jeans regime is not a significant loss mechanism for nitrogen from Pluto, at the present time nor during the Wild Years.

Assuming instead that escape proceeded at the energy-limited rate throughout the entire simulation time or the age of the solar system gives an upper limit to the total amount of N_2 loss via atmospheric escape. During the Wild Years, we estimate that 1.2 km GEL would escape, using the energy-limited escape rate rather than the enhanced Jeans rate. Over the age of the solar system (including the Wild Years), the total amount lost would be 3.9 km GEL, which is similar in magnitude to the amount of N_2 ice contained within Sputnik Planitia. Only in this extreme case could atmospheric escape be a significant loss of N_2 from Pluto, relative to the known present-day inventory.

4.7 Discussion

4.7.1 Comparison of Photochemical Destruction, Impact Erosion, and Jeans Escape

Sections 4.4 (Photochemical Destruction), 4.5 (Impact Erosion and Delivery), and 4.6 (Atmospheric Jeans Escape) are presented in order of decreasing significance to the nitrogen budget on Pluto. Photochemical destruction could remove up to 1270 cm GEL of N_2, the net effect from impacts could deliver up to -90 cm GEL of N_2, and atmospheric Jeans escape could remove up to 100 cm GEL over the age of the solar system. These values are summarized in Table 4.2 and shown graphically in Figure 4.9. During the Wild Years, photochemical destruction is largest loss of N_2, followed by atmospheric escape and then impact erosion.

Sputnik Planitia, which likely contains the bulk of Pluto's present-day nitrogen inventory,

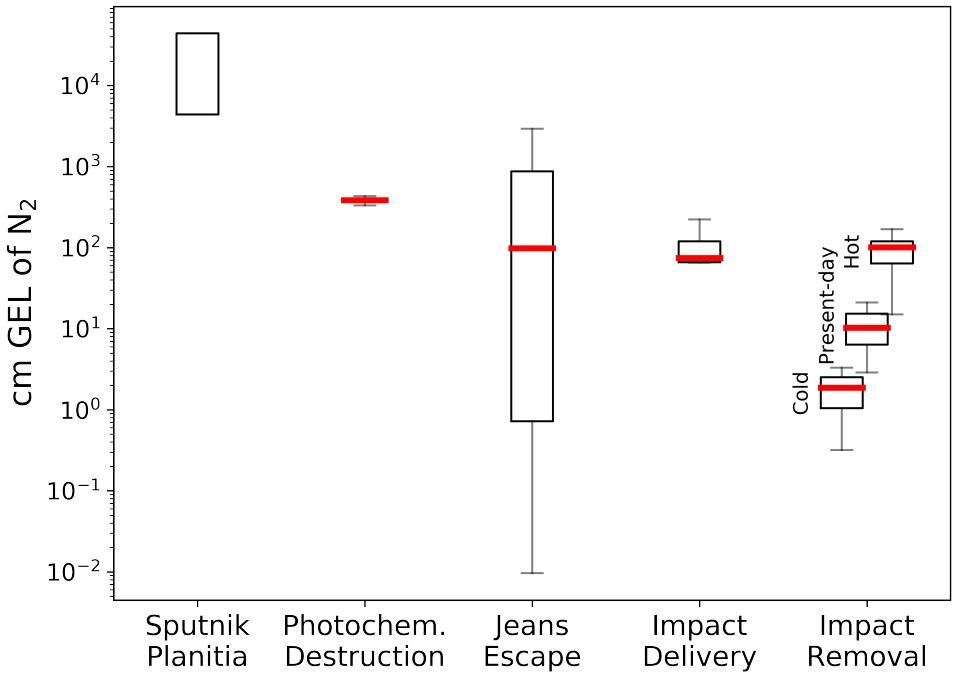

Figure 4.9: Whisker plot showing the amount of N_2 in Sputnik Planitia, the amount of N_2 lost during the Wild Years via photochemical destruction, atmospheric Jeans escape, and impact erosion, and the amount delivered by impacts. The red lines are the median value, from the ensemble of 53 Plutinos for photochemical destruction and atmospheric escape and from the 100 random samples drawn for the impact escape and delivery. The boxes encompass the 25th to 75th percentiles, and the whiskers are the 5th and 95th percentiles.

Table 4.2: Summary of the nitrogen loss, in cm GEL, resulting from each of the loss mechanisms investigated here.

Loss Mechanism		**During Wild Years** (30 - 130 My after CAIs)	**Age of Solar System** (130 My after CAIs - present)	**Total**
Photochemical Destruction		385^{+13}_{-23} cm GEL	885 cm GEL	1270 cm GEL
Impact Delivery		-70^{+49}_{-4} cm GEL	-70^{+49}_{-4} cm GEL	-140 cm GEL
Impact Removal	Hot Atmo.:	85^{+34}_{-21} cm GEL	$12^{+3.3}_{-5.7}$ cm GEL	97 cm GEL
	Present-day Atmo.:	$12^{+3.3}_{-5.7}$ cm GEL		24 cm GEL
	Cold Atmo.:	$1^{+1.5}_{-0.4}$ cm GEL		13 cm GEL
Jeans Escape		98^{+773}_{-97} cm GEL	2.35 cm GEL	100.35 cm GEL

amounts to 44 to 440 m GEL. In total, the three loss mechanisms analyzed here account for a net loss of 1270 - 90 + 100 = 1280 cm GEL, or nearly 13 m GEL. Thus, Pluto's primordial nitrogen inventory could have been 3% to 30% higher than the present-day value.

4.7.2 Implications for Pluto's Composition

Glein and Waite (2018) also estimated Pluto's primordial N_2 inventory and concluded that unless Pluto's atmospheric escape rate was significantly higher in the past, that the inventory would be dominated by the N_2 ice contained within Sputnik Planitia. In their "Large Loss" model, they assumed an energy-limited escape rate of 10^{27} - 10^{28} N_2/s for Pluto, active over the age of the solar system (but they did not include any orbital migration; Pluto's orbital parameters were held constant at their present-day values) and calculated a net amount of N_2 lost via escape of 1.5 - 15 km GEL, which dwarfs the amount of N_2 in Sputnik Planitia (0.044 - 0.44 km GEL). In this scenario, Pluto's large N_2 inventory is most consistent with a solar-like composition. In their alternative scenario using the present-day escape rate over the age of the solar system ("Past Like Present"), Pluto's smaller N_2 inventory is consistent with a cometary composition. This means that the icy planetesimals that accreted together to form Pluto, which are assumed to have compositions similar to comets such as 67P/Churyumov-Gerasimenko (Rubin et al., 2015), could have delivered sufficient N_2 to explain Pluto's present-day inventory. In the "Large Loss" scenario, the comet explanation fails to deliver sufficient nitrogen to account for the observed amount of N_2 in Sputnik

Planitia and the 1.5-15 km GEL lost via atmospheric escape.

The enhanced Jeans escape model that we use here predicts a slightly larger amount of N_2 lost to space than the "Past Like Present" scenario from Glein and Waite (2018), 100 cm GEL vs. 8 cm GEL, but both are small relative to the amount in Sputnik Planitia. Our estimates of photochemical destruction and impact erosion/delivery are also small relative to the amount of N_2 contained within Sputnik Planitia. Thus, although this work uses a time-dependent escape rate based on the early Sun's output and incorporates Pluto's early orbital migration, we find that the loss of N_2 from Pluto over the age of the solar system is small. This is consistent with a cometary composition for Pluto, based on the work of Glein and Waite (2018).

4.7.3 Consideration of Non-thermal Escape Processes

In Section 4.6, we discussed thermal escape from the atmosphere, in particular modified Jeans escape. However, there are other, non-thermal escape mechanisms that can contribute to atmospheric loss, which we will now briefly discuss. Escape process are categorized into five general groups: (1) thermal Jeans escape, (2) hydrodynamic escape, (3) photochemical escape (different but related to the photochemical destruction discussed in Section 4.4), (4) sputtering, and (5) ion escape.

Historically, Pluto's atmosphere was thought to be in the hydrodynamic escape regime (e.g. Trafton et al. (1997); Tian and Toon (2005); Strobel (2008)), meaning that the escaping material can be treated as a fluid or bulk outflow moving at a single velocity. Models predicted N_2 escape rates of the order 10^{28} N_2/s, and were subject to the same energy-limit rate used in this work. They assumed an upper atmosphere temperature of 97 K for Pluto, but *New Horizons* observations suggest a much cooler atmosphere of only 65-68 K (Young et al., 2018), contributing to the lower estimation of Pluto's escape rate (10^{22} N_2/s) post-flyby. Post-flyby atmosphere models include cooling mechanisms such as water vapor (Strobel and Zhu, 2017) or haze particles (Zhang et al., 2017; Lavvas et al., 2021; Wan et al., 2021). In our simple model here we adopted the haze cooling scenario, resulting in a cooler temperature in the upper atmosphere and a enhanced-Jeans regime

for thermal escape instead of the hydrodynamic regime. More recently, Direct Simulation Monte Carlo (DSMC) models have shown that Pluto's atmosphere escape remains in an enhanced Jeans regime and doesn't reach the hydrodynamic regime even with increased solar heating (Zhu et al., 2014; Erwin et al., 2013).

When N_2 is photochemically destroyed in the upper atmosphere, the constituent N atoms or ions can receive enough energy to escape directly. According to the photochemical model of Krasnopolsky (2020), most of the N_2 that gets destroyed combines with hydrocarbon radicals to form nitriles, predominantly HCN. Due to the strong triple bond, any HCN formed cannot be photochemically destroyed and thus precipitates to the surface. The N atoms which do not get incorporated into other species can escape to space, and Krasnopolsky (2020) calculate that N will be lost to escape at a rate of 1.2 x 10^{23} s^{-1}, 50 times lower than the present-day N_2 photochemical destruction rate. We do not account for the direct escape of N during the Wild Years in this work.

Ion escape and sputtering both involve interactions between particles in Pluto's atmosphere and the solar wind. These interactions were not well-studied prior to the *New Horizons* flyby, but Trafton et al. (1997) argued that non-radiative effects such as these could be significant at Pluto, due to its large distance from the Sun. However, *New Horizons* observations revealed that Pluto does not have strong interactions with the solar wind (Bagenal et al., 2016), at least at present. The early Sun had a stronger solar wind, with a mass loss rate as much as 1000 times higher during the Wild Years relative to the present-day rate (Wood et al., 2002). Thus, during the Wild Years sputtering may have been a significant loss mechanism of atmospheric volatiles, although quantifying the loss rate due to solar wind interactions is beyond the scope of this work.

4.7.4 Implications for Hypothesized Ancient Glaciation on Pluto

Pluto has evidence for present-day glaciers and glacial processes. Sputnik Planitia is interpreted to be a large glacial ice sheet and glacial flow is needed to maintain the level, crater-free surface that was observed by *New Horizons* (Bertrand et al., 2018). Additionally, flow features from the east of Sputnik Planitia that appear to empty into the basin are also interpreted to be

active glaciation in the present-day (Howard et al., 2017).

There is geologic evidence which implies glacial processes were active in certain regions during ancient times, as well. Howard et al. (2017) identify dissected terrains, containing a multitude of valleys with various morphologies, to the west, north, and northeast of Sputnik Planitia, and favor an ancient-glaciation interpretation for their formation. If the glaciers purportedly responsible for sculpting these valleys are sufficiently thick (1-4 km, (McKinnon et al., 2016)), they could exhibit basal melting, which increases the erosive ability of a glacier. Increased ice temperatures also would increase flow rates and reduce the thickness needed to induce basal melting.

Additionally, Howard et al. (2017) hypothesizes that ancient glaciation could be responsible for dislodging the water-ice blocks from the bedrock surrounding Sputnik Planitia and emplacing them into the ice sheet itself, forming the observed mountain ranges, such as al-Idrisi Montes, near the edge of Sputnik Planitia. Sometime in the past, deep glacial flows from the surrounding highlands could have displaced the 10-km sized blocks (perhaps created by fracturing of the ice crust during the impact which created Sputnik Planitia) and transported them to their present location 100 km from the edge of Sputnik Planitia. The timing of this transport is uncertain, but could potentially be even more ancient than the glaciation that produced the highland valleys.

The loss mechanisms studied in this work, taken together, imply a total loss of N_2 on the order of 10 m GEL over the age of the solar system, which is mostly due to photochemical destruction of N_2. This potential loss of N_2 ice is far less than the km-thickness necessary to explain glacial carving of highland valleys or transport of water-ice blocks into Sputnik Planitia, if the km-thickness ice mantle covered the entire globe of Pluto. If instead the km-thick mantle of N_2 ice was restricted to only the latitude band where ancient glaciation is hypothesized (-30°S to 60°N, $\approx$ 70% of Pluto's surface area), the global equivalent layer of 10 m could explain a 14 m-thick layer in this latitude band. If the N_2 ice mantle was restricted even further to only the localized regions of hypothesized ancient glaciation ($\approx$ 5% of Pluto's surface), then a global loss of 10 m GEL would form a 200 m thick layer. Even in this very restricted region, the loss mechanisms analysed here are insufficient to explain a km-thick glacial layer, capable of carving valleys or transporting blocks. An alternative

explanation would be stipulating that this ancient glacial activity occurred before essentially all of Pluto's volatile inventory became sequestered in the Sputnik Planitia basin, and/or invoking a past climate epoch in which N_2 ice was restricted to the latitude band where the dissected valley terrains are observed. If escape proceeded at the energy-limited rate over the age of the solar system, Pluto could have lost close to 4 km GEL of N_2, which would be sufficient to explain the proposed ancient glaciation. As observed by *New Horizons*, the N_2 in Pluto's atmosphere is currently escaping at a rate 5 orders of magnitude lower than the energy-limited rate, so for this explanation to work, Pluto would have needed to be in a period of unusually low levels of escape at the time of the flyby.

4.8 Conclusions

The main conclusions of this work are summarized below:

(1) During the Wild Years (30 - 130 My after the condensation of CAIs), Pluto likely spent <10 My closer to the Sun than its present-day orbit, therefore <10 My at temperatures hotter than the present day 37 K. This likelihood is based on the median Plutino from our sample, which spent 9 My at heliocentric distances less than 30 AU. Typical heliocentric distances are between 15 and 80 AU. Surface temperatures never exceed 63 K (the triple point for N_2, so liquid N_2 is never stable at the surface.)

(2) The photochemical destruction rate of N_2 in Pluto's atmosphere was higher in the past, due to the early Sun's enhanced UV flux, and we estimate a total loss of about 10 m GEL (Global Equivalent Layer) over the age of the solar system. This is the largest loss out of the three mechanisms studied here (photochemical destruction, impact delivery/erosion, and atmospheric escape). As much as 30% of the total photochemical destruction over the age of the solar system probably occurred during the short, 100 My Wild Years period, due to the enhanced UV output from the young Sun.

(3) Impacts are a net source of N_2 for Pluto, and impact erosion of the atmosphere is minimal in contrast. Impacts could have delivered up to -90 cm GEL of N_2 between the start of the

giant planet instability and the present time. As much as 50% of the total impact delivery and removal likely occurred in the aftermath of the giant planet instability, when impact rates were higher than the present-day impact rate.

(4) Atmospheric escape, calculated using an enhanced Jeans framework, is not a significant loss mechanism for nitrogen, during the Wild Years or otherwise. Over the age of the solar system, 100 cm GEL could have escaped, the large majority of which occurs during the Wild Years when Pluto was closer to the Sun. If Pluto's atmosphere escaped at the energy-limited rate for the bulk of its history, then escape on the order of 4 km GEL is possible.

(5) Sputnik Planitia alone contains 44 - 440 m GEL of N_2 ice, which dwarfs the potential loss due to photochemical destruction/escape or potential delivery by impacts. Thus, Pluto's primordial nitrogen inventory was likely very similar to its observed present-day inventory.

Acknowledgments

This work was supported by NASA SSW grant NNX15AH35G. X.Z. was supported by NASA SSW grant 80NSSC19K0791. We would like to thank Randy Gladstone and Bill McKinnon for helpful conversations and their expert feedback on this work, as well as the participants of the *New Horizons* Summer Science Workshop in July 2021 for their early interest, encouragement, and advice for this work.

Chapter 5

Conclusions and Paths Forward

5.1 Main Conclusions of this Thesis

The work in this thesis is united by the body, Pluto, but touches on three different subfields (climate, geophysics, and orbital dynamics) and three different time periods (modern era, 4 billion years ago, and 4.5 billion years ago). In this way, this thesis is a broad study of Pluto's volatiles and how they interact with and shape Pluto as a whole throughout its entire lifetime.

From Chapter 2, I concluded that variation in atmospheric pressure was not responsible for creating the observed surface heterogeneity. Due to Pluto's atmosphere being in vapor pressure equilibrium with its surface ice deposits, knowledge of the spatial distribution of ice can constrain the atmospheric pressure at a given time, and vice versa. The atmospheric pressure controls processes like winds and geologic erosion and haze production, underscoring the importance of volatiles and volatile transport to Pluto in general. This work strengthened the existing suggestion that Pluto's atmosphere does not collapse at aphelion, as once thought. In part due to the presence of Sputnik Planitia near the equator, it appears that there is always a sufficient amount of illuminated nitrogen ice deposits in order to maintain a global atmosphere.

In Chapter 3, I determined just how important insolation patterns and topography are for the transport of nitrogen across Pluto's surface, and how that transport can be powerful enough to tilt the entire body of Pluto. All else being equal, topographic depressions on Pluto are cold traps, so volatiles will naturally be sequestered there. I calculated that within 10 million years all available nitrogen migrates into the 2-3 km deep Sputnik Planitia basin. The mass of the resulting ice sheet is

enough to overwhelm Pluto's moment of inertia and reorient the body, demonstrating the powerful effect that surface ice can have on Pluto as a whole. Subject to assumptions about the internal structure of Pluto, this work limited the thickness of nitrogen ice in Sputnik Planitia to 1 - 2 km. Any thicker, and the larger mass of ice would cause a larger reorientation and place Sputnik closer to the anti-Charon point than what is observed, while thinner ice sheets aren't massive enough to reorient the basin as far as it needs to be. What Chapter 3 added to the understanding of true polar wander on Pluto was the connection to climate and volatile transport. Coupling my climate model to an existing true polar wander model allowed determination of the rate of infill, based on condensation rates from the atmosphere, as well as further constraints on the initial location of the impact basin. If the initial basin is too close to the north pole, Pluto's solar insolation pattern, in which the poles receive more sunlight than the equator on average, prevents large amount of ice from forming there and thus no true polar wander can occur. If the initial basin was too close to the equator, then infilling and subsequent true polar wander bring it too close to the equator, contradicting observations. My work showed that there is a "sweet spot," between 35° and 50°N where the initial basin most likely formed.

In Chapter 4, I showed that Pluto's early orbital migration during the "Wild Years" is important for accurately estimating the loss of nitrogen via photochemical destruction, atmospheric escape, and impact erosion. While none of these loss mechanisms are significant relative to the present-day inventory, using loss rates based on Pluto's present-day orbit and the present-day behavior of the Sun will be significant underestimates of the total loss. Photochemical destruction could account for a loss of a global equivalent layer (GEL) of 13 m of nitrogen over the age of the solar system, while escape could contribute on the order of 0.1 m GEL. Impacts, on the other hand, are likely a net source of nitrogen, with atmospheric erosion from impacts being a small loss in all except extremely hot and extended past atmospheres. This understanding that Pluto never had significantly more nitrogen that it does now implies that another explanation must be responsible for the purported ancient glaciation implied by Pluto's geomorphology.

5.2 Future Work and Broader Impacts

Pluto is the best-studied Kuiper Belt Object (KBO), and only one of two to be visited by a spacecraft (the other being cold-classical KBO Arrokoth, also visited by *New Horizons*). Pluto is thus the "poster child" for the Kuiper Belt and conclusions drawn for Pluto can be extended for other KBOs as well. For example, the conclusions about orbital migration and time spent closer to/further from the Sun from Chapter 4 apply to Plutinos (KBOs in 3:2 resonance with Neptune, like Pluto) in general, not just Pluto. Characterizing Pluto's volatile inventory and the implied formation mechanism can constrain the inventories and formations of other KBOs, after adjusting for size.

Since publishing my work on the climate-true polar wander connection in Chapter 3, there have been several papers published regarding the ability of Pluto's ice shell to maintain the topographic signature of a subsurface ocean uplift and how the basin topography would relax over 4 billion years. Denton et al. (2021) modeled the Sputnik-forming impact and found that models with a thick 150 km subsurface ocean were most consistent with observations. The presence of a subsurface ocean could lead to ocean uplift, in which the ice shell is thinned underneath an impact basin and the ocean extends into that space in order to maintain isostatic balance. The overall gravity signature of the impact basin is a combination of the gravity signatures of the ice sheet, the empty basin, and the ocean uplift. Kihoulou et al. (2022) modeled the cooling and relaxation of Pluto's ice shell and underlying ocean in order to see how long a subsurface ocean uplift could be maintained. They included a layer of insulating methane clathrates at the ice shell/ocean interface in order to extend the lifetime of the uplift. When the ice shell is warm right after the impact, it relaxes and the topographic signature of the subsurface ocean is diminished. If the ice shell is thinner, it cools more quickly, and the subsurface ocean uplift topography can be maintained to the present-day. In the future, it would be possible to link the processes of ice infill and ice shell cooling/ocean uplift relaxation in order to calculate the true polar wander reorientation resulting from the processes in combination. This represents a more realistic basin structure than the cylindrical

hole in the ground used for Johnson et al. (2021a), and should improve estimates for the amount of N_2 ice in the Sputnik Planitia ice sheet and also the initial formation location of the basin.

An example of true polar wander caused by volatile transport on Pluto raises the question of volatile-transport-driven true polar wander on Triton, thought to be an escaped KBO similar to Pluto in many ways. The possibility of climate-driven polar wander has been proposed for Triton before (Rubincam, 2003), but it has not been fully explored with a coupled climate-polar wander model like the one I developed for Chapter 3. Volatile-driven true polar wander, if feasible, provides a possible explanation for Triton's bright southern terrain and has implications for leading/trailing hemisphere cratering statistics. Rubincam (2003) suggests that large polar ice caps should build up on Triton, because the equator receives more sunlight on average than the winter pole and thus any ice deposits at the equator will sublime and migrate to the cold winter pole. If the polar ice cap grows massive enough, it can overcome the oblateness of the moon, and true polar wander will reorient the body, moving the ice cap towards the equator. Specifics of where the ice cap ends up depends on assumptions of the oblateness and internal structure of Triton. If the ice cap ends up at the sub- or anti-Neptune point (the point on the surface that always faces or directly opposes Neptune), the reorientation would not affect the leading-trailing hemisphere crater count asymmetry. Conversely, if Triton's internal structure is such that the ice cap ends up on the equator in either the leading or trailing hemisphere, then the cratering asymmetry will be disturbed. Triton is tidally-locked to Neptune, and is observed to have more craters on its leading hemisphere (the side of Triton that is always aligned with the direction of motion about Neptune) than its trailing hemisphere. In the future, I would like to use my coupled climate-true polar wander model to investigate if (1) there is sufficient ice mass on Triton and a sufficiently large insolation difference between the equator and pole to build up a cap large enough to cause reorientation within one Triton winter, and (2) what internal structures and oblateness values cause a reorientation that preserves the leading/trailing hemisphere cratering asymmetry.

Ground-based occultations have been instrumental in understanding Pluto's atmosphere, both before and after the *New Horizons* flyby. I used the record of occultations going back 30 years

to constrain my predictions for Pluto's surface pressure in Chapter 2. Since publishing Johnson et al. (2021b), more occultations have been observed, tentatively showing that Pluto's surface pressure has reached or will soon reach a plateau. The timing of the peak and the rate at which Pluto's atmospheric pressure decreases afterward are dependent on the distribution of nitrogen ice in Pluto's unseen southern hemisphere. The southern hemisphere is currently in polar night, and won't be fully sunlit again for over a century. Continuing to monitor the pressure will thus allow indirect determination of the location of southern ice deposits, before they are able to be directly observed. In the future, I hope to incorporate new measurements from occultations into my model of Pluto's surface pressure in order to further constrain the spatial distribution of nitrogen on the surface.

KBOs are likely the most abundant class of objects in our solar system, by number. They are a missing piece of the planet and solar system formation puzzle, with information that is not recorded elsewhere. Detecting individual exo-Plutos and exo-KBOs is a long way off, but understanding the ones in our own solar system will go a long way for understanding their role in solar system formation in general.

The *New Horizons* mission revolutionized our knowledge of Pluto and I am immensely lucky that the timing of my graduate school career coincided with this "golden era" of Pluto research. It took 85 years to go from Pluto's discovery by Clyde Tombaugh to the first visit by a spacecraft, and it will be another 157 years until Pluto completes its first full orbit since being discovered. Timescales on Pluto are inevitably long, and the next dedicated mission to Pluto is surely a long ways off. This inter-mission time is a theorist's playground, with demand for predictions high and a need for creative and imaginative ideas in the face of a dearth of data. I'm excited to be part of it. I started this thesis with the line "dim, distant, and diminutive Pluto was not known to the ancient astronomers." I'll end it with a more upbeat line:

Dazzling and dynamic, Pluto has made itself known to humanity.

Bibliography

Andersson, L. E. (1978). Eclipse Phenomena of Pluto and its Satellite. In Bulletin of the American Astronomical Society, volume 10, page 586.

Arakawa, S., Hyodo, R., and Genda, H. (2019). Early formation of moons around large trans-Neptunian objects via giant impacts. Nature Astronomy, 3:802–807.

Arimatsu, K., Hashimoto, G. L., Kagitani, M., Sakanoi, T., Kasaba, Y., Ohsawa, R., and Urakawa, S. (2020). Evidence for a rapid decrease of Pluto's atmospheric pressure revealed by a stellar occultation in 2019. Astronomy and Astrophsyics, 638:L5.

Bagenal, F., Horányi, M., McComas, D. J., McNutt and Elliott, H. A. and Hill, M. E. and Brown, L. E. and Delamere, P. A. and Kollmann, P. and Krimigis, S. M. and, R. L. Kusterer, M., Lisse, C. M., Mitchell, D. G., Piquette, M., Poppe, A. R., Strobel, D. F., Szalay, J. R., Valek, P., Vand egriff, J., Weidner, S., Zirnstein, E. J., Stern, S. A., Ennico, K., Olkin, C. B., Weaver, H. A., Young, L. A., Gladstone, G. R., Grundy, W. M., McKinnon, W. B., Moore, J. M., Spencer, J. R., Andert, T., Andrews, J., Banks, M., Bauer, B., Bauman, J., Barnouin, O. S., Bedini, P., Beisser, K., Beyer, R. A., Bhaskaran, S., Binzel, R. P., Birath, E., Bird, M., Bogan, D. J., Bowman, A., Bray, V. J., Brozovic, M., Bryan, C., Buckley, M. R., Buie, M. W., Buratti, B. J., Bushman, S. S., Calloway, A., Carcich, B., Cheng, A. F., Conard, S., Conrad, C. A., Cook, J. C., Cruikshank, D. P., Custodio, O. S., Dalle Ore, C. M., Deboy, C., Dischner, Z. J. B., Dumont, P., Earle, A. M., Ercol, J., Ernst, C. M., Finley, T., Flanigan, S. H., Fountain, G., Freeze, M. J., Greathouse, T., Green, J. L., Guo, Y., Hahn, M., Hamilton, D. P., Hamilton, S. A., Hanley, J., Harch, A., Hart, H. M., Hersman, C. B., Hill, A., Hinson, D. P., Holdridge, M. E., Howard, A. D., Howett, C. J. A., Jackman, C., Jacobson, R. A., Jennings, D. E., Kammer, J. A., Kang, H. K., Kaufmann, D. E., Kusnierkiewicz, D., Lauer, T. R., Lee, J. E., Lindstrom, K. L., Linscott, I. R., Lunsford, A. W., Mallder, V. A., Martin, N., Mehoke, D., Mehoke, T., Melin, E. D., Mutchler, M., Nelson, D., Nimmo, F., Nunez, J. I., Ocampo, A., Owen, W. M., Paetzold, M., Page, B., Parker, A. H., Parker, J. W., Pelletier, F., Peterson, J., Pinkine, N., Porter, S. B., Protopapa, S., Redfern, J., Reitsema, H. J., Reuter, D. C., Roberts, J. H., Robbins, S. J., Rogers, G., Rose, D., Runyon, K., Retherford, K. D., Ryschkewitsch, M. G., Schenk, P., Schindhelm, E., Sepan, B., Showalter, M. R., Singer, K. N., Soluri, M., Stanbridge, D., Steffl, A. J., Stryk, T., Summers, M. E., Tapley, M., Taylor, A., Taylor, H., Throop, H. B., Tsang, C. C. C., Tyler, G. L., Umurhan, O. M., Verbiscer, A. J., Versteeg, M. H., Vincent, M., Webbert, R., Weigle, G. E., White, O. L., Whittenburg, K., Williams, B. G., Williams, K., Williams, S., Woods, W. W., and Zangari, A. M. (2016). Pluto' interaction with its space environment: Solar wind, energetic particles, and dust. Science, 351(6279):aad9045.

Bertrand, T. and Forget, F. (2016). Observed glacier and volatile distribution on Pluto from atmosphere-topography processes. Nature, 540:86–89.

Bertrand, T. and Forget, F. (2017). 3D modeling of organic haze in Pluto's atmosphere. Icarus, 287:72–86.

Bertrand, T., Forget, F., Umurhan, O. M., Grundy, W. M., Schmitt, B., Protopapa, S., Zangari, A. M., White, O. L., Schenk, P. M., and Singer, K. N. (2018). The nitrogen cycles on Pluto over seasonal and astronomical timescales. Icarus, 309:277–296.

Bertrand, T., Forget, F., Umurhan, O. M., Moore, J. M., Young, L. A., Protopapa, S., Grundy, W. M., Schmitt, B., Dhingra, R. D., Binzel, R. P., Earle, A. M., Cruikshank, D. P., Stern, S. A., Weaver, H. A., Ennico, K., Olkin, C. B., and New Horizons Science Team (2019). The CH_4 cycles on Pluto over seasonal and astronomical timescales. Icarus, 329:148–165.

Bertrand, T., Forget, F., White, O., Schmitt, B., Stern, S. A., Weaver, H. A., Young, L. A., Ennico, K., and Olkin, C. B. (2020). Pluto's Beating Heart Regulates the Atmospheric Circulation: Results From High-Resolution and Multiyear Numerical Climate Simulations. Journal of Geophysical Research (Planets), 125(2):e06120.

Binzel, R. P. and Schindler, K. (2021). The Discoveries of Pluto and the Kuiper Belt. In Stern, S. A., Moore, J. M., Grundy, W. M., Young, L. A., and Binzel, R. P., editors, The Pluto System After New Horizons, pages 3–8. University of Arizona, Tucson.

Binzel, R. P., Tholen, D. J., Tedesco, E. F., Buratti, B. J., and Nelson, R. M. (1985). The Detection of Eclipses in the Pluto-Charon System. Science, 228(4704):1193–1195.

Bressan, A., Marigo, P., Girardi, L., Salasnich, B., Dal Cero, C., Rubele, S., and Nanni, A. (2012). PARSEC: stellar tracks and isochrones with the PAdova and TRieste Stellar Evolution Code. MNRAS, 427(1):127–145.

Brown, M. E. and Schaller, E. L. (2007). The Mass of Dwarf Planet Eris. Science, 316(5831):1585.

Brozović, M., Showalter, M. R., Jacobson, R. A., and Buie, M. W. (2015). The orbits and masses of satellites of Pluto. Icarus, 246:317–329.

Buhler, P. B. and Ingersoll, A. P. (2018). Sublimation pit distribution indicates convection cell surface velocities of ∼10 cm per year in Sputnik Planitia, Pluto. Icarus, 300:327–340.

Buie, M. W., Grundy, W. M., Young, E. F., Young, L. A., and Stern, S. A. (2010). Pluto and Charon with the Hubble Space Telescope. II. Resolving Changes on Pluto's Surface and a Map for Charon. AJ, 139(3):1128–1143.

Buie, M. W., Hofgartner, J. D., Bray, V. J., and Lellouch, E. (2021). Future Exploration of the Pluto System. In Stern, S. A., Moore, J. M., Grundy, W. M., Young, L. A., and Binzel, R. P., editors, The Pluto System After New Horizons, pages 569–586. University of Arizona, Tucson.

Buie, M. W., Tholen, D. J., and Horne, K. (1992). Albedo maps of Pluto and Charon: Initial mutual event results. Icarus, 97(2):211–227.

Buratti, B. J., Hofgartner, J. D., Hicks, M. D., Weaver, H. A., Stern, S. A., Momary, T., Mosher, J. A., Beyer, R. A., Verbiscer, A. J., Zangari, A. M., Young, L. A., Lisse, C. M., Singer, K., Cheng, A., Grundy, W., Ennico, K., and Olkin, C. B. (2017). Global albedos of Pluto and Charon from LORRI New Horizons observations. Icarus, 287:207–217.

Canup, R. M. (2011). On a Giant Impact Origin of Charon, Nix, and Hydra. AJ, 141(2):35.

Canup, R. M., Kratter, K. M., and Neveu, M. (2021). On the Origin of the Pluto System. In Stern, S. A., Moore, J. M., Grundy, W. M., Young, L. A., and Binzel, R. P., editors, The Pluto System After New Horizons, pages 475–506. University of Arizona, Tucson.

Castillo-Rogez, J. C., Matson, D. L., Sotin, C., Johnson, T. V., Lunine, J. I., and Thomas, P. C. (2007). Iapetus' geophysics: Rotation rate, shape, and equatorial ridge. Icarus, 190(1):179–202.

Chen, Y., Girardi, L., Bressan, A., Marigo, P., Barbieri, M., and Kong, X. (2014). Improving PARSEC models for very low mass stars. MNRAS, 444(3):2525–2543.

Cheng, A. F., Summers, M. E., Gladstone, G. R., Strobel, D. F., Young, L. A., Lavvas, P., Kammer, J. A., Lisse, C. M., Parker, A. H., Young, E. F., Stern, S. A., Weaver, H. A., Olkin, C. B., and Ennico, K. (2017). Haze in Pluto's atmosphere. Icarus, 290:112–133.

Christy, J. W. and Harrington, R. S. (1978). The satellite of Pluto. AJ, 83:1005.

Connelly, J. N., Bizzarro, M., Krot, A. N., Nordlund, Å., Wielandt, D., and Ivanova, M. A. (2012). The Absolute Chronology and Thermal Processing of Solids in the Solar Protoplanetary Disk. Science, 338(6107):651.

Cruikshank, D. P., Pilcher, C. B., and Morrison, D. (1976). Pluto: Evidence for Methane Frost. Science, 194(4267):835–837.

Dell'Oro, A., Campo Bagatin, A., Benavidez, P. G., and Alemañ, R. A. (2013). Statistics of encounters in the trans-Neptunian region. A&A, 558:A95.

Denton, C. A., Johnson, B. C., Wakita, S., Freed, A. M., Melosh, H. J., and Stern, S. A. (2021). Pluto's Antipodal Terrains Imply a Thick Subsurface Ocean and Hydrated Core. Geophys. Res. Lett., 48(2):e91596.

Dias-Oliveira, A., Sicardy, B., Lellouch, E., Vieira-Martins, R., Assafin, M., Camargo, J. I. B., Braga-Ribas, F., Gomes-Júnior, A. R., Benedetti-Rossi, G., Colas, F., Decock, A., Doressoundiram, A., Dumas, C., Emilio, M., Fabrega Polleri, J., Gil-Hutton, R., Gillon, M., Girard, J. H., Hau, G. K. T., Ivanov, V. D., Jehin, E., Lecacheux, J., Leiva, R., Lopez-Sisterna, C., Mancini, L., Manfroid, J., Maury, A., Meza, E., Morales, N., Nagy, L., Opitom, C., Ortiz, J. L., Pollock, J., Roques, F., Snodgrass, C., Soulier, J. F., Thirouin, A., Vanzi, L., Widemann, T., Reichart, D. E., LaCluyze, A. P., Haislip, J. B., Ivarsen, K. M., Dominik, M., Jørgensen, U., and Skottfelt, J. (2015). Pluto's Atmosphere from Stellar Occultations in 2012 and 2013. ApJ, 811(1):53.

Dobrovolskis, A. R. and Harris, A. W. (1983). The obliquity of Pluto. Icarus, 55(2):231–235.

Dobrovolskis, A. R., Peale, S. J., and Harris, A. W. (1997). Dynamics of the Pluto-Charon Binary. In Stern, S. A. and Tholen, D. J., editors, Pluto and Charon, page 159. Tucson: University of Arizona Press.

Douté, S., Schmitt, B., Quirico, E., Owen, T. C., Cruikshank, D. P., de Bergh, C., Geballe, T. R., and Roush, T. L. (1999). Evidence for Methane Segregation at the Surface of Pluto. Icarus, 142(2):421–444.

Earle, A. M. and Binzel, R. P. (2015). Pluto's insolation history: Latitudinal variations and effects on atmospheric pressure. Icarus, 250:405–412.

Earle, A. M., Binzel, R. P., Young, L. A., Stern, S. A., Ennico, K., Grundy, W., Olkin, C. B., Weaver, H. A., and New Horizons Geology and Geophysics Imaging Team (2017). Long-term surface temperature modeling of Pluto. Icarus, 287:37–46.

Earle, A. M., Binzel, R. P., Young, L. A., Stern, S. A., Ennico, K., Grundy, W., Olkin, C. B., Weaver, H. A., and New Horizons Surface Composition Theme (2018). Albedo matters: Understanding runaway albedo variations on Pluto. Icarus, 303:1–9.

Edgeworth, K. E. (1943). The evolution of our planetary system. Journal of the British Astronomical Association, 53:181–188.

Edgeworth, K. E. (1949). The origin and evolution of the Solar System. MNRAS, 109:600–609.

Elliot, J. L., Dunham, E. W., Bosh, A. S., Slivan, S. M., Young, L. A., Wasserman, L. H., and Millis, R. L. (1989). Pluto's atmosphere. Icarus, 77:148–170.

Elliot, J. L., Person, M. J., and Qu, S. (2003). Analysis of Stellar Occultation Data. II. Inversion, with Application to Pluto and Triton. Astronomical Journal, 126(2):1041–1079.

Eluszkiewicz, J. (1991). On the microphysical state of the surface of Triton. Journal of Geophysical Research, 96:19217–19229.

Erwin, J., Tucker, O. J., and Johnson, R. E. (2013). Hybrid fluid/kinetic modeling of Pluto's escaping atmosphere. Icarus, 226(1):375–384.

Forget, F., Bertrand, T., Vangvichith, M., Leconte, J., Millour, E., and Lellouch, E. (2017). A post-new horizons global climate model of Pluto including the N_2, CH_4 and CO cycles. Icarus, 287:54–71.

Fraser, W. C., Brown, M. E., Morbidelli, A., Parker, A., and Batygin, K. (2014). The Absolute Magnitude Distribution of Kuiper Belt Objects. ApJ, 782(2):100.

Fray, N. and Schmitt, B. (2009). Sublimation of ices of astrophysical interest: A bibliographic review. Planetary and Space Science, 57:2053–2080.

Fulchignoni, M., Ferri, F., Angrilli, F., Ball, A. J., Bar-Nun, A., Barucci, M. A., Bettanini, C., Bianchini, G., Borucki, W., Colombatti, G., Coradini, M., Coustenis, A., Debei, S., Falkner, P., Fanti, G., Flamini, E., Gaborit, V., Grard, R., Hamelin, M., Harri, A. M., Hathi, B., Jernej, I., Leese, M. R., Lehto, A., Lion Stoppato, P. F., López-Moreno, J. J., Mäkinen, T., McDonnell, J. A. M., McKay, C. P., Molina-Cuberos, G., Neubauer, F. M., Pirronello, V., Rodrigo, R., Saggin, B., Schwingenschuh, K., Seiff, A., Simões, F., Svedhem, H., Tokano, T., Towner, M. C., Trautner, R., Withers, P., and Zarnecki, J. C. (2005). In situ measurements of the physical characteristics of Titan's environment. Nature, 438(7069):785–791.

Gabasova, L. R., Schmitt, B., Grundy, W., Bertrand, T., Olkin, C. B., Spencer, J. R., Young, L. A., Ennico, K., Weaver, H. A., Stern, S. A., and New Horizons Composition Team (2021). Global compositional cartography of Pluto from intensity-based registration of LEISA data. Icarus, 356:113833.

Gao, P., Fan, S., Wong, M. L., Liang, M.-C., Shia, R.-L., Kammer, J. A., Yung, Y. L., Summers, M. E., Gladstone, G. R., Young, L. A., Olkin, C. B., Ennico, K., Weaver, H. A., Stern, S. A., and New Horizons Science Team (2017). Constraints on the microphysics of Pluto's photochemical haze from New Horizons observations. Icarus, 287:116–123.

Gladstone, G. R., Stern, S. A., Ennico, K., Olkin, C. B., Weaver, H. A., Young, L. A., Summers, M. E., Strobel, D. F., Hinson, D. P., Kammer, J. A., Parker, A. H., Steffl, A. J., Linscott, I. R., Parker, J. W., Cheng, A. F., Slater, D. C., Versteeg, M. H., Greathouse, T. K., Retherford, K. D., Throop, H., Cunningham, N. J., Woods, W. W., Singer, K. N., Tsang, C. C. C., Schindhelm, E., Lisse, C. M., Wong, M. L., Yung, Y. L., Zhu, X., Curdt, W., Lavvas, P., Young, E. F., Tyler, G. L., Bagenal, F., Grundy, W. M., McKinnon, W. B., Moore, J. M., Spencer, J. R., Andert, T., Andrews, J., Banks, M., Bauer, B., Bauman, J., Barnouin, O. S., Bedini, P., Beisser, K., Beyer, R. A., Bhaskaran, S., Binzel, R. P., Birath, E., Bird, M., Bogan, D. J., Bowman, A., Bray, V. J., Brozovic, M., Bryan, C., Buckley, M. R., Buie, M. W., Buratti, B. J., Bushman, S. S., Calloway, A., Carcich, B., Conard, S., Conrad, C. A., Cook, J. C., Cruikshank, D. P., Custodio, O. S., Ore, C. M. D., Deboy, C., Dischner, Z. J. B., Dumont, P., Earle, A. M., Elliott, H. A., Ercol, J., Ernst, C. M., Finley, T., Flanigan, S. H., Fountain, G., Freeze, M. J., Green, J. L., Guo, Y., Hahn, M., Hamilton, D. P., Hamilton, S. A., Hanley, J., Harch, A., Hart, H. M., Hersman, C. B., Hill, A., Hill, M. E., Holdridge, M. E., Horanyi, M., Howard, A. D., Howett, C. J. A., Jackman, C., Jacobson, R. A., Jennings, D. E., Kang, H. K., Kaufmann, D. E., Kollmann, P., Krimigis, S. M., Kusnierkiewicz, D., Lauer, T. R., Lee, J. E., Lindstrom, K. L., Lunsford, A. W., Mallder, V. A., Martin, N., McComas, D. J., McNutt, R. L., Mehoke, D., Mehoke, T., Melin, E. D., Mutchler, M., Nelson, D., Nimmo, F., Nunez, J. I., Ocampo, A., Owen, W. M., Paetzold, M., Page, B., Pelletier, F., Peterson, J., Pinkine, N., Piquette, M., Porter, S. B., Protopapa, S., Redfern, J., Reitsema, H. J., Reuter, D. C., Roberts, J. H., Robbins, S. J., Rogers, G., Rose, D., Runyon, K., Ryschkewitsch, M. G., Schenk, P., Sepan, B., Showalter, M. R., Soluri, M., Stanbridge, D., Stryk, T., Szalay, J. R., Tapley, M., Taylor, A., Taylor, H., Umurhan, O. M., Verbiscer, A. J., Versteeg, M. H., Vincent, M., Webbert, R., Weidner, S., Weigle, G. E., White, O. L., Whittenburg, K., Williams, B. G., Williams, K., Williams, S., Zangari, A. M., and Zirnstein, E. (2016). The atmosphere of Pluto as observed by New Horizons. Science, 351:aad8866.

Glein, C. R. and Waite, J. H. (2018). Primordial N_2 provides a cosmochemical explanation for the existence of Sputnik Planitia, Pluto. Icarus, 313:79–92.

Gomes, R., Levison, H. F., Tsiganis, K., and Morbidelli, A. (2005). Origin of the cataclysmic Late Heavy Bombardment period of the terrestrial planets. Nature, 435(7041):466–469.

Grundy, W. M., Bertrand, T., Binzel, R. P., Buie, M. W., Buratti, B. J., Cheng, A. F., Cook, J. C., Cruikshank, D. P., Devins, S. L., Dalle Ore, C. M., Earle, A. M., Ennico, K., Forget, F., Gao, P., Gladstone, G. R., Howett, C. J. A., Jennings, D. E., Kammer, J. A., Lauer, T. R., Linscott, I. R., Lisse, C. M., Lunsford, A. W., McKinnon, W. B., Olkin, C. B., Parker, A. H., Protopapa, S., Quirico, E., Reuter, D. C., Schmitt, B., Singer, K. N., Spencer, J. A., Stern, S. A., Strobel, D. F., Summers, M. E., Weaver, H. A., Weigle, G. E., Wong, M. L., Young, E. F., Young, L. A., and Zhang, X. (2018). Pluto's haze as a surface material. Icarus, 314:232–245.

Grundy, W. M. and Buie, M. W. (2001). Distribution and Evolution of CH_4, N_2, and CO Ices on Pluto's Surface: 1995 to 1998. Icarus, 153(2):248–263.

Grundy, W. M. and Fink, U. (1996). Synoptic CCD Spectrophotometry of Pluto Over the Past 15 Years. Icarus, 124(1):329–343.

Haisch, Karl E., J., Lada, E. A., and Lada, C. J. (2001). Disk Frequencies and Lifetimes in Young Clusters. ApJL, 553(2):L153–L156.

Hamilton, D. P., Stern, S. A., Moore, J. M., Young, L. A., Binzel, R. P., Buie, M. W., Buratti, B. J., Cheng, A. F., Ennico, K., Grundy, W. M., Linscott, I. R., McKinnon, W. B., Olkin, C. B., Reitsema, H. J., Reuter, D. C., Schenk, P., Showalter, M. R., Spencer, J. R., Tyler, G. L., and Weaver, H. A. (2016). The rapid formation of Sputnik Planitia early in Pluto's history. Nature, 540(7631):97–99.

Hansen, C. J. and Paige, D. A. (1996). Seasonal Nitrogen Cycles on Pluto. Icarus, 120(2):247–265.

Hansen, C. J., Paige, D. A., and Young, L. A. (2015). Pluto's climate modeled with new observational constraints. Icarus, 246:183–191.

Hapke, B. (1993). Theory of reflectance and emittance spectroscopy. UK: Cambridge University Press.

Hinson, D. P., Linscott, I. R., Young, L. A., Tyler, G. L., Stern, S. A., Beyer, R. A., Bird, M. K., Ennico, K., Gladstone, G. R., Olkin, C. B., Pätzold, M., Schenk, P. M., Strobel, D. F., Summers, M. E., Weaver, H. A., and Woods, W. W. (2017). Radio occultation measurements of Pluto's neutral atmosphere with New Horizons. Icarus, 290:96–111.

Howard, A. D., Moore, J. M., Umurhan, O. M., White, O. L., Anderson, R. S., McKinnon, W. B., Spencer, J. R., Schenk, P. M., Beyer, R. A., Stern, S. A., Ennico, K., Olkin, C. B., Weaver, H. A., Young, L. A., and New Horizons Science Team (2017). Present and past glaciation on Pluto. Icarus, 287:287–300.

Howett, C. J. A., Robbins, S. J., Holler, B. J., Hendrix, A., Fielhauer, K. B., Perry, M. E., Siddique, F. E., Apland, C. T., Leary, J. C., Stern, S. A., Elliott, H., Nimmo, F., Porter, S. B., Protopapa, S., Singer, K. N., Tucker, O. J., Verbiscer, A. J., Andrews, B. B., Bushman, S. S., Crifasi, A. V., Crowley, D., Edwards, C. L., Ernst, C. M., Fonville, B. D., Frankford, D. P., Gallagher, D. T., Holdridge, M. E., Hunt, Jack W., J., Kavelaars, J. J., Krupiarz, C. J., Kuhn, J. S., McKinnon, W., Nair, H., Napolillo, D. H., Pineau, J. P., Radebaugh, J., Sholder, R. O., Spencer, J. R., Thodey, A., Walters, S. R., Williams, B. D., Wilson, R. J., and Young, L. A. (2021). Persephone: A Pluto-system Orbiter and Kuiper Belt Explorer. PSJ, 2(2):75.

Hubbard, W. B., Hunten, D. M., Dieters, S. W., Hill, K. M., and Watson, R. D. (1988). Occultation evidence for an atmosphere on Pluto. Nature, 336(6198):452–454.

Hussmann, H., Choblet, G., Lainey, V., Matson, D. L., Sotin, C., Tobie, G., and van Hoolst, T. (2010). Implications of Rotation, Orbital States, Energy Sources, and Heat Transport for Internal Processes in Icy Satellites. SSRv, 153(1-4):317–348.

Jewitt, D. and Luu, J. (1993). Discovery of the candidate Kuiper belt object 1992 QB_1. Nature, 362(6422):730–732.

Johnson, B. C., Bowling, T. J., Trowbridge, A. J., and Freed, A. M. (2016). Formation of the Sputnik Planum basin and the thickness of Pluto's subsurface ocean. Geophys. Res. Lett., 43(19):10,068–10,077.

Johnson, P. E., Keane, J. T., Young, L. A., and Matsuyama, I. (2021a). New Constraints on Pluto's Sputnik Planitia Ice Sheet from a Coupled Reorientation-Climate Model. PSJ, 2(5):194.

Johnson, P. E., Young, L. A., Nesvorný, D., and Zhang, X. (2023). Nitrogen Loss from Pluto's Birth to the Present Day via Atmospheric Escape, Photochemical Destruction, and Impact Erosion. PSJ. (in prep).

Johnson, P. E., Young, L. A., Protopapa, S., Schmitt, B., Gabasova, L. R., Lewis, B. L., Stansberry, J. A., Mandt, K. E., and White, O. L. (2021b). Modeling Pluto's minimum pressure: Implications for haze production. Icarus, 356:114070.

Johnson, R. E., Oza, A., Young, L. A., Volkov, A. N., and Schmidt, C. (2015). Volatile Loss and Classification of Kuiper Belt Objects. ApJ, 809(1):43.

Keane, J. T., Matsuyama, I., Kamata, S., and Steckloff, J. K. (2016). Reorientation and faulting of Pluto due to volatile loading within Sputnik Planitia. Nature, 540(7631):90–93.

Khare, B. N., Sagan, C., Arakawa, E. T., Suits, F., Callcott, T. A., and Williams, M. W. (1984). Optical constants of organic tholins produced in a simulated Titanian atmosphere: From soft x-ray to microwave frequencies. Icarus, 60(1):127–137.

Kihoulou, M., Kalousová, K., and Souček, O. (2022). Evolution of Pluto's Impact-Deformed Ice Shell Below Sputnik Planitia Basin. Journal of Geophysical Research (Planets), 127(6):e07221.

Krasnopolsky, V. A. (2020). A photochemical model of Pluto's atmosphere and ionosphere. Icarus, 335:113374.

Kuiper, G. P. (1951). On the Origin of the Solar System. Proceedings of the National Academy of Science, 37(1):1–14.

Lampland, C. O. (1933). Lowell photographic observations of Pluto in 1915, 1929, and 1930. In Publications of the American Astronomical Society, volume 7 of Publications of the American Astronomical Society, page 7.

Lavvas, P., Lellouch, E., Strobel, D. F., Gurwell, M. A., Cheng, A. F., Young, L. A., and Gladstone, G. R. (2021). A major ice component in Pluto's haze. Nature Astronomy, 5:289–297.

Lellouch, E., Santos-Sanz, P., Lacerda, P., Mommert, M., Duffard, R., Ortiz, J. L., Müller, T. G., Fornasier, S., Stansberry, J., and Kiss, C. (2013). "TNOs are Cool": A survey of the trans-Neptunian region. IX. Thermal properties of Kuiper belt objects and Centaurs from combined Herschel and Spitzer observations. Astronomy and Astrophysics, 557:A60.

Lewis, B. L., Stansberry, J. A., Holler, B. J., Grundy, W. M., Schmitt, B., Protopapa, S., Lisse, C., Stern, S. A., Young, L. A., Weaver, H. A., Olkin, C., Ennico, K., and the New Horizons Science Team (2019). Distribution and Energy Balance of Pluto's Nitrogen Ice, as seen by New Horizons in 2015. Icarus. In press.

Lisse, C. M., Young, L. A., Cruikshank, D. P., Sandford, S. A., Schmitt, B., Stern, S. A., Weaver, H. A., Umurhan, O., Pendleton, Y. J., Keane, J. T., Gladstone, G. R., Parker, J. M., Binzel, R. P., Earle, A. M., Horanyi, M., El-Maarry, M. R., Cheng, A. F., Moore, J. M., McKinnon, W. B., Grundy, W. M., Kavelaars, J. J., Linscott, I. R., Lyra, W., Lewis, B. L., Britt, D. T., Spencer, J. R., Olkin, C. B., McNutt, R. L., Elliott, H. A., Dello-Russo, N., Steckloff, J. K., Neveu, M., and Mousis, O. (2021). On the origin & thermal stability of Arrokoth's and Pluto's ices. Icarus, 356:114072.

Malhotra, R. (1993). Orbital Resonances in the Solar Nebula: Strengths and Weaknesses. Icarus, 106(1):264–273.

Malhotra, R. and Williams, J. G. (1997). Pluto's Heliocentric Orbit. In Stern, S. A. and Tholen, D. J., editors, Pluto and Charon, page 127. Tucson: University of Arizona Press.

Mandt, K. E., Luspay-Kuti, A., Cheng, A., Jessup, K. L., and Gao, P. (2021). Photochemistry and Haze Formation. In Stern, S. A., Moore, J. M., Grundy, W. M., Young, L. A., and Binzel, R. P., editors, The Pluto System After New Horizons, pages 279–296. University of Arizona, Tucson.

Martin, C. R. and Binzel, R. P. (2021). Ammonia-water freezing as a mechanism for recent cryovolcanism on Pluto. Icarus, 356:113763.

Matsuyama, I., Nimmo, F., and Mitrovica, J. X. (2014). Planetary Reorientation. Annual Review of Earth and Planetary Sciences, 42:605–634.

McGovern, P. J., White, O. L., and Schenk, P. M. (2021). Tectonism and Enhanced Cryovolcanic Potential Around a Loaded Sputnik Planitia Basin, Pluto. Journal of Geophysical Research Planets. submitted.

McKinnon, W. B., Glein, C. R., Bertrand, T., and Rhoden, A. R. (2021). Formation, Composition, and History of the Pluto System: A Post-New Horizons Synthesis. In Stern, S. A., Moore, J. M., Grundy, W. M., Young, L. A., and Binzel, R. P., editors, The Pluto System After New Horizons, pages 507–543. Tucson: University of Arizona Press.

McKinnon, W. B., Nimmo, F., Wong, T., Schenk, P. M., White, O. L., Roberts, J. H., Moore, J. M., Spencer, J. R., Howard, A. D., Umurhan, O. M., Stern, S. A., Weaver, H. A., Olkin, C. B., Young, L. A., Smith, K. E., Beyer, R., Buie, M., Buratti, B., Cheng, A., Cruikshank, D., Dalle Ore, C., Gladstone, R., Grundy, W., Lauer, T., Linscott, I., Parker, J., Porter, S., Reitsema, H., Reuter, D., Robbins, S., Showalter, M., Singer, K., Strobel, D., Summers, M., Tyler, L., Banks, M., Barnouin, O., Bray, V., Carcich, B., Chaikin, A., Chavez, C., Conrad, C., Hamilton, D., Howett, C., Hofgartner, J., Kammer, J., Lisse, C., Marcotte, A., Parker, A., Retherford, K., Saina, M., Runyon, K., Schindhelm, E., Stansberry, J., Steffl, A., Stryk, T., Throop, H., Tsang, C., Verbiscer, A., Winters, H., Zangari, A., New Horizons Geology, G., and Team, I. T. (2016). Convection in a volatile nitrogen-ice-rich layer drives Pluto's geological vigour. Nature, 534(7605):82–85.

Meza, E., Sicardy, B., Assafin, M., Ortiz, J. L., Bertrand, T., Lellouch, E., Desmars, J., Forget, F., Bérard, D., Doressoundiram, A., Lecacheux, J., Oliveira, J. M., Roques, F., Widemann, T., Colas, F., Vachier, F., Renner, S., Leiva, R., Braga-Ribas, F., Benedetti-Rossi, G., Camargo, J. I. B., Dias-Oliveira, A., Morgado, B., Gomes-Júnior, A. R., Vieira-Martins, R., Behrend, R., Tirado, A. C., Duffard, R., Morales, N., Santos-Sanz, P., Jelínek, M., Cunniffe, R., Querel,

R., Harnisch, M., Jansen, R., Pennell, A., Todd, S., Ivanov, V. D., Opitom, C., Gillon, M., Jehin, E., Manfroid, J., Pollock, J., Reichart, D. E., Haislip, J. B., Ivarsen, K. M., LaCluyze, A. P., Maury, A., Gil-Hutton, R., Dhillon, V., Littlefair, S., Marsh, T., Veillet, C., Bath, K. L., Beisker, W., Bode, H. J., Kretlow, M., Herald, D., Gault, D., Kerr, S., Pavlov, H., Faragó, O., Klös, O., Frappa, E., Lavayssière, M., Cole, A. A., Giles, A. B., Greenhill, J. G., Hill, K. M., Buie, M. W., Olkin, C. B., Young, E. F., Young, L. A., Wasserman, L. H., Devogèle, M., French, R. G., Bianco, F. B., Marchis, F., Brosch, N., Kaspi, S., Polishook, D., Manulis, I., Ait Moulay Larbi, M., Benkhaldoun, Z., Daassou, A., El Azhari, Y., Moulane, Y., Broughton, J., Milner, J., Dobosz, T., Bolt, G., Lade, B., Gilmore, A., Kilmartin, P., Allen, W. H., Graham, P. B., Loader, B., McKay, G., Talbot, J., Parker, S., Abe, L., Bendjoya, P., Rivet, J. P., Vernet, D., Di Fabrizio, L., Lorenzi, V., Magazzú, A., Molinari, E., Gazeas, K., Tzouganatos, L., Carbognani, A., Bonnoli, G., Marchini, A., Leto, G., Sanchez, R. Z., Mancini, L., Kattentidt, B., Dohrmann, M., Guhl, K., Rothe, W., Walzel, K., Wortmann, G., Eberle, A., Hampf, D., Ohlert, J., Krannich, G., Murawsky, G., Gährken, B., Gloistein, D., Alonso, S., Román, A., Communal, J. E., Jabet, F., deVisscher, S., Sérot, J., Janik, T., Moravec, Z., Machado, P., Selva, A., Perelló, C., Rovira, J., Conti, M., Papini, R., Salvaggio, F., Noschese, A., Tsamis, V., Tigani, K., Barroy, P., Irzyk, M., Neel, D., Godard, J. P., Lanoiselée, D., Sogorb, P., Vérilhac, D., Bretton, M., Signoret, F., Ciabattari, F., Naves, R., Boutet, M., De Queiroz, J., Lindner, P., Lindner, K., Enskonatus, P., Dangl, G., Tordai, T., Eichler, H., Hattenbach, J., Peterson, C., Molnar, L. A., and Howell, R. R. (2019). Lower atmosphere and pressure evolution on Pluto from ground-based stellar occultations, 1988-2016. Astronomy and Astrophysics, 625:A42.

Moore, J. M., McKinnon, W. B., Spencer, J. R., Howard, A. D., Schenk, P. M., Beyer, R. A., Nimmo, F., Singer, K. N., Umurhan, O. M., White, O. L., Stern, S. A., Ennico, K., Olkin, C. B., Weaver, H. A., Young, L. A., Binzel, R. P., Buie, M. W., Buratti, B. J., Cheng, A. F., Cruikshank, D. P., Grundy, W. M., Linscott, I. R., Reitsema, H. J., Reuter, D. C., Showalter, M. R., Bray, V. J., Chavez, C. L., Howett, C. J. A., Lauer, T. R., Lisse, C. M., Parker, A. H., Porter, S. B., Robbins, S. J., Runyon, K., Stryk, T., Throop, H. B., Tsang, C. C. C., Verbiscer, A. J., Zangari, A. a. M., Chaikin, A. L., Wilhelms, D. E., Bagenal, F., Gladstone, G. R., Andert, T., Andrews, J., Banks, M., Bauer, B., Bauman, J., Barnouin, O. S., Bedini, P., Beisser, K., Bhaskaran, S., Birath, E., Bird, M., Bogan, D. J., Bowman, A., Brozovic, M., Bryan, C., Buckley, M. R., Bushman, S. S., Calloway, A., Carcich, B., Conard, S., Conrad, C. A., Cook, J. C., Custodio, O. S., Ore, C. M. D., Deboy, C., Dischner, Z. J. B., Dumont, P., Earle, A. M., Elliott, H. A., Ercol, J., Ernst, C. M., Finley, T., Flanigan, S. H., Fountain, G., Freeze, M. J., Greathouse, T., Green, J. L., Guo, Y., Hahn, M., Hamilton, D. P., Hamilton, S. A., Hanley, J., Harch, A., Hart, H. M., Hersman, C. B., Hill, A., Hill, M. E., Hinson, D. P., Holdridge, M. E., Horanyi, M., Jackman, C., Jacobson, R. A., Jennings, D. E., Kammer, J. A., Kang, H. K., Kaufmann, D. E., Kollmann, P., Krimigis, S. M., Kusnierkiewicz, D., Lee, J. E., Lindstrom, K. L., Lunsford, A. W., Mallder, V. A., Martin, N., McComas, D. J., McNutt, R. L., Mehoke, D., Mehoke, T., Melin, E. D., Mutchler, M., Nelson, D., Nunez, J. I., Ocampo, A., Owen, W. M., Paetzold, M., Page, B., Parker, J. W., Pelletier, F., Peterson, J., Pinkine, N., Piquette, M., Protopapa, S., Redfern, J., Roberts, J. H., Rogers, G., Rose, D., Retherford, K. D., Ryschkewitsch, M. G., Schindhelm, E., Sepan, B., Soluri, M., Stanbridge, D., Steffl, A. J., Strobel, D. F., Summers, M. E., Szalay, J. R., Tapley, M., Taylor, A., Taylor, H., Tyler, G. L., Versteeg, M. H., Vincent, M., Webbert, R., Weidner, S., Weigle, G. E., Whittenburg, K., Williams, B. G., Williams, K., Williams, S., Woods, W. W., and Zirnstein, E. (2016). The geology of Pluto and Charon through the eyes of New Horizons. Science, 351(6279):1284–1293.

Morbidelli, A., Nesvorny, D., Bottke, W. F., and Marchi, S. (2021). A re-assessment of the Kuiper belt size distribution for sub-kilometer objects, revealing collisional equilibrium at small sizes. Icarus, 356:114256.

Mumma, M. J. and Charnley, S. B. (2011). The Chemical Composition of Comets—Emerging Taxonomies and Natal Heritage. ARA&A, 49(1):471–524.

Nadeau, A. and McGehee, R. (2017). A simple formula for a planet's mean annual insolation by latitude. Icarus, 291:46–50.

Nesvorný, D. (2015). Evidence for Slow Migration of Neptune from the Inclination Distribution of Kuiper Belt Objects. AJ, 150(3):73.

Nesvorný, D. (2018). Dynamical Evolution of the Early Solar System. ARA&A, 56:137–174.

Nimmo, F., Hamilton, D. P., McKinnon, W. B., Schenk, P. M., Binzel, R. P., Bierson, C. J., Beyer, R. A., Moore, J. M., Stern, S. A., Weaver, H. A., Olkin, C. B., Young, L. A., Smith, K. E., Moore, J. M., McKinnon, W. B., Spencer, J. R., Beyer, R., Binzel, R. P., Buie, M., Buratti, B., Cheng, A., Cruikshank, D., Ore, C. D., Earle, A., Gladstone, R., Grundy, W., Howard, A. D., Lauer, T., Linscott, I., Nimmo, F., Parker, J., Porter, S., Reitsema, H., Reuter, D., Roberts, J. H., Robbins, S., Schenk, P. M., Showalter, M., Singer, K., Strobel, D., Summers, M., Tyler, L., White, O. L., Umurhan, O. M., Banks, M., Barnouin, O., Bray, V., Carcich, B., Chaikin, A., Chavez, C., Conrad, C., Hamilton, D. P., Howett, C., Hofgartner, J., Kammer, J., Lisse, C., Marcotte, A., Parker, A., Retherford, K., Saina, M., Runyon, K., Schindhelm, E., Stansberry, J., Steffl, A., Stryk, T., Throop, H., Tsang, C., Verbiscer, A., Winters, H., Zangari, A., Stern, S. A., Weaver, H. A., Olkin, C. B., Young, L. A., and Smith, K. E. (2016). Reorientation of Sputnik Planitia implies a subsurface ocean on Pluto. Nature, 540(7631):94–96.

Nimmo, F. and McKinnon, W. B. (2021). Geodynamics of Pluto. In Stern, S. A., Moore, J. M., Grundy, W. M., Young, L. A., and Binzel, R. P., editors, The Pluto System After New Horizons, pages 89–103. University of Arizona, Tucson.

Nimmo, F., Umurhan, O., Lisse, C. M., Bierson, C. J., Lauer, T. R., Buie, M. W., Throop, H. B., Kammer, J. A., Roberts, J. H., McKinnon, W. B., Zangari, A. M., Moore, J. M., Stern, S. A., Young, L. A., Weaver, H. A., Olkin, C. B., and Ennico, K. (2017). Mean radius and shape of pluto and charon from new horizons images. Icarus, 287:12–29. Special Issue: The Pluto System.

Olkin, C. B., Spencer, J. R., Grundy, W. M., Parker, A. H., Beyer, R. A., Schenk, P. M., Howett, C. J. A., Stern, S. A., Reuter, D. C., Weaver, H. A., Young, L. A., Ennico, K., Binzel, R. P., Buie, M. W., Cook, J. C., Cruikshank, D. P., Dalle Ore, C. M., Earle, A. M., Jennings, D. E., Singer, K. N., Linscott, I. E., Lunsford, A. W., Protopapa, S., Schmitt, B., Weigle, E., and the New Horizons Science Team (2017). The Global Color of Pluto from New Horizons. Astronomical Journal, 154(6):258.

Olkin, C. B., Young, E. F., Young, L. A., Grundy, W., Schmitt, B., Tokunaga, A., Owen, T., Roush, T., and Terada, H. (2007). Pluto's Spectrum from 1.0 to 4.2 μm: Implications for Surface Properties. AJ, 133(2):420–431.

Owen, T. C., Roush, T. L., Cruikshank, D. P., Elliot, J. L., Young, L. A., de Bergh, C., Schmitt, B., Geballe, T. R., Brown, R. H., and Bartholomew, M. J. (1993). Surface Ices and the Atmospheric Composition of Pluto. Science, 261:745–748.

Poro, A., Ahangarani Farahani, F., Bahraminasr, M., Hadizadeh, M., Najafi Kodini, F., Rezaee, M., and Seifi Gargari, M. (2021). Study of Pluto's atmosphere based on 2020 stellar occultation light curve results. A&A, 653:L7.

Porter, S. B., Verbiscer, A. J., Weaver, H. A., Cook, J. C., and Grundy, W. M. (2021). The Small Satellites of Pluto. In Stern, S. A., Moore, J. M., Grundy, W. M., Young, L. A., and Binzel, R. P., editors, The Pluto System After New Horizons, pages 457–472. University of Arizona, Tucson.

Protopapa, S., Grundy, W. M., Reuter, D. C., Hamilton, D. P., Dalle Ore, C. M., Cook, J. C., Cruikshank, D. P., Schmitt, B., Philippe, S., Quirico, E., Binzel, R. P., Earle, A. M., Ennico, K., Howett, C. J. A., Lunsford, A. W., Olkin, C. B., Parker, A., Singer, K. N., Stern, A., Verbiscer, A. J., Weaver, H. A., Young, L. A., and New Horizons Science Team (2017). Pluto's global surface composition through pixel-by-pixel Hapke modeling of New Horizons Ralph/LEISA data. Icarus, 287:218–228.

Protopapa, S., Olkin, C. B., Grundy, W. M., Li, J.-Y., Verbiscer, A., Cruikshank, D. P., Gautier, T., Quirico, E., Cook, J. C., Reuter, D., Howett, C. J. A., Stern, A., Beyer, R. A., Porter, S., Young, L. A., Weaver, H. A., Ennico, K., Dalle Ore, C. M., Scipioni, F., and Singer, K. (2020). Disk-resolved Photometric Properties of Pluto and the Coloring Materials across its Surface. Astronomical Journal, 159(2):74.

Ribas, I., Guinan, E. F., Güdel, M., and Audard, M. (2005). Evolution of the Solar Activity over Time and Effects on Planetary Atmospheres. I. High-Energy Irradiances (1-1700 Å). ApJ, 622(1):680–694.

Robuchon, G. and Nimmo, F. (2011). Thermal evolution of Pluto and implications for surface tectonics and a subsurface ocean. Icarus, 216(2):426–439.

Rubin, M., Altwegg, K., Balsiger, H., Bar-Nun, A., Berthelier, J. J., Bieler, A., Bochsler, P., Briois, C., Calmonte, U., Combi, M., De Keyser, J., Dhooghe, F., Eberhardt, P., Fiethe, B., Fuselier, S. A., Gasc, S., Gombosi, T. I., Hansen, K. C., Hässig, M., Jäckel, A., Kopp, E., Korth, A., Le Roy, L., Mall, U., Marty, B., Mousis, O., Owen, T., Rème, H., Sémon, T., Tzou, C. Y., Waite, J. H., and Wurz, P. (2015). Molecular nitrogen in comet 67P/Churyumov-Gerasimenko indicates a low formation temperature. Science, 348(6231):232–235.

Rubincam, D. P. (2003). Polar wander on Triton and Pluto due to volatile migration. Icarus, 163(2):469–478.

Sabadini, R., Vermeersen, B., and Cambiotti, G. (2016). Global Dynamics of the Earth: Applications of Viscoelastic Relaxation Theory to Solid-Earth and Planetary Geophysics. Springer.

Schenk, P. M., Beyer, R. A., McKinnon, W. B., Moore, J. M., Spencer, J. R., White, O. L., Singer, K., Nimmo, F., Thomason, C., Lauer, T. R., Robbins, S., Umurhan, O. M., Grundy, W. M., Stern, S. A., Weaver, H. A., Young, L. A., Smith, K. E., Olkin, C., New Horizons Geology, and Geophysics Investigation Team (2018). Basins, fractures and volcanoes: Global cartography and topography of Pluto from New Horizons. Icarus, 314:400–433.

Schindler, K. and Grundy, W. M. (2018). Pluto and Lowell Observatory: a history of discovery at Flagstaff. History Press, Charleston.

Schlichting, H. E., Sari, R., and Yalinewich, A. (2015). Atmospheric mass loss during planet formation: The importance of planetesimal impacts. Icarus, 247:81–94.

Schmitt, B., Philippe, S., Grundy, W. M., Reuter, D. C., Côte, R., Quirico, E., Protopapa, S., Young, L. A., Binzel, R. P., and Cook, J. C. (2017). Physical state and distribution of materials at the surface of Pluto from New Horizons LEISA imaging spectrometer. Icarus, 287:229–260.

Sicardy, B., Ashok, N. M., Tej, A., Pawar, G., Deshmukh, S., Deshpande, A., Sharma, S., Desmars, J., Assafin, M., Ortiz, J. L., Benedetti-Rossi, G., Braga-Ribas, F., Vieira-Martins, R., Santos-Sanz, P., Chand, K., and Bhatt, B. C. (2021). Pluto's Atmosphere in Plateau Phase Since 2015 from a Stellar Occultation at Devasthal. ApJL, 923(2):L31.

Singer, K. N., Greenstreet, S., Schenk, P. M., Robbins, S. J., and Bray, V. J. (2021). Impact Craters on Pluto and Charon and Terrain Age Estimates. In Stern, S. A., Binzel, R. P., Grundy, W. M., Moore, J. M., and Young, L. A., editors, *The Pluto System*. University of Arizona, Tucson.

Singer, K. N. and Stern, S. A. (2015). On the Provenance of Pluto's Nitrogen (N_2). ApJL, 808(2):L50.

Spencer, J. R. and Moore, J. M. (1992). The influence of thermal inertia on temperatures and frost stability on Triton. Icarus, 99(2):261–272.

Spencer, J. R., Stansberry, J. A., Trafton, L. M., Young, E. F., Binzel, R. P., and Croft, S. K. (1997). Volatile Transport, Seasonal Cycles, and Atmospheric Dynamics on Pluto. In Stern, S. A. and Tholen, D. J., editors, Pluto and Charon, page 435. Tucson: University of Arizona Press.

Stansberry, J. A., Pisano, D. J., and Yelle, R. V. (1996). The emissivity of volatile ices on Triton and Pluto. Planetary and Space Science, 44(9):945–955.

Stern, S. A., Bagenal, F., Ennico, K., Gladstone, G. R., Grundy, W. M., McKinnon, W. B., Moore, J. M., Olkin, C. B., Spencer, J. R., Weaver, H. A., Young, L. A., Andert, T., Andrews, J., Banks, M., Bauer, B., Bauman, J., Barnouin, O. S., Bedini, P., Beisser, K., Beyer, R. A., Bhaskaran, S., Binzel, R. P., Birath, E., Bird, M., Bogan, D. J., Bowman, A., Bray, V. J., Brozovic, M., Bryan, C., Buckley, M. R., Buie, M. W., Buratti, B. J., Bushman, S. S., Calloway, A., Carcich, B., Cheng, A. F., Conard, S., Conrad, C. A., Cook, J. C., Cruikshank, D. P., Custodio, O. S., Dalle Ore, C. M., Deboy, C., Dischner, Z. J. B., Dumont, P., Earle, A. M., Elliott, H. A., Ercol, J., Ernst, C. M., Finley, T., Flanigan, S. H., Fountain, G., Freeze, M. J., Greathouse, T., Green, J. L., Guo, Y., Hahn, M., Hamilton, D. P., Hamilton, S. A., Hanley, J., Harch, A., Hart, H. M., Hersman, C. B., Hill, A., Hill, M. E., Hinson, D. P., Holdridge, M. E., Horanyi, M., Howard, A. D., Howett, C. J. A., Jackman, C., Jacobson, R. A., Jennings, D. E., Kammer, J. A., Kang, H. K., Kaufmann, D. E., Kollmann, P., Krimigis, S. M., Kusnierkiewicz, D., Lauer, T. R., Lee, J. E., Lindstrom, K. L., Linscott, I. R., Lisse, C. M., Lunsford, A. W., Mallder, V. A., Martin, N., McComas, D. J., McNutt, R. L., Mehoke, D., Mehoke, T., Melin, E. D., Mutchler, M., Nelson, D., Nimmo, F., Nunez, J. I., Ocampo, A., Owen, W. M., Paetzold, M., Page, B., Parker, A. H., Parker, J. W., Pelletier, F., Peterson, J., Pinkine, N., Piquette, M., Porter, S. B., Protopapa, S., Redfern, J., Reitsema, H. J., Reuter, D. C., Roberts, J. H., Robbins, S. J., Rogers, G., Rose, D., Runyon, K., Retherford, K. D., Ryschkewitsch, M. G., Schenk, P., Schindhelm, E., Sepan, B., Showalter, M. R., Singer, K. N., Soluri, M., Stanbridge, D., Steffl, A. J., Strobel, D. F., Stryk, T., Summers, M. E., Szalay, J. R., Tapley, M., Taylor, A., Taylor, H., Throop, H. B., Tsang,

C. C. C., Tyler, G. L., Umurhan, O. M., Verbiscer, A. J., Versteeg, M. H., Vincent, M., Webbert, R., Weidner, S., Weigle, G. E., White, O. L., Whittenburg, K., Williams, B. G., Williams, K., Williams, S., Woods, W. W., Zangari, A. M., and Zirnstein, E. (2015). The Pluto system: Initial results from its exploration by New Horizons. Science, 350(6258):aad1815.

Stern, S. A., Binzel, R. P., Earle, A. M., Singer, K. N., Young, L. A., Weaver, H. A., Olkin, C. B., Ennico, K., Moore, J. M., McKinnon, W. B., Spencer, J. R., New Horizons Geology, Geophysics, and Atmospheres Teams (2017). Past epochs of significantly higher pressure atmospheres on Pluto. Icarus, 287:47–53.

Strobel, D. F. (2008). N $_2$ escape rates from Pluto's atmosphere. Icarus, 193(2):612–619.

Strobel, D. F. (2021). Atmospheric Escape. In Stern, S. A., Moore, J. M., Grundy, W. M., Young, L. A., and Binzel, R. P., editors, The Pluto System After New Horizons, pages 363–377. University of Arizona, Tucson.

Strobel, D. F. and Zhu, X. (2017). Comparative planetary nitrogen atmospheres: Density and thermal structures of Pluto and Triton. Icarus, 291:55–64.

Summers, M., F. Strobel, D., and Gladstone, G. (1997). Chemical models of pluto's atmosphere. Pluto and Charon, -1:391.

Tian, F. and Toon, O. B. (2005). Hydrodynamic escape of nitrogen from Pluto. Geophys. Res. Lett., 32(18).

Trafton, L. and Stern, S. A. (1983). On the global distribution of Pluto's atmosphere. Astrophysical Journal, 267:872–881.

Trafton, L. M., Hunten, D. M., Zahnle, K. J., and McNutt, R. L., J. (1997). Escape Processes at Pluto and Charon. In Stern, S. A. and Tholen, D. J., editors, Pluto and Charon, page 475. Tucson: University of Arizona Press.

Trowbridge, A. J., Melosh, H. J., Steckloff, J. K., and Freed, A. M. (2016). Vigorous convection as the explanation for Pluto's polygonal terrain. Nature, 534(7605):79–81.

Wan, L., Zhang, X., and Bertrand, T. (2021). Effects of Haze Radiation and Eddy Heat Transport on the Thermal Structure of Pluto's Lower Atmosphere. ApJ, 922(2):244.

Weaver, H. A. (2021). Appendix B: The New Horizons Instrument Suite. In Stern, S. A., Moore, J. M., Grundy, W. M., Young, L. A., and Binzel, R. P., editors, The Pluto System After New Horizons, pages 641–644. University of Arizona, Tucson.

White, O. L., Moore, J. M., McKinnon, W. B., Spencer, J. R., Howard, A. D., Schenk, P. M., Beyer, R. A., Nimmo, F., Singer, K. N., Umurhan, O. M., Stern, S. A., Ennico, K., Olkin, C. B., Weaver, H. A., Young, L. A., Cheng, A. F., Bertrand, T., Binzel, R. P., Earle, A. M., Grundy, W. M., Lauer, T. R., Protopapa, S., Robbins, S. J., Schmitt, B., and New Horizons Science Team (2017). Geological mapping of Sputnik Planitia on Pluto. Icarus, 287:261–286.

Williams, J. P. and Cieza, L. A. (2011). Protoplanetary Disks and Their Evolution. ARA&A, 49(1):67–117.

Wood, B. E., Müller, H.-R., Zank, G. P., and Linsky, J. L. (2002). Measured Mass-Loss Rates of Solar-like Stars as a Function of Age and Activity. ApJ, 574(1):412–425.

Young, E., Young, L. A., Johnson, P. E., and PHOT Team (2021). More Evidence that Pluto's Atmosphere is Freezing Out: Central Flash Results from the 15-AUG-2018 Occultation. In AAS/Division for Planetary Sciences Meeting Abstracts, volume 53 of AAS/Division for Planetary Sciences Meeting Abstracts, page 307.06.

Young, E. F. and Binzel, R. P. (1993). Comparative Mapping of Pluto's Sub-Charon Hemisphere: Three Least Squares Models Based on Mutual Event Lightcurves. Icarus, 102(1):134–149.

Young, E. F., Galdamez, K., Buie, M. W., Binzel, R. P., and Tholen, D. J. (1999). Mapping the Variegated Surface of Pluto. AJ, 117(2):1063–1076.

Young, L. A. (2012). Volatile transport on inhomogeneous surfaces: I - Analytic expressions, with application to Pluto's day. Icarus, 221:80–88.

Young, L. A. (2013). Pluto's Seasons: New Predictions for New Horizons. Astrophysical Journal Letters, 766(2):L22.

Young, L. A. (2017). Volatile transport on inhomogeneous surfaces: II. Numerical calculations (VT3D). Icarus, 284:443–476.

Young, L. A., Kammer, J. A., Steffl, A. J., Gladstone, G. R., Summers, M. E., Strobel, D. F., Hinson, D. P., Stern, S. A., Weaver, H. A., Olkin, C. B., Ennico, K., McComas, D. J., Cheng, A. F., Gao, P., Lavvas, P., Linscott, I. R., Wong, M. L., Yung, Y. L., Cunningham, N., Davis, M., Parker, J. W., Schindhelm, E., Siegmund, O. H. W., Stone, J., Retherford, K., and Versteeg, M. (2018). Structure and composition of Pluto's atmosphere from the New Horizons solar ultraviolet occultation. Icarus, 300:174–199.

Young, L. A., Stansberry, J. A., Protopapa, S., Schmitt, B., Earle, A. M., Schenk, P. M., Howard, A. D., Stern, S., Weaver, H. A., Olkin, C. B., Ennico, K., and New Horizons Science Team (2020). Think globally, act locally: sublimation and condensation at Pluto's northern mid-latitudes. In American Astronomical Society Meeting Abstracts, volume 52 of American Astronomical Society Meeting Abstracts, page 438.01.

Yu, Q. and Tremaine, S. (1999). The Dynamics of Plutinos. AJ, 118(4):1873–1881.

Zahnle, K., Schenk, P., Levison, H., and Dones, L. (2003). Cratering rates in the outer Solar System. Icarus, 163(2):263–289.

Zhang, X., Strobel, D. F., and Imanaka, H. (2017). Haze heats Pluto's atmosphere yet explains its cold temperature. Nature, 551(7680):352–355.

Zhu, X., Strobel, D. F., and Erwin, J. T. (2014). The density and thermal structure of Pluto's atmosphere and associated escape processes and rates. Icarus, 228:301–314.

Appendix A

Approximating Temperatures with VT3D

This appendix, along with Chapter 2, was originally published in the Icarus "Pluto System, Kuiper Belt, and Kuiper Belt Objects" Special Issue (Johnson et al., 2021b).

A.1 Temperature from Analytic Approximation

Volatile Transport 3D (VT3D) uses an analytic approximation of the temperature evolution as an initial solution for the more accurate numerical solution. On its own, the analytic solution is often a good approximation and it is computationally more expedient. This appendix explains how to use the analytic approximation to calculate surface pressures over a period of one Pluto orbit, using the reference model as described in Chapter 2.

The diurnally- and spatially-averaged incident insolation $S(t)$ can be represented using an analytic Fourier approximation:

$$S_0 = \frac{1}{P}\int_0^P S(t)dt \tag{A.1}$$

$$S_m = \frac{2}{P}\int_0^P S(t)e^{-im\omega t}dt \qquad m > 0 \tag{A.2}$$

where P is the period of the solar forcing (in this case, one Pluto year) and ω is the corresponding frequency. m is an integer corresponding to the mth Fourier term. For the reference model insolation, the first 11 Fourier terms are provided in Table A.1. These terms are for the diurnally- and spatially-averaged insolation onto the N_2-covered regions. The diurnally-averaged incident insolation as a function of latitude λ can be calculated via:

$$\overline{S(\lambda,t)} = \frac{\sin\lambda\sin\lambda_0 h_{max} + \cos\lambda\cos\lambda_0\sin h_{max}}{\pi}\frac{S_{1AU}}{r^2} \tag{A.3}$$

where λ_0 is the subsolar latitude, $S_{1AU} = 1361$ W m^{-2}, and r is the heliocentric distance, in AU. The maximum illuminated hour angle at that latitude, h_{max}, can be found using: $\cos h_{max} = max(1, min(-\tan\lambda\tan\lambda_0, 1))$. The time variable, t, represent time within in one Pluto year, and timesteps must be larger than one Pluto day (we used $\Delta t = 0.5$ Earth years). To spatially-average over the N_2-covered regions, we calculate:

$$S(t) = \frac{\int_{N_2}\overline{S(\lambda,t)}\Omega d\Omega}{\int_{N_2}\Omega d\Omega} \tag{A.4}$$

where Ω is the solid angle area of a patch on the surface covered by N_2 and the integral is performed over all patches.

Table A.1: Fourier terms for the incident insolation for the reference model.

m	S_m $[W/m^2]$
0	0.220561
1	0.115454 - 0.136762i
2	0.043688 - 0.068281i
3	0.015757 - 0.029367i
4	0.007107 - 0.011570i
5	0.003849 - 0.004378i
6	0.002244 - 0.001651i
7	0.001404 - 0.000616i
8	0.000920 - 0.000234i
9	0.000615 - 0.000097i
10	0.000408 - 0.000062i

These insolation terms can be converted into temperatures using the following equation:

$$T(\zeta,t) = -\frac{F\zeta}{\Gamma\sqrt{\omega}} + T_0 + Re\left[\sum_{m=1}^{M} T_m e^{im\omega t}e^{\sqrt{im}\zeta}\right] \tag{A.5}$$

T_0 is the average temperature assuming thermal emission balances solar insolation and internal heat flux, F: $T_0 = ([(1-A)S_0 + F]/\epsilon\sigma)^{1/4}$. $\zeta = z/Z$ is the unitless depth of the layer, scaled by the skin depth, $Z = \sqrt{k/(\rho c\omega)}$. For N_2 ice, we use density $\rho = 1000$ kg m^{-3}, specific heat c =

1300 $J\ kg^{-1}\ K^{-1}$, and calculate the heat conductivity k based on the selected thermal inertia value ($\Gamma = \sqrt{k\rho c}$). For surface temperatures, the depth $z = 0$.

Each temperature Fourier coefficient for $m > 0$ is given by:

$$T_m = \frac{(1-A)S_m}{\Phi_E(T_0)} \frac{4}{4 + \sqrt{im}\Theta_S(T_0) + im\Theta_A(T_0)} \qquad m > 0 \tag{A.6}$$

where Φ_E is the derivative of the thermal emission with respect to temperature:

$$\Phi_E(T_0) = 4\epsilon\sigma T_0^3 \tag{A.7}$$

where the Stefan-Boltzmann constant $\sigma = 5.67$ x 10^{-8} W m^{-2}. The dimensionless thermal parameters Θ_S (buffering of volatile temperature due to thermal conduction to neighboring layers) and Θ_A (buffering due to latent heat of sublimation) are defined as:

$$\Theta_S(T_0) = \frac{\sqrt{\omega}\Gamma}{\Phi_E(T_0)/4} \tag{A.8}$$

$$\Theta_A(T_0) = \frac{\omega \frac{L_s}{f_v g} \frac{dp_s}{dT_V}\Big|_{T_0}}{\Phi_E(T_0)/4} \tag{A.9}$$

where L_s is the latent heat of sublimation for N_2: approximately 2.7 x 10^5 J kg^{-1} for α-phase (below 35.6 K) and 2.4 x 10^5 J kg^{-1} for β-phase (above 35.6 K). The surface gravity g is 0.62 m s^{-2}. The fraction of the surface covered by nitrogen ice, using our reference map, f_v, is 0.102. dp_s/dT_V is the derivative of the vapor pressure with respect to the volatile temperature, evaluated at T_0:

$$\frac{dp_s}{dT_V}\bigg|_{T_0} = \frac{L_s m_V p_s(T_0)}{k_B T_0^2} \tag{A.10}$$

where m_v is the molecular mass of N_2, $p_s(T_0)$ is the equilibrium vapor pressure above solid N_2 at temperature T_0, and k_B is the Boltzmann constant.

A.2 Selecting Albedo, Thermal Inertia, and Emissivity

As described in Chapter 2 VT3D has three free parameters that describe the nitrogen frost: the Bond albedo, A, the thermal inertia, Γ (in units of "tiu", J m^{-2} K^{-1} s$^{-1/2}$), and the emissivity,

ϵ. We select values for A and Γ, and then choose a corresponding value for ϵ such that the pressure predicted by the model at the time of the New Horizons flyby is 11.5 μbar. In Chapter 2, we iteratively calculate pressures with different emissivities until we find a solution that predicts the correct pressure in 2015. Here, we present a polynomial fit to the relationship this process derived. The coefficients k_i (which are each a function of A) in Table A.2 can be used along with the equation below to calculate the emissivity needed for the chosen albedo and thermal inertia value. The relationship predicts the necessary emissivity to within 2% of the correct value for most A and Γ values. Once the emissivity value for the chosen A and Γ has been calculated, Equation A.5 can be used to calculate the temperature at every point t within Pluto's orbit.

$$\epsilon(A,\Gamma) = k_0(A) + k_1(A)\Gamma + k_2(A)\Gamma^2 + k_3(A)\Gamma^3 + k_4(A)\Gamma^4 \tag{A.11}$$

Table A.2: Coefficients (as a function of albedo) needed to calculate the emissivity.

Albedo	$\mathbf{k}_0$	$\mathbf{k}_1$	$\mathbf{k}_2$	$\mathbf{k}_3$	$\mathbf{k}_4$
0.500	2.378e+00	-2.141e-03	1.760e-06	-7.190e-10	1.150e-13
0.525	2.254e+00	-2.116e-03	1.804e-06	-7.581e-10	1.240e-13
0.550	2.128e+00	-2.081e-03	1.835e-06	-7.910e-10	1.319e-13
0.575	2.001e+00	-2.033e-03	1.851e-06	-8.167e-10	1.385e-13
0.600	1.872e+00	-1.974e-03	1.855e-06	-8.378e-10	1.447e-13
0.625	1.741e+00	-1.901e-03	1.840e-06	-8.488e-10	1.488e-13
0.650	1.607e+00	-1.808e-03	1.795e-06	-8.429e-10	1.496e-13
0.675	1.473e+00	-1.700e-03	1.731e-06	-8.268e-10	1.484e-13
0.700	1.336e+00	-1.575e-03	1.642e-06	-7.961e-10	1.444e-13
0.725	1.198e+00	-1.430e-03	1.521e-06	-7.467e-10	1.365e-13
0.750	1.060e+00	-1.272e-03	1.378e-06	-6.843e-10	1.260e-13
0.775	9.222e-01	-1.097e-03	1.206e-06	-6.034e-10	1.115e-13
0.800	7.870e-01	-9.185e-04	1.026e-06	-5.191e-10	9.667e-14
0.825	6.551e-01	-7.360e-04	8.343e-07	-4.262e-10	7.994e-14
0.850	5.288e-01	-5.562e-04	6.371e-07	-3.277e-10	6.177e-14
0.875	4.102e-01	-3.872e-04	4.459e-07	-2.302e-10	4.352e-14
0.900	3.022e-01	-2.428e-04	2.810e-07	-1.458e-10	2.766e-14
0.925	2.064e-01	-1.265e-04	1.449e-07	-7.470e-11	1.412e-14
0.950	1.247e-01	-4.950e-05	5.585e-08	-2.858e-11	5.377e-15
0.975	5.706e-02	-1.293e-05	1.536e-08	-8.019e-12	1.512e-15